FEBRUARY 15, 1991

Analytical CHEMISTRY

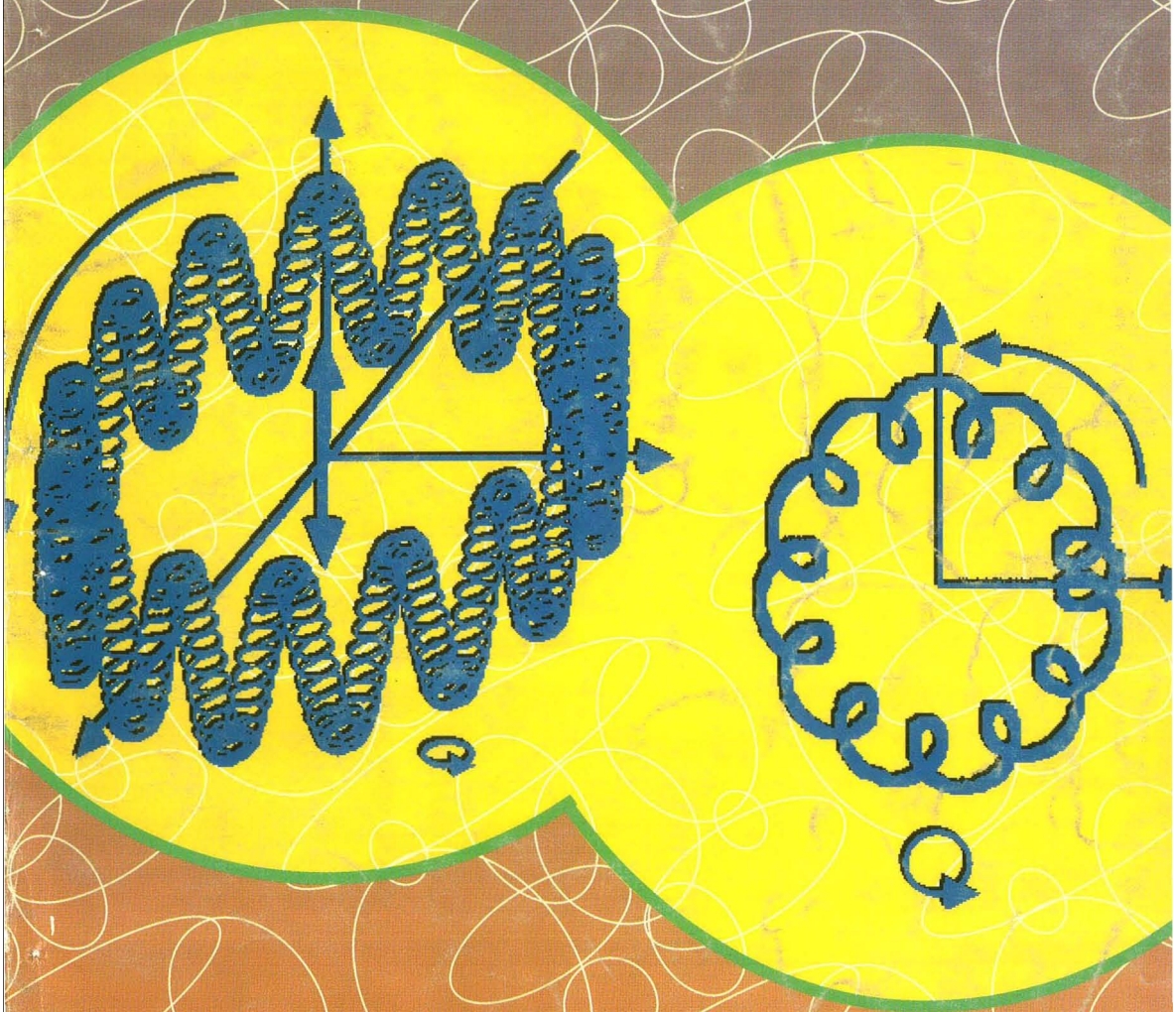

FT-ICRMS: THE TEENAGE YEARS

215 A

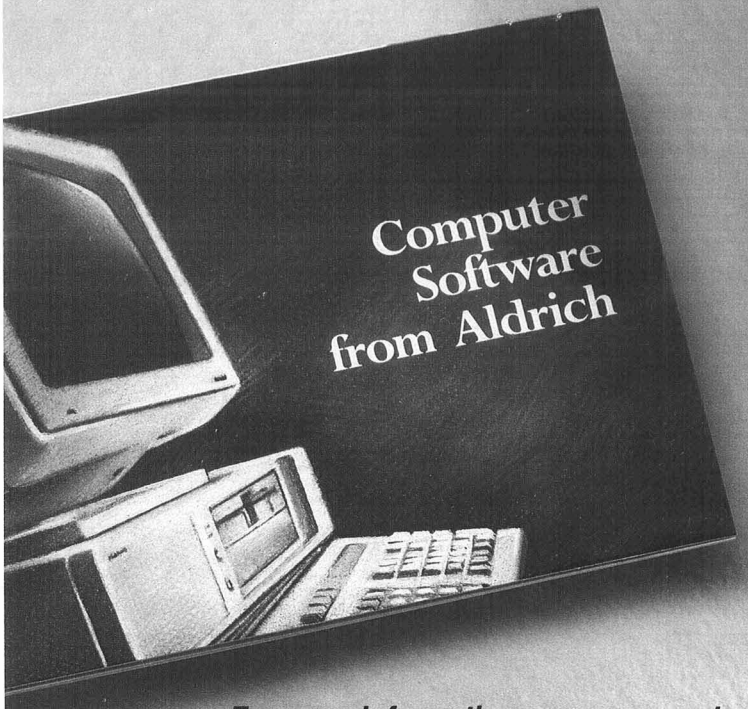

For more information on our computer products, please call for our Computer Software Brochure at 800-231-8327.

Aldrich Vapor-Phase FT-IR Library for the HP 59970C IRD Chemstation

A new FT-IR library, produced on the HP 59970B IR detector and optimally formatted for searching with the HP 59970C IRD Chemstation, is the fifth generation infrared collection at Aldrich.

Library features include:

- Over 5,000 IR spectra of organics
- Additional data—boiling point, CAS number, density, melting point, molecular formula, molecular weight, refractive index and RTECS number.
- Fully cross-referenced to the other Aldrich FT-IR and Safety publications.

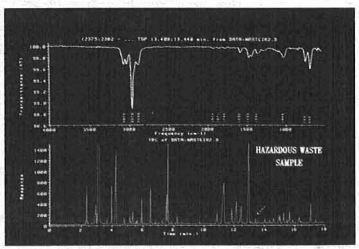

Z21,400-0; Z21,401-9

IBM is a registered trademark of International Business Machines Corp. VAX is a trademark of Digital Equipment Corp.

Z21,399-3

NIST/EPA/MSDC Mass Spectral Database on CD-ROM

A database of over 53,000 complete mass spectra with structures for 96% of the compounds. One can identify unknown spectra and locate spectra of compounds with specific characteristics. EPA approved for the analysis of Tentatively Identified Compounds (TICs). **For IBM® personal computers.**

Searchable by:

- chemical name • empirical formula
- CAS number • molecular weight
- user spectra • sequential spectra
- database identification number
- abundance of major peaks

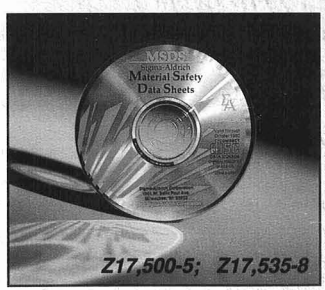

Z17,500-5; Z17,535-8

Sigma-Aldrich Material Safety Data Sheets

A database of over 58,000 complete, printable material safety data sheets with chemical structures. We can accommodate single and multiple PC and Macintosh users with CD-ROM software which is searchable by over 290,000 names/synonyms, CAS number, molecular formula and more. **Magnetic tape for IBM® or VAX™ mainframe systems is also available.** An annual subscription includes quarterly updates.

chemists helping chemists in research & industry

aldrich chemical co.

P.O. Box 355, Milwaukee, WI 53201 USA • Phone (414) 273-3850 • 800-558-9160 & FAX 800-962-9591

Come visit us at Pittcon! Booth number 1665

CIRCLE 1 ON READER SERVICE CARD

Install Confidence In Your Lab.

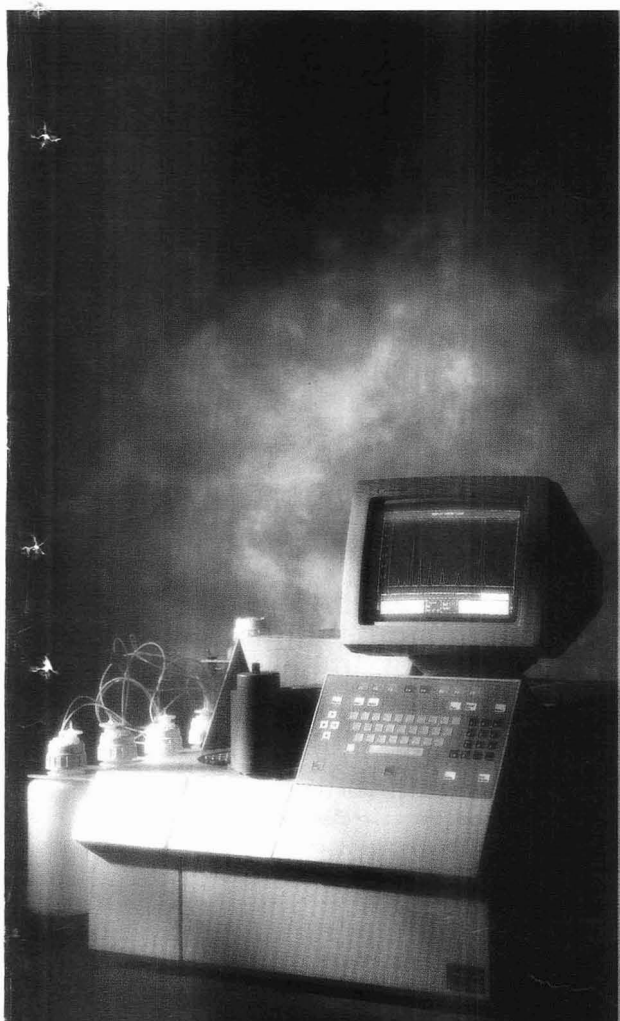

See us at the Pittsburgh Conference — Booth #4162.

Perkin-Elmer's new Integral 4000 liquid chromatograph will enhance your confidence in analysis.

It provides all information needed to satisfy GLP, GMP, and regulatory agencies while providing overall improvement in data quality: instrument diagnostics, column performance tests, error checking, and system precision tests.

To assure reliability, each instrument design is tested for thousands of hours before it ever reaches your lab.

And the Integral 4000 is compatible with PE Nelson LIMS systems, offering you more data-handling capability than ever before.

And like all Perkin-Elmer products, it is backed by all the power of PE, including PE XPRESS—ready to ship in-stock consumables within 24 hours.

For literature on the Integral 4000, call us at 1-800-762-4000. Or contact your local sales office for more information on Perkin-Elmer LC products to make your lab more productive.

With confidence in analysis.

PERKIN ELMER

The Perkin-Elmer Corporation
Norwalk, CT 06859-0012

The System Suitability Test (SST) checks the effectiveness of the system in compliance with standard protocols.

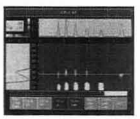

A real time topographical display of spectral data to validate method integrity.

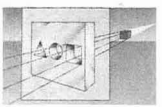

The Integral 4000 validates your method against the instrument configuration to ensure correct results.

Monitoring of the complete system performance minimizes error.

Perkin-Elmer combines experience, expertise, and worldwide resources to provide unmatched products, service, and support for analytical laboratories.

Circle 108 for Information only.
Circle 109 for Sales Call.

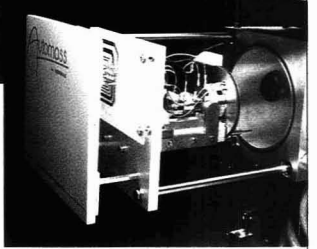

Automass

The Power of Original Thinking

When Nermag set out to develop the premier Automated Benchtop GC/MS Workstation, we were aware there was a need - *your need*, for more analytical power. Power that is simple to use, yet flexible enough to tackle the toughest problems. A true research-grade mass spectrometer was required, not a compromised mass analyzer camouflaged by glitzy game-show software.

Introducing Automass, the benchtop mass spectrometer that only Nermag could build, and the only one of its kind in the world today. The basis of Automass is a state of the art quadrupole with plug-in prefilters and an optimized Ionization Source for EI, CI, and negative ions. Our original Off Axis Ion - Photon Conversion Detector and patented Resolver electronics are enhanced by a differentially pumped vacuum system for real CI spectra.

Automass is controlled by our exclusive LUCY™ software. LUCY does window after window of instrument configuration setting, auto or manual tuning, calibration, mass spectra, chromatographic trace, and data reduction; while simultaneously examining the complete library and quantifying results. You'll Love LUCY.

Automass can flawlessly perform routine analysis all day virtually unattended, or help you tackle the most difficult analytical problem.

Automass advances Mass Spectrometry into the 90's.

Powerfully.

DELSI NERMAG
INSTRUMENTS

France: Delsi-Nermag Instruments, 98terBlvd. Heloise, Argenteuil 9500, Tel: (1) 39.47.66.22, Fax: (1) 39.47.85.66
USA: Delsi Inc., 15701 West Hardy Rd. Houston, TX 77060, Tel: (713) 847-0811, Fax (713) 591-2132
Netherlands: Delsi Instruments BV, Gebouw aetsvelt, van Houten Ind Pk 11, 1381 Weesp, Tel: (0)2940-19611
U.K.: Delsi Instruments Ltd, 38 Thrapston Rd., Brampton, Huntington, Cambs PE 18 8TE, Tel: 0480 431 609
West Germany: Delsi Instruments Gmbh, Oizbachstr 1 D4020 Mettmann, Tel: 02104/25086-87-88
Belgium: Intersmatt, 103, Av. des Volontaires, 1160 Bruxelles, Tel: 2 733.16.32

CIRCLE 30 ON READER SERVICE CARD

FEBRUARY 15, 1991
VOLUME 63
NUMBER 4

The Audit Bureau

ANCHAM
63(4) 205A–256A/305–400 (1991)
ISSN 0003-2700

ANALYTICAL CHEMISTRY (ISSN 0003-2700) is published semimonthly by the American Chemical Society at 1155 16th St., N.W., Washington, DC 20036. Editorial offices are located at the same ACS address (202-872-4570; FAX 202-872-4574; Bitnet rmh96@cas; TDD 202-872-8733). Second-class postage paid at Washington, DC, and additional mailing offices. Postmaster: Send address changes to ANALYTICAL CHEMISTRY Member & Subscriber Services, P.O. Box 3337, Columbus, OH 43210.

Claims for missing numbers will not be allowed if loss was due to failure of notice of change of address to be received in the time specified; if claim is dated (a) North America: more than 90 days beyond issue date, (b) all other foreign: more than one year beyond issue date, or if the reason given is "missing from files."

Advertising Management: Centcom, Ltd., 500 Post Rd. East, Westport, CT 06880 (203-226-7131)

1991 subscription rates include air delivery outside the U.S., Canada, and Mexico

	Members	Nonmembers (personal)	Nonmembers (institutional)
U.S.	31	69	289
Canada and Mexico	67	105	325
Europe	112	210	370
Other countries	131	229	389

Nonmember rates in Japan: Rates above do not apply to nonmember subscribers in Japan, who must enter subscription orders with Maruzen Company Ltd., 3–10 Nihonbashi 2-chome, Chuo-ku, Tokyo 103, Japan. Tel: (03) 272-7211.

For multi-year and other rates, call toll free 800-227-5558 in the U.S. and Canada; in the Washington, DC, metropolitan area and outside the U.S., call 202-872-4363; FAX 202-872-4615.

Subscription orders by phone may be charged to VISA, MasterCard, or American Express. Call toll free 800-333-9511 in the continental U.S.; outside the continental U.S., call 614-447-3776. Mail orders for new and renewal subscriptions should be sent with payment to American Chemical Society, Department L-0011, Columbus, OH 43268-0011.

Subscription service inquiries and changes of address (Include both old and new addresses with ZIP code and *recent mailing label*) should be directed to the ACS Columbus address noted above. Please allow six weeks for changes to become effective.

ACS membership information: Lorraine Bowlin (202-872-4567)

Single issues, current year, $13.00 except review issue, $26.00, and LabGuide, $50.00; **back issues and volumes and microform editions** available by single volume or back issue collection. For information or to order, call the number listed for subscription orders by phone; or write the Microform & Back Issues Office at the Washington address.

Analytical® CHEMISTRY

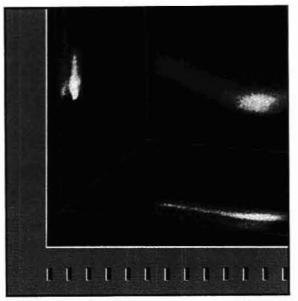

BRIEFS

Articles

* Corresponding author

How to Succeed at ppb Analysis...

Simple! Use only the highest purity gases. But to maintain gas purity throughout your delivery system and into your instrument, your gas handling equipment must be ultra-clean and prevent contamination. Inboard diffusion is the major culprit in the contamination of high purity gases.

Solution: The Matheson Model 9001 Pressure Control Module with a 9300 ULTRA-LINE regulator and valve will deliver your high purity gas with virtually no inboard diffusion.

The Matheson Pressure Control Module achieves this by utilizing semiconductor gas handling technology: 316L stainless steel body and diaphragm, metal-to-metal seals, clean room assembly and packaging; electropolished stainless steel tubing, butt welded VCR and CGA connections and a permanent wall mountable installation. The entire system is then tested to meet a minimum inboard helium leak rate of 1×10^{-9} cc/sec.

At Matheson we understand your needs because we are solving them every day, and allowing you to challenge the limits of ppb analysis.

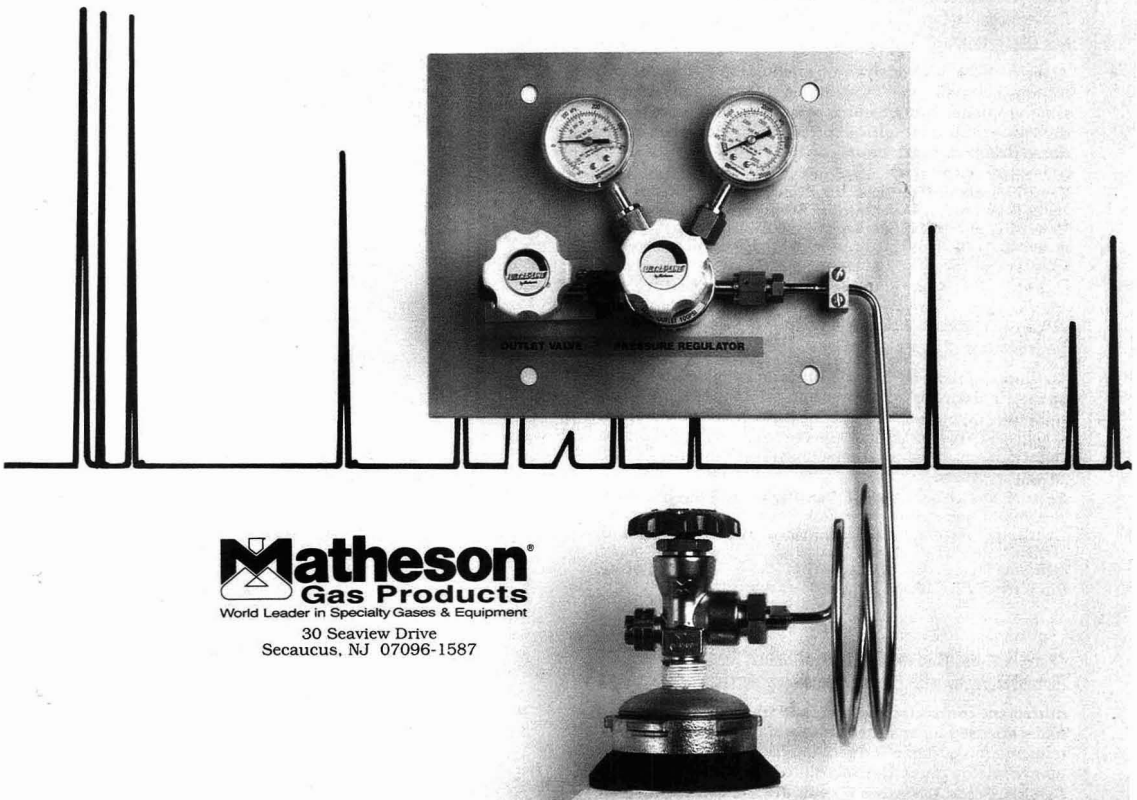

Matheson®
Gas Products
World Leader in Specialty Gases & Equipment

30 Seaview Drive
Secaucus, NJ 07096-1587

SEE US AT PITTSBURGH CONFERENCE BOOTH 2202.

CIRCLE 90 ON READER SERVICE CARD

Technical Notes

Restek Corporation . . .
Your #1 Source for Chemical Standards

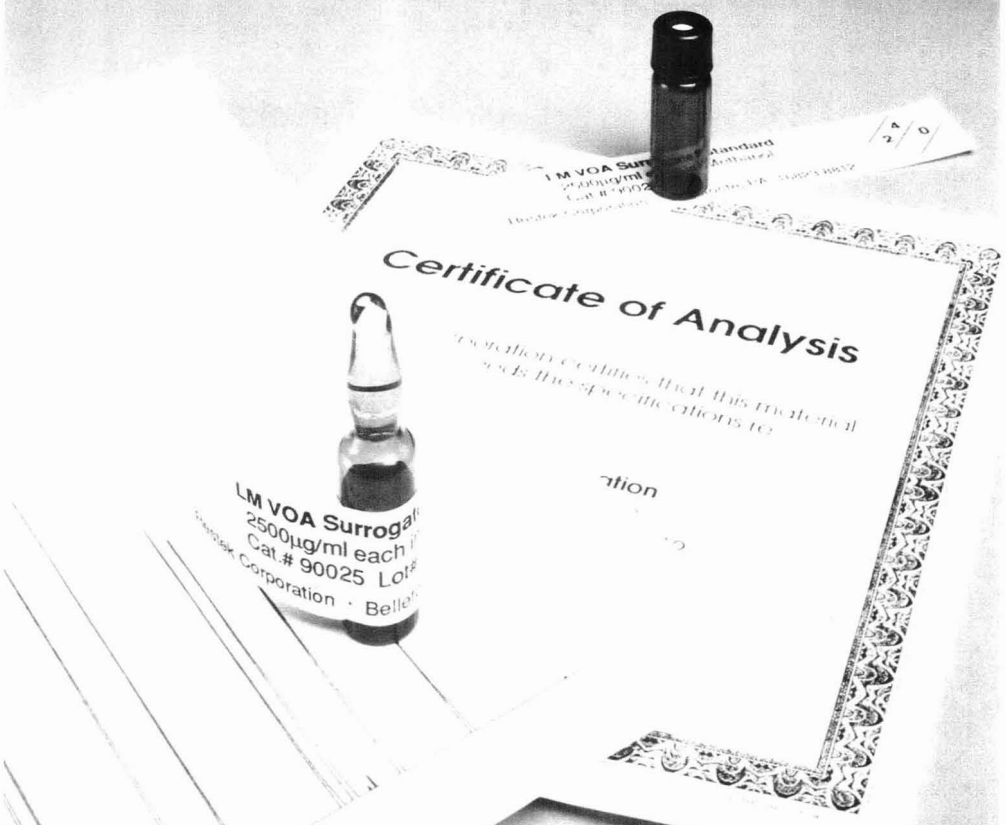

Yes! Restek manufactures environmental standards for the EPA 600 series, Contract Lab Program, and 502.2 methods. These standards are extensively tested to ensure accuracy and come with a certificate of analysis to prove it!

Our unique packaging includes an ampule cracker™, a silanized amber vial, and an extra label for sample transfer and storage. Complete QA data packs are available for each lot of material produced.

The quality of the data your lab generates depends on the quality of the reference standards you use. *Can your lab afford to use anything less than the best?*

Restek Corporation
110 Benner Circle • Bellefonte, PA 16823-8812
Phone: 800-356-1688 • Fax: 814-353-1309

RESTEK CORPORATION

Visit us at Pittsburgh Conference Booth #2253

CIRCLE 120 ON READER SERVICE CARD

Separate Complex Hydrocarbon Mixtures and Get...

- High Resolution
- High Efficiency
- Reproducibility

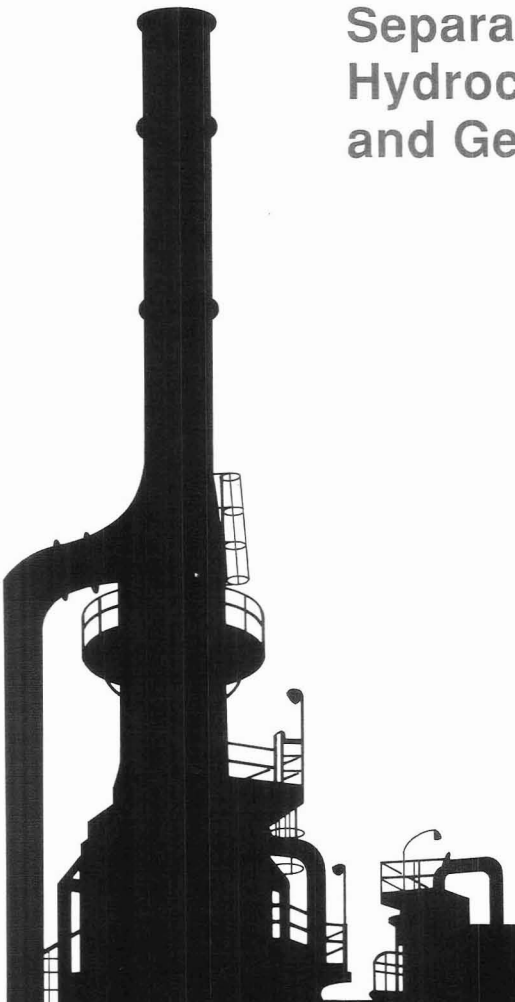

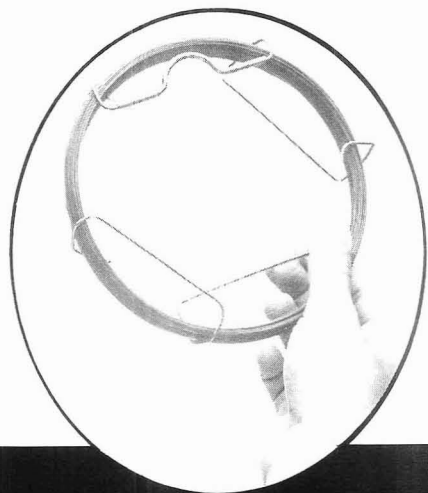

Our Petrocol™ DH family of capillary columns is specifically designed and tested for detailed GC hydrocarbon analysis. You can separate closely eluting isomers and light hydrocarbon gases, or achieve detailed separations of highly complex mixtures.

Each fused silica column is rigorously tested to ensure highly consistent polarity and film thickness. Now you can be assured of consistent column-to-column performance.

For more information, call our Technical Service Department at 814-359-3041 and ask for our new *Petroleum/Chemical Applications Guide.*

Fused Silica Capillary Columns

Petrocol DH 50.2
50m x 0.20mm x 0.50μm d_f

Petrocol DH
100m x 0.25mm x 0.50μm d_f

Petrocol DH 150
150m x 0.25mm x 1.0μm d_f

Fused silica columns manufactured under HP US Pat. No. 4,293,415.

To Order, Call: 800-247-6628
TWX: 510-670-3600 FAX: 814-359-3044

SUPELCO
SEPARATION TECHNOLOGIES
DIVISION OF ROHM AND HAAS

CIRCLE 128 ON READER SERVICE CARD

NEWS

Bucky Ball Chemistry

Now that a synthesis of Buckminsterfullerene, the soccer-ball-shaped C_{60} molecule, and its oblong-shaped C_{70} analogue has been found, scientists are scrambling to unravel their chemistry. One of the first reports comes from researchers at the Santa Barbara and Los Angeles campuses of the University of California. They recently announced that electrochemical experiments—cyclic voltammetry and bulk electrolysis—found that both forms accept up to three electrons per molecule. "Both have almost identical tendencies to accept electrons," explains Santa Barbara chemist Fred Wudl. This high electron affinity suggests that the fullerenes could have electrical properties similar to semiconductors, although Wudl says the data also suggest that they can take a metallic form.

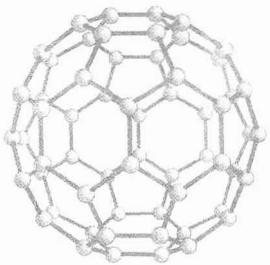

The experiments were run in dichloromethane, *o*-dichlorobenzene, tetrahydrofuran, and benzonitrile. Wudl also reports that the electrolysis experiments resulted in some interesting color changes. For instance, the purple color of C_{60} in *o*-dichlorobenzene turned silver brown when one electron was added. Further details will appear in the *Journal of the American Chemical Society.*

Analytical Instruments for Undergraduates

Hewlett-Packard has provided 18 colleges and universities with benchtop GC/MS systems for their undergraduate laboratories. Each system is valued at $53,000. "The purpose of the grants is to help upgrade the level of undergraduate chemical education by exposing students to modern instrumentation," said HP's grant administrator and R&D manager James Serum.

For 1991, grants were awarded to Arkansas College, Batesville; California State University, Long Beach; Calvin College, Grand Rapids, MI; Massachusetts Institute of Technology, Cambridge; Northern Arizona University, Flagstaff; the University of Michigan, Ann Arbor; the University of Minnesota, Minneapolis; the University of Puerto Rico—Mayaguez; and the University of Wisconsin—Stevens Point. Nine grants will also be awarded in 1992. Instruments will go to Beloit College, Beloit, WI; the College of William and Mary, Williamsburg, VA; Hendrix College, Conway, AR; James Madison University, Harrisonburg, VA; Skidmore College, Saratoga Springs, NY; Union College, Schenectady, NY; the University of Louisville, KY; the University of Texas at El Paso; and the University of Wisconsin—Eau Claire.

Proposed IUPAC Bioanalytical Nomenclature

Because of the involvement of different disciplines in the practice of clinical laboratory medicine, the terminology is often vague, inexact, and, in some cases, at variance with conventional and official terminology. To rectify this situation, the International Federation of Clinical Chemistry, the International Union of Pure and Applied Chemistry, and the International Union of Biochemistry have compiled a general set of definitions. This document includes sections on general terminology as well as terms that describe body fluids, enzymology, and immunology. Other relevant topics will be included in subsequent reports.

Copies of the document are available by writing to ANALYTICAL CHEMISTRY at our Washington, DC, address. Comments on the definitions are welcome and should be sent by October 31 to Carl Burtis, Oak Ridge National Laboratory, P.O. Box 2008, Bldg. 4500-M, MS-6194, Oak Ridge, TN 37831.

CFCs: Worse Than Ever

Recent measurements of ozone-destroying chlorofluorocarbons (CFCs) by Sherwood Rowland's group from the University of California—Irvine indicate that levels of these chemicals in the atmosphere continue to rise. "As of June 1990," explains Rowland, "the concentrations of CFC-11 and CFC-12, the two compounds long identified as the major CFCs in the atmosphere, are growing at a steady rate. The yearly release of CFC-13 [used primarily to clean electronics] is increasing rapidly and has reached a level almost as large as the other two."

Rowland's analysis was based on measurements of air samples from different locations in the Pacific ranging from Alaska to New Zealand. "The total amount of CFCs going into the atmosphere in 1989 appears to be the largest of any year," adds Rowland. Because CFCs take approximately 10 years to reach the stratosphere where they can remain for up to 100 years, it appears that the worst ozone depletions are yet to come.

For Your Information

The Association of Official Analytical Chemists (AOAC) has announced newly approved analytical methods in pesticide formulations and disinfectants, drugs, foods, microbiology, feeds and fertilizers, and environmental quality. For more information, contact AOAC, Suite 400, 2200 Wilson Blvd., Arlington, VA 22201-3301 (703-522-3032, fax: 703-522-5468).

The Board of Chicago's famed Museum of Science and Industry has approved a $50 million renovation program. Included in the plans are new exhibits that explore recent developments in lasers, genetics, robotics, and a "trip" through various simulated climates and environments.

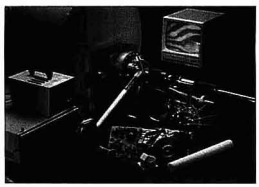

Laser Probe™ FT/MS®

New surface probe instrument combines the power of EXTREL's 2001 FT/MS system with laser ablation and sample viewing for solving tough materials characterization problems. A versatile, easy-to-use industrial problem solver for analysis of advanced polymers, biopolymers, catalysts, ceramics, superconductors and fibers. Features high-resolution, accurate mass measurement, simultaneous measurement of all ions and MS/MS. Call EXTREL FTMS at (608) 273-8262.

CIRCLE 35

Components for FT/MS® and ICR

Build award-winning FT/MS systems with the finest FT/MS components available: data systems, electronic modules, trapped-ion cells, vacuum components and superconducting magnets. A patented dual ion source/analyzer provides excellent sensitivity for many ionization methods. Nonmagnetic cells are manufactured through proprietary processes that minimize magnetic susceptibility and engineered for easy maintenance and cleaning. EXTREL FTMS components save time, money and frustration when building an FT/MS System. Call EXTREL FTMS at (608) 273-8262.

CIRCLE 35

Superconducting Magnets for Instruments

EXTREL FTMS superconducting magnets are designed for versatility and ease of use. Large, horizontal bores provide convenient access and positioning in powerful, highly homogenous central fields. Low field drift provides high magnetic stability for long periods. Proprietary engineering means low maintenance, low coolant consumption, reliable operation and rapid installation. Available with bores up to eight inches (20 cm) and in multiple field strengths with a variety of accessories. Call EXTREL FTMS at (608) 273-8262.

CIRCLE 35

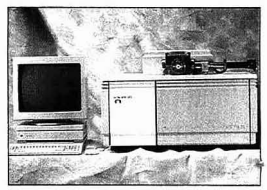

benchmark™ LC/MS

benchmark, a liquid chromatography/mass spectrometry (LC/MS) system, is designed to be a fully integrated LC detection system. It provides highly accurate qualitative and quantitative analysis for both target and unknown compounds separated by high-performance liquid chromatography (HPLC). The MS detector fits well into LC laboratories, requiring only 37 inches of bench space. With the ThermaBeam™ particle beam interface or Thermospray, the system has the versatility to solve a wide range of problems. For more information, call Extrel Corp. at (412) 963-7530.

CIRCLE 36

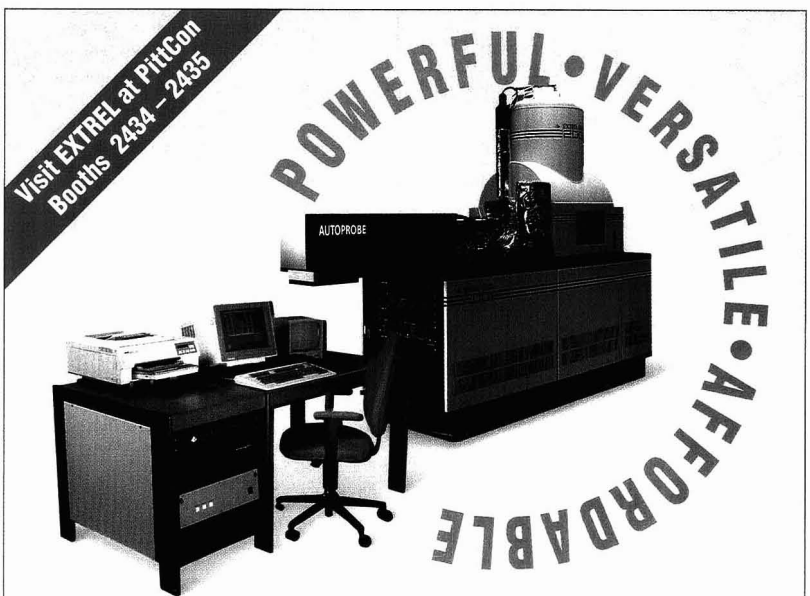

2001 Fourier Transform Mass Spectrometer

EXTREL's new 2001 FT/MS® system makes high-performance analytical mass spectrometry *easy* and *affordable*. This problem solver gives you unprecedented analytical power: ultra-high resolution better than 1,000,000 at m/z 131... accurate mass measurements better than 2 ppm ... mass ranges upwards of 16,000 u ... and pico to attomole detection limits. Plus, our patented dual ion source/analyzer design allows you to trap and then manipulate ions in both space and time.

Our revolutionary SWIFT™ method provides unmatched experimental versatility. And our software — the most powerful in the industry — is menu-driven, making it easy to use. Plus, the unique Autoprobe™ improves sample throughput.

Power. Versatility. Ease of use. At an affordable price. Once again, EXTREL pushes technology further — giving you more in a mass spectrometer. For more information on the 2001 FT/MS system, call EXTREL FTMS today.

EXTREL

EXTREL FTMS • 6416 SCHROEDER ROAD • MADISON, WI 53711 • (608) 273-8262 • FAX (608) 273-8719

ELQ 400-3 Triple Quadrupole MS

Perform more high-level analyses with this flexible triple quad. Provides the widest array of inletting and ionization techniques in the industry: LC, GC, SFC or probes ... EI, CI or FAB for ThermaBeam™ particle beam MS. Plus, switch inletting techniques in minutes without venting. Full range of pumping options, mass ranges up to 4000 u and new 2000 data software for automatic data batching. Call Extrel Corp. at (412) 963-7530.

CIRCLE 36

Questor II High-Speed Process Analyzer

Over 98.5% uptime monitoring hundreds of process streams in production plants, pilot plants and process research facilities worldwide. Fast and accurate, it replaces multiple instruments to boost efficiency and provide rapid payback. Easy communications with control and host computers, enclosures for classed environments, ready-to-use statistical packages, menu-driven software and applications support from EXTREL process engineers. Call Extrel Corp. at (412)963-7530.

CIRCLE 36

CIRCLE 35 ON READER SERVICE CARD

FOURIER TRANSFORM ION CYCLOTRON RESONANCE MASS SPECTROMETRY: THE TEENAGE YEARS

Alan G. Marshall[1] and Peter B. Grosshans
Department of Chemistry
The Ohio State University
120 West 18th Avenue
Columbus, OH 43210

Fourier transform ion cyclotron resonance mass spectrometry (FT-ICRMS or FT-MS) is a technique that effectively converts ionic mass-to-charge ratio, m/q, to an experimentally measurable ion cyclotron orbital frequency, ν_c, given approximately by

$$\nu_c = \frac{qB_0}{2\pi m} \text{ (S.I. units)} \qquad (1)$$

in which B_0 is the strength of an applied static magnetic field. Because frequency can be measured more accurately than any other physical property (*1*), FT-ICRMS offers potentially ultrahigh mass measurement accuracy (1 part in 10^9 or better) as well as other advantages that will be discussed later. Note that the chemical formula of an ion may be determined directly from its mass alone, if the mass is measured accurately: for example, N_2^+ at 28.0056 u versus CO^+ at 27.9944 u.

Although ions in a static magnetic field execute circular ICR orbital motion (see Figure 1), simply placing such ions between a pair of detection electrodes will not produce a signal, any more than placing a sample in an FT-NMR spectrometer will spontaneously generate an NMR signal. It is necessary to excite a packet of ions of a given mass-to-charge ratio coherently to larger ICR orbital radius, so that the spatially coherent orbiting ion packet induces an oscillating difference in charge between two opposed detection electrodes. Current will then flow (at the cyclotron frequency) between the detection plates. Forcing that current to pass through an impedance "converts" the current to a voltage difference between the electrodes. That voltage difference can then be amplified to give a time domain free ion decay signal (see glossary, p. 216 A) that can be digitized and Fourier transformed to yield a frequency domain spectrum. Conversion from the frequency scale to a mass (actually mass-to-charge ratio) scale may then be performed algebraically from Equation 1 or from more accurate expressions discussed below.

Seventeen years ago (*2*) the infant FT-ICRMS technique exhibited the same genetic traits that distinguished its FT-IR and FT-NMR spectroscopic forebears: the multiplex (Fellgett) advantages for speed (by a factor up to 10^6) or signal-to-noise ratio (S/N) (factor of up to 10^3) compared with its single-channel ICR parent technique, as well as the unique advantage of potentially ultrahigh resolving power. As with any promising youngster, FT-ICRMS grew rapidly in unforeseen ways, and behavioral flaws that were excusable in an infant soon became unacceptable for an adult. In this article, we describe the adolescent maturation of the FT-ICRMS technique.

The initial enthusiasm and early applications for FT-ICRMS were based on its highly linear behavior: In uniform magnetic (and no electric) field, m/q is linearly related to the observed ICR orbital frequency, ν_c (in Hz), according to Equation 1, and the detected FT-ICR signal (i.e., differential voltage induced between two infinite parallel electrodes) is directly proportional both to the number of ions of a given m/q value and to their cyclotron orbital radius.

For on-resonance single-frequency excitation between infinite parallel electrodes, the postexcitation cyclotron orbital radius of an ion is proportional to the product of the radiofrequency (rf) excitation voltage magni-

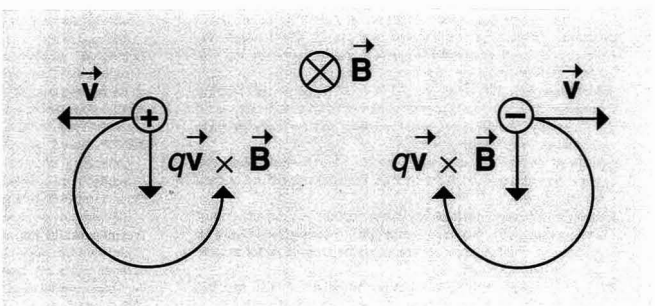

Figure 1. Magnetic force acting on a positive (left) and negative (right) ion, each with velocity, **v**, subjected to a static magnetic field, **B**, directed into the plane of the paper.
Note the opposite sense of rotation for ions of opposite charge, because changing the sign of q in Equation 2 ($\mathbf{F} = q\mathbf{v} \times \mathbf{B}$) changes the sign (and thus the direction) of the Lorentz magnetic force.

[1] Also a member of the Department of Biochemistry.

0003-2700/91/0363-215A/$02.50/0

tude and duration (*3*). In this idealized case, the mass-to-charge ratio of ions of any m/q value could be determined with ultrahigh precision simply by determining B_0 from the FT-ICR spectral frequency, ν_c, for ions of a single known m/q value. Moreover, the observed relative FT spectral magnitudes at various ν_c values would directly reflect the relative numbers of ions of corresponding m/q values.

However, as we shall see, an actual FT-ICR experiment requires that ions be confined ("trapped") within a finite volume bounded by conductive electrodes (which may be plates, screens, rods, or wires). Those electrodes necessarily produce spatially warped static and rf electric fields in the ion trap with several generally undesirable consequences. First, the relation between ICR orbital frequency and m/q becomes nonlinear, making mass calibration more difficult (*4–8*). Second, ICR signal strength no longer varies linearly with rf excitation magnitude and duration (*9*, *10*) or even ICR orbital radius (*9*, *11*, *12*), and (even worse) some of these nonlinearities are mass dependent. Third, coulomb forces between ions broaden and shift the mass spectral peaks (*6*, *13*, *14*). Finally, the spatially nonuniform excitation field may even eject ions axially before they can be detected (*15–19*).

Although a full analytical solution

Glossary

Broadband: Simultaneous transmission or detection covering a wide range of frequencies

Burst excitation (see also impulse excitation): A shaped brief rf waveform whose frequency domain spectrum covers a wide range centered at the excitation frequency

Critical mass: Ion mass above which ions cannot be trapped in stable ICR orbits (see Equation 7)

Cyclotron motion: Rotation of an ion about a fixed applied magnetic field (see Figure 7)

Daughter ions: Ions formed by nonreactive or reactive ion–neutral collisions

Differential charge, ΔQ: Charge induced on one detector electrode minus the charge induced on an opposed detector electrode

Differential voltage, ΔV: Voltage difference between two opposed detector (or transmitter) electrodes, usually connected through an impedance

Direct-mode ICR detection: Amplification and analog-to-digital conversion of the signal obtained directly from the differential voltage induced between the detector electrodes

Fellgett advantage: The advantage in speed (for a given resolution) or S/N (for a given total data acquisition period) gained by simultaneous detection of the whole spectrum rather than single-channel scanning of one spectral element at a time. For an N-point spectrum, the Fellgett speed advantage is a factor of N and the S/N advantage is $\sqrt{N}$

Free ion decay: Time domain ICR signal (by analogy to free-induction decay in magnetic resonance)

Frequency domain spectrum: Spectrum obtained by Fourier transformation of a time domain signal

Frequency sweep (chirp) excitation: Excitation waveform in which frequency varies linearly with time over a period that is short compared with the damping constant for exponential disappearance of the time domain ICR signal

Hadamard transform: A particular algorithm for encodement and decodement corresponding to simultaneous detection of the daughter ions of approximately half of the parent ions of interest

Harmonic frequency: An integral multiple of the fundamental frequency; the fundamental frequency is also known as the first harmonic frequency

Heterodyne mode ICR detection: As in direct mode, except that the detected differential voltage is amplified and multiplied by the output from a fixed ("carrier") frequency oscillator and low-pass-filtered to yield a relatively narrowband signal

Impulse excitation: dc excitation in such a short period that signals spanning effectively all of the spectral range of interest are excited simultaneously

Magnetron motion: Slow (typically a few hundred Hz) circular drift of an ion along a path of constant electrostatic potential (see Figure 7); magnetron motion occurs as a result of the crossed radial electric field and axial magnetic field

Mass calibration: In ICR, conversion of observed ICR spectral frequencies to accurate mass-to-charge ratios (see Equation 8)

Mass resolving power: $m/\Delta m$, in which m is ionic mass and Δm is the width of the mass peak (typically taken as the full width at half-maximum FT-ICR mass spectral peak height). Δm is also known as the mass resolution

Modulation: Variation (often sinusoidal) of one observable resulting from oscillation of some other quantity (e.g., variation in ICR orbital frequency, ν_c, because of trapping oscillation of ions between regions of different electric or magnetic field strength). The amplitude (AM) and/or frequency (FM) may be modulated

MS/MS: Mass spectrometry/mass spectrometry, in which the first stage of mass separation is designed to select parent ions of a given mass-to-charge ratio, and the second stage is designed to detect all of the daughter ions resulting from fragmentation or ion–molecule reaction of the initially selected parent ions

Narrowband: Transmission or detection covering a narrow range of frequencies

Parametric excitation and detection: In a hyperbolic ion trap, application or detection of the voltage between the (unbroken) ring electrode and the end cap electrodes

Parent ions: Ions selected in the first stage of an MS/MS experiment

Penning ion trap: A hyperbolic ion trap operating in an axial magnetic field

Quadrature: Used to denote either the second channel in a two-channel quadrature experiment or an experiment in which both the unshifted and 90° phase-shifted quadrature components of a signal are transmitted or detected simultaneously

Quadrupolar potential: Defined in Equation 6, it approximates the actual electrostatic potential near the center of an ICR ion trap and may be generated exactly by a hyperbolic trap (see p. 224 A)

Radial ejection: Excitation of ion cyclotron orbital motion to an ICR orbital radius larger than the transverse boundary of the ion trap

Reciprocity: The principle that relates the electric potential at a field point within an ion trap when a potential is applied to a detector electrode to the charge induced on that electrode by a unit charge placed at the same position (see p. 225 A)

Resonance: The condition in which the excitation frequency is the same as a natural frequency (e.g., cyclotron, magnetron, trapping, or combinations or multiples thereof) of the system

Sidebands: Signals (usually of reduced magnitude) that appear at equally spaced intervals above or below the fundamental frequency (see p. 223 A)

Solenoidal supercon magnet: A magnet constructed with superconducting wire wound around a cylinder so as to produce a strong magnetic field along the central axis

Spatial coherence: Ions bunched in a packet whose dimensions are much less than the ICR orbital radius

SWIFT: Stored waveform inverse Fourier transform, a means for generating an arbitrary excitation waveform for mass-selective excitation or ejection of ions (see p. 220 A)

Time domain ICR signal: Detected differential voltage between the ICR detector electrodes

Trapping oscillation: Axial back-and-forth motion of ions trapped between two plates to which a positive dc potential, relative to the other plates, has been applied

Two-dimensional ICR: Hadamard or Fourier methods for extending the Fellgett advantage to the first stage (i.e., parent ion selection) of an MS/MS experiment

***z*-ejection:** Excitation of ion-trapping oscillation to an amplitude exceeding the z-boundary of the trap

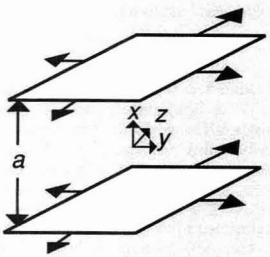

Excitation $V(x) = \frac{2x}{a} V_{ex}$

Detection $\Delta Q = -\frac{2x}{a} q$

Reciprocity $\frac{\Delta Q}{q} = \frac{-V(x)}{V_{ex}}$

Figure 2. The reciprocity principle, demonstrated for infinitely extended parallel planar electrodes located at $x = \pm a/2$.

If a potential V_{ex} is applied to the upper electrode and $-V_{ex}$ to the lower electrode, the potential anywhere between the electrodes is $V_{ex}(2x/a)$. By symmetry, the potential cannot depend on y or z; thus, only a linear function of x can satisfy Laplace's equation, $\nabla^2 V = 0$. Alternatively, if a point charge, q, is located somewhere between the electrodes, it can be shown that the difference, ΔQ, between the charge induced on the upper and lower electrodes is $-q(2x/a)$. The relationship, $\Delta Q/q = -V/V_{ex}$, illustrated here for infinitely extended electrodes, holds in general; we denote this relation as reciprocity.

for ion behavior in an electromagnetic ion trap is not feasible, most of the critical features of the problem may be understood from simplified models. We therefore begin with a brief review of ion cyclotron orbital motion in a uniform magnetic (and no electric) field, and then show how addition of a spatially uniform rf electric excitation field produced from two infinitely extended parallel electrodes generates an observable ICR signal at the frequency given by Equation 1.

The basis for optimal selection (by stored waveform inverse FT, or SWIFT, excitation) of ions of one or more m/q values is presented, along with two general approaches (Hadamard and Fourier) to two-dimensional (2D) experiments designed for MS/MS applications. Next, we show how the confinement of the ions in a finite electromagnetic box shifts the ICR orbital frequency and introduces two new kinds of natural motions (trapping and magnetron). Finally, we show how the placement of (and interconnections between) various electrodes affect the magnitude, frequency, and linearity of the detected signal(s), and how the inherent nonlinearity may be eliminated or exploited.

Linear ICR behavior

ICR orbital frequency, resolving power, radius and energy, and upper mass limit. At first glance, any attempt to describe the motion of as many as a million ions subjected to static magnetic as well as static and time-varying electric fields might appear dauntingly difficult. Fortunately, it can be shown that the center-of-mass motion of an ion packet (spatially coherent or not) is unaffected by ion–ion coulomb forces, provided that the applied magnetic field is spatially uniform, the applied electric field varies at most linearly with position, and no other species are present (*20*). These conditions are satisfied for the idealized case of ions of a given m/q in the region between two infinite parallel electrodes with an applied, uniform magnetic field.

Let the coordinate normal to the electrodes be x (see Figure 2); by symmetry, in the absence of ions, the electric potential between the electrodes cannot depend on y or z. For the potential field, V, to satisfy Laplace's equation ($\nabla^2 V = 0$), the potential must be a linear function of x; that is, the applied electric field is spatially uniform (i.e., $E_x = -\partial V/\partial x = \text{constant}$).

Moreover, if the ions of a given m/q are spatially coherent (i.e., the ions are bunched in a packet whose dimensions are small compared with the ICR orbital radius—see below), then the signal from N ions is simply N times as large as the signal from one ion. In other words, under the stated conditions, the behavior of N identical ions can be understood simply from the behavior of a single ion. Therefore, we begin our description of ion cyclotron motion with a single ion moving under the influence of a spatially uniform magnetic field in the region between two infinite parallel electrodes (i.e., spatially uniform electric field).

The Lorentz force acting on an ion of mass, m, and charge, q, moving at velocity, $\mathbf{v}$, and subjected to an electric field, $\mathbf{E}$, and a static magnetic field, $\mathbf{B}_0$, is given by

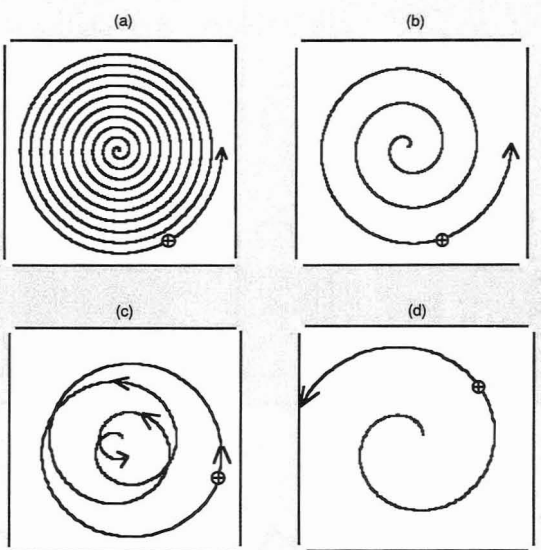

Figure 3. Effects of various ion excitation schemes.

(a, b) Archimedes spirals for ions of two different m/q values excited on resonance for the same length of time at the same excitation voltage magnitude. The ion of lower m/q has the higher cyclotron frequency. (c) Off-resonance excitation resulting in only a small absorption of energy. To make the ion trajectory visible, the scale of this diagram has been greatly enlarged compared with those of the other diagrams in this figure. (d) Ion ejection resulting from high-amplitude resonant excitation.

$$m\frac{d^2\mathbf{r}}{dt^2} = m\frac{d\mathbf{v}}{dt} = q\mathbf{E} + q\mathbf{v}\times\mathbf{B}_0 \quad (2)$$

in which $\mathbf{r}$ is the vector position of the ion and t is time. Let $\mathbf{B}_0 = B_0\mathbf{k}$: The z-axis points along the direction of the magnetic field whose magnitude, B_0, is constant. In the absence of an electric field, ($\mathbf{E} = 0$), Equation 2 is independent of ion position. An ion moving with speed, $\mathbf{v}$, in a plane perpendicular to $\mathbf{B}_0$ will be bent into a circular (ion cyclotron) orbit by the magnetic force that is always directed perpendicular to both $\mathbf{B}_0$ and the ion velocity vector (Figure 1); because there are no forces acting in the z-direction, the axial (z) motion is unrestrained. Equation 1 then follows immediately from Equation 2, in which ion cyclotron angular velocity, $2\pi\nu_c = \omega_c = v/r$, where r is the radius of the ion cyclotron orbit. ICR frequencies at $B_0 = 3$ T fall within the range 5 MHz $\geq \nu_c \geq$ 5 kHz for singly charged ions of 10 u $\leq m \leq$ 10 000 u.

Apart from its fundamental connection between m/q and ν_c, Equation 1 has several other immediately useful consequences. First, by taking the differential of Equation 1, we quickly find that mass (or mass-to-charge ratio) resolving power, $m/\Delta m$, is the same as frequency resolving power, $\nu_c/\Delta\nu_c$

$$\frac{m}{\Delta m} = \frac{\nu_c}{\Delta\nu_c} \quad (3)$$

in which Δm is the width (say, at half-maximum peak height) of an ICR mass spectral peak and $\Delta\nu_c$ is the corresponding frequency domain peak width (*21*). In the high-pressure limit (i.e., data acquired for several damping periods of the time domain signal), $\Delta\nu_c$ is directly related to the ion–neutral collision frequency, which is not a strong function of m/q; thus, Equations 1 and 3 may be combined to show that ICR mass resolving power varies approximately inversely with m/q. Nevertheless, FT-ICR mass resolving power as high as $\sim 10^6$ has been attained at $m/z \approx 900$ u/e, where e is the charge of an electron (*22*), and more than 10^8 at $m/z = 40$ u/e (*23*).

Second, Equation 1 can be rearranged to yield the ion cyclotron orbital radius, r, if the transverse component of the velocity is known:

$$r = \frac{mv}{qB_0} \text{ in general,} \quad (4a)$$

or $r = (2mkT/q^2B_0^2)^{1/2}$ for an ion of thermal root mean square speed

$$v = (2kT/m)^{1/2} \quad (4b)$$

in which k is the Boltzmann constant and T is temperature (in K). From Equation 4b, one finds that room-temperature singly charged ions of typical mass, 15 u $< m <$ 1000 u, have preexcitation ICR orbital radii $<$ 0.25 mm at $B_0 = 3.0$ T (i.e., much smaller than the maximum radius allowed by a typical ion trap [10–25-mm radius]). Moreover, a singly charged ion of 100 u excited to an ion cyclotron orbital radius of $\sim$1 cm at $B_0 = 3.0$ T possesses a translational energy of 434 eV and can generally be induced to fragment on collision with neutral atoms or molecules.

Finally, because $r \propto \sqrt{m}$ in Equation 4b, it is clear that ions of sufficiently high m/q will have thermal ICR orbital radii large enough that some of these ions will collide with one of the trap electrodes. For example, at 300 K and 3 T, an ion of average thermal speed will have an ICR orbital diameter > 1 in. when the ion mass exceeds 2 700 000 u. From the Boltzmann or some other velocity distribution, one could calcu-

late the fraction of ions lost in such a case. In addition, for finite dimension ion traps, there is a "critical" upper mass limit above which ions of even zero initial velocity cannot be trapped.

Excitation and detection of an ICR signal with infinitely extended electrodes. Figure 2 shows the electrostatic potential produced by applying a differential voltage, $\Delta V = 2V_{ex}$, across two infinitely extended flat conductive parallel plate electrodes. Note that the potential varies linearly with distance from either plate. Because force is the negative gradient of potential, the electric force, $F = qE$, on an ion of charge, q, will be independent of ion position between the plates.

Next, let the applied differential voltage oscillate at the ICR orbital frequency $V_{ex} = V_0 \cos(\omega_c t)$ (i.e., linearly polarized resonant excitation). Generally, in FT-ICR, electric field calculations are performed as if the problem were an electrostatic one. That approximation is excellent provided that the wavelength associated with the highest cyclotron frequency of interest is much larger than the trap's dimensions, as is always the case in practice.

The spatially uniform time-varying

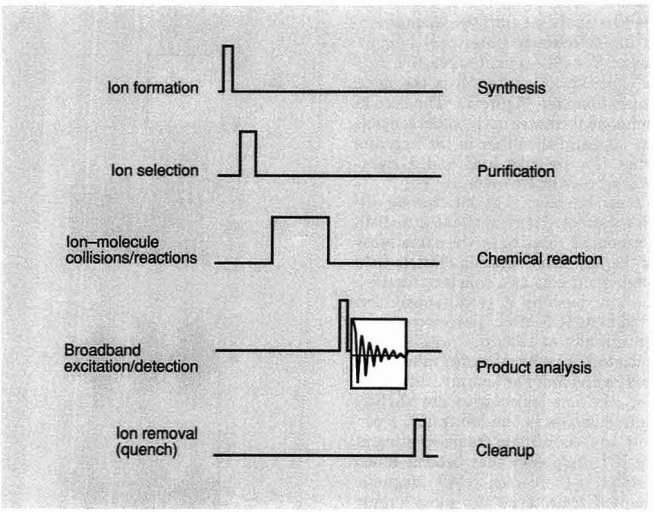

Figure 4. Generalized FT-ICRMS event sequence (left), labeled by the corresponding conventional chemical manipulations (right).

Ions of many m/q values are formed initially. One or more of these parent species may be isolated for subsequent chemical reaction or fragmentation. The parent ions and any daughter ions formed during the reaction period are then mass analyzed. Finally, all ions are swept out of the trap by applying a large potential difference between the trapping plates. (Adapted with permission from Reference 26.)

electric field, E, between the plates may be analyzed into two counter-rotating (circularly polarized) components: $E = (V_0/a)\exp(+i2\pi\nu_c t) + (V_0/a)\exp(-i2\pi\nu_c t)$, where a is the plate separation (see Figure 2). The second component rotates in the same sense as the ions and the other in the opposite sense (for positive ions and a right-handed coordinate system).

It can be shown that the ion is significantly affected only by the electric field component rotating in the same sense as the ion. That rotating electric field component acts as a constant force on the ion, pushing it continuously forward in its ICR orbit. Therefore, for an ion initially at rest, the resultant ion trajectory is an Archimedes spiral (Figures 3a and 3b). For ions not initially at rest, the ion trajectories are slightly more complex in the lab frame. However, in a coordinate frame rotating at the ICR frequency they become much simpler (*24*), just as NMR magnetic moment trajectories are more simply represented in a coordinate frame rotating at the Larmor frequency.

It turns out that ions of different m/q are excited to the same ICR orbital radius when irradiated by resonant ($\nu = \nu_c$) rf electric fields of the same magnitude for the same amount of time. This fortunate property allows us to excite ions having a whole range of m/q values simply by irradiating them with "flat" rf power: The frequency domain spectrum of the excitation signal is constant over the frequencies of interest. Finally, ions subjected to off-resonance irradiation ($\nu \neq \nu_c$) undergo a forced oscillation (*24*) in ICR radius (Figure 3c; note expanded scale), rather than the continuous increase in ICR orbital radius produced by resonant excitation.

One purpose of an excitation event is to produce a spatially localized ion "packet" in preparation for the detection event. Figure 2 also shows the differential charge, ΔQ, induced between two infinitely extended flat parallel conductive electrodes by an ion of charge, q. In the limit that the ion is infinitesimally close to the upper electrode, a charge of $-q$ is induced on it. Midway between the electrodes ($x = 0$ in Figure 2), the difference in induced charge between the electrodes is zero.

It can be shown that ΔQ is a linear function of the transverse coordinate, x; thus ΔQ increases linearly with ICR orbital radius (*25*). Later we will discuss the similarity or reciprocity between ΔV and ΔQ that is exemplified in Figure 2. The unamplified ICR "signal" is the voltage difference produced by the oscillating differentially induced charge across an RC network connecting the two plates. By design, the ICR signal is essentially independent of frequency, at least for small to moderate m/q values, because the circuit is predominantly capacitive reactive, so that two ions of different m/q with the same trajectory will produce the same ICR signal amplitude.

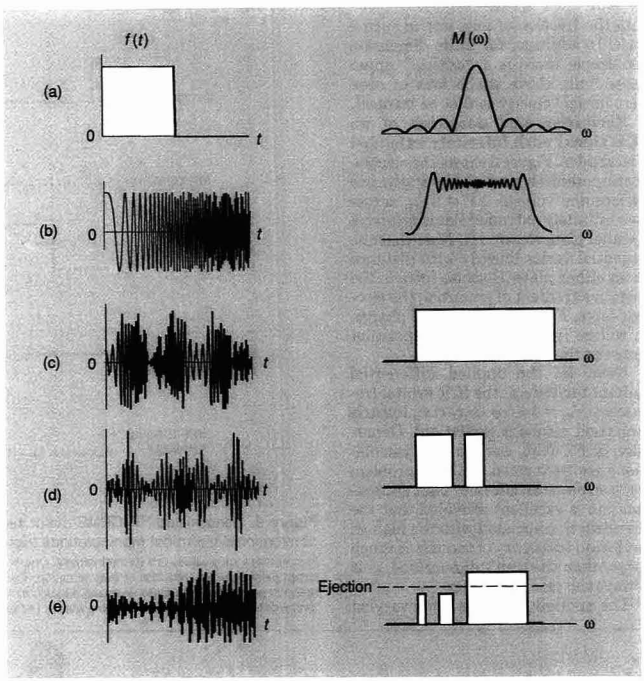

Figure 5. Frequency domain magnitude mode spectra (right) of several FT-ICRMS time domain excitation waveforms (left).

(a) Rectangular pulse excitation waveform. The shorter the duration of the pulse, the more broadband the excitation. (b) Frequency sweep ("chirp") excitation results in a more or less constant frequency domain magnitude over the swept range of frequencies. (c) SWIFT excitation to produce a truly flat frequency domain spectrum over an arbitrary frequency range. (d) SWIFT excitation to produce constant-magnitude excitation over two nonadjacent frequency ranges. (e) SWIFT excitation designed to eject ions within one frequency range and (simultaneously) to excite with equal magnitude ions within either of two other frequency ranges. Note the high uniformity and high selectivity offered by SWIFT excitation and/or ejection in c–e.

Excitation of an ICR signal: Impulse, frequency sweep, and SWIFT. Resonant excitation may be exploited in two ways. First, ions may be ejected by exciting them to an ICR orbital radius at which the ions strike the boundary electrodes and are removed (Figure 3d). Alternatively, if ions are excited to a radius ~1 cm and the rf voltage is then turned off, each packet of ions of a given m/q value will persist in circular orbit until collisions with neutrals and/or field inhomogeneities disperse the ions (in ICR orbital radius, phase angle, and orbit center) and they no longer form a coherent packet. During this randomization process, the ions are detected. The basic FT-ICR experimental event sequence (Figure 4; Reference 26) is based on combinations of ion formation, ejection (to select ions of one or more m/q values by ejecting ions of other m/q values), excitation, and detection.

One of the advantages of FT-ICRMS is the ability to simultaneously (or nearly so) excite a wide mass range; obviously, a single-frequency excitation waveform is not well suited for this purpose. Thus we must consider the effects of other waveforms on ions of a given m/q. For the infinite electrode limit (Figure 2), the ICR signal magnitude is proportional to the rf electric field excitation magnitude (i.e., the system is linear), and we need not compute the actual ion trajectory to predict an ion's response to a given excitation waveform. We may simply use a Fourier transform to determine the frequen-

cy domain spectrum of the time domain excitation waveform itself.

Figure 5 shows the effect (i.e., frequency domain magnitude spectrum) of three such waveforms that are capable of producing broadband excitation: a rectangular pulse ("impulse" [*2, 27, 28;* Figure 5a]), frequency sweep ("chirp" [*29, 30;* Figure 5b]), and SWIFT (*31, 32;* Figure 5c–5e). The chirp waveform requires vastly less (factor of 1–1000) excitation voltage magnitude than the impulse function and has until recently been the excitation method of choice in virtually all of the approximately 110 FT-ICR mass spectrometers in use worldwide.

Although both the rectangular pulse and the chirp waveforms can excite ions over a wide m/q range, the excitation magnitude envelope is far from flat over most of the frequency range and is not optimally selective (i.e., broad "shoulders" at each end of the irradiated frequency range). In 1985 we showed that because Fourier transforms work in reverse (i.e., from frequency to time domain) as well as forward (from time to frequency domain), one can specify almost any desired excitation magnitude spectral profile as a discrete magnitude spectrum, and then inverse Fourier transform that data to produce the corresponding time domain excitation waveform. The resulting SWIFT excitation provides optimally flat and selective excitation (Figures 5c and 5d) and/or ejection (Figure 5e) for FT-ICRMS and is now the method of choice for ion selection and excitation in the FT-ICR experimental event sequence of Figure 4. Approximately one-fifth of the FT-ICR mass spectrometers worldwide should be equipped with SWIFT capability by the end of this year.

One- and two-dimensional MS/MS: Hadamard versus Fourier. FT-ICR is uniquely suited for high-resolution multiple-stage MS because the analyte ions remain in the ion trap throughout the experiment. A one-dimensional MS/MS experiment might proceed as follows. Parent ions of all but a chosen m/q value are ejected and then the remaining ions are excited to higher ICR orbital radius and thus higher translational velocity. During a variable delay period, the mass-selected parent ions collide with neutrals and fragment to form daughter ions. Subsequent broadband excitation and detection of the daughter ions yield a high-resolution mass spectrum from which one may reconstruct part or all of the parent ion structure from the chemical formulae of its daughter fragments.

Alternatively, ions of a given m/q value may be isolated and then allowed to react (rather than fragment) with neutrals to establish ion–molecule reaction pathways, kinetics, energetics, and equilibria, as described in various recent reviews (*32–49*). For example, we recently used SWIFT excitation and ejection to establish the structures of several osmium cluster ions, Os_n^+, based on the kinetics of their condensation reactions with their corresponding neutral clusters (*50*). Multiple-stage MS^n experiments have been used to sort out even more complex ion–molecule reaction pathways (see, e.g., Reference 39).

Although FT-ICRMS offers the multiplex advantage that all of the daughter ions are detected simultaneously in an MS/MS experiment, an obvious disadvantage is that parent ions of all but one m/q are discarded at the outset. Two recent innovations have made it possible to include either half or all of the parent ions simultaneously in 2D MS/MS experiments.

In Hadamard 2D ICR (*51*), SWIFT excitation is used to eject a linear combination of approximately half of the N possible parent ions; the remaining parent ions are then excited and allowed to fragment by ion–neutral collisions, and all of the resulting daughters are excited and detected afterward. The process is then repeated for N linearly independent combinations of selected parent ions. (The Hadamard code [*26*] simply specifies how to choose the various parent ion combinations and how to decode the resulting mass spectra afterward to extract the daughter ion spectrum corresponding to each of the individual parent ions.) Because approximately half of the N parent ions are involved in each measurement (rather than just one), the Hadamard 2D ICR experiment offers a potential gain of a factor of $\sim N/2$ in speed (for the same S/N) or $\sim(N/2)^{1/2}$ in S/N (for the same total experiment time) over N 1D FT-ICRMS/MS experiments.

The second 2D ICR experiment is

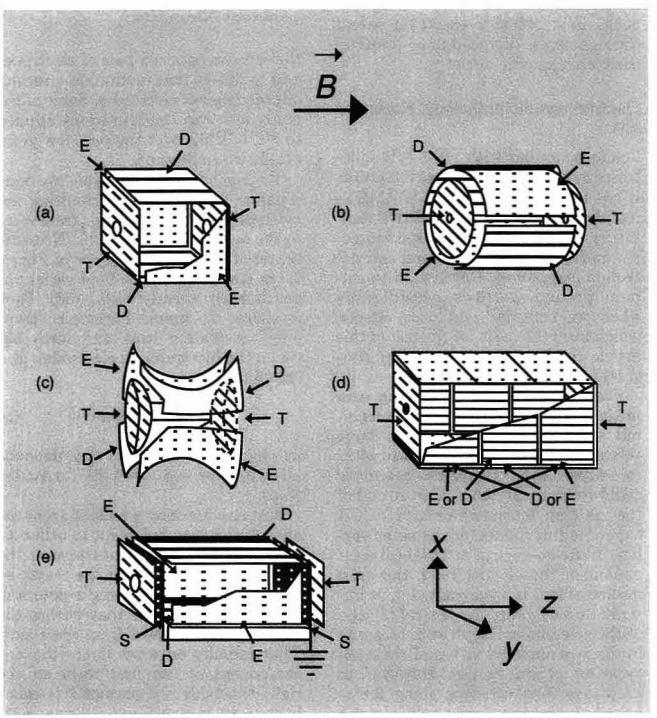

Figure 6. Several ion trap geometries designed for use in FT-ICRMS.
(a) Standard cubic trap. (b) Standard cylindrical trap. (c) Hyperbolic or Penning trap with ring electrode segmented to operate in the standard mode. (d) Elongated and segmented ion trap, designed to facilitate detection in a central electric field-free region. (e) Screened ion trap designed to produce a particle-in-a-box-like potential (see also Figure 10). The excitation, detection, trap, and screen electrodes are designated E, D, T, and S, respectively.

modeled after the so-called NOESY (nuclear Overhauser enhancement spectroscopy) 2D FT-NMR experiment (*52*). It is based on the principle that ions can be "de-excited" back to their starting points by use of a 180° phase shift in either a single-frequency (*53*) or frequency sweep (*54*) excitation. In the 2D FT-ICR experiment, all ions are excited to a given ICR orbital radius; following a variable delay period (whose duration defines the time scale for the second FT), the ions are excited again. Depending on the ICR frequency of the ions of interest, the second excitation will be in phase, out of phase, or somewhere in between with respect to the first. The ICR radius and the translational energy of the parent ion (and hence the abundance of daughter ions) can thus be modulated according to the ICR frequency of the corresponding parent ion by incrementing the delay period in successive experiments (*55*). In the resulting 2D FT mass spectrum, off-diagonal peaks reveal ion–molecule reactions and/or fragmentation, just as off-diagonal peaks in a NOESY spectrum reveal through-space dipole–dipole coupling between magnetic nuclei.

Electromagnetic pathology: Nonlinear ICR

Readers familiar with FT-NMR spectroscopy will recognize many features it has in common with FT-ICRMS in its linear approximation: SWIFT excitation, 180° pulse, 2D FT spectroscopy, and quadrature excitation and detection (see below). However, the common ground narrows considerably when we consider nonlinear effects, which form the basis for the rest of this article (and much of the recent progress in FT-ICRMS).

Finite electrodes: Trapping and magnetron motions. Typical solenoidal superconducting magnets have good spatial homogeneity (e.g., to within ~1 part in 10^5) over the relatively small volume (say, $2.5 \times 2.5 \times 10$ cm) of the ion trap within which an FT-ICR experiment is conducted. As noted earlier, in the absence of an axial (z) component of the electric field, the axial motion of ions is unrestrained. Ions initially formed along the central (z) axis of the solenoid are kept from escaping in the x–y plane by virtue of their ion cyclotron orbital motion. However, to keep ions from escaping along the z-axis, it is necessary to apply a static voltage, V_T (typically a few volts), to each of the two "trapping" electrodes located at $z = \pm c/2$ at each end of the ion trap. Moreover, it is experimentally convenient to excite ICR orbital motion on one opposed pair of electrodes and to detect that motion on a second opposed pair of electrodes. Some of the many ion trap configurations applied to FT-ICRMS over the past few years are shown in Figure 6.

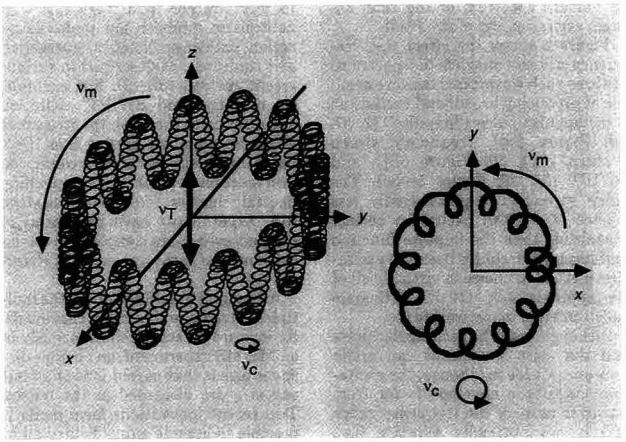

Figure 7. Ionic trajectory (left) within an ion trap, with all three fundamental modes (cyclotron, magnetron, and trapping) excited, and the projection (right) of that trajectory onto the x–y plane.

For clarity, the relative magnitude of the magnetron oscillation has been exaggerated. In typical FT-ICRMS experiments, the magnetron radius is much smaller than the cyclotron radius. (Adapted with permission from Reference 26.)

To a good approximation, we may separate the forces and resulting ion motions that are parallel or transverse to the magnetic field (z) axis. Near the center of any of the ion traps of Figure 6, the trapping electric field varies approximately linearly with z (*56*). Thus ions execute simple harmonic "trapping" oscillation back and forth between the two trapping electrodes, at a trapping frequency

$$\nu_T = (q\alpha V_T/\pi^2 m a^2)^{1/2} \qquad (5)$$

in which α is a constant that depends on trap shape (e.g., $\alpha = 1.386$ for a cubic trap).

Just as squeezing a balloon from the ends forces it to bulge out in other directions, "squeezing" ions toward the center of the trap along the z-axis by introduction of a trapping z-potential also produces a force that pushes the ions radially outward from the z-axis. That radially outward force (the x–y component of the first term on the right-hand side of Equation 2) is exactly opposite in direction to the magnetic component of the Lorentz force (second term on the right-hand side of Equation 2). In other words, it is as if the magnetic field strength has been reduced by adding the trapping potential. Because ICR orbital frequency is proportional to B_0 (Equation 1), we infer that introduction of the trapping potential will lower the observed ICR orbital frequency from its value ($\nu_c = qB_0/2\pi m$) in the absence of the trapping potential.

Fortunately, the electrostatic potential in any of the ion traps in Figure 6 is well approximated (at least, near the center of the trap) by a "quadrupolar" potential (*13*)

$$V(x,y,z) = V_T[\gamma - (\alpha/a^2)(x^2 + y^2 - 2z^2)] \qquad (6)$$

in which α and γ have fixed numerical values for a given trap shape and a is a characteristic trap dimension. Substitution of the resulting electric field, $\mathbf{E} = -\nabla V(x,y,z)$, into Equation 2 leads to a system of three linear second-order differential equations. The equation involving only the z-coordinate may be solved independently to yield the sinusoidal trapping motion of Equation 5. The two remaining coupled differential equations in x and y have two solutions (*56*): the ion cyclotron orbital motion, whose frequency is shifted (downward, as noted above) to

$$\omega_+ = \frac{1}{2}[\omega_c + \omega_c(1 - m/m_{crit})^{1/2}]$$

$$\text{where } m_{crit} = qa^2B_0^2/8\alpha V_T \qquad (7a)$$

and a natural magnetron motion at frequency

Table I. Natural ion motional frequencies (Hz) for singly charged ions trapped in a quadrupolar potential (Equation 6) at a static magnetic field strength of 3.0 T[a,b]

Motion	m = 100	1000	10,000	m_{crit} = 50,492
$\nu_+ \approx qB/2\pi m$	460,430	45,837	4,366	456
$\nu_- \approx \alpha V_T/\pi a^2 B$	228	229	240	456
$\nu_T = (\alpha q V_T/\pi^2 m a^2)^{1/2}$	14,496	4,584	1,450	645

Note: Masses are listed in u.

[a] Although the cyclotron frequency ν_+ varies strongly with mass, the trapping frequency, ν_T, exhibits a much weaker mass dependence and the magnetron frequency ν_- is nearly mass- and charge-independent.

[b] Assumptions: a = 1.0 in. (cubic trap); α = 1.386 (cubic trap); B = 3.0 T; V_T = 1.0 V.

$$\omega_- = \frac{1}{2}[\omega_c - \omega_c(1 - m/m_{crit})^{1/2}] \quad (7b)$$

The three natural ICR motions are illustrated in Figure 7, and typical experimental values are listed in Table 1. We shall next discuss their implications.

ICR orbital frequency shift and mass calibration. From Equation 7a it is clear that the relation between observed ICR orbital frequency, ω_+, and ionic charge-to-mass ratio, q/m, is no longer linear. As a result, Equation 7a leads to a mass calibration equation that has two adjustable parameters (A and B) rather than one (*6*):

$$m = A/\nu_+ + B/\nu_+^2 \quad (8)$$

Equation 8 has proved accurate in practice, leading to sub-part-per-million mass measurement accuracy over a wide mass range (e.g., $60 \leq m/z \leq 500$) when an internal calibrator is provided. Addition of more terms to Equation 8 does not materially improve mass measurement accuracy (*8*).

Reduction of upper mass limit. From Equations 7a and 7b it is clear that above a "critical" mass, m_{crit}, the cyclotron and magnetron frequency expressions become mathematically complex. Physically, what happens is that the outwardly directed electric force can no longer be overcome by the inwardly directed magnetic force: Ions of $m \geq m_{crit}$ simply spiral radially outward until they strike one of the trap electrodes. In other words, ions of $m > m_{crit}$ cannot be trapped. The resulting upper mass limit, m_{crit}, can be relatively low (e.g., ~50 000 u for singly charged ions at 3.0 T in a 1-in. cubic trap with V_T = 1 V).

From Equation 7 it is also clear that the upper mass limit may be increased by increasing q (i.e., multiply charged ions), increasing B_0 (larger magnet), increasing α (larger ion trap), reducing V_T (smaller trapping voltage), and/or decreasing α (e.g., changing the trap electrode geometry). Of these options, the simplest and most effective is to change the trap configuration.

Harmonics. Over the past few years, it has become evident that the nonlinearities of the ICR experiment can produce responses not only at the three natural trapping, cyclotron, and magnetron frequencies, but also at various multiple and combination frequencies (see box).

Of these, the easiest to understand is the appearance of spectral signals at (odd) "harmonic" frequencies (*57*). Consider an ion executing a perfectly circular orbit centered on the z-axis in a cylindrical ion trap (Figure 8). When the ICR orbital radius, r, is much less than r_0 (the inner radius of the detector electrode), the difference in induced charge between the two opposed detector electodes is small but nearly sinusoidal. The corresponding FT frequency domain spectrum of that signal therefore consists of a single peak at the "fundamental" or "first harmonic" ICR orbital frequency, ω_+. However, as the ICR orbital radius approaches r_0, the detected time domain signal more closely resembles a chopped square wave whose spectrum now contains peaks at both fundamental and odd harmonic frequencies: $M\omega_+$, M = 1, 3, 5, ... (Only odd harmonics are observed, because the ICR signal is detected "differentially"—as the difference between the signals induced on the two opposed detector electrodes.) In practice, harmonic signals are generally small in magnitude (a few percent) relative to the signal at the fundamental ICR orbital frequency, but they may be exploited or amplified for special applications (see below).

Sidebands. A second type of distortion resulting from nonlinear ICR behavior is modulation, in which a response is observed at combination frequencies between two or all three of the fundamental ICR motions. For example, it is well known that the amplitude of the detected signal from an ion un-

Fundamental frequencies of motion of an ion in an ion trap under the quadrupolar approximation (top) and the frequencies detected with various detection schemes (bottom)

Fundamental ICR frequencies

$\nu_+ \approx \nu_c - \nu_- \approx \nu_c - \alpha V_T/\pi a^2 B$
$\nu_- \approx \alpha V_T/\pi a^2 B$
$\nu_T = (\alpha q V_T/\pi^2 m a^2)^{1/2}$

Experimentally observed frequencies

ν_c	(Infinite detection electrodes)
ν_c, $3\nu_c$, $5\nu_c$, $7\nu_c$, ...	(Finite detection electrodes, V_T = 0)
ν_c, $2\nu_c$, $3\nu_c$, $4\nu_c$, ...	(Off-axis ions, finite electrodes, V_T = 0)
$\nu_+ \pm \nu_-$, $\nu_+ \pm 2\nu_-$, ...	(Single detection electrode: $\nu_+ + \nu_- = \nu_c$)
$\nu_+ \pm 2\nu_-$, $\nu_+ \pm 4\nu_-$, ...	(Differential two-electrode detection)
$\nu_+ \pm \nu_T$, $\nu_+ \pm 2\nu_T$, ...	(Trap and magnetic field axes not parallel)
$\nu_+ \pm 2\nu_T$, $\nu_+ \pm 4\nu_T$, ...	(Trap and magnetic field axes parallel)
ν_T, $3\nu_T$, $5\nu_T$, ...	(Differential detection on trapping plates)
$2\nu_T$, $4\nu_T$, ...	(Differential two-electrode detection)
ν_c, $2\nu_+$, $2\nu_-$	(Quadrupole detection mode)

[a] Some observable frequencies are not mentioned because they are of no interest. In general, the higher the order of the harmonic or sideband, the lower its relative magnitude.

dergoing cyclotron motion depends on the axial position of the ion (*9*, *11*, *12*). In particular, the amplitude of the signal at frequency, ω_+, is maximal at the center of the trap ($z = 0$) and minimal at the trap plates where it actually drops to zero. Thus, for an ion undergoing combined cyclotron and trapping motions, the FT spectrum of the observed time domain ICR signal exhibits sidebands at $\omega_+ \pm 2\omega_T$, which have been observed experimentally (*16*). From symmetry arguments, it is possible to show that there should be no sidebands at $\omega_+ \pm \omega_T$ in a properly aligned trap; the magnitude of any such sidebands therefore provides a useful diagnostic index for aligning the trap with respect to the applied magnetic field. Magnetron sidebands (e.g., $\omega_+ \pm n\omega_-$, $n = 1, 2, \ldots$) have also been observed; their utility will be discussed later.

The *z*-excitation: Mass-dependent mass spectral peak magnitudes. Up to now, we have considered the effects of the true static electric field. However, the rf electric field is nonuniform because of the finite dimensions of the transmitter electrodes and the presence of the remaining detector and trap electrodes, which warp the rf electric field between the transmitter electrodes. There are at least three direct consequences of nonuniform rf electric field.

First, the effective rf electric excitation field is weaker than that predicted from the infinite electrode approximation (e.g., by a factor of ~0.72 for a cubic trap [*10*, *15*]).

Second, because the electric field lines curve rather than extend in straight lines between the two transmitter electrodes, an rf electric field excitation in the *x*-direction will have a component along the *z* direction. If that component happens to oscillate at twice the trapping frequency (or even at one of the cyclotron/trapping sidebands), ions will be excited (or even ejected) axially as the result of transverse excitation (*15*, *17–19*). The effect is mass dependent: For a given irradiation period at twice the trapping frequency, lowest mass ions gain the most energy and are more readily ejected. Because the rf electric field curvature varies with radial distance from the *z*-axis, the ejection effect varies with ICR orbital radius, leading to mass- and radius-dependent FT-ICR relative mass spectral peak heights (*17*).

Third, the transverse component of the rf electric field is strongest near the midplane ($z = 0$) of the trap and weakens as one proceeds toward either trap electrode. Thus ions with low trapping amplitude will be excited to higher ICR orbital radius than ions of large trapping amplitude. Also, because ICR orbital frequency varies with ICR orbital radius in a nonquadrupolar trap, the effect is to produce inhomogeneous line-broadening caused by a superposition of signals of different ICR orbital frequency from ions of different trapping oscillation amplitude and/or different ICR orbital radius (*14*).

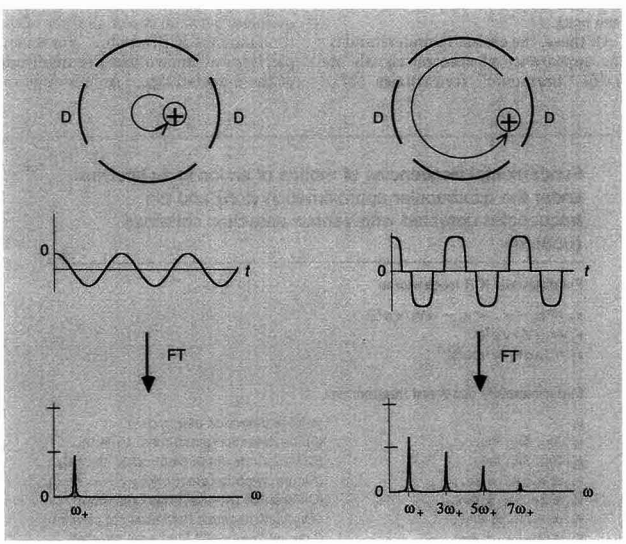

Figure 8. Origin of odd-integer harmonic signals in FT-ICR mass spectra, illustrated for a positive ion moving in a circular orbit in a cylindrical ion trap.

Left: The time domain ICR signal induced on opposed cylindrical detector electrodes, D, is small but approximately sinusoidal when the ICR orbital radius, *r*, is much smaller than the radius, r_0, of the detector electrode. The corresponding FT frequency spectrum therefore consists of a single peak at the fundamental ICR orbital frequency, ω_+. Right: As *r* approaches r_0, the detected time domain signal approaches a square wave whose spectrum contains peaks at all odd harmonics of the fundamental ICR frequency of the ion. (Adapted with permission from Reference 26.)

Description, exploitation, and/or elimination of nonlinear effects

The problems resulting from nonlinear ICR behavior are empirically well known but have only recently been quantitatively analyzed or rectified. In this section, we try to show how a better description of the problems has led to some remarkable improvements in the performance and reliability of the FT-ICR technique.

In search of a quadrupolar potential: Hyperbolic trap. A perfect quadrupolar electrostatic potential (Equation 6) offers the very important advantage that the ICR orbital frequency, ω_+ of Equation 7a, is independent of ICR orbital radius (*6*, *56*). Thus there is no "spread" in ICR frequencies (inhomogeneous spectral peak broadening) for ions with different ICR motional amplitude. Most early ICR ion trap configurations produce an approximately quadrupolar field only near the trap center. Fortunately, there is a trap geometry that produces a near-perfect quadrupolar potential: a "hyperbolic" trap (see Figure 6c) formed from a "ring" electrode and two "end caps," all of whose surfaces are hyperboloids of revolution (*56*).

If the "ring" electrode is unbroken, it turns out that ions must be introduced off axis to provide for "parametric" excitation and detection (*6*). Alternatively, the "ring" electrode may be cut along two perpendicular planes to yield a trap that is configured just like a cubic trap except that the electrode surfaces are curved (*58*). We have shown that such a segmented hyperbolic trap indeed reduces FT-ICR spectral peak widths and also improves mass accuracy based on the quadrupolar mass calibration formula of Equation 8. However, the hyperbolic trap has the following disadvantages: The curved electrodes produce a highly nonuniform rf excitation field, further exacerbating problems associated with *z*-ejection (see above); and the static electric field quadrupolar potential produces a radial electric field, $E(r) = E_0 r$, which re-

duces the upper mass limit (see above) as in the tetragonal and cylindrical traps.

Quantitating ion behavior for nonhyperbolic traps: Reciprocity. Because even a perfectly quadrupolar trap is not optimally suited for FT-ICRMS, we are forced to consider other trap geometries. Unfortunately, the algebraic complexity of computing the electric field (rf plus static) and the ICR signal (from the differential charge induced between two opposed detector electrodes) can become truly formidable. For example, the electrostatic potential alone for a simple tetragonal trap of length, c, and cross-sectional width, a, is given by

$$V(x,y,z) = \frac{16V_T}{\pi^2} \times \sum_{m,n=0}^{\infty} \left\{ (-1)^{m+n} \cos\left[\frac{(2m+1)\pi x}{a}\right] \times \cos\left[\frac{(2n+1)\pi y}{a}\right] \cosh\left[\frac{k_{mn}\pi z}{a}\right] \Big/ (2m+1)(2n+1)\cosh\left[\frac{k_{mn}\pi c}{2a}\right] \right\} \quad (9)$$

in which $k_{mn} \equiv [(2m+1)^2 + (2n+1)^2]^{1/2}$ and the geometric center of the trap is taken as the coordinate frame origin (*56*). Moreover, it is much more difficult to compute the induced ICR signal than to compute the electric potential for the same arrangement.

Fortunately, the simple relation between the excitation and detection "fields," shown (for infinitely extended electrodes) in Figure 2, turns out to be a special case of the very useful "reciprocity" theorem (*12*). One way of stating the theorem is that the potential (in volts) at a given point in the trap, produced by applying +1 V and −1 V to two opposed "transmitter" electrodes, is numerically identical to the differential charge that would be induced between the same two (grounded) electrodes by placing a unit charge at that same point. In other words, if (as is generally the case) we are able to obtain an algebraic expression for the potential at any point within a particular ion trap with ±1 V applied to the two detection electrodes (+1 V to one, −1 V to the other), then we have automatically solved the converse problem of determining the ICR signal for an ion at the same point—we need simply compute the ICR signal for each of 100 points around the circumference of one ICR orbit (in steps of 3.6° each) and Fourier transform it to discover the FT-ICR frequency spectrum for ions following that trajectory.

ICR orbital radius and ion energy determination. Nonlinear effects are not all bad. For example, such useful devices as laser-doubling crystals and rf mixers are based on nonlinear phenomena (*26*). We may therefore seek to capitalize on some of the nonlinear effects of ICR. For example, the relative magnitudes of the first, third, fifth, . . . harmonics increase with ICR orbital radius, r, approximately as r, r^3, r^5, . . . (*59*). Thus the experimentally measurable ratio of the magnitude of the third harmonic to that of the first harmonic, $M(3\omega_+)/M(\omega_+)$, increases approximately as the square of the ICR orbital radius (Figure 9). Thus measurement of $M(3\omega_+)/M(\omega_+)$ provides the first direct measure of the orbital cyclotron radius of an excited ion (and thus its translational energy).

Moreover, now that we are able to calculate the ICR signal induced by an ion at a given ICR orbital radius, we should be able to determine the number of ions from their measured radius and measured ICR signal. These new tools should prove exceedingly valuable for testing current theories of ICR signal relaxation: for example, loss of ions from a coherently orbiting packet, diffusion of a packet of ions around their cyclotron orbit, decrease in ICR orbital radius, and ion–molecule momentum transfer collision mechanism.

As an alternative to measuring cyclotron radii, we have expressed the exact excitation potential in cylindrical coordinates to compute the postexcitation cyclotron radius of ions in response to on-resonance single-frequency excitation. We find that the infinite electrode model overestimates the ICR orbital radius by a factor of ~1.39 for a cubic trap. Because the translational energy, $q^2B_0^2r^2/2m$, of an rf-excited ion varies as the square of its ICR orbital radius, we find that ions in a cubic trap are excited to only about half the energy previously estimated from the infinite electrode model (which had been used to determine collisionally induced dissociation energy thresholds).

We have been able to demonstrate good agreement between the experimental and calculated onset of radial ejection attributable to rf electric field excitation in a cubic trap (*10*). Our results allow for similar computations for tetragonal or cylindrical traps of arbitrary aspect (i.e., length-to-width) ratio (*10*, *11*). Fortunately, the rate of increase of ICR orbital radius with the product of rf electric field excitation magnitude and duration is still approximately linear, but with a slope reduced by a factor of ~0.72, and thus does not pose a problem for most routine analytical work.

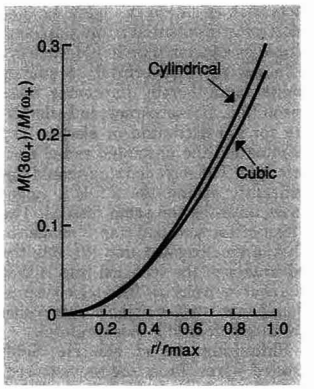

Figure 9. Ratio of the magnitude of the third harmonic to that of the fundamental, $M(3\omega_+)/M(\omega_+)$, versus ICR orbital radius, r, for cylindrical ($c/2r_{max} = 1$) and cubic ion traps.

Both curves are approximately quadratic. From such curves, the ICR orbital radius (and thus ion orbital translational energy) may be determined directly from experimental FT-ICRMS magnitude mode peak heights. (Adapted from Reference 60.)

Shimming the static electric field: Screened trap. The two general ways to approach physical problems are to seek a complete mathematical description of the conventional system or to devise a new system for which the desired behavior is realized more closely. FT-ICRMS ion traps offer good examples of each approach.

Until recently, it was thought that the optimal trap geometry for FT-ICR should be hyperbolic; that is, $V(x,y,z) - V(0,0,0) = (\alpha V_T/a^2)[2z^2 - (x^2+y^2)]$, so as to produce simple harmonic oscillation in ion position along the z-axis and a position-independent cyclotron frequency. However, as noted above, the trapping potential that is applied axially is necessarily accompanied by a radially outward electric field that shifts the ICR orbital frequency in a mass-dependent way and reduces the upper mass limit. Furthermore, the excitation field in such a trap has a strong axial component that may exacerbate z-ejection problems.

In 1989 we introduced a new kind of ion trap in which grounded screens are placed just inside the trapping electrodes (*60*). Just as a bubble can penetrate through a screen door by only about one mesh spacing, the electric field from the trapping plates is effectively shielded from ions in the trap until the ions nearly touch the screens. In other words, we have effectively replaced the harmonic oscillator potential by the simpler particle-in-a-box

potential, as shown in Figure 10. The electrostatic potential in the trap is reduced by a factor of up to 100, virtually eliminating ICR orbital frequency shifts (and thereby improving mass resolution, mass accuracy, and selectivity for ion excitation or ejection) by eliminating the unwanted radial electric field. The screened trap should significantly extend the FT-ICR upper mass limit for the same reasons. The effect of the screened trap is similar to that of an elongated trap (*61*, *62*); the advantage of the screened trap is that the near-zero electric field region is produced in a smaller volume over which the magnetic field is more uniform.

Shimming the rf electric field: Guard wires. From the previous section, the reader may have guessed that it is also possible to design an ion trap for which the rf excitation electric field is more uniform than that of a conventional tetragonal, cylindrical, or hyperbolic trap. The trick here is to shim ("unwarp") the rf electric field by adding conductive elements whose positions and rf voltages are adjusted so as to flatten the rf field and make it spatially uniform anywhere between the two transmitter electrodes. The problems associated with the nonuniform excitation field were discussed earlier.

Figure 11 shows one of several possible rf-shimmed ion trap designs (*63*, *64*) and the resultant improvement in rf electric field homogeneity. With our rf-shimmed trap, the variation in relative FT-ICR mass spectral peak heights with ICR orbital radius was reduced from a factor of more than 10 down to a few percent for a cubic trap. Even better quantitative precision should be possible with somewhat elongated ion traps that reduce the effects of electrostatic field nonuniformity. Finally, we note that the rf-shimmed trap of Figure 11 effectively incorporates some of the advantages of the screened trap with those of the rf-shimmed trap by its placement of shim wires in front of the trapping electrodes.

Quadrature excitation and detection. Until recently, FT-ICRMS was conducted with linearly polarized rf excitation and detection (i.e., use of just one pair of opposed electrodes for excitation and a second pair for detection). It can be shown that this configuration is half as efficient as quadrature excitation and detection, in which both pairs of electrodes are active simultaneously.

The inefficiency of the standard mode of operation during the excitation event can be understood as follows: The orbits of positive ions all rotate in the same sense (counterclockwise, when viewed along a magnetic field directed into the plane of the paper). The linearly polarized excitation field may be decomposed into two counter-rotating (clockwise and counterclockwise) electric fields, of which the clockwise-rotating component has almost no net effect upon the ions. Thus half of the excitation field magnitude is wasted.

By introducing a second pair of opposed excitation plates with an excitation waveform that is phase-shifted 90° relative to the first pair, we can construct a circularly polarized excitation field that rotates in the same sense as the ions. The resulting quadrature excitation is clearly twice as efficient as its linearly polarized counterpart.

The argument that demonstrates the relative efficiency of quadrature detection proceeds similarly: By using only one pair of detection plates, we obtain a linearly polarized time domain signal. In other words, the detector cannot distinguish between clockwise and counterclockwise rotation, even though the ions are actually rotating in only one sense.

By detecting simultaneously and independently from a second pair of opposed plates oriented at 90° relative to the first pair, we can distinguish between clockwise and counterclockwise components: The time domain signals

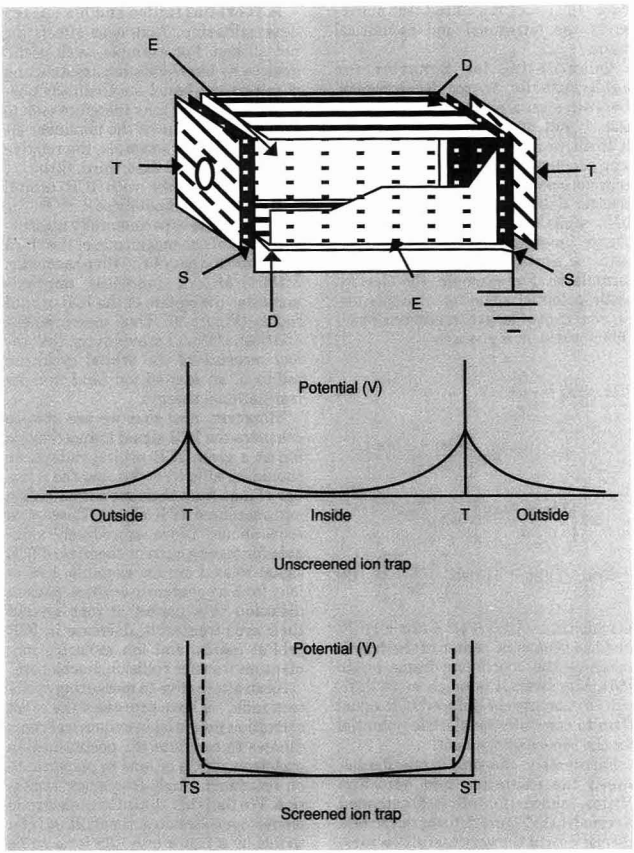

Figure 10. Screened tetragonal ion trap.
A conductive screen, typically 10–20 wires per inch, is placed in front of each trapping electrode. Holding the screens at ground potential produces the particle-in-a-box potential along the *z*-axis of the trap shown at the bottom of the figure. For comparison, the axial potential for the corresponding unscreened trap is also shown (middle). Note that the screens effectively shield most of the trap volume from the (mostly undesirable) effects of the trapping potential (see text). The excitation, detection, trap, and screen electrodes are designated E, D, T, and S, respectively.

from the two pairs of plates are identified as real and imaginary components of a mathematically complex input to the FFT algorithm, and the clockwise- and counterclockwise components are then manifested as negative- and positive-frequency peaks in the resulting FT spectrum. Thus, for a given coherently rotating ion packet, quadrature detection yields a S/N that is higher by a factor of $\sqrt{2}$ (i.e., signal increased by a factor of 2 and noise increased by a factor of $\sqrt{2}$) than would be obtained with linearly polarized detection.

Several groups have recently demonstrated various forms of quadrature detection, based either on independent acquisition of signals from two pairs of opposed detector electrodes (*65*) or (for heterodyne mode only) on splitting the signal from one pair of detector electrodes in half and phase-shifting one of the two signals by 90° (*66*, *67*). The FT data reduction is essentially the same, except that the raw data from linearly polarized detection are treated as mathematically real, whereas each pair of data points from the two quadrature channels is treated as mathematically complex (one real, the other imaginary). Various nuances of quadrature data reduction and display are discussed at length elsewhere (*26*).

Multipole excitation and detection. Quadrature excitation and detection offer one of many recently explored multiple-electrode arrangements for FT-ICRMS. Perhaps the most clever and useful is the quadrupole detection scheme of Schweikhard et al. (*68*). The signals from one pair of opposed detector electrodes are added together and then subtracted from the sum of the signals from the second pair of opposed detector electrodes oriented perpendicular to the first pair. Depending on the relative magnitudes of the cyclotron and magnetron orbital radii (which can be varied in their experiment), the FT-ICR frequency (mass) spectrum contains a harmonic signal at $2\nu_+$ and (more interestingly) a new signal at the sum of the cyclotron and magnetron frequencies ($\nu_+ + \nu_-$).

The striking advantage of this experiment is now evident from Equation 7: namely, $(\nu_+ + \nu_-) = \nu_c$. In other words, this experiment extracts the unshifted ion cyclotron orbital frequency, even though ions are trapped by the usual quadrupolar potential, which would shift the conventionally detected signal, ν_+, to a value lower than ν_c. This same sideband can be generated from more conventional traps by grounding either of the detection electrodes and ensuring that both modes are excited as shown by Allemann et al. (*69*). Magnetron motion has also been observed directly (*70*).

Several research groups have devised ion traps specifically designed to increase the strength of various harmonic signals at the expense of the fundamental (*57*, *71*, *72*). Such designs were motivated by the hope that mass resolving power might increase with harmonic order, because two closely spaced peaks are three times farther apart at the third harmonic than at their fundamental ICR orbital frequencies. However, the precision with which an ICR signal (or any other discretely sampled spectral signal) can be determined is proportional to the product of S/N and the square root of the number of data points per linewidth (*73*).

Because the maximum magnitude of the Mth harmonic signal is in general less than $1/M$ of that of the fundamental signal for conventional two-electrode differential detection in standard traps (*10*), detection of the Mth harmonic signal thus offers no theoretical advantage in precision (e.g., for accurate mass determination) over detection at the fundamental ICR orbital frequency. In other words, for conventional ICR detection, the harmonic peaks may be farther apart, but their smaller magnitudes more than make up for their increased peak separation, with respect to mass measurement accuracy.

Various multielectrode ion trap designs can increase the strength of harmonic signals at the expense of the fun-

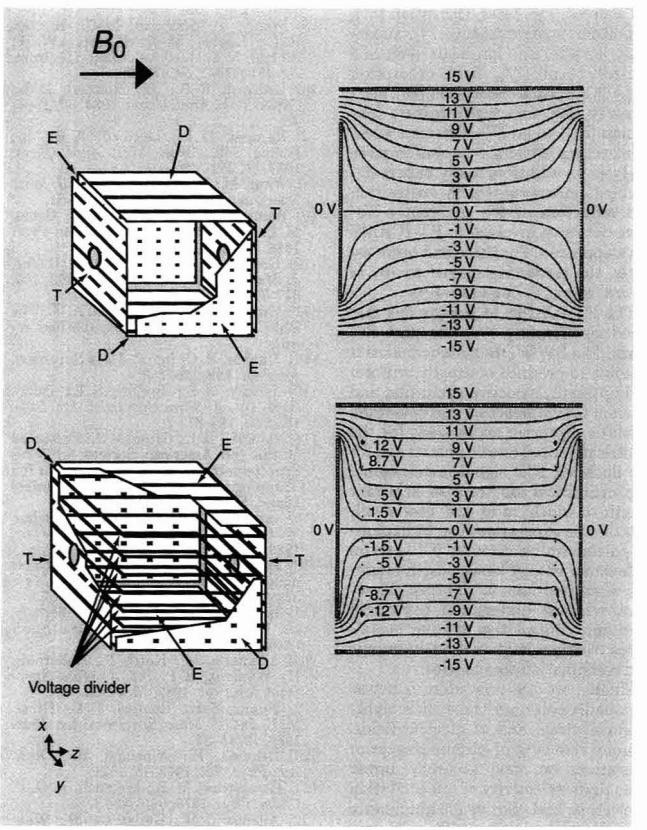

Figure 11. Standard (top left) and rf-shimmed (bottom left) cubic ion traps and their corresponding rf isopotential contours (right).

An rf potential of ±15 V is applied to the excitation electrodes, with rf potentials of decreasing magnitude applied to the shim wires as shown. Note the much flatter rf isopotential contours (and thus much more uniform rf electric field magnitude) for the rf-shimmed trap, with resultant elimination of mass-dependent z-ejection (see text). The excitation, detection, and trap electrodes are designated E, D, and T, respectively.

damental to overcome the factor of $1/M$ loss in S/N that is inherent in conventional two-electrode detection. Unfortunately, a detailed analysis shows that the spectral linewidth is not necessarily independent of M (*59*); furthermore, one always encounters multiple peaks corresponding to the same m/q, leading to more complex mass spectra.

Directions for future research

We have considered recent developments in our fundamental understanding of the processes of ion trapping, excitation, and detection in FT-ICRMS. An additional ongoing major development not treated here is the external injection of ions through the fringing field of a solenoidal superconducting magnet. Such injection has made possible the coupling of various ion sources (e.g., laser desorption [*36*], fast atom bombardment [*74*], supersonic jet [*75*], Cs^+ ion beam [*76*], SF_6 neutral beam [*77*], field desorption [*78*], ^{252}Cf plasma desorption [*79*], electrospray [*80*], and high-pressure ionization [*81*]) to an FT-ICR mass spectrometer for ultrahigh resolution mass analysis. In addition, many papers describing improvements in acquisition and reduction of the inherently discrete data sets involved in FT-ICRMS have appeared. For these and other aspects, the reader is referred to any of several recent reviews (*32–49*).

The FT-ICRMS technique has matured significantly over the past five years. The SWIFT technique makes it possible to produce optimally uniform and optimally selective excitation and ejection for ion selection and detection. Analytic algebraic expressions for the electric potential (static plus rf) and for the detected ICR signal in tetragonal and cylindrical ion traps of arbitrary length-to-width ratio are now available. Those expressions can be exploited to determine directly ICR orbital radius and energy as well as the number of excited ions in the trap. Moreover, we now understand the origin (and can control the relative magnitudes of) signals at various harmonic and combination frequencies.

Finally, we are now able to devise nonquadrupolar ion traps with highly uniform static and rf electric fields, thereby reducing or eliminating prior limitations on mass accuracy, upper mass limit, selectivity of ion excitation or ejection, and relative ion abundance precision and reproducibility. The way is now cleared for applications of FT-ICRMS to the full range of mass spectrometric analysis.

Because most of the existing FT-ICR mass spectrometers were acquired before the advent of the above-mentioned improvements, it is reasonable to project that the next doubling period for growth in the number of FT-ICR instruments should be much shorter than the first.

This work was supported by National Science Foundation grant no. CHE-8721498 and The Ohio State University.

References

(1) Wineland, D. J. *Science* **1984,** *226,* 395–400.
(2) Comisarow, M. B.; Marshall, A. G. *Chem. Phys. Lett.* **1974,** *25,* 282–83.
(3) a. Comisarow, M. B. *Int. J. Mass Spectrom. Ion Proc.* **1978,** *26,* 369–78; b. Comisarow, M. B. *J. Chem. Phys.* **1978,** *69,* 4097.
(4) Ledford, E. B., Jr.; Ghaderi, S.; White, R. L.; Spencer, R. B.; Kulkarni, P. S.; Wilkins, C. L.; Gross, M. L. *Anal. Chem.* **1980,** *52,* 463–68.
(5) Francl, T.; Sherman, M. G.; Hunter, R. L.; Locke, M. J.; Bowers, W. D.; McIver, R. T., Jr. *Int. J. Mass Spectrom. Ion Proc.* **1983,** *54,* 189–99.
(6) Ledford, E. B., Jr.; Rempel, D. L.; Gross, M. L. *Anal. Chem.* **1984,** *56,* 2744–48.
(7) Rempel, D. L.; Ledford, E. B., Jr.; Huang, S. K.; Gross, M. L. *Anal. Chem.* **1987,** *59,* 2527–32.
(8) Wang, M.; Marshall, A. G. *Int. J. Mass Spectrom. Ion Proc.* **1989,** *86,* 31–51.
(9) Rempel, D. L.; Huang, S. K.; Gross, M. L. *Int. J. Mass Spectrom. Ion Proc.* **1986,** *70,* 163–84.
(10) Grosshans, P. B.; Marshall, A. G. *Int. J. Mass Spectrom. Ion Proc.* **1990,** *100,* 347–79.
(11) Grosshans, P. B.; Marshall, A. G., The Ohio State University, unpublished results.
(12) Dunbar, R. C. *Int. J. Mass Spectrom. Ion Proc.* **1984,** *56,* 1–9.
(13) Jeffries, J. B.; Barlow, S. E.; Dunn, G. H. *Int. J. Mass Spectrom. Ion Proc.* **1983,** *54,* 169–87.
(14) Rempel, D. L.; Gross, M. L. Presented at the 2nd American Society for Mass Spectrometry Sanibel Conference on Ion Trapping in Mass Spectrometry, Sanibel Island, FL, January 1990.
(15) van der Hart, W. J.; van de Guchte, W. J. *Int. J. Mass Spectrom. Ion Proc.* **1988,** *82,* 17–31.
(16) DeLong, S. E.; Mitchell, D. W.; Cherniak, D. J.; Harrison, T. M. *Int. J. Mass Spectrom. Ion Proc.* **1989,** *91,* 273–82.
(17) Kofel, P.; Allemann, M.; Kellerhals, H.; Wanczek, K-P. *Int. J. Mass Spectrom. Ion Proc.* **1986,** *74,* 1–12.
(18) Allemann, M.; Kofel, P.; Kellerhals, H.; Wanczek, K-P. *Int. J. Mass Spectrom. Ion Proc.* **1987,** *75,* 47–54.
(19) Huang, S. K.; Rempel, D. L.; Gross, M. L. *Int. J. Mass Spectrom. Ion Proc.* **1986,** *72,* 15–31.
(20) Dehmelt, H.; Wineland, D. J. *Bull. Am. Phys. Soc.* **1973,** *18,* 1571.
(21) Comisarow, M. B.; Marshall, A. G. *J. Chem. Phys.* **1976,** *64,* 110–19.
(22) Allemann, M.; Kellerhals, H.; Wanczek, K-P. *Int. J. Mass Spectrom. Ion Proc.* **1983,** *46,* 139–42.
(23) Bamberg, M.; Allemann, M.; Wanczek, K-P. *Proceedings of the 35th American Society for Mass Spectrometry Conference on Mass Spectrometry & Allied Topics;* Denver, CO, May 1987; pp. 1116–17.
(24) Wang, M.; Marshall, A. G. *Int. J. Mass Spectrom. Ion Proc.* **1990,** *100,* 323–46.
(25) Jackson, J. D. *Classical Electrodynamics;* John Wiley and Sons, Inc.: New York, 1975.
(26) Marshall, A. G.; Verdun, F. R. *Fourier Transforms in Optical, NMR, and Mass Spectrometry: A User's Handbook;* Elsevier: Amsterdam, 1990.
(27) McIver, R. T., Jr.; Hunter, R. L.; Baykut, G. *Anal. Chem.* **1989,** *61,* 489–91.
(28) McIver, R. T., Jr.; Baykut, G.; Hunter, R. L. *Int. J. Mass Spectrom. Ion Proc.* **1989,** *89,* 343–58.
(29) Comisarow, M. B.; Marshall, A. G. *Chem. Phys. Lett.* **1974,** *26,* 489–90.
(30) Marshall, A. G.; Roe, D. C. *J. Chem. Phys.* **1980,** *73,* 1581–90.
(31) Marshall, A. G.; Wang, T-C.L.; Ricca, T. L. *J. Am. Chem. Soc.* **1985,** *107,* 7893–97.
(32) Marshall, A. G.; Wang, T-C.L.; Chen, L.; Ricca, T. L. In *Fourier Transform Mass Spectrometry: Evolution, Innovation, and Applications;* Buchanan, M.V., Ed.; ACS: Washington, DC, 1987; pp. 21–33.
(33) Asamoto, B. *Spectroscopy* **1988,** *3,* 38–46.
(34) Buchanan, M. V.; Comisarow, M. B. In *Fourier Transform Mass Spectrometry: Evolution, Innovation, and Applications;* Buchanan, M.V., Ed.; ACS: Washington, DC, 1987; pp. 1–20.
(35) Chiarelli, M. P.; Gross, M. L. In *Analytical Applications of Spectroscopy;* Creaser, C. S.; Davies, A.M.C., Eds.; Royal Society of Chemistry: London, 1988; pp. 263–73.
(36) *Lasers in Mass Spectrometry;* Lubman, D. M., Ed.; Oxford University Press: New York, 1990; Chapter 7, pp. 11–15.
(37) Cody, R. B. *Analysis* **1988,** *16,* 30–36.
(38) Freiser, B. S. In *Techniques for the Study of Ion Molecule Reactions;* Farrar, J. M.; Saunders, W. H., Jr., Eds.; Wiley: New York, 1988; Chapter 2, pp. 61–118.
(39) Freiser, B. S. *Chemtracts—Anal. Phys. Chem.* **1989,** *1,* 65–109.
(40) Gord, J. R.; Freiser, B. S. *Anal. Chim. Acta* **1989,** *225,* 11–24.
(41) Hanson, C. D.; Kerley, E. L.; Russell, D. H. In *Treatise on Analytical Chemistry,* 2nd ed.; Winefordner, J. D., Ed.; Wiley: New York, 1988; Vol. 11, Chapter 2; pp. 117–87.
(42) Marshall, A. G. *Acc. Chem. Res.* **1985,** *18,* 316–22.
(43) Marshall, A. G. *Adv. Mass Spectrom.* **1989,** *11A,* 651–69.
(44) Nibbering, N.M.M. *Adv. Phys. Org. Chem.* **1988,** *24,* 1–55.
(45) Nibbering, N.M.M. *Acc. Chem. Res.* **1990,** *23,* 279–85.
(46) Russell, D. H. *Mass Spectrom. Rev.* **1986,** *5,* 167–89.
(47) Sharpe, P.; Richardson, D. E. *Coord. Chem. Rev.* **1989,** *93,* 59–85.
(48) Wanczek, K-P. *Int. J. Mass Spectrom. Ion Proc.* **1989,** *95,* 1–38.
(49) Wilkins, C. L.; Chowdhury, A. K.; Nuwaysir, L. M.; Coates, M. L. *Mass Spectrom. Rev.* **1989,** *8,* 67–92.
(50) Mullen, S. L.; Marshall, A. G. *J. Am. Chem. Soc.* **1988,** *110,* 1766–74.
(51) Williams, E. R.; Loh, S. Y.; McLafferty, F. W.; Cody, R. B. *Anal. Chem.* **1990,** *62,* 698–703.
(52) Ernst, R. R.; Bodenhausen, G.; Wokaun, A. *Principles of Nuclear Magnetic Resonance in One and Two Dimensions;* Clarendon: Oxford, 1987.
(53) Marshall, A. G.; Wang, T-C.L.; Ricca, T. L. *Chem. Phys. Lett.* **1984,** *105,* 233–36.
(54) Noest, A. J.; Kort, C.W.F. *Comput. Chem.* **1983,** *7*(2), 81–86.

(55) Pfändler, P.; Bodenhausen, G.; Rapin, J.; Walser, M-E.; Gäumann, T. *J. Am. Chem. Soc.* **1988,** *110,* 5625–28.
(56) a. Byrne, J.; Farago, P. S. *Proc. Phys. Soc. London* **1965,** *86,* 801–20; b. See also Sharp, T. E.; Eyler, J. R.; Li, E. *Int. J. Mass Spectrom. Ion Phys.* **1972,** *9,* 421–39.
(57) Pan, Y. P.; Ridge, D. P.; Rockwood, A. L. *Int. J. Mass Spectrom. Ion Proc.* **1988,** *84,* 293–304.
(58) Wang, M.; Ledford, E. B., Jr.; Marshall, A. G. *Abstracts of Papers,* FACSS XIV, Detroit, MI; FACSS: October 1987; Abstract 43.
(59) a. Grosshans, P. B.; Shields, P.; Marshall, A. G. *J. Am. Chem. Soc.* **1990,** *112,* 1275–77; b. Nikolaev, E. N.; Gorshkov, M. V. *Int. J. Mass Spectrom. Ion Proc.* **1985,** *64,* 115–25.
(60) Wang, M.; Marshall, A. G. *Anal. Chem.* **1989,** *61,* 1288–93.
(61) Hunter, R. L.; Sherman, M. G.; McIver, R. T., Jr. *Int. J. Mass Spectrom. Ion Phys.* **1983,** *50,* 259–74.
(62) Marshall, A. G.; Grosshans, P. B.; Wang, M.; Ricca, T. L.; Ledford, E. B., Jr. *Proceedings of the 36th American Society for Mass Spectrometry Conference on Mass Spectrometry and Allied Topics;* San Francisco, CA, June 1988; pp. 592–93.
(63) Wang, M.; Marshall, A. G. *Anal. Chem.* **1990,** *62,* 515–20.
(64) Hanson, C. D.; Castro, M. E.; Kerley, E. L.; Russell, D. H. *Anal. Chem.* **1990,** *62,* 520–26.
(65) Verdun, F. R.; Mullen, S. L.; Ricca, T. L.; Marshall, A. G. *Adv. Mass Spectrom.* **1988,** *11A,* 670–71.
(66) Wachter, E. A.; Farrar, T. C.; Kontney, M. J. *Int. J. Mass Spectrom. Ion Proc.,* in press.
(67) Fujiwara, M.; Katakura, H.; Inoue, M. *Rapid Commun. Mass Spectrom.* **1990,** *4,* 237–38.
(68) Schweikhard, L.; Lindinger, M.; Kluge, H-J. *Int. J. Mass Spectrom. Ion Proc.* **1990,** *98,* 25–33.
(69) Allemann, M.; Kellerhals, H.; Wanczek, K-P. *Chem. Phys. Lett.* **1981,** *84,* 547–51.
(70) Dunbar, R. C.; Chen, J. H.; Hayes, J. D. *Int. J. Mass Spectrom. Ion Proc.* **1984,** *57,* 39–56.
(71) Pan, Y. P.; Ridge, D. P.; Wronka, J.; Rockwood, A. L. *Rapid Commun. Mass Spectrom.* **1987,** *1*(7/8), 120–21.
(72) Nikolaev, E. N.; Gorshkov, M. V.; Mordehai, A. V.; Talrose, V. L. *Rapid Commun. Mass Spectrom.* **1990,** *4,* 144–46.
(73) Chen, L.; Cottrell, C. E.; Marshall, A. G. *Chemom. Intell. Lab. Syst.* **1986,** *1,* 51–58.
(74) Hunt, D. F.; Shabanowitz, J.; McIver, R. T., Jr.; Hunter, R. L.; Syka, J.E.P. *Anal. Chem.* **1985,** *57,* 765–68.
(75) Alford, J. M.; Williams, P. E.; Trevor, D. J.; Smalley, R. E. *Int. J. Mass Spectrom. Ion Proc.* **1986,** *72,* 33–51.
(76) Hunt, D. F.; Shabanowitz, J.; Yates, J. R., III; Zhu, N-Z.; Russell, D. H.; Castro, M. E. *Proc. Natl. Acad. Sci. U.S.A.* **1987,** *84,* 620–23.
(77) Shomo, R. E., II; Delmore, J. E.; Appelhans, A. D.; Dahl, D. A.; Marshall, A. G. *Proceedings of the 36th American Society for Mass Spectrometry Conference on Mass Spectrometry & Applied Topics;* San Francisco, CA, June 1988; pp. 1217–18.
(78) Ipezsa, I.; Knoll, H.; Wanczek, K-P.; Linden, H. B. *Proceedings of the 36th American Society for Mass Spectrometry Conference on Mass Spectrometry & Allied Topics;* San Francisco, CA, June, 1988; pp. 618–19.
(79) Loo, J. A.; Williams, E. R.; Amster, I. J.; Furlong, J.J.P.; Wang, B. H.; McLafferty, F. W.; Chait, B. T.; Field, F. H. *Anal. Chem.* **1987,** *59,* 1882–84.
(80) Henry, K. D.; Williams, E. R.; Wang, B. H.; McLafferty, F. W.; Shabanowitz, J.; Hunt, D. F. *Proc. Natl. Acad. Sci. U.S.A.* **1989,** *86,* 9075–78.
(81) Kofel, P.; McMahon, T. B. *Int. J. Mass Spectrom. Ion Proc.* **1990,** *98,* 1–24.

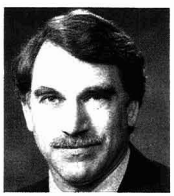

Alan G. Marshall received his Ph.D. in physical chemistry from Stanford University in 1970. He joined the faculty at the University of British Columbia (Vancouver, Canada) in 1969 and moved to The Ohio State University in 1980 as professor of chemistry and biochemistry and director of the Chemical Instrument Center. He is best known for his co-invention (with M. B. Comisarow) and continuing development of FT-ICRMS, recognized by the ACS Division of Analytical Chemistry Award in Chemical Instrumentation, the Eastern Analytical Symposium Award, the ACS Akron Section Award, and his election to the rank of fellow in both the American Physical Society and the American Association for the Advancement of Science.

Peter B. Grosshans received his B.S. degree from the University of Colorado, Boulder, in 1983. He won an OSU Presidential Graduate Fellowship on the way to obtaining his Ph.D. in chemical physics in June 1990. Currently he is a postdoctoral fellow with Alan Marshall, who was also his graduate adviser. His research concerns the physics behind the FT-ICR technique; most notably, he is trying to linearize excitation and detection events simultaneously to make quantitative data accurate.

MEETINGS

Conferences

■ **21st International Symposium on Environmental Analytical Chemistry.** May 20–22. Jekyll Island, GA. *Contact: Wayne Garrison, Environmental Research Laboratory, U.S. EPA, College Station Rd., Athens, GA 30613 (404-546-3145)*

■ **21st Annual Symposium on Advances in Applied Analytical Chemistry.** May 22–23. Kenner, LA. *Contact: Judy Timpa, SRRC, ARS, USDA, P.O. Box 19687, New Orleans, LA 70179 (504-286-4360)*

■ **BioPharm Conference.** June 10–11. San Francisco, CA. *Contact: BioPharm Conference, 859 Willamette St., P.O. Box 10460, Eugene, OR 97440 (503-343-1200)*

■ **14th International EPR Symposium.** July 28–Aug. 1. Denver, CO. *Contact: Gareth Eaton, Dept. of Chemistry, University of Denver, Denver, CO 80208 (303-871-2980)*

■ **Inter/Micro-91.** July 29–Aug. 1. Cambridge, U.K. *Contact: Nancy Daerr, McCrone Research Institute, 2820 S. Michigan Ave., Chicago, IL 60616 (312-842-7100)*

■ **9th International Bioanalytical Forum—Bioanalysis of Drugs.** Sept. 3–6. Guildford, U.K. *Contact: E. Reid, Guildford Academic Associates, 72 The Chase, Guildford GU2 5UL, U.K.*

■ **19th Annual Water Quality Technology Conference.** Nov. 10–14. Orlando, FL. *Contact: American Water Works Association, 6666 West Quincy Ave., Denver, CO 80235 (303-794-7711)*

Short Courses and Workshops

For information on the following courses to be held in New Brunswick, NJ, contact Office of Continuing Professional Education, Cook College, Rutgers University, P.O. Box 231, New Brunswick, NJ 08903 (908-932-9271)

■ **Enzymes: Principles and Applications.** March 13–14
■ **Bioreactors for Biotechnology.** April 10–11
■ **HPLC/CZE.** May 7–9
■ **Genetic Engineering for Nonspecialists.** May 14–15

For information on the following courses to be held in Chicago, IL, contact Nancy Daerr, McCrone Research Institute, 2820 S. Michigan Ave., Chicago, IL 60616 (312-842-7100)

■ **Microscopical Identification of Asbestos.** March 18–22, April 8–12, April 29–May 3, May 13–17, June 17–21, July 8–12, Sept. 9–13, Sept. 30–Oct. 4, Oct. 14–18, Nov. 18–22, and Dec. 16–20
■ **Advanced Asbestos Identification.** March 18–22, April 29–May 3, June 3–7, July 15–19, Aug. 26–30, Sept. 30–Oct. 4, Oct. 28–Nov. 1, and Dec. 2–6
■ **TEM Introduction.** April 1–5, Sept. 9–13, and Dec. 9–13
■ **TEM Asbestos Analysis.** April 8–12, May 20–24, Sept. 16–20, Oct. 28–Nov. 1, and Dec. 16–20
■ **TEM Applications.** May 6–10 and Oct. 7–11
■ **Photomicrography for Asbestos Analysts.** May 13–17
■ **Quantitative Asbestos Analysis.** June 10–12 and Nov. 4–6
■ **Special Asbestos Problems.** Aug. 26–30

For information on the following courses, contact Susan Millman, University of Cincinnati, NIOSH Educational Resource Center, Kettering Laboratory, 3223 Eden Ave., Cincinnati, OH 45267 (513-558-1732)

■ **Biological Monitoring Techniques.** March 27–28. Cincinnati, OH
■ **Survey of Industrial Hygiene.** May 7–10. Cincinnati, OH

For information on the following courses to be held in St. Paul, MN, contact Stat-Ease, 2021 East Hennepin Ave., Suite 191, Minneapolis, MN 55413 (612-378-9449)

■ **Statistical Process Control Made Easy.** April 9–12
■ **Advanced Experiment Design.** April 23–26
■ **Advanced Statistical Process Control.** May 7–10

For information on the following courses to be held in Madison, WI, contact Extension Services in Phar-

macy, University of Wisconsin, 425 N. Charter St., Madison, WI 53706 (608-262-3130)

■ **Pharmacokinetics.** May 6–10
■ **Introduction to the Regulatory Process for Pharmaceutical Scientists.** May 20–22
■ **Basic Pharmacology.** May 20–24

■ **Polymer Testing and Characterization.** June 6–7. Lowell, MA. *Contact: Plastics Institute of America, Suite 100, 277 Fairfield Rd., Fairfield, NJ 07004 (201-808-5950)*
■ **Colorimetry: An Intensive Short Course for Scientists and Engineers.** June 11–13. Rochester, NY. *Contact: Colleen McCabe, Munsell Color Science Lab., Rochester Inst. of Tech., P.O. Box 9887, Rochester, NY 14623 (716-475-7189)*

These events are newly listed in the JOURNAL. See back issues for other events of interest.

Call for Papers

■ **1992 Winter Conference on Plasma Spectrochemistry.** San Diego, CA. Jan. 6–11, 1992. Program topics will include automation, expert systems, and robotics with plasma spectroscopy; chemometric applications in plasma spectrochemistry; chromatography with plasma source detection; flow-injection plasma spectrometry; glow discharge and low-pressure plasma atomic and mass spectrometry; laser-assisted plasma spectrochemistry; mechanisms and processes in plasma sources; modern sample preparation and calibration techniques; new instrumentation; plasma source MS; process control, remote, and on-line plasma analysis; sample introduction techniques and phenomena; spectrochemical applications of plasma sources; and transform spectroscopy. Authors wishing to contribute oral or poster presentations should submit titles and 50-word abstracts by July 1 to R. M. Barnes, Dept. of Chemistry, GRC Towers, University of Massachussetts, Amherst, MA 01003 (413-545-2294).

■ **5th Conference on Computer Applications in Analytical Chemistry (Compana '92).** Jena, Germany. Aug. 24–27, 1992. The program will consist of invited lectures and contributed oral and poster presentations on the following topics: chemometrics for environmental analysis and monitoring, principles of artificial intelligence in analytical chemistry, statistical data analysis, multivariate experimental design and optimization, structure–activity and composition–quality relations, simulation and modeling of processes, evaluation of spectroscopic and chromatographic data, computer-coupled hyphenated methods in analytical chemistry, laboratory automation and information management, and principles of image analysis in analytical chemistry. Authors wishing to contribute oral or poster presentations should request information from K. Danzer, Friedrich Schiller University Jena, Institute of Inorganic and Analytical Chemistry, Steiger 3, Haus 3, DDR-6900 Jena, Germany. Preliminary applications should be submitted by June 1991.

BOOKS

Chromatography, MS, IR and Raman Spectroscopy, and the Determination of Molecular Weight and Chemical Composition

Chromatographic Analysis of Pharmaceuticals. John A. Adamovics, Ed. ix + 688 pp. Marcel Dekker, 270 Madison Ave., New York, NY 10016. 1990. $125

Reviewed by Lawrence A. Pachla, Sterling Research Group, Malvern, PA 19355

This monograph is directed at chemists with responsibilities in the areas of analytical research and development, pharmaceutics, quality control, and manufacturing. It provides a comprehensive overview of the chromatographic methods of analysis for pharmaceuticals. It is divided into four major sections: Section 1, Regulatory Considerations; Section 2, Sample Handling; Section 3, Chromatographic Methods Development; and Section 4, a comprehensive tabular review of available chromatographic methods for pharmaceuticals.

One strength of the book is the discussion of regulatory requirements for the chromatographer. This topic is rarely covered in other monographs and is a definite attribute. This section provides an overview of which regulatory considerations should be evaluated when developing a method, rather than a mere compilation of regulatory acts. Section 2 discusses sample pretreatment and automation of methods. The contributors have attained their objective, which is to address those manual and automated approaches that have an impact on providing sample pretreatment for optimum method performance.

Section 3 discusses the various aspects of materials, hardware, detection, sampling, and applications associated with TLC, GC, HPLC, and headspace analysis. The authors do not review theory in depth but discuss the topics from a practical point of view. Because of this approach, the practicing chromatographer will find these chapters useful.

The major portion of this monograph is Section 4, which reviews the application of chromatographic techniques in pharmaceutical analysis. Approximately 400 pages are devoted to the tabular review of available chromatographic pharmaceutical methods. The literature cited indicates that 1137 manuscripts have been reviewed. The majority of references were published prior to 1985. Less than 4% of the citations date to the period 1986–87. This section will quickly become outdated. Nevertheless, it is a valuable feature at present.

Introduction to Infrared and Raman Spectroscopy, 3rd ed. Norman B. Colthup, Lawrence H. Daly, and Stephen E. Wiberley. xii + 547 pp. Academic Press, 1250 Sixth Ave., San Diego, CA 92101. 1990. $70

Reviewed by Chris W. Brown, Department of Chemistry, University of Rhode Island, Kingston, RI 02881

During the developmental years, interpretation of IR spectra became almost an art form. There were a number of superb practitioners of this art who apparently learned their trade by interpreting many, many spectra. Most of these experts worked in industrial laboratories and had access to spectra of derivatives of similar molecules, which aided in their understanding of the spectra.

During this same period (the late 1940s and 1950s), many publications appeared on the assignments of IR spectra of organic molecules. These were closely followed by a rash of publications on the force constants of molecules. The practical and useful knowledge of vibrational spectroscopy was beginning to unfold.

By the 1960s spectra of enough compounds had been measured and interpreted to allow correlations to be made between the spectra and molecular compositions. The primary correlations were between the appearance of a band in a certain frequency range and the presence of a functional group in a molecule. Eventually, these correlations led to a set of rules for interpreting spectra.

The primary objective of this book is to convey the rules and correlations to the novice and to those of us who have an occasional need for interpreting spectra. However, it is also an excellent reference for those more experienced in interpretation. The first edition, published in 1964, brought together a large body of information into one well-written and well-conceived book. I would say that my copy of that edition has been the most used book in my library.

The newest edition contains some useful improvements over the earlier ones. Previously, Raman spectroscopy appeared in the title as well as in the theory and experimental sections, but Raman spectra were noticeably lacking in the chapters on interpretation. The emphasis is still on IR; however, Raman plays a larger role and some nice examples are presented.

I have emphasized the spectral interpretation aspects of the book, but it contains much more. In fact, it has all of the ingredients for an excellent introductory text on IR (and Raman) spectroscopy. The first chapter presents a splendid discussion of the basic aspects of vibrational and rotational spectra. The approach is from the classical mechanical point of view, but it conveys to the novice a basic picture of the relationship between energy and the fundamental motions of molecules. For those desiring a greater understanding of vibrations, detailed theoretical aspects are discussed at the end of the book in Chapter 14.

Experimental considerations of IR spectroscopy are covered in Chapter 2. The coverage is at the level of a general instrumental analysis text and proba-

bly should have been left to that source. Chapter 3 does a good job of covering molecular symmetry and its applications to vibrational spectra. This is important for future users.

Chapter 4, on the vibrational origin of group frequencies, is the pivotal point of the book. Here, theory meets application, and the basic rules for spectral interpretation are developed. The authors' many years of experience are conveyed to the reader in simple and understandable fashion. They connect the spectral bands to the motions of molecules and show the dependence on masses, bond strengths, adjacent atoms, and groups. The authors start with the motions of diatomics and "build" larger and larger vibrating structures.

Chapters 5 through 11 cover the major organic functional groups containing C, H, O, and N, whereas Chapter 12 covers groups containing B, Si, P, S, and halogens. In these chapters the correlation and/or lack of correlations are discussed. The individual discussions are brief but very useful in helping to sort out the spectrum of a complex molecule.

The famous IR correlation charts, which consist of spectra of bars indicating the appearance of a band related to a particular group, are given in Chapter 13. These are useful, but even more practical are the 624 miniature IR spectra and 36 miniature Raman spectra of organic molecules. As the novice matures in the art of interpretation, the pages containing these spectra will be the most used of the entire book. They provide understanding and help in problem solving. Often, the spectrum one is trying to interpret will not appear in the figures, but many of the key features can be identified by flipping through the pages of spectra.

This book should be on the desk of every spectroscopist and everyone involved with IR and Raman spectra of organic molecules. In addition, it is a great starting place for anyone interested in learning about vibrational spectroscopy.

Determination of Molecular Weight. Anthony R. Cooper, Ed. xiv + 526 pp. John Wiley & Sons, 605 Third Ave., New York, NY 10158. 1989. $95

Reviewed by Howard G. Barth, Central Research & Development, E. I. du Pont de Nemours & Company, Experimental Station, P.O. Box 80228, Wilmington, DE 19880-0228

The determination of average molecular weights and molecular weight distribution of polymers is a fundamental measurement needed for polymer characterization. Although size-exclusion chromatography (SEC) is perhaps the premier technique for rapidly measuring these parameters, there are also available a number of classical approaches and new techniques. The purpose of this multi-authored book is to provide a survey of these methods. The major techniques covered include osmometry, light and neutron scattering, ultracentrifugation, viscometry, fractionation, chromatography, mass spectrometry, NMR, and FT-IR.

For the most part, each chapter includes theory, instrumentation, and application sections. Coverage generally ranges from brief surveys to comprehensive treatments. Pertinent references, extending to 1986–87, are given.

"This book provides an excellent survey of current techniques that are available."

Most chapters are well written; however, a number of typos were noticed, including a misplaced line in the middle of a paragraph. Several chapters use the term "daltons" to describe molecular mass, rather than the acceptable terminology "g/mol."

Chapter 1 (A. R. Cooper) briefly lists definitions of molecular weight averages and distribution functions; it is not very informative, especially for a leadoff chapter. Chapter 2 (Cooper) provides a short overview on the use of colligative properties and end-group analysis for the determination of number-average molecular weight. Vapor pressure osmometry is covered in Chapter 3 (C.E.M. Morris), although not very extensively. Membrane osmometry, treated in Chapter 4 (H. Coll), is a comprehensive survey of the subject and includes a number of practical suggestions.

Chapter 5 on light scattering (B. Chu) is an advanced treatment of the subject. The emphasis is on the use of both static and dynamic light scattering measurements to estimate molecular weight distributions. Unfortunately, practical limitations of the technique are not discussed in detail. Also, the determination of radius of gyration is only briefly mentioned.

The use of neutron and X-ray scattering to measure molecular weights is reviewed in Chapter 6 (R. W. Richards). Although the author stresses that neutron and X-ray scattering are best employed for determining structural information, the chapter, which focuses primarily on neutron scattering, does provide an excellent overview of these techniques and their comparison to light scattering. One serious error, however, is a statement in the introduction claiming that it is doubtful if the radius of gyration can be obtained for random polymers of $< 5 \times 10^5$ g/mol. With present-day laser light sources, the lower limit is closer to 1×10^5 g/mol.

Chapter 7 (A. R. Cooper) is a good survey of ultracentrifugation of synthetic polymers. Topics include equilibrium sedimentation, density gradient, and sedimentation velocity methods. Although ultracentrifugation has been almost supplanted by SEC, the author demonstrates the usefulness of this technique in a variety of applications.

Chapter 8 (K. Kamide and M. Saito) represents one of the more comprehensive treatments of intrinsic viscosity available; the authors are to be commended for their clear and well-written discussions. Coverage includes most aspects of dilute solution viscosity measurements. Also included is an appendix containing the derivation of Einstein's viscosity equation and the Kirkwood–Riseman theory.

Polymer fractionation based on solubility differences is covered in Chapter 9 (K. Kamide and S. Matsuda). Theory and applications of this classical approach are adequately reviewed; however, the long and tedious derivation of several equations was unnecessary—primary references would have sufficed. All fractionation approaches, including turbidimetric titrations, are discussed. It is unfortunate, however, that the authors take a rather defensive position when comparing fractionation techniques to SEC. It would have been preferable to treat them as complementary approaches, depending on the application.

Chapter 10 on SEC, authored by M. C. Styring and A. E. Hamielec, was a joy to read. The sections on theory, calibration approaches, and data treatment are concise and well written. A good overview of aqueous SEC is also presented. In discussing concentration effects, the authors cite an outdated reference, which suggests that injected sample solutions should have a viscosity less than twice that of the mobile phase. Although appropriate for conventional columns, this ratio is not applicable to high-performance columns where a relative viscosity of < 1.1 is typically required.

Chapter 11 (G. S. Greschner) describes an interesting separation technique, phase distribution chromatography, in which a polymer is separated on the basis of molecular weight using a stationary phase of the same chemical type as the sample. Separation is accomplished by operating the system below the theta temperature of the sample in the mobile phase. Although this procedure has been used only for polystyrene, theory suggests wide applicability, especially for polymers of low polydispersities (< 1.01).

The use of sedimentation, thermal, and flow field-flow fractionation (FFF) techniques for determining molecular weight distributions is covered in detail in Chapter 12 (J. C. Giddings, K. D. Caldwell, and L. F. Kesner). A number of useful applications are given; the most striking is determination of polydispersities of polystyrene as low as 1.003 using thermal FFF.

Chapter 13 (B. E. Richter) is an overview of the application of supercritical fluid chromatography for the separation of oligomers. Various approaches using MS to determine molecular weights of polymers, mainly oligomers, are reviewed in Chapter 14 (R. P. Lattimer, R. E. Harris, and H-R. Schulten). Methods examined include rapid heating, californium plasma desorption, secondary ion, field desorption, electrohydrodynamic ionization, laser desorption, and thermospray.

The next two chapters deal with the characterization of insoluble, crosslinked polymers. Chapter 15 (A. M. Zaper and J. L. Koenig) contains an excellent section on the theory of networks. Characterization methods discussed include chemical, thermal, and spectroscopic approaches. The sections on solid-state NMR and FT-IR are quite informative. Chapter 16 (J-P. Queslel and J. E. Mark) focuses on mechanical and solvent-swelling methods for characterizing insoluble polymers. Network topology and molecular elasticity theory are covered.

The last chapter, compiled by P. H. Verdier and L. E. Smith, is a source listing of commercially available polymer standards of known molecular weight.

This book provides an excellent survey of current techniques that are available for molecular weight measurements. It is not an introductory text, but should serve as a reference book for those experienced in this area. Both analytical and polymer chemists will find it of considerable value.

Determination of Chemical Composition and Molecular Structure, Part B. Bryant A. Rossiter and John F. Hamilton, Eds. xi + 971 pp. John Wiley & Sons, 605 Third Ave., New York, NY 10158. 1989. $150

Reviewed by Philip J. Savickas, Analytical Sciences Laboratory, The Dow Chemical Co., Midland, MI 48667

This book, at just under 1000 pages, is part of a comprehensive collection of topics for the *Physical Methods of Chemistry* series. The series was started under the title *Physical Methods of Organic Chemistry* in 1945 by the late Arnold Weissberger and is now in the second edition (fourth overall) under the current title. This particular work is part of a two-book volume that is one of eight projected in this edition covering many aspects of physical chemistry. A comprehensive accumulation of knowledge such as the full set would best suit a technical library. For someone interested in only one of the topics, however, each book is self-sufficient. For convenience, related topics are generally discussed in the same book. The contributions of 12 authors on eight topics were coordinated by Rossiter and Hamilton. The chapters in this book include: Chiroptical Spectroscopy, Determination of Dipole Moments in Ground and Excited States, Static Magnetic Techniques and Applications, Electron Spin Resonance, New Nuclear Magnetic Resonance Experiments in Liquids, Gas Chromatography, Size-Exclusion Chromatography, and Field Flow Fractionation.

The book provides, for technically trained scientists, an introduction to the topics discussed along with sufficient bibliographical information to supply further resources for the readers' advancement. I would call this work more than just an appreciative treatment, as the serious reader will use it as a fundamental introduction and guide toward further information. The book excels with a thorough yet concise treatment of each topic.

One challenge to the editors is to coach the authors in providing a consistent, accurate, and relevant introduction without getting lost in the details of current research. The editors state in their preface that the use of selected applications by the authors is intended to complement the basic theory and descriptions, and to illustrate the techniques' capabilities and limitations. I liked this approach because many readers will be using the book for practical applications as well as for academic reasons.

Bibliographies are critical in compilations such as this. Although the basis of any subject can be discussed without reference to current literature, the deeper understanding of any technical topic constantly changes and applications certainly require timely references. The book's references generally extend through 1984 with a few in 1985, which makes it a bit dated in terms of current understanding and application. This generally will not be to the readers' disadvantage, as the book is intended to provide a basis rather than a current overview. The bibliographies are very good; some authors provide not only a list of references but also suggestions on textbooks, journals, and data compilations, as well as further representative applications.

This book competes with many other sources of information on these topics. These sources range from current review articles to full textbooks. The book under review cannot, by its self-imposed physical constraints, compete with all these other sources. Not everyone will find this format to be ideal or even appealing. I did, however, and the book, in fine fashion, fills a valuable niche in depth of coverage and convenience.

A Computer-Assisted Chromatography System. Kiyokatsu Jinno. viii + 271 pp. Hüthig Buch Verlag GmbH, Im Weiher 10, Postfach 10 26 40, D-6900 Heidelberg, Germany. 1990. $70

Reviewed by Edward J. Kikta, Jr., FMC Corporation, P.O. Box 8, Princeton, NJ 08543

A Computer-Assisted Chromatography System by Kiyokatsu Jinno offers the reader an interesting insight into the development of a microcomputer-based chromatography system. The author develops a system that integrates four highly important predictive and/or organizational concepts: retention prediction, optimization of separa-

tion conditions, a database, and automatic solute identification. The goals of this monograph are lofty, and success, in a limited manner, is achieved.

The organization of this book is very similar to a thesis for an advanced degree. This serves both as an asset and as a detriment. The author often switches between computer-related and chromatographic concepts. In one sense they must be interrelated, but the presentation does not effectively show the relationship.

Chapters 1 and 2 (the introduction and description of a database system) are too brief given the import of the topics at hand. The use of PAHs as a model system for retention behavior, however, is an excellent choice.

Chapter 3, in this reviewer's opinion, is the heart of the book. In fact the bulk of Chapter 3 with some inclusions from Chapter 5 would make an excellent review article, one that would be much tighter and to the point. The work with phenylthiohydantoin amino acids should be expanded upon in a future edition of this book.

Chapter 4, which reviews detection systems, is much too brief and out of place in this book; the concepts are covered in significantly better depth in many publications. A liberal paragraph in the introductory chapter referring to this topic would have been sufficient. An appendix containing 62 pages of BASIC code is not particularly useful to most readers and is unnecessary to most.

This book is a good attempt at tackling a very relevant topic in chromatographic automation, namely integrated systems, but it falls somewhat short of its goals. It is not generally useful to the practicing chromatographer but will be useful to systems developers whether they are programmers or chromatographers.

Biomedical Applications of Mass Spectrometry, Vol. 34. Clarence H. Suelter and J. Throck Watson, Eds. xiii + 396 pp. John Wiley & Sons, 605 Third Ave., New York, NY 10158. 1990. $45

Reviewed by Richard B. van Breemen, Department of Chemistry, Box 8204, North Carolina State University, Raleigh, NC 27695-8204

Volume 34 of the series "Methods of Biochemical Analysis" differs from the previous volumes by focusing all the chapters on a particular analytical technique instead of covering a variety of methods. This volume contains five chapters, the first of which is an introduction to instrumentation and data interpretation. The next four chapters, each written by an expert in the field, discuss applications to carbohydrate analysis, peptide sequencing, analysis of nucleic acid components, and pharmacology.

The editors state that this book is intended to serve as a reference for a course in MS applied to biology. In this regard, the text fills a significant void by providing chapters on the analysis of several specific classes of biological compounds that are accessible to students of MS. The requirements of sample purity, quantity, and handling, as well as methods of derivatization, are discussed in great detail, followed by careful interpretation of the resulting mass spectra with an emphasis on structure determination. Researchers who are not mass spectrometrists but are interested in the structural determination of carbohydrates, peptides, or nucleic acid components or in the pharmacology topics of drug metabolism, pharmacokinetics, and detection and quantitation of pharmaceuticals in biological samples would also benefit by reading the appropriate chapters of this book. Even experienced mass spectrometrists should learn some new methods, since few will be experts in the analysis of all types of samples.

The introductory chapter provides an overview of instrumentation, ionization methods, and data interpretation. Although it is necessarily concise, perhaps the desorption ionization techniques and mass analyzers that are mentioned in later chapters should have been discussed more completely. Laser desorption and Fourier transform mass spectrometers are not discussed, although they appear as examples in the chapters on peptide sequencing and nucleotides.

The chapters on the analysis of specific classes of compounds provide detailed accounts of procedures for sample preparation and analysis by classical as well as more recent techniques. Numerous examples are discussed, and extensive bibliographies that include many reviews as well as original papers through 1988 are provided. The book contains a complete author index for all references and a less complete but satisfactory subject index. The chapter on pharmacology includes interesting applications of MS to the identification of drug metabolites and drug detection in biological fluids, but it lacks the tight focus on the analysis of a particular class of compounds found in the other applications chapters. Detailed accounts of sample preparation and data analysis are not presented, but numerous examples of quantitation using MS and the use of MS in medicine are provided. Therefore, it is indispensable as a textbook detailing biomedical applications of MS.

Although every chapter contains examples from the author's own laboratory, many others are discussed that were published by other researchers. These examples are typically presented with original mass spectra. For some reason, the chapter on MS of nucleic acid components contains no figures or spectra from laboratories other than that of the author. Noticeably absent from this chapter are spectra of oligonucleotides using fast atom bombardment, tandem MS, plasma desorption MS, and LC/MS, all of which are discussed in the text.

The main problems with this book are the limited number of classes of biological compounds that are discussed and the timeliness of the cited references. Although the applications of MS to the analysis of carbohydrates, peptides, and nucleic acids are vitally important to biology and medicine, other significant topics have been overlooked. An important addition would have been a chapter on lipid analysis by MS that discussed compounds such as fatty acids, acylglycerols, and phospholipids. Another chapter might have included the analysis of steroids and bile acids.

Mass spectrometric instrumentation and techniques for biomedical applications are advancing so rapidly that, by the time of publication, any text in this area will be outdated. This book is no exception. For example, the introductory chapter states that plasma desorption MS has been used to measure the highest molecular weight compounds, in excess of 25 000, and cites a 1988 reference. The chapter on peptide sequencing (slightly more up to date) cites another 1988 reference in which the mass of bovine serum albumin (MW 67 000) was determined by using matrix-assisted laser desorption MS. By 1989, papers were published that reported the observation of molecular ion species of proteins weighing up to 250 000. In 1990, this mass range exceeded 300 000 daltons.

Other recent advances that are not discussed in this book include LC/MS applications such as electrospray, SFC/MS of carbohydrates, and continuous flow-fast atom bombardment MS of oligonucleotides. Although new methods, applications, and instrumentation have been reported since this book was written, the basic methodology discussed in all of the chapters will remain in widespread use for at least several more years if not indefinitely.

Personal Dosimeters: Analytical Chemistry on a Lapel

For anyone who works with radioisotopes, a film badge is often standard wearing apparel. The badge provides the wearer with an individualized measure of radiation exposure. Over the last decade other personal dosimeters, small lightweight collection devices that can be easily worn or carried, have been developed for airborne volatile organic compounds (VOCs) and particulate contaminants in the workplace. That same concept of individual measurement is now being extended to determine a wider range of potentially harmful agents, in both the workplace and the community.

"It is driven by the EPA's [Environmental Protection Agency] desire to measure direct human exposures to contaminants at levels 10 to 1000 times lower than before," explains Paul Lioy, director of the Exposure, Measurement, and Assessment Division at the University of Medicine and Dentistry of New Jersey. In particular, EPA is interested in measuring contaminants in home atmospheres and those associated with personal activities, which are found at much lower levels than in workplace environments. By combining information on home atmospheres with data on workplace and outdoor pollutants, public health researchers hope to gain a measure of total human exposure to various contaminants (*1*).

Currently, says Lioy, about 25 volatile organics can be measured by personal dosimeters. "That is a small suite of compounds. We need to be a little more clever." In particular, inorganics such as chromium species and semivolatile organics such as polyaromatic hydrocarbons (PAHs) are not easily measured by personal dosimeters.

The design of these personal samplers can be broadly divided into passive and active (pump-driven) types. Passive samplers are lighter and simpler than active devices and generally require longer sampling periods to collect sufficient samples for analysis. Passive samplers depend on either permeation- (onto a membrane) or diffusion-controlled collection.

FOCUS

Diffusion-controlled passive samplers are designed with a gap between the inlet and the collection medium. This gap may include filters or well-defined channels between the environment and the sorbent material, providing a region of quiet air. Mass transport in this area occurs solely by diffusion, offering a mathematical model for sampling rate. For instance, if the ratio of the length to diameter of the diffusion channel is at least eight, Fick's first law determines mass flow (*2*).

Several different sorbents can be used to collect pollutants in these samplers, although Tenax (porous 2,6-diphenyl-*p*-phenylene oxide) appears to be the most popular. Tenax quantitatively absorbs a host of VOCs at ppb levels, remains inert, and has a low affinity for water. Analytes are desorbed by heating Tenax to 150 °C or higher (the material also displays good thermal stability), typically in a He flow, and are collected in a cold trap for subsequent analysis by GC or GC/MS. Unfortunately, to obtain quantitative results all of the analyte must be desorbed and collected in a cold trap. Thus sample tubes must be handled with care.

In the future, says Lioy, supercritical fluid extraction (SFE) may replace thermal desorption. Preliminary experiments with supercritical CO_2 have shown quantitative recovery of PAHs from Tenax (*3*). Besides extracting less volatile organics, SFE offers the possibility of using only a fraction of the sorbent for analyte extraction, retaining the remainder for different or repetitive measurements.

The other commonly used sorbent is activated charcoal, which retains many of the same VOCs as Tenax. However, charcoal has a greater affinity for water

and higher desorption temperatures.

The chief limitation of any sorbent centers on how much of a particular pollutant it can retain. Because of the small quantities of sorbent involved in these studies, generally < 0.5 g, researchers measure retention in terms of breakthrough volumes. Related to retention volumes, the breakthrough volume is defined as the volume at which an analyte flowing steadily over the adsorbate saturates the material and appears in the tube's effluent. This value is often recorded as liters of analyte per gram of sorbent. As a rule, compounds with low boiling points, such as *n*-pentane or CCl_3F, or high polarities, such as methanol, have low breakthrough volumes (< 30 L/g) on Tenax.

Fortunately, several important VOCs such as benzene, toluene, and benzaldehyde have high breakthrough volumes on Tenax. For instance, a recent British study of styrene vapor retention on a commercially available passive sampler (90 mm long with a 5-mm i.d.) loaded with 200 mg of Tenax found that the rate of uptake began to drop only after more than 5 h of exposure. In this study, the styrene air concentration in an occupational setting was 70 ppm and desorption conditions were 250 °C for 10 min with analysis by GC. Field studies of the sampler demonstrated that the coefficient of variation for workplace styrene measurements is about 6% (*4*). It remains to be determined how it will perform at the ppb range found outside the workplace.

One factor that can influence measurements is the presence of strong oxidizers in ambient air. For example, although Tenax does not retain ozone, it has been shown that this reactive gas can convert bound styrene into benzaldehyde or benzoic acid (*5*).

Polar molecules require a different type of sorbent. One example from Japan is a model diffusive personal sampler for acetone vapors in occupational settings. In a simple experiment, 3 mL of water were used as the sorbent and a syringe as the holder. A porous polypropylene membrane allowed only low molecular weight vapors to pass into the water, and a 2-cm glass fiber filter paper provided the diffusion gap. According to the researchers, acetone in atmospheric concentrations ranging from 200 to 1000 ppm is steadily and linearly absorbed by this sampler for periods up to 8 h (*6*).

"Combining sorbents leads to a more versatile passive sampler."

Combining several sorbents creates a more versatile passive sampler (Figure 1). In one study, airflows were directed sequentially across three sorbents: Tenax, Ambersorb XE-340 (a pyrocarbon-modified charcoal), and activated charcoal. The latter two sorbents are better suited for collecting low-boiling organics than Tenax, with the trade-off of greater water retention.

This multisorbent sampler was assembled in a 203-mm tube with 14 mm of glass beads in the inlet. Silanized glass wool separated the three sorbents, which were loaded in respective amounts of 85.5, 167, and 48 mg. After exposure, the analytes were purged from the sorbents for several minutes at 275 °C. GC and GC/MS were employed for analysis. In a series of field tests, researchers found that for a number of representative low-boiling organics at ppb levels, such as 1,1,1-trichloroethane and ethylbenzene, the typical accuracy of this passive sampler was ±5% (*7*).

Measurements of radioisotopes require somewhat different techniques. For instance, personal aerosol samplers containing activated charcoal have been used for "grab sampling" of Rn. The captured isotope is measured by its γ emission, and that value is generalized to an entire area. Radon daughters are measured in a similar manner by capture on a filter.

One obvious weakness of passive samplers is that humans actively sample air. A person generally inhales about 20 L/min. Portable, battery-operated pumps worn on a belt can typically pull about 2–4 L/min through personal samplers. "The idea is to get a representative, high-volume sample," explains John Johnson, manager of Pacific Northwest Laboratory's Health Physics Department.

Johnson recently published a study of an active sampler used by workers who handle and process α-emitting radioactive fuels. The sampler consisted of a particle-collecting Millipore filter head worn on the lapel or shirt pocket that is connected by a flexible hose to a commercial pump. Typically, particles in the range of 0.1–10 μm (activity median aerodynamic diameter) are collected. After sample collection the filter is placed in an α spectrometer to determine exposure. The α energy spectrum identifies the various isotopes, providing health officers with a detailed picture of exposure. For instance, ^{238}Pu carries a greater health risk than ^{233}U.

In addition, the filter can be sandwiched between two damage track detectors, which then are electrochemically etched. This provides a crude estimate of particle size and has a bearing on total exposure calculations for the worker (*8*).

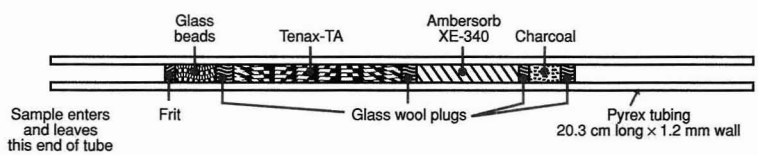

Figure 1. Schematic of a passive sampler employing three sorbents.
(Courtesy Envirochem, Inc.)

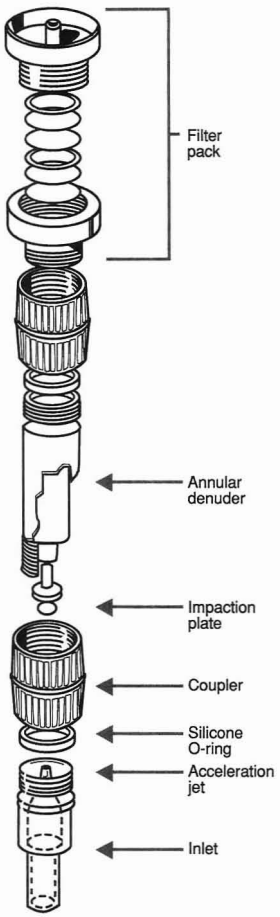

Figure 2. Schematic of a personal sampler with an annular denuder.
(Adapted with permission from Reference 10.)

To discriminate between different-sized particles, another device for actively collecting airborne material relies on a nozzle-shaped inlet backed by a circular membrane filter. A laminar airflow is pulled in through the nozzle, which narrows to a 4-mm diameter. The sampler then opens to a filter as large as 50 mm in diameter. Large particles are carried by inertia to the center of the filter, whereas small particles follow the airflow toward the edges. Particles on the order of 1–10 μm are sorted by size. The collected particles can then be further analyzed by X-ray fluorescence. A prototype of this sampler weighs 200 g, not including the portable pump (*9*).

For measuring particulates in outside air and contaminants in home atmospheres, a sophisticated active sampler with an annular denuder was recently designed (Figure 2). The inlet of the sampler measures 5 cm in length with a 0.8-cm i.d. and is coated with Teflon. Air is fed through the inlet and into an acceleration jet, a 1.1-cm-long tube with an i.d. of 0.25 cm. The jet impacts a porous glass disk that captures particles. At a flow rate of 4 L/min, the disk has a 50% aerodynamic particle cutoff of 2.5 μm.

The flow then passes through the annular denuder, a double-walled cylinder. By coating the cylinder with citric acid, ambient ammonia (in outside air) or nicotine vapors from tobacco smoke (in indoor air) can be trapped for analysis. Eliminating ammonia protects the analysis of the generally acidic particles. However, a basic coating such as sodium carbonate offers the possibility of collecting acidic contaminants such as HNO_2 or HNO_3 instead.

Following passage through the denuder, the air sample flows through a filter pack. A Teflon filter collects the fine particles. To trap any nicotine vapor that passes through the denuder, a second glass fiber filter coated with citric acid is added.

Ammonia trapped on the denuder and sulfates on the particles are determined by ion chromatography. Nicotine is extracted with a $NaHCO_3$–water mixture and, after work-up, quantified by GC. Tests showed that the sampler quantitatively collects NH_3 at ppb levels during a 24-h collection period and 95% of airborne nicotine at levels of 40 and 170 $\mu g/m^3$ over 1–6-h periods (*10*).

Personal samplers can even be "smart." A sampler designed in Sweden uses a microprocessor to change particle collection filters (*11*). This active sampler draws air into it at 0.4 L/min. Heavy particles impact on a thin foil, whereas smaller particles are swept past and collected on a Nuclepore filter. The filters are mounted on wheels with 18 collection spots. The wheels can be turned at regular timed intervals to introduce fresh filters for collecting, or when a pressure transducer detects a pressure drop caused by clogged filters. The microprocessor keeps track of sampling time. The collection device weighs < 300 g, and the additional weight of the pump and associated electronics is carried on a belt.

A somewhat different smart dosimeter comes from Japan. Unlike the devices discussed thus far, this γ-ray dosimeter (*12*) measures fields and not airborne contaminants. It includes a microprocessor powered by a 1.3-V Ni–Cd rechargeable battery, providing 15 h of continuous operation. The device weighs just 175 g and measures 116 × 71 × 19 mm.

To conserve power, the microprocessor operates only 50 ms every minute, drawing less than 9 mA. An 8-kbyte memory stores worker name and identification number, date of birth, medical details, and other personal data. As the worker enters the plant, time and date are recorded in the memory. The integrated dosage is then updated when the worker leaves. An RS-232 port allows health officials to access the data through an external computer.

Finally, personal dosimeters can offer real-time analysis. A prototype dosimeter that responds to neutrons over a range of 150 keV to 15 MeV has been reported by Japanese researchers (*13*). This device consists of two silicon p–n junction detectors, one doped with ^{10}B for measuring neutrons below 1 MeV (through α particles generated in the reaction $^{10}B[n,\alpha]^7Li$). A polyethylene moderator improves the sensitivity to intermediate-energy neutrons.

As personal dosimeters evolve and become more user-friendly, they will provide a clearer picture of how environmental and workplace contaminants affect our health. Restricted in weight, size, and power, they also offer a challenge in designing analytical devices. *Alan R. Newman*

References

(1) Lioy, P. *Environ. Sci. Technol.* **1990**, *24*, 938.
(2) Lewis, R. G.; Mulik, J. D. In *Advances in Air Sampling;* Lewis: Chelsea, MI, 1988; p. 117.
(3) Hawthorne, S. B.; Miller, D. J. *J. Chromatogr. Sci.* **1986**, *24*, 258.
(4) Brown, R. H.; Saunders, K. J.; Walkin, K. T. *Am. Ind. Hygiene Assoc. J.* **1987**, *48*, 760.
(5) Pellizzari, E. D.; Krost, K. J. *Anal. Chem.* **1984**, *56*, 1813.
(6) Uchida, Y.; Kawai, T.; Yasugi, T.; Ikeda, M. *Bull. Environ. Contam. Toxicol.* **1990**, *44*, 900.
(7) Hodgson, A. T.; Binenboym, J.; Girman, J. R. In *Advances in Air Sampling;* Lewis: Chelsea, MI, 1988; p. 143.
(8) Johnson, J. R.; Kalos, F. *Radiat. Prot. Dosim.* **1989**, *26*, 97.
(9) Prodi, V.; Belosi, F.; Mularoni, A.; Lucialli, P. *Am. Ind. Hygiene Assoc. J.* **1988**, *49*, 75.
(10) Koutrakis, P.; Fasano, A. M.; Slater, J. L.; Spengler, J. D.; McCarthy, J. F.; Leaderer, B. P. *Atmos. Environ.* **1989**, *23*, 2767.
(11) Malmqvist, K. G.; Bohgard, M.; Johansson, G. I.; Akselsson, K. R. *J. Aerosol Sci.* **1983**, *14*, 409.
(12) Izumi, S.; Kitaguchi, H.; Mitani, S.; Kikuchi, H. *IEEE Trans. Nucl. Sci.* **1989**, *36*, 1150.
(13) Nakamura, T.; Horiguchi, M.; Suzuki, T.; Yamano, T. *Radiat. Prot. Dosim.* **1989**, *27*, 149.

NEW PRODUCTS

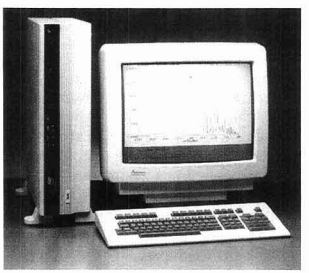

Model 680D spectroscopic workstation provides high-speed data acquisition and digital signal processing. The system contains a Motorola DSP56001 processor chip that allows total spectral processing of a 64K transform interferogram in 3 s. Nicolet 201

Instrumentation

Detector. Model 486 tunable absorbance detector includes a wavelength range of 190 to 600 nm, automatic calibration, and a programmable lamp standby feature. Cells are available for microbore, analytical, and preparative applications. Waters Chromatography Division of Millipore 202

Laser. Innova 328 ion laser system provides 1-W multiline UV output and requires only 208 VAC input power. The actively stabilized optical cavity uses automatic servo control to continuously optimize the output power of the system. Coherent 203

Oil. LABLAN oil/aromatic hydrocarbon monitor measures the total oil concentration in water or soil samples and also displays the aromatic hydrocarbon content. The monitor, which incorporates a three-wavelength optical system, is waterproof and insensitive to vibration. General Analysis Corp. 204

GC. Pyrojector II is a microprocessor-controlled, continuous-mode, constant-temperature microfurnace pyrolyzing unit that attaches directly onto the gas chromatograph injector. The unit is supplied with septum, septumless, and Pelletiser injection heads. Scientific Glass Engineering 205

ECR. 9200 ECR system features load lock, automatic pressure control, symmetrical high-throughput pumping up to 2200 L/s, heated and cooled wafer platens, 10 gas lines, computer-controlled data acquisition, and ports for Langmuir probe and optical spectrometries. Microscience 206

Thermal analysis. TGA 50 thermogravimetric analyzer measures the weight change of materials in response to heat over the temperature range ambient to 900 °C. The system accommodates samples up to 50 mg and is sensitive to weight changes of 5 μg. TA Instruments 207

LC. Marathon AutoSampler is designed for use in pharmaceutical, petrochemical, and environmental HPLC quality control. Features include 96-sample capacity, a built-in column heater, and optional detached keyboard for remote programming and display. Varian Associates 208

Moisture. MA 50 moisture analyzer determines moisture levels as low as 100 ppm. Features include a controlled temperature range of 40–160 °C, five operating modes, and the ability to program and store up to 10 drying routines. Sartorius Instruments 209

Surface analysis. PHI 670 Auger Nanoprobe includes a magnetic sample introduction system, an enhanced ultrahigh vacuum environment that permits ion beam Auger depth profiling, and an HP Apollo 32-bit UNIX workstation. Perkin-Elmer 210

Sensors. Integrated microoptical laser volumetric sensors IMOLV-0.2(LD) and IMOLV-0.3(LD) feature a solid-state laser diode and capillary block assembly. The flow cell is constructed of borosilicate glass; other wetted surfaces are Teflon. Particle Measuring Systems 211

TOC. SAN TOC analyzer employs continuous UV promoted persulfate oxidation for complete oxidation and elimination of interferences with an IR or a flame ionization detector. Sample volume is variable up to 20 mL, and the minimum detection limit is 5 ppb. Skalar 212

SFE. CCS 3200P parallel SFE system allows the simultaneous extraction of six samples. Features include programmable extraction conditions, static and dynamic extraction, and a reciprocating 10 000-psi pump. Computer Chemical Systems 213

Photodiode array. InGaAs photodiode array ETX 100 MLA 256 is a 100 μm × 12.8 mm array that consists of 30 × 100 μm pixels separated by 50 μm. The dark current and optical response are uniform across the array to within 5% over a minimum of 246 pixels. Epitaxx 214

Software

Data analysis. Data Visualizer allows interactive 3D viewing and animation of large volumes of scalar and vector information such as temperatures, pressures, densities, probabilities, and velocities. The software runs on graphics workstations from DEC, HP, IBM, and Silicon Graphics. Wavefront Technologies 215

Scientific computing. SciencePak is a subprogram library that includes programs for mathematics, statistics, and graphics. A spectroscopy/chromatography program is available that provides algebraic conversion of data, multicomponent analysis, and Gaussian and Lorentzian curve fitting. Scientific Logics 216

Peaks. PeakFit is designed for the analysis of multiple, overlapping peaks or functional forms using a state-of-the-art user interface and a graphical approach to curve fitting. Twenty-seven built-in functions are grouped according to research applications. Jandel Scientific 217

LIMS. LabVantage II version 3.12 laboratory information management sys-

Companies interested in a listing in this department should send their releases directly to ANALYTICAL CHEMISTRY, Attn: New Products, 1155 16th Street, N.W., Washington, DC 20036.

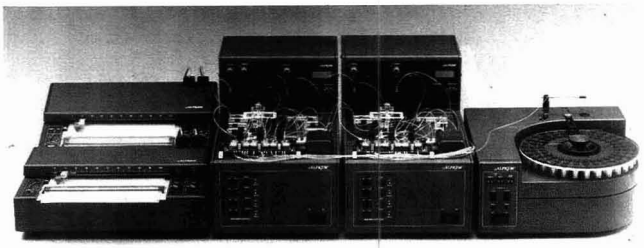

RFA/2 is a microcontinuous flow analyzer based on microsegmented flow technology. Designed for multichannel operation, the system can be used to simultaneously determine up to eight analytes in one sample. Alpkem **223**

tem provides storage, retrieval, and analysis of lab test results. The software allows users to view and edit raw data from an instrument while looking at the final test result in the database. Laboratory MicroSystems **218**

Chromatography. Chrom/RTG, designed for GC, HPLC, or ion chromatography applications, provides real-time data collection, peak integration, report generation, and LIMS compatibility. Data can be simultaneously collected from multiple instruments. Laboratory Technologies Corp. **219**

Chemometrics. Pirouette is a PC-based multivariate statistics program that provides pattern recognition, modeling, prediction, calibration, classification, and exploratory data analysis in a windowing, graphical interface. Infometrix **220**

FT-IR. TPH software facilitates the IR analysis of total petroleum hydrocarbons in accordance with EPA method 418.1. The program, which provides sample tracking, accounting, and hard-copy spectra, quantitates the absorbance at 2931 cm^{-1} and relates that value to concentration. Midac Corp. **221**

ACS Publications and Services

Principles of Environmental Analysis. Written to increase understanding of the factors involved in analyzing environmental samples, this free booklet discusses quality control, verification and validation, precision and accuracy, sampling, measurements, documentation, and other topics. 9 pp. **222**

U.S. National Chemistry Olympiad. Free booklet describes U.S. National Chemistry Olympiad, an ACS program designed to encourage high school students to achieve excellence in chemistry. Top students attend a study camp in Colorado and then compete in the International Chemistry Olympiad. 16 pp. **224**

ACS software. Free catalog lists scientific software for IBM and Macintosh PCs available from the ACS. Programs for drawing chemical structures, molecular modeling, and maintaining a chemical inventory are included. An order form is provided. 26 pp. **225**

Manufacturers' Literature

Multicomponent analysis. Data sheet describes the use of UV spectroscopy and multicomponent analysis software in pharmaceutical and life sciences laboratories. 16 pp. Beckman Instruments **226**

TLC. Brochure highlights the AMD system for automated multiple development of thin-layer chromatograms. Principles of operation, features, and applications are discussed. 12 pp. Camag **227**

Chromatography. *Varex Report*, Vol. 4, No. 1, includes information on preparative GC, preparative HPLC columns, and applications of the evaporative light-scattering detector. 16 pp. Varex **228**

Analyzers. Brochure describes Ströhlein analyzers for carbon, sulfur, oxygen, nitrogen, and hydrogen. Applications include the analysis of steel, iron, alloys, cement, coal, oil, and soil. 8 pp. Standard Instrumentation **229**

GC. Brochure highlights the AutoSystem gas chromatograph, designed for the automated determination of organic compounds. Sampling, injection, and hardware components are discussed. 12 pp. Perkin-Elmer **230**

Catalogs

Instrumentation. Catalog includes balances, calibrators, conductivity meters, controllers, pH meters, recorders, refractometers, temperature sensors, timers, and viscosity meters. 44 pp. Extech Instruments **231**

Ion chromatography. Catalog contains instrumentation, columns, eluants, certified standards, sample-handling products, metal-free tubing, and fittings. Column and eluant selection guides are provided. Alltech Associates **232**

Filtration. Catalog includes disposable syringe filters for ion chromatography and HPLC sample preparation as well as disposable membrane filter disks for vacuum and pressure filtration applications. Anotec Separations **233**

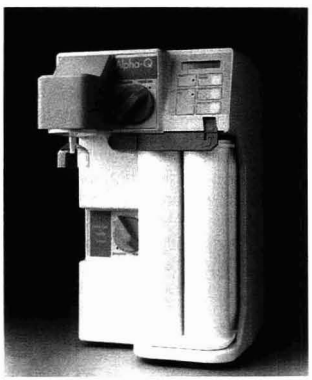

Alpha-Q water system produces up to 0.5 L/min of ultrapure water directly from the tap without pretreatment. Applications include HPLC, ion chromatography, and AAS. Millipore **234**

For more information on instrumentation and software products, and/or to obtain the free available information on other listed items, please circle the appropriate numbers on one of our Readers' Service Cards.

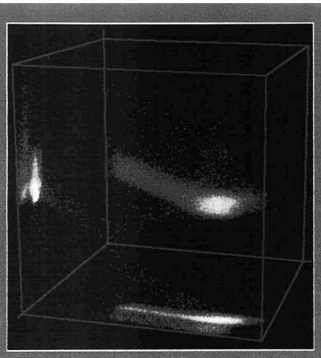

Concentration Histogram Imaging

A Scatter Diagram Technique for Viewing Two or Three Related Images

D. S. Bright and D. E. Newbury
Center for Analytical Chemistry
National Institute of Standards and Technology
Gaithersburg, MD 20899

In order to characterize the chemistry of materials on a fine scale, we employ compositional mapping techniques. Quantitative compositional mapping produces images that depict the concentrations of elemental and/or molecular constituents of a specimen on a spatial scale of ~1 μm or less (*1*). The images can be created from a variety of microanalytical instruments: for example, the electron probe microanalyzer, analytical electron microscope, ion microprobe, ion microscope, and laser Raman microprobe. A common problem is that much of the quantitative concentration information is lost when numerical concentration information is presented in the form of an ordinary gray scale or color scale image. Ideally, we wish to simultaneously present both spatially resolved information and numerical concentration data, often for two or more constituents.

A/C INTERFACE

For one constituent, techniques are available that satisfy the requirements of spatial and numerical display. Depiction of positional information as an image is straightforward—the concentration data are encoded with one of a variety of gray or color scales. Gray scale representation coupled with image processing for selective enhancement provides excellent display of compositional contrast, but it is difficult for an observer to relate specific gray levels to particular numerical concentration values. The human visual process is better adapted to viewing colors. The thermal color scale, which uses the sequence of colors emitted from a black body upon heating (deep red through cherry, orange, and yellow to white), provides a "logical" color scale in which particular colors can be more easily recognized and the approximate corresponding numerical value identified.

When two or more constituents are to be presented simultaneously, the

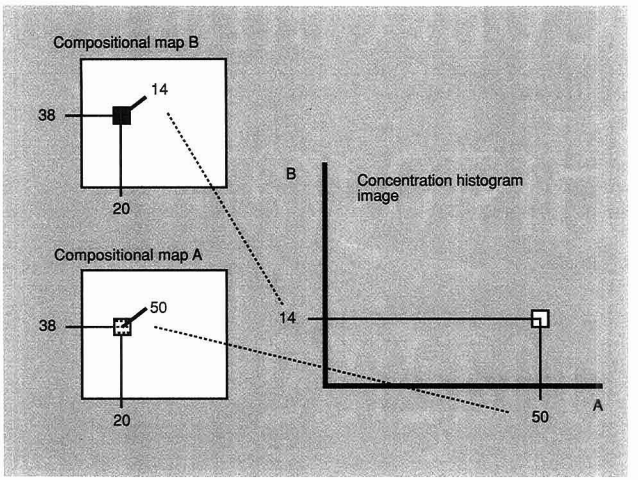

Figure 1. Schematic for construction of a CHI.
Pixels in location (20,38) have intensities 50 and 14. Histogram bin (50,14) is incremented for this image location.

thermal scale cannot be applied. A partial solution to this display problem is to use primary color overlays in which the individual constituent images are superimposed, with each applied as a primary color (i.e., a separate constituent is applied to the red, green, and blue channels of the video display). Spatial coincidence of two constituents is revealed by the appearance of secondary colors; however, information on relative amounts is lost. In principle, color scales with varying intensity can be established to depict relative amounts, but in practice such scales are difficult to use and are even more difficult to transfer to printed media.

To overcome these limitations, we have adapted the technique of scatter diagrams and have developed a method in which the compositional maps are transformed from spatial to concentration dimensions. We call this transformation the Concentration Histogram Image (CHI) (*2, 3*).

The CHI is much like a scatter diagram or bivariate histogram, which is more informative than a one-dimensional intensity histogram (*4–6*). Unlike the scatter diagram, the CHI is displayed as an image by encoding the frequency information with the thermal color scale. Also, the image or pixel representation of the CHI lends itself to a reverse operation called the "traceback" function (explained in detail below), which enables clearer rendering of both two- and three-dimensional information.

The CHI provides a direct numerical view of the concentration or intensity relationships between two or three constituents. The traceback algorithm permits rapid determination of the correspondence between features in the numerical display with specific places in the original compositional or intensity maps. CHIs complement the normal primary color overlay composites and are useful for evaluating data, diagnosing experimental problems, and detecting relationships of concentrations. A similar image analysis technique—using scatter diagrams but without traceback—has been applied by Prutton et al. (*7*) to intensity maps generated by Auger electron spectroscopy.

Producing the CHI

Although the CHI is most often applied to images representing concentrations of analyzed constituents, the technique can be applied equally well to any two or three registered images, as it is on our image processing systems (*8*). Consider an $n \times n$ pixel image for constituent A, represented by an array with elements $a(x,y)$, each giving a concentration or intensity value for A at location x,y. Also consider a similar image for constituent B with elements $b(x,y)$ that is in pixel by pixel registration with image A. The CHI is constructed by incrementing an element of the array $h(i,j)$ where i and j correspond to the values a and b of concentration or intensity for every location (x,y) in the images. A FORTRAN code for this procedure is listed in the box on p. 247 A.

Figure 1 shows this procedure schematically. After the CHI array is calculated, it is displayed as an image (described below). Apart from visualization of the array, this procedure is like the construction of a two-dimensional

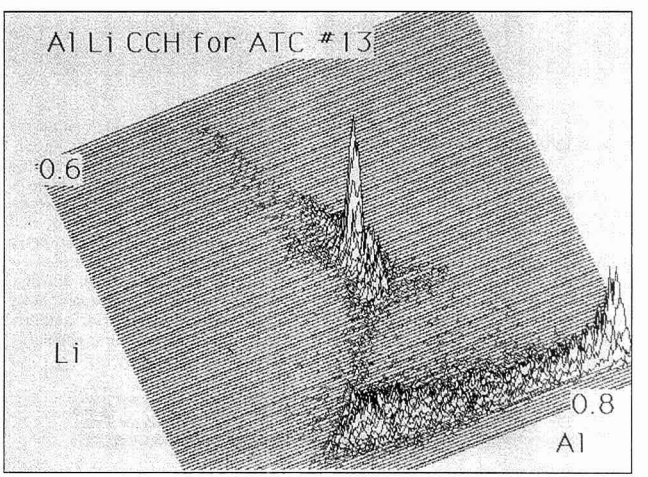

Figure 2. CHI of ion microscope compositional maps of an aluminum–lithium alloy plotted as a mesh plot.
(Specimen courtesy K. Soni and D. Williams, Lehigh University.)

Figure 3. The same CHI as Figure 2, shown as a gray scale image.

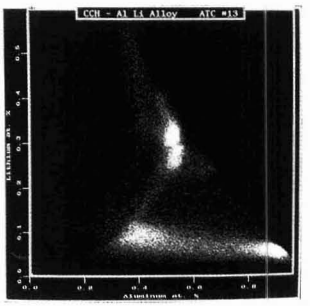

Figure 4. The same CHI as Figures 2 and 3, shown as an image with the thermal pseudocolor scale: 0—black, 1—red, 2–255—dark orange–yellow–white.

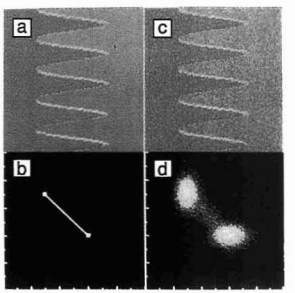

Figure 5. Simulated microprobe maps (a and c) and their corresponding CHIs (b and d).

The maps are shown as color overlays of one image in red and the other in green. Each map has two phases or regions separated by the wavy line. Each region in (a) has a constant amount of the red and the green elements—the color is determined by the predominant element. The map–CHI pair (c) and (d) includes some noise to simulate counting statistics.

or bivariate histogram—or like the plotting of a scatter diagram with limited precision—that is, with clumping the data into bins.

Displaying the CHI

The CHI can be displayed as a mesh plot, in the way bivariate histograms are usually plotted (Figure 2), showing intensity along the vertical axis. However, because the CHI is an array, similar to the images from which it was made, it is natural to display it also as an image (Figure 3).

When displayed with a gray scale, bins with a few counts are too dim to be seen against the background. Because these more diffuse regions may be as interesting as the more compact and intense regions (higher counts), we can overcome the limitation of the gray

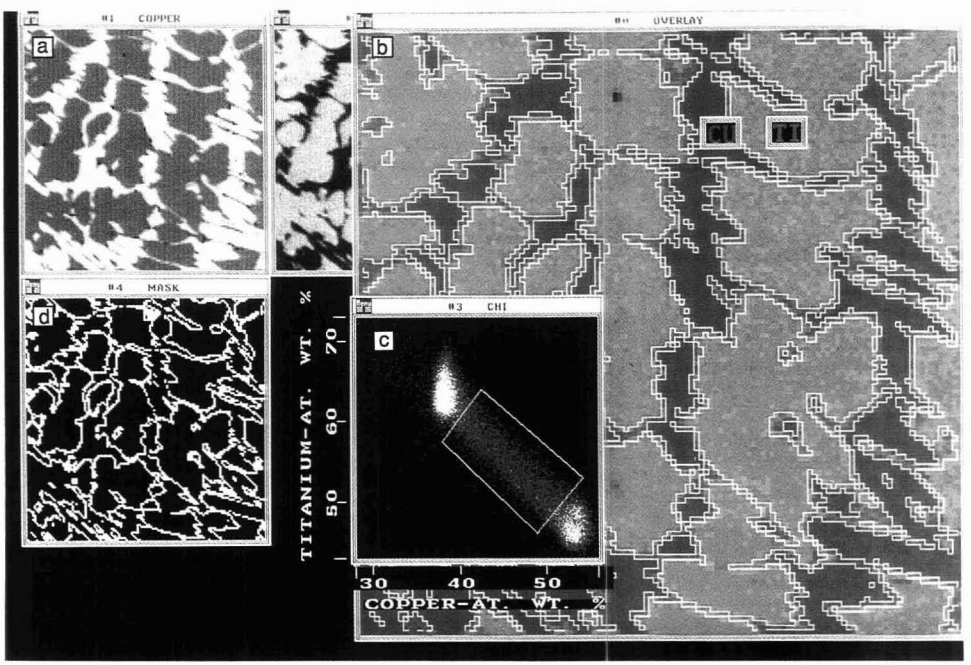

Figure 6. Electron probe maps and corresponding CHIs of a Cu–Ti alloy.

(a) Left: copper map, 128 × 128 pixels. Edge of field is 125 μm. Right: Ti map (partly hidden). (b) Color overlay: Cu is red, Ti is green. Edge of field is 125 μm. (c) CHI. (d) Traceback mask image using outlined area in CHI (bottom right). Selected pixels outlined in white in color overlay.

FORTRAN code for producing a CHI

```
do y = 1,n
do x = 1,n
   i = a(x,y)
   j = b(x,y)
   h(i,j) = h(i,j) + 1
end do
end do
```

FORTRAN code for the traceback function

```
do y = 1,n
do x = 1,n
   i = a(x,y)
   j = b(x,y)
   if (i,j) fall within the selected region
   of the CHI then
      m(x,y) = 1
   else
      m(x,y) = 0
   end if
end do
end do
```

scale by displaying the CHI with a thermal scale (Figure 4) constructed so that zero count is black, one count is red, and higher counts range from orange to yellow to white. In this way, the centers of the high-intensity clumps are visualized as well as the scattered bins with only one count each.

This display method also works well for higher dimensional CHIs. Although the mesh plot (Figure 2) shows, in a quantitative way, the relative counts per bin or relative areas in the original images, Figure 4 shows more clearly the relative positions and sizes of clumps and the individual bins with few counts. It is also easier to determine concentration values from Figure 4 using the axes, and to outline selected areas for applying the reverse transformation (traceback).

Properties of the CHI

To introduce some properties of the CHI, Figure 5 shows compositional X-ray maps simulated on the computer to specify the counting statistics. The first synthetic image consists of two "phases," with no variation in apparent concentration from counting statistics (Figure 5a). The two phases have a predominance of either the "red" or the "green" element and a wavy boundary between the two. A pixel through which the boundary passes has "concentrations" calculated from the relative fractional area of the pixel that is in either phase. The resulting CHI in Figure 5b has one point at each of the concentration values for the two phases and a line between the points corresponding to pixels on the boundary. The upper left point in Figure 5b is high in element green and corresponds to the green phase. Parts of the yellow line that are near this point represent boundary pixels that are mostly in the green phase. The map–CHI pair, Figures 5c and 5d, is the same as that on the left except that counting statistics have been added. The two points spread out into clumps, and the line spreads into a diffuse band (Figure 5d). This CHI looks very similar to actual experimentally measured systems of two phases (see Figure 6c).

Traceback

Having generated the CHI, the observer is likely to be interested in the relationship of features recognized in the CHI to features in the original maps. This relationship can be discovered with a modification of the CHI algorithm, which we call the traceback function. The traceback function selects pixels in the original images on the basis of intensity correlations; this is analogous to selecting pixels in a single image by setting an intensity threshold. This function is implemented by marking a mask image, $m(x,y)$ (Figure 6d), on the basis of regions previously selected from the CHI. A pixel in the mask is marked if the corresponding CHI bin lies inside the selected region of the CHI. The FORTRAN code for the traceback function appears in the box.

Mask m is a binary image that is in registration with images a and b and that labels the pixels in both images as corresponding to the selected region of the CHI. The mask thus selected can be viewed as an image in its own right, or it can be used to mark the original maps.

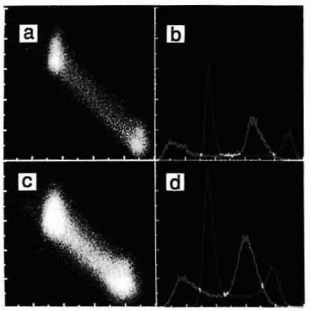

Figure 7. The effect of resolution on CHIs and one-dimensional histograms.
(a) CHI for the lower resolution (128 × 128 pixels) maps in Figure 6a. (b) One-dimensional histograms for these maps (colors in overlay and those of histograms correspond). (c,d) Maps of same sample area as top, taken at higher resolution (256 × 256 pixels). Cu—x axis on CHI and red plot: 44–98 atomic percent. Ti—y axis on CHI and green plot: 37–67 atomic percent.

Practical details

Scaling. Many images, especially images representing concentrations, do not have pixels with integer values. To construct a CHI, the pixels are therefore scaled to integers ranging from 0 to 255, or to a range matching the dimensions of the CHI array. If the images are originally integer images with a small range of values, then care must be taken when scaling to avoid stripes in the

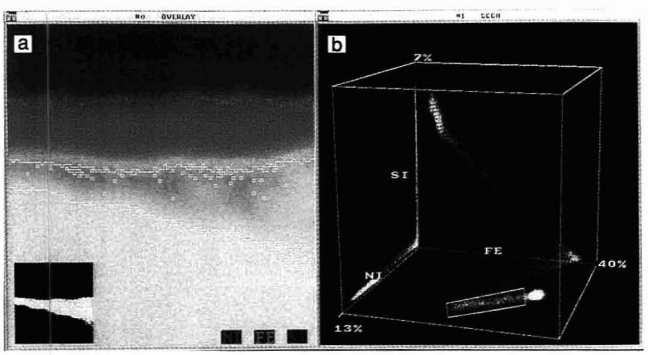

Figure 8. (a) Color overlay of three maps (Ni—red, Fe—green, Si—blue) of electron probe microanalyzer compositional maps of a diffusion zone at a metal–glass seal and (b) corresponding CHI.
Edge of field is 25 μm. Areas outlined in white on overlay correspond to outlined feature of CHI. Inset: traceback mask image. (Specimen courtesy J. Mecholsky, Jr., University of Florida.)

CHI caused by periodically missing bins or doubling counts in bins. If the intensity range of the image is on the order of, or smaller than, the number of available bins along a CHI axis, it is best to use the intensities directly or to scale the images with care.

Comparison of one- and two-dimensional histograms at two resolutions. Does the resolution at which the images are taken affect the appearance of the CHIs? Figure 6a shows Cu and Ti electron probe compositional maps (128 × 128 pixels) of a binary alloy and Figure 6b shows a color overlay with Cu in red and Ti in green. We often display corresponding images as a color overlay to examine the spatial relationships of the constituents. The color overlay shows a boundary between the two phases that has moderate concentrations of both Cu and Ti. Whether the boundary is a diffusion zone or an instrumental artifact caused by the finite width of each pixel and the finite electron interaction volume in which the X-rays are generated cannot be determined from either the images or the CHI. This is because the boundary is one pixel [1 μm] thick or less. The width of the interaction volume for the Cu–Ti alloy at 20 keV is about 1 μm.

Figures 7a and 7b show standard one-dimensional histograms and CHIs that correspond to maps in Figure 6a, whereas Figures 7c and 7d derive from maps of the same area that were taken at twice the spatial resolution (256 × 256 pixels). (The higher resolution maps are difficult to distinguish visually from the lower resolution maps and are not shown in Figure 6.) Because the higher resolution maps have four times the number of pixels, the corresponding CHI has four times the number of counts and appears broader, but the features are essentially the same. Note that with conventional one-dimensional histograms alone, it cannot be determined which phase in one histogram corresponds to a particular phase in the other histogram. The CHI shows this type of correspondence immediately.

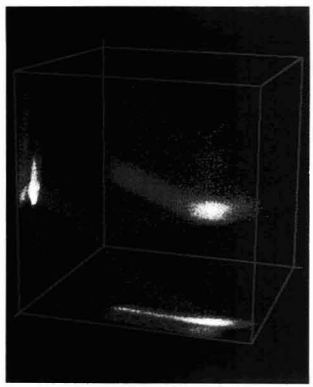

Figure 9. CHI for electron probe microanalyzer compositional maps of an Fe–Ni–Cr alloy with one major phase.
A secondary cluster is seen in front of the primary cluster in projections on the bottom and left face of cube; this secondary cluster is not visible from this viewpoint of the three-dimensional presentation within the cube.

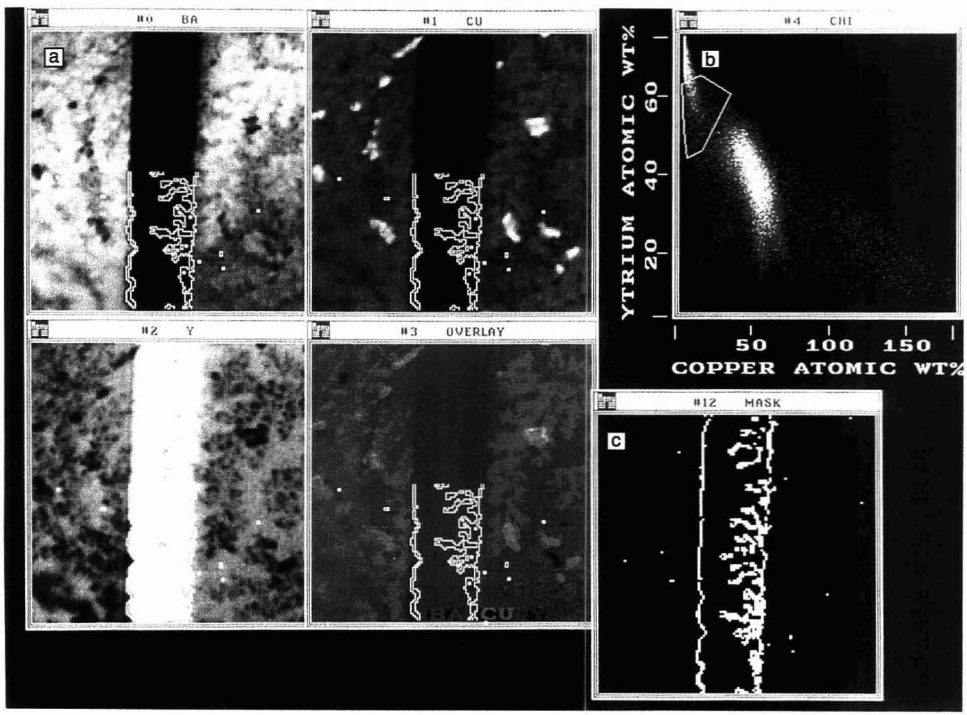

Figure 10. Element maps and the CHI for a small element of a superconducting ceramic integrated circuit.
(a) Ba, Cu, and Y maps and color overlay (labeled in banners). Center strip is conduction barrier. Image width is 125 μm. (b) CHI (Y vs. Cu) for two of the maps on the left. Outlined region corresponds to tendrils. (c) Traceback mask image corresponds to outlined region in CHI. Matching pixels are outlined in white in bottom half of maps and overlay. Top halves are not outlined to show tendrils better. (Specimen courtesy R. Ono, NIST.)

Three-dimensional CHIs. The pseudocolored display of the CHI lends itself directly to adding another dimension. Just as the two-dimensional histogram is plotted inside a square, the three-dimensional histogram is plotted inside a virtual cube and is rendered as a projection. To present three axes of concentration data, the only choice possible for the frequency information is color encoding. Figure 8a shows a color overlay for electron probe compositional maps of a diffusion zone at a metal–glass seal and the corresponding CHI is shown in Figure 8b. The CHI is snakelike in shape and is three-dimensional, taking two sharp turns.

When the histogram is viewed in projection, there is always a danger of missing some structure along the line of sight. Viewing the histogram from several angles helps, and presenting the CHI as a stereo pair (*9*) works even better, although the need for special optical devices to view the stereo pair makes this approach somewhat impractical. A practical way to view the histogram is to use one, two, or three ancillary projections onto the rear faces of the virtual cube. A projection on the left face is shown in Figure 8b, which makes it easier to see that the part of the snake ending near the bottom face is in fact lying on the bottom face and not heading upward (increasing in Si concentration), as might be mistakenly deduced without the projection. The white outlines and mask (inset) illustrate the traceback function (see below) for this feature.

Another example is given in Figure 9, which depicts a CHI of a set of maps for a Fe–Ni–Cr alloy. A small clump of points is visible in the projections on the bottom and left face of the cube but is hidden in the interior of the three-dimensional presentation within the cube.

A third possibility is to view a three-dimensional CHI in a display that permits real-time rotation of the plot. Such a display, when in motion, provides a feel for the shape of the plot and allows searching from arbitrary viewpoints for features of interest.

Examples of the traceback function

The traceback feature identifies which areas of the image correspond to which features of the CHI. As an illustration, Figure 10a shows Ba, Cu, and Y electron probe microanalyzer compositional maps and the color overlay for a superconducting thin-film circuit element. There are tendrils of Cu stretching across the vertical band in the center that is supposed to be Cu-free. These tendrils are not seen on the color overlay and are barely visible as depletions in the Y map. We wished to select the tendrils from the rest of the image. Inverting the Y map of Figure 10 shows the tendrils to a degree, but it also shows the large darker areas on both sides of the band.

From inspection of the maps, the tendrils were presumed to be high to intermediate in Y and low (but not zero) in Cu. The outline for such an area is shown in white on the CHI (Figure 10b), and the traceback is shown as a mask in Figure 10c and as outlines in Figure 10a. The tendrils are outlined along with pixels on the other side of the strip, which suggests a similar process at an earlier stage; this feature was missed in the previous figures.

Figure 11 shows the traceback applied to the projection of a CHI. Although (strictly speaking) one should outline parts of this three-dimensional object with a surface (or box), the use of

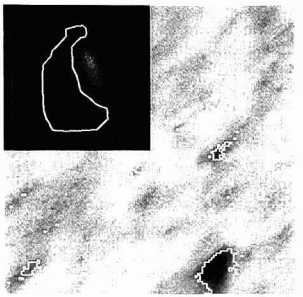

Figure 11. Traceback applied to the projection of a CHI.

Color overlay for Ba (red), Cu (green), and Y (blue) maps for superconducting ceramic thin film. White boundary surrounds regions corresponding to outlying points in CHI. Image width is 50 μm. Inset: CHI with white line surrounding outlying points. Ba—lower left axis, 21–38 atomic percent. Cu—lower right axis, 12–23 atomic percent. Y—vertical axis, 11–19 atomic percent.

the projection shown here often works well. This CHI is of a superconducting thin film and appears as an ellipsoid with outlying bins (outlined in white). The traceback function applied to most of the outlying bins is seen outlined in white on the color overlay and reveals discontinuities in the film.

The raw X-ray count maps measured with the electron probe microanalyzer require several steps in the calculation process to convert the X-ray counts into concentrations. Sometimes the changes on quantitation of the relative image intensities are subtle. A CHI corresponding to Figure 7a before the X-ray counts in the maps have been corrected for instrumental effects shows fragmentation of the two clumps. The traceback feature shows that the fragments correspond to the high Cu phase on the right side of the map in Figure 6b, suggesting that the clump fragmentation is caused by spectrometer defocusing (*10*). The secondary clump in Figure 9 similarly seems to be attributable to instrumental artifacts that have not been completely corrected.

Conclusion

The CHI is a useful diagnostic tool for examining compositional maps. This technique of image presentation is a useful adjunct to conventional images and is especially effective for detecting inhomogeneities in materials, recognizing and highlighting rare events, checking quantitative correction procedures needed to produce compositional maps, and evaluating sampling and measurements statistics. The CHI is also useful for selecting features of interest for further analysis.

References

(1) Newbury, D. E.; Fiori, C. E.; Marinenko, R. B.; Myklebust, R. L.; Swyt, C. R.; Bright, D. S. *Anal. Chem.* **1990,** *62*(22), 1159 A–1166 A.

(2) Bright, D. S.; Newbury, D. E.; Marinenko, R. B. *Concentration–Concentration Histograms: Scatter Diagrams Applied to Quantitative Compositional Maps;* San Francisco Press: San Francisco, 1988; pp. 18–24.

(3) Newbury, D. E.; Bright, D. S. In *Secondary Ion Mass Spectrometry (SIMS VII);* Benninghoven, A.; Evans, C. A.; McKeegan, K. D.; Storms, H. A.; Werner, H. W., Eds.; Wiley: New York, 1990; pp. 929–33.

(4) Browning, R. *Materials Analysis by Scanning Auger Microscopy: Why the Information Crunch is Needed;* San Francisco Press: San Francisco, 1987; pp. 311–16.

(5) Browning, R. *J. Vac. Sci. Technol.* **1985,** *A3*(3), 1959–64.

(6) Trivedi, S. S.; Herman, G. T.; Udupa, J. K. *IEEE Trans. Med. Imaging* **1986,** *MI-5*(2), 116–19.

(7) Prutton, M.; El Gomati, M. M.; Walker, G. C. *Quantitative Imaging in the Scanning Auger Microscope;* San Francisco Press: San Francisco, 1987; pp. 304–10.

(8) Bright, D. S. *J. Microsc.* **1987,** *148,* 51–87.

(9) Bright, D. S.; Myklebust, R. L.; Newbury, D. E. *J. Microsc.* **1984,** *136,* 113–20.

(10) Marinenko, R. B.; Myklebust, R. L.; Bright, D. B.; Newbury, D. E. *J. Microsc.* **1987,** *145,* 207–23.

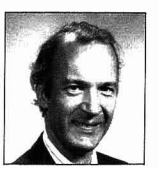

David S. Bright (left) received his Ph.D. in biophysics from Colorado State University in 1975 and has been a research chemist at the National Institute of Standards and Technology (NIST) since 1976. He joined the microanalysis research group in 1984. His research interests include using image analysis techniques to automate instruments, identify diffraction patterns, and enhance and correlate X-ray maps.

Dale E. Newbury received a B.S. degree in metallurgy and materials science from Lehigh University in 1969 and a D.Phil. in metallurgy and materials science from the University of Oxford in 1972. He has been at NIST since 1972. His interests include materials characterization by microscopy and microanalysis.

INDEX TO ADVERTISERS IN THIS ISSUE

Directory section, see page 250A.

** See ad in ACS Laboratory Guide.*

Advertising Management for the American Chemical Society Publications

CENTCOM, LTD

President
James A. Byrne

Executive Vice President
Benjamin W. Jones

Robert L. Voepel, *Vice President*
Joseph P. Stenza, *Production Director*

500 Post Road East
P.O. Box 231
Westport, Connecticut 06880
(Area Code 203) 226-7131
Telex No.643310
FAX: 203-454-9939

ADVERTISING SALES MANAGER
Bruce E. Poorman

ADVERTISING PRODUCTION MANAGER
Jane F. Gatenby

SALES REPRESENTATIVES

Philadelphia, PA . . . CENTCOM, LTD., GSB Building, Suite 405, 1 Belmont Avenue, Bala Cynwyd, Pa. 19004. Telephone: 215-667-9666, FAX: 215-667-9353

New York/New Jersey . . . Dean A. Baldwin, John F. Raftery, CENTCOM, LTD., Schoolhouse Plaza, 720 King Georges Post Road, Fords, NJ 08863, Telephone: 908-738-8200, FAX: 908-738-6128

Westport, CT . . . Edward M. Black, CENTCOM, LTD., 500 Post Road East, P.O. Box 231, Westport, Ct. 06880. Telephone: 203-226-7131, Telex 643310, FAX: 203-454-9939

Cleveland, OH . . . Bruce E. Poorman, CENTCOM, LTD., 325 Front St., Suite 2, Berea, Ohio 44017. Telephone: 216-234-1333, FAX: 216-234-3425

Chicago, IL . . . Michael J. Pak, CENTCOM, LTD., 540 Frontage Rd., Northfield, Ill. 60093. Telephone: 312-441-6383, FAX: 312-441-6382

Houston, TX . . . Michael J. Pak, CENTCOM, LTD. Telephone: 312-441-6383

San Francisco, CA . . . Paul M. Butts, CENTCOM, LTD., Suite 1070, 2672 Bayshore Frontage Road, Mountain View, CA 94043. Telephone: 415-969-4604, FAX: 415-969-2104

Los Angeles, CA . . . Paul M. Butts, CENTCOM, LTD. Telephone: 415-969-4604.

Boston, MA . . . Edward M. Black, CENTCOM, LTD. Telephone: 203-226-7131

Atlanta, GA . . . CENTCOM, LTD. Telephone: 216-234-1333

Denver, CO . . . Paul M. Butts, CENTCOM, LTD. Telephone: 415-969-4604

United Kingdom

Reading, England . . . Malcolm Thiele, Technomedia Ltd., Wood Cottage, Shurlock Row, Reading RG10 OQE, Berkshire, England. Telephone: 073-434-3302, Telex #848800, FAX: 073-434-3848

Lancashire, England . . . Technomedia Ltd., c/o Meconomics Ltd., Meconomics House, 31 Old Street, Ashton Under Lyne, Lancashire, England. Telephone: 061-308-3025

Continental Europe . . . Andre Jamar, International Communications, Inc., Rue Mallar 1, 4800 Verviers, Belgium. Telephone: (087) 22-53-85, FAX: (087) 23-03-29

Tokyo, Japan . . . Sumio Oka, International Media Representatives Ltd., Room 100, 21 Bldg., 2-2-22 Okusawa, Setagaya-ku, Tokyo 158 Japan. Telephone: 502-0656, Telex #22633, FAX: 5706-7349

Analytical CHEMISTRY

EDITOR: **ROYCE W. MURRAY**

ASSOCIATE EDITORS: **Catherine C. Fenselau, Georges Guiochon, Walter C. Herlihy, Robert A. Osteryoung, Edward S. Yeung**

Editorial Headquarters

1155 Sixteenth St., N.W.
Washington, DC 20036
Phone: 202-872-4570
Telefax: 202-872-4574
Bitnet: rmh96@cas

Managing Editor: Sharon G. Boots

Assistant Managing Editor: Mary Warner

Associate Editor: Louise Voress

Assistant Editors: Jane K. Baker, Grace K. Lee, Alan R. Newman

Editorial Assistant: Felicia Wach

Contributing Editor: Marcia Vogel

Director, Operational Support: C. Michael Phillippe

Head, Production Department: Leroy L. Corcoran

Art Director: Alan Kahan

Designers: Robert Sargent, Lori Seskin-Newman

Production Editor: Elizabeth E. Wood

Circulation: David Schulbaum

Editorial Assistant, LabGuide: Joanne Mullican

Journals Dept., Columbus, Ohio

Associate Head: Marianne Brogan

Journals Editing Manager: Joseph E. Yurvati

Associate Editor: Terri Bailey

Staff Editor: Stephanie R. Harrell

Published by the
AMERICAN CHEMICAL SOCIETY
1155 16th Street, N.W.
Washington, DC 20036

Publications Division

Director: Robert H. Marks

Journals: Charles R. Bertsch

Special Publications: Randall E. Wedin

Manuscript requirements are published in the January 1, 1991 issue, page 89. Manuscripts for publication (4 copies) should be submitted to ANALYTICAL CHEMISTRY at the ACS Washington address.

AUTHOR INDEX

Use of Conformal Maps To Model the Voltammetric Response of Collector–Generator Double-Band Electrodes

Bruno Fosset and Christian A. Amatore*

Ecole Normale Superieure, Laboratoire de Chimie, 24 Rue Lhomond, 75231 Paris, France

Joan E. Bartelt, Adrian C. Michael,[1] and R. Mark Wightman*

Department of Chemistry, University of North Carolina, Chapel Hill, North Carolina 27599-3290

The utility of coordinate transformation in electrochemical problems, specifically those associated with nonlinear diffusion at microelectrodes, is discussed. The use of the Schwarz–Christoffel transformation of space is shown to provide a simple route to an exact expression for the steady-state limiting current of a double-band electrode as a function of the width-to-gap ratio. Additionally, the transformation approach allows improved accuracy and decreased computation time of digital simulations, over those done in the traditional real-space coordinates. Experiments with chemically stable systems, ferrocene and 9,10-diphenylanthracene (DPA) in acetonitrile, provide verification of digital simulations of the double-band electrode response. Agreement is also found between simulations of chemical reactions accompanying electron transfer and experiments for the oxidation of DPA in the presence of pyridine in acetonitrile, a system that shows a pseudo-first-order rate constant of 100 s^{-1}.

INTRODUCTION

Arrays of band electrodes have become increasingly popular in recent years. Such arrays are particularly useful to study the fate of electrogenerated species when adjacent bands are operated at different potentials (*1–8*). Molecules generated at one electrode, termed the generator, are examined at the other nearby electrodes. Thus, this experiment is analogous to the classical rotated ring disk electrode. Arrays offer several distinct advantages for such experiments, however, because they can be used in solutions with large resistance or with very high concentrations because of the general immunity of ultramicroelectrodes to distortion by ohmic drop. The lifetime of the electrogenerated species can be quite short, and detection is still possible, because the critical time scale with arrays is the time to diffuse across the gap, which can be made vanishingly small (*9*). Thus, these devices should enable the investigation of very rapid chemical reactions coupled to electron transfer under conditions used in typical organic and organometallic chemical experiments, rather than adapting these systems to conventional electrochemical conditions.

One obstacle to the investigation of coupled chemical reactions at the array of band electrodes is the lack of a general theoretical approach for the quantitative interpretation of data. Mathematical solutions of the flux equations at ultramicroelectrodes of almost all geometries is complex because of the nonuniform current distribution at the surface of electrodes where diffusion occurs in more than one dimension (see, for instance, Figure 2 of ref 5). To simplify the approach to solutions of these problems, the current has been evaluated with the steady-state assumption for the flux (*10*), or uniform current distribution (*11*) has been assumed (which may occur as a result of kinetic and ohmic effects). General analytical solutions of coupled electrochemical kinetic phenomena have not been reported.

An alternate approach is to use digital simulation of the concentration profiles to arrive at the appropriate solutions. The attractive features of this approach are that the mathematics required are relatively simple and the method can be adapted to a variety of kinetic schemes which may occur at the electrode surface. The principal limitation is that the amount of computer time and memory may be unrealistically large for an accurate description of the diffusion layer when the dimensions of the diffusion layer exceed the dimensions of the elements of the array. In an effort to reduce the number of grid elements required, simulations of ultramicroelectrodes have employed an exponential space grid (*2, 3*). This has the advantage of producing a high grid density in the vicinity of the electrode, without a dramatic increase in the overall number of elements required for the simulation of the complete diffusion layer. When combined with the hopscotch algorithm, this leads to enhanced performance with respect to the time efficiency of the simulation (*12*). It does, however, have several disadvantages. Although the grid can be implemented appropriately in the dimension perpendicular to the array surface, it is difficult to implement across the electrode. This is a critical problem because the current density is largest at the edge of the electrode and, thus, the highest grid density is required at this location (*13*). The most significant disadvantage, however, is that the grid lines do not follow the actual lines of flux to the electrode surface which are highly contorted near the edges of the electrode. An accurate description of the flux lines requires, therefore, a high number of grid elements even when the exponential grid is used.

The difficulties associated with simulations that employ the real-space or exponential-space grids can be effectively overcome if the grid is appropriately defined in two dimensions. An ideal grid should be defined by the lines of flux to the electrode and the equal concentration lines. Because the shape of the concentration profiles is time dependent, this is impossible to accomplish for all times with a single grid. For experiments at short times (i.e., where linear diffusion predominates), the real-space grid is most appropriate. In contrast, as the current approaches a steady-state value, the appropriate grid depends on the electrode geometry. For the case of importance in this work, arrays of two interacting bands, the steady-state solution is the one of most interest. To achieve an appropriate space grid for this case, the use of a conformal map is particularly useful and leads to a spatial conformation similar to a thin-layer cell, from which solutions are readily obtained.

For many cases, the use of a conformal map provides a simple way to arrive at the steady-state currents. To the best

* To whom correspondence should be addressed.
[1] Present address: Department of Chemistry, University of Pittsburgh, Pittsburgh, PA 15260.

0003-2700/91/0363-0306$02.50/0

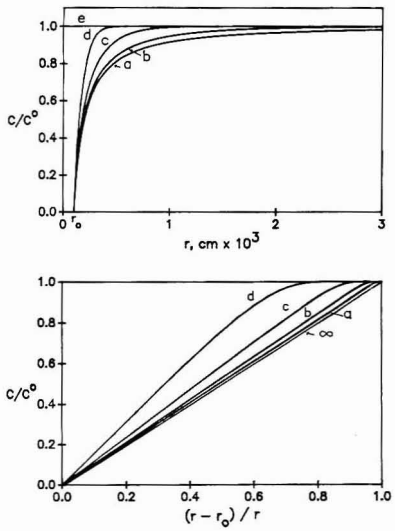

Figure 1. Diffusion layer profiles of a spherical electrode. Upper: real space. Lower: transformed space. Curves shown are for a diffusion coefficient of 1×10^{-5} cm²/s and the following times after the potential step: A, 1 s; B, 0.1 s; C, 0.01 s; D, 0.001 s; E, 0 s.

of our knowledge, the first use of conformal mapping for the evaluation of the steady-state current at two-dimensional electrodes was by Saito (*14*). We have used this approach to solve for the flux at electrodes with the geometry of a sphere (*15*), cylinder (*16*), band (*17*), and disk (*18*) and arrays of bands (*19*). Subsequently, the method has been used to analytically describe the current at infinite interdigitated arrays (*20–22*). Because of the widespread use of this approach, one of the purposes of this paper is to review the simplification provided by a conformal map in the digital simulation of the current at a wide range of ultramicroelectrode geometries. In addition, we will show how it can be extended to the case of the double-band electrodes to permit simulation of the currents found with various homogeneous kinetic schemes. In this paper, we focus on the double-band geometry because it is particularly desirable due to its high information content and relative ease of fabrication (*5*).

THEORY

Change of Space Coordinates for a Sphere. The utility of a spatial change of coordinates is most easily seen with a one-dimensional problem. Consider diffusion at a spherical electrode of radius r_0. During a chronoamperometric experiment at potentials sufficient for the concentration of the electroactive species at the electrode surface to be zero, the concentration in the diffusion layer at infinite time is given by

$$C(r,\infty)/C^0 = (r - r_0)/r \tag{1}$$

where C^0 is the bulk concentration. Plots of the diffusion layer at different times approaching this limit are given in the upper part of Figure 1. The current at any time is evaluated by the gradient of the concentration integrated over the electrode area. An alternate way to view the diffusion layer is to plot the concentration ratio as a function of y where $y = (r - r_0)/r$ as in the lower part of Figure 1. This has the effect of expanding space near the electrode, where the concentration profile changes most rapidly, and compressing space at distances further away from the electrode. Then, Fick's second law in spherical coordinates is transformed from

$$\frac{\partial C}{\partial t} = D\left[\frac{\partial^2 C}{\partial r^2} + \frac{2}{r}\frac{\partial C}{\partial r}\right] \tag{2}$$

to

$$\partial C/\partial t = D^*[\partial^2 C/\partial y^2] \tag{3}$$

where D is the diffusion coefficient and D^* is a function of the distance from the electrode (see Appendix I). For spherical coordinates, $D^* = D(1-y)^4/r_0^2$. At infinite times, the concentration profile is linear, and as can be seen in the lower part of Figure 1, the concentration profiles at times less than infinity are more linear than in the original coordinate system. The concentration gradient at steady state can be evaluated directly to obtain the current by using Fick's first law written in a way appropriate for the conformal map:

$$i = nFA\left[r_0 D^* \frac{\mathrm{d}C}{\mathrm{d}y}\right]_{y=0} = 4\pi r_0 nFDC^0 \tag{4}$$

If the concentration profiles are evaluated in this space by digital simulation, less iterations are required because of the greater linearity of the concentration profiles relative to those in the r coordinate system. Thus, the simulation converges to the correct solution more quickly for conditions that approach the steady-state limiting case. As this simple example shows, the effect of the use of an appropriate coordinate system can lead to a simplification of steady-state and near-steady-state problems.

Generation of a Conformal Map. In the above example, the solution to the steady-state condition is analytically known. However, for other cases where the steady-state solution is not known because of the complexity of the analytical solutions, an alternate procedure must be used. Since at steady state $\partial C/\partial t = 0$, the concentration profiles are solutions of $\nabla^2 C = 0$. Solutions can be found more readily when the space coordinates are transformed from the real ones to ones in which the space is limited by a partially or completely closed space (*18–20, 22*). This can be achieved by the use of the Schwarz–Christoffel transformation (*23*) as illustrated in Figure 2. This procedure allows transformation of one complex plane into another. The points of coordinate (x_k, y = 0; with $k = -n, ..., 0, ..., n$) are the points that map respectively to the points of coordinate Z_k in the conformal space and are referred to as the poles of inversion. The angles in the transformed space are indicated by γ_k. Any point of coordinate z ($=x + jy$) is transformed into a point in the conformal space Z ($=\Gamma + j\Theta$) with

$$Z = K\int_0^z \prod_{k=-n}^{n} [(z - x_k)^{\gamma_k/\pi - 1}]\, \mathrm{d}z \tag{5}$$

where K is a scaling factor and $j = (-1)^{1/2}$. Thus, eq 5 allows the transformation of the (x,y) coordinate system to any convenient system (Γ,Θ). For electrochemical problems, one selects the transformation (the appropriate inversion poles and angles) to linearize the flux lines. Because the transformation is only of space, the use of the conformal map does not affect parameters that are time dependent such as rates of chemical reactions accompanying electron transfer. Therefore, the rate laws are unchanged and can be used as in conventional simulation techniques.

Conformal Map of a Single Band. The diffusion equation for a two-dimensional problem such as the band electrode is

$$\partial C/\partial t = D[\partial^2 C/\partial x^2 + \partial^2 C/\partial y^2]$$

The use of the Schwarz–Christoffel transformation for the

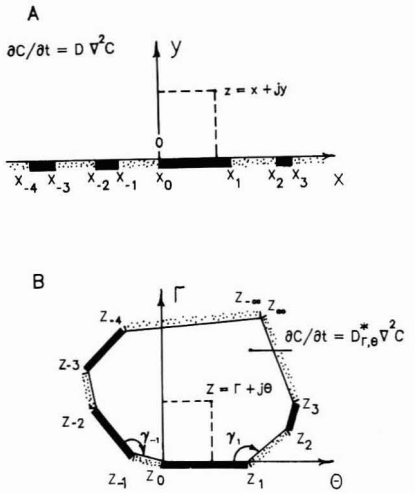

Figure 2. General representation of the Schwarz–Christoffel transformation between the upper half of the x–y plane (A) and the interior of the Γ–Θ plane (B). The points labeled $Z_{-\infty}$ and Z_{∞} correspond to the left and right infinity points in real space, respectively. The diffusion equation in each space is also shown.

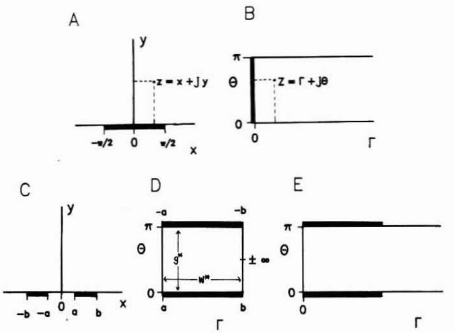

Figure 3. Representation of band electrodes in two spaces. Single-band real space (A) and conformal space (B). From eq 5, $\gamma_k = \pi/2$ and $x_k = \pm w/2$. Double-band electrode represented in real space (C), conformal space for steady-state conditions analogous to a thin-layer cell (D), and conformal space for simulations (E).

single band is illustrated in Figure 3 (A and B). The transformation involves two poles, one at each edge of the electrode ($x_k = \pm w/2$), and rotations of 90° ($\gamma_k = \pi/2$). From eq 5, the new coordinate for the single band, Z_b, is

$$Z = K\int_0^z (z^2 - w^2/4)^{-1/2}\,dz = K\int_0^{z'} ((z')^2 - 1)^{-1/2}\,dz' \tag{6}$$

where $z' = 2z/w$. The right-hand side of eq 6 can be evaluated with standard integral tables:

$$Z = K\cosh^{-1}(z') + C \tag{7}$$

As indicated in Figure 3, the point $z = w/2$ corresponds to $Z = 0$ and the point $z = -w/2$ corresponds to $Z = j\pi$, so that

$$0 = K\cosh^{-1}(1) + C$$

and

$$j\pi = K\cosh^{-1}(-1) + C = Kj\pi + C$$

From these two equations, it is seen that $C = 0$ and $K = 1$, so that the required transformation is given by

$$z' = \cosh Z \tag{8}$$

or, equally,

$$x + jy = (w/2)\cosh(\Gamma + j\Theta)$$

and

$$x + jy = (w/2)(\cosh\Gamma\cos\Theta + j\sinh\Gamma\sin\Theta)$$

Thus, it can be seen that the transformation of (x,y) coordinates to (Θ,Γ) coordinates simply involves the expressions

$$x = (w/2)(\cosh\Gamma)(\cos\Theta) \tag{9a}$$

$$y = (w/2)(\sinh\Gamma)(\sin\Theta) \tag{9b}$$

and the diffusion equation given previously now becomes

$$\partial C/\partial t = D^*[\partial^2 C/\partial\Gamma^2 + \partial^2 C/\partial\Theta^2] \tag{10}$$

where $D^* = D/[(w/2)^2(\sinh^2\Gamma + \sin^2\Theta)]$. The coordinate system in the transformed spaces is identical with that for a recessed electrode, a geometry for which solutions are readily obtained.

The use of this new coordinate system enables the digital simulation of the concentration profiles and current at the band electrode over all time scales, from the condition of linear diffusion to the quasi-steady-state limit (*17*). The same transformed coordinates are also useful to determine the steady-state concentration profiles at a disk electrode of radius r_0 when the real space coordinates are expressed as x/r_0 and y/r_0, with D^* in this case equal to $D/[r_0^2(\sin^2\Theta + \sinh^2\Gamma)]$ (*18*). The simulations can be readily modified to incorporate different diffusional boundary conditions and finite electron-transfer kinetics.

Conformal Maps for a Double Band. A suitable transformation of coordinates can also be obtained for the double-band electrode with the Schwarz–Christoffel transformation. Figure 3 (C, D, E) shows the conformal map technique applied to the double-band electrode. The first conformal map to be considered (Figure 3D) is the one that best describes the steady-state condition which will occur at infinite time, when the potentials of the two electrodes are held such that the concentration of diffusant is zero at the generator and equal to the bulk concentration at the collector. The conformal space for these conditions is constructed so that the two electrodes resemble a thin-layer cell that has been insulated at the sides to produce a closed box. There is a diffusional exit from the system at the point indicated by $\pm\infty$. However, as time approaches infinity, the current that flows through this point approaches zero (vide infra). Because of the requirements for conservation of fluxes in the closed space, at infinite time the generator and collector currents must be equal but of opposite sign, resulting in a true steady state (*24*). In this conformal map, the steady-state lines of flux will be straight and perpendicular to the electrodes.

The limiting current (i_{db}) when $t \to \infty$ can be evaluated as if the system were a thin-layer cell. The currents at the generator and collector will be equal, and Ψ, the dimensionless current function, is

$$(\Psi_g)_\infty = (\Psi_c)_\infty = (i_{db})_\infty/(nFlDC^0) = w^*/g^* \tag{11}$$

where l is the length of the bands, g^* is the gap width in the conformal space, and w^* is the width of the electrodes in the conformal space. To evaluate the steady-state current, g^* and w^* must be evaluated. The derivation below is given for the special case where the width of the collector and generator are the same. The Schwarz–Christoffel transformation re-

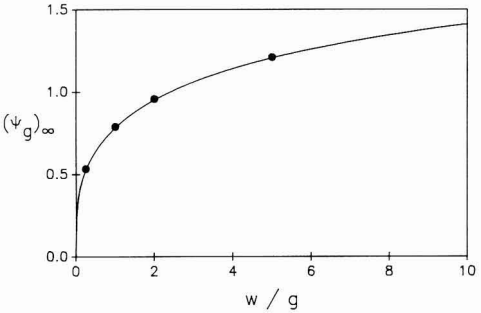

Figure 4. Dimensionless limiting current of the generator in the double-band electrode as a function of the width-to-gap ratio for infinite time. Solid line: numerical calculation of eq 11. Points: simulated results at time scales near steady state, $p = 5 \times 10^{-9} = (g/2)(nFv/RTD)^{1/2}$.

quired to give the coordinate for the double band, Z_{db}, for the change from Figure 3C to Figure 3D is

$$Z = K\int_0^z [(z^2 - a^2)(z^2 - b^2)]^{-1/2}\,dz \qquad (12)$$

From eq 12, one obtains

$$\frac{w^*}{g^*} = \frac{\int_a^b [(z^2 - a^2)(z^2 - b^2)]^{-1/2}\,dz}{j\int_{-a}^a [(z^2 - a^2)(z^2 - b^2)]^{-1/2}\,dz} \qquad (13)$$

where $a = g/2$ and $b = w + g/2$. The integrals in eq 13 are elliptic integrals of the first kind (25), and their ratio can be evaluated numerically by Simpson's method. The limiting steady-state current is then obtained by the use of eq 11 as a function of the electrode width to gap ratio (Figure 4).

The steady-state approximation given above for the double-band electrode was obtained by assuming that $\partial C/\partial\Theta = 0$ at $\pm\infty$ (Figure 3D). The implications of this assumption will now be evaluated. Conservation of fluxes requires that the flux at the generator must equal the sum of the other fluxes in space. At steady state, inside the conformal space

$$i_g = i_c + i(\pm\infty,\text{on})$$

where i_g and i_c are the flux at the generator and collector, respectively, and $i(\pm\infty,\text{on})$ specifies the flux at $\pm\infty$ when the collector electrode is on. When the collector electrode is off, the generator behaves as a single band with flux i_b. Again, due to the required conservation of flux, $i_b = i(\pm\infty,\text{off})$ and we can write

$$(i_c/i_g) + [i(\pm\infty,\text{on})/i(\pm\infty,\text{off})](i_b/i_g) = 1 \qquad (14)$$

The quantities i_c/i_g and i_g/i_b can be determined experimentally and are defined as the collection efficiency and amplification factor, respectively.

To describe the behavior of the double-band electrode at all times, we would like to know how the amplification factor varies with the collection efficiency. The limits of such a plot can be constructed by consideration of the appropriate conditions. At times where the diffusion layer does not extend across the gap, the current at the generator will be equal to that of the band, giving an amplification factor of one and a collection efficiency of zero. In the other limit, where steady state is obtained, the collection efficiency will be one and the inverse of the amplification factor will be zero. The value of $i(\pm\infty,\text{on})/i(\pm\infty,\text{off})$ (eq 14) allows estimation of the limiting slope of a plot of these two parameters at near-steady-state conditions (i.e., collection efficiencies slightly less than unity).

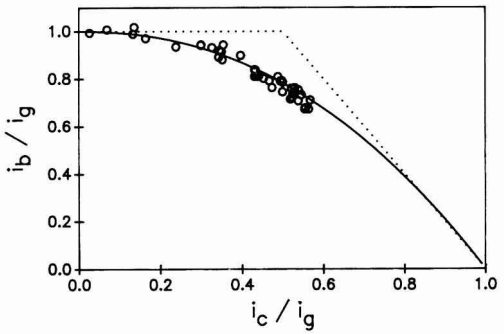

Figure 5. General working curve for the double-band electrode, with the inverse amplification factor plotted as a function of collection efficiency. Solid line: simulated currents. Circles: experimental data points. Dotted lines: theoretical behavior as the collection efficiency approaches 0 and 1.

For a twin-electrode thin-layer cell, the concentration profile between the generator and collector is linear such that the steady-state concentration at $\pm\infty$ (i.e., the midpoint between the two electrodes) is $C^0/2$. At the double band, the concentration at $\pm\infty$ is C^0, so $i(\pm\infty,\text{on})$ is proportional to $C^0 - C^0/2$. With similar reasoning, $i(\pm\infty,\text{off})$ can be obtained. For a thin-layer cell with one electrode at steady state, a concentration of zero is found at all points, and thus $i(\pm\infty,\text{off})$ is proportional to $C^0 - 0$. From these results, the limit of $i(\pm\infty,\text{on})/i(\pm\infty,\text{off})$ is 0.5 and a plot of i_b/i_g vs i_c/i_g will have a limiting slope of −2 as shown in Figure 5. Construction of the complete curve for Figure 5 requires digital simulation.

Although the conformal map shown in Figure 3D is ideal for the evaluation of the steady state, it is less useful for digital simulation of other time scales because of the necessity of evaluating elliptic integrals in the complex plane at each node of the grid. Therefore, we have used the conformal map shown in Figure 3E for the simulation. The transformation is the same as used at the single band (eq 9). The gap is located on the Θ axis and extends from 0 to π while the electrodes are placed on the Γ axis, which necessitates the definition of $z' = 2z/g$. The conformal map is defined by the following equations:

$$x = (g/2)(\cosh\Gamma)(\cos\Theta) \qquad (15a)$$

$$y = (g/2)(\sinh\Gamma)(\sin\Theta) \qquad (15b)$$

These equations are very similar to eqs 9a and 9b for the single band. The diffusion equation is the same as eq 10 except that the width of the gap (g) is employed rather than the width of the band (w).

EXPERIMENTAL SECTION

Chemicals. Ferrocene ($FeCp_2$) (Aesar, Johnson Matthey) was purified by sublimation before use. Solutions of $FeCp_2$ (1 mM) were prepared in acetonitrile as received (Burdick & Jackson) with 0.2 M tetrabutylammonium perchlorate (TBAP). TBAP (Aldrich) was recrystallized twice from a pentane–ethyl acetate mixture. 9,10-Diphenylanthracene (DPA) (Aldrich) was recrystallized twice from absolute ethanol before use. Solutions of DPA (about 0.5 mM) were prepared in acetonitrile with 0.1 M tetrabutylammonium hexafluorophosphate ($(TBA)PF_6$). The acetonitrile was degassed by three freeze–pump–thaw cycles before transfer to the drybox. $(TBA)PF_6$ (Aldrich) was recrystallized twice from 95% ethanol and dried at 60 °C before use. Pyridine was obtained from conventional sources and also was subjected to three freeze–pump–thaw cycles prior to use in the drybox.

Electrodes. The multiple band electrodes were constructed of platinum foil and Mylar film as described previously (5). Electrodes were polished with a slurry of 1-μm cerium oxide and

fine polished with 0.25-μm diamond paste on a napless cloth (all, Buehler). The surface of the electrode was initially cleaned by sonication in both methanol and water. The surface was cleaned between experiments by wiping with a tissue soaked in acetonitrile. The electrode and gap dimensions were measured to the nearest 0.5 μm from slide-projected photographs taken with an inverted stage light microscope (Zeiss, Axiovert 35) calibrated with 2 μm divisions. Typical values for the electrode widths and interelectrode gap width were 4–6 μm. It was apparent from these photographs that in some cases the bands were misaligned lengthwise by a maximum of 5%. To correct for this, the values of i_b (single-band current) and i_g (generator current) were reduced by a proportional amount for calculations of collection efficiency and inverse amplification factor. The collection efficiency is defined as $(i_c/i_g)_{exp} = [i_c/(i_g - fi_b)]$ where i_c is the collector current and f is the fraction of the electrode length misaligned on one end. The inverse amplification factor is defined as $(i_b/i_g)_{exp} = (i_b - fi_b)/(i_g - fi_b)$. The length of a band electrode was determined by comparison of a slow scan cyclic voltammogram to its simulation, using a previously reported conformal map program of the single-band electrode (*17*) and the known values of all the other parameters. The electrode length obtained in this manner were identical within the accuracy of the measurements with that observed through a Bausch & Lomb Stereo Zoom microscope, and typical values were 0.3–0.5 cm.

The diffusion coefficient used for ferrocene in 0.2 TBAP/CH_3CN was 2.2×10^{-5} cm^2 s^{-1} (*26*). The diffusion coefficient for DPA in 0.1 M (TBA)PF_6 was determined to be 1.3×10^{-5} cm^2 s^{-1} by comparison of slow scan (20–50 mV s^{-1}) cyclic voltammograms of both the ferrocene and DPA solutions at a 5-μm-radius platinum disk electrode as well as single-band electrodes. A 50-μm-radius Pt disk electrode was used to obtain cyclic voltammograms in DPA/pyridine solutions for scan rates between 1 and 1000 V s^{-1}.

Instrumentation. Potential control for the paired band electrodes was maintained with a bipotentiostat of conventional design. Potential control for experiments at Pt disk electrodes (5- and 50-μm radii) was maintained by a locally constructed potentiostat capable of scan rates up to 1000 V s^{-1} and currents on the order of nanoamperes. Voltammograms at scan rates of 1 V s^{-1} and lower were recorded on an x–yy' recorder and at higher scan rates on a Nicolet 320 oscilloscope. A conventional three-electrode cell was employed with a large Pt counter electrode and either an SSCE reference electrode or a Ag wire quasi-reference electrode. The currents for calculation of collection efficiencies and the inverse amplification factor were measured at a potential 257 mV more positive than the formal potential of the redox couple. Experiments that involved DPA solutions were performed in a nitrogen-containing drybox.

Simulations. Programs were written in the Fortran and Pascal languages by using a two-dimensional version of the Hopscotch algorithm (*27*). The Pascal compiler (Professional Pascal, Metaware, Inc., Santa Cruz, CA) was used for the majority of the simulations. In some cases, a Fortran compiler was used (NDP Fortran-386, MicroWay, Inc., Kingston, MA). In both cases, the collector and generator were always the same width. Simulations were carried out on an 80386-based personal computer with a 16-MHz clock speed (Z-386 Model 40, Zenith Data Systems, St. Joseph, MI) and equipped with an 80387 numerical coprocessor. The details of the simulation programs are included in Appendix II. Simulation and experimental data for the limiting currents are shown at $\xi = nF(E - E^0)/RT = 10$.

RESULTS AND DISCUSSION

Simulation of the Double-Band Electrode. The simulation program was first evaluated at the limiting cases described in the theory section. When the boundary conditions were established so that the collector was off, the simulated currents agreed with published values for the single band within 1.5%. This simulation is least favorable for the conformal map because of the high curvature of the concentration profile at the outer edge of the generator. Nevertheless, the accuracy is considered satisfactory. The other limit evaluated is that given by eq 11, that is, the current at infinite time (very slow scan rates) where the collection efficiency will be unity.

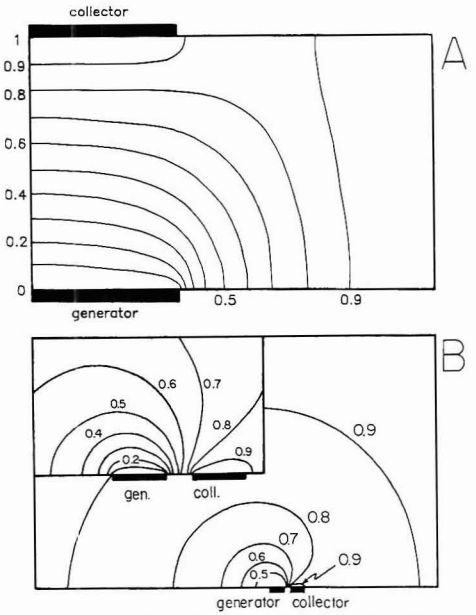

Figure 6. Concentration profiles in the conformal (A) and real (B) space obtained from digital simulations of the double band. Profiles for $w/g = 2$, $p = 0.05$. Numbers on the curves are the values of C/C^0.

The simulated currents are superimposed on the analytically derived curve for several values of w/g in Figure 4, and excellent agreement is observed. In this domain, the conformal map is most efficient, and 5000 iterations (approximate run time of 30 min on the 386 computer) were required for accurate values.

Figure 6A shows a concentration profile in the conformal space under conditions where feedback occurs. It can be noted that the equiconcentration lines are relatively evenly spaced across the gap. Curvature is only apparent at the outer edge of the generator. As is illustrated by the figure, the majority of the flux is in a region that is well mapped in the conformal space. In contrast, considerable curvature of the same equiconcentration lines is seen in real space (Figure 6B). This is dramatically illustrated for the region near the electrode shown in the insert.

The dotted lines in Figure 5 define the limits for the double-band inverse amplification factor as a function of the collection efficiency. Voltammograms were simulated over a wide range of scan rates and width-to-gap ratios. The solid line in Figure 5 was constructed from these data and describe how the currents will deviate from the limiting cases. This line follows the empirical equation $i_b/i_g = 1 - (i_c/i_g)^{2.21}$ and was found by nonlinear regression from 46 individual simulations. In these simulations, the width-to-gap ratio varied between 0.1 and 5 and the dimensionless scan rates varied between 10^{-8} and 0.2, corresponding to values of the scan rate of 10^{-13}–50 V s^{-1} at a double-band electrode with micron dimensions. As expected, the ratio i_b/i_g approaches one at low collection efficiencies (small width-to-gap ratios or high scan rates) and approaches zero at high collection efficiencies (large width-to-gap ratios or slow scan rates).

The dimensionless generator current from simulations is shown as a function of the dimensionless scan rate in Figure 7 for various width-to-gap ratios. Additionally, this figure

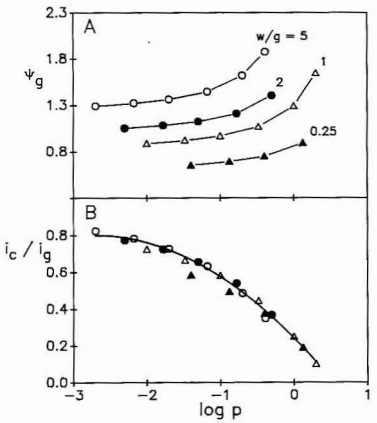

Figure 7. (A) Dimensionless generator current, Ψ_g, as a function of dimensionless scan rate, p, from simulations of the double-band electrode. (B) Collection efficiency, i_c/i_g, as a function of p.

shows the dependence of the collection efficiency on scan rate. Excluding the values for $w/g = 0.25$, a smooth curve can be drawn through the points which can be expressed as

$$i_c/i_g = 0.2415 - 0.4091(\log p) - 0.07487(\log p)^2 \qquad (16)$$

Note that this empirical expression is only useful for $w/g \geq 1$. Since this result is a function of scan rate, it should be more useful for routine characterization of double bands than the relation previously given for chronoamperometry (*2*).

To evaluate the increased efficiency of the conformal map, a simulation program for the double-band electrode was written in a form patterned after that shown previously (*2*, *3*). This simulation operates in real space, i.e., the space division was uniform across the generator, collector, and gap (for comparisons with prior work, six grid elements were used across each electrode and the gap), but with an exponentially expanding grid at the sides of the electrodes and above them. Comparisons of this simulation to the conformal map simulation under similar computation times (identical number of grid elements, 5000 iterations, 1-h computation) showed that the real-space simulation gave incorrect results. The real space simulation failed to give the correct value for the generator current amplitude unless the number of grid elements was increased to 80 across each electrode and the gap and the number of iterations was increased to 44 000; the computation time was increased to 6.5 h. Thus, the conformal space leads to a more efficient simulation, because the grid spacing more closely follows the flux lines. This is true even though an exact correspondence is only achieved at infinite time.

Voltammetry at the Double Band. Illustrated in Figure 8 are the results from a collector–generator experiment for one-electron oxidation of DPA in acetonitrile containing 0.1 M $(TBA)PF_6$. The simulation superimposed is in excellent agreement and employed the exact parameters used in the experiment with no adjustable parameters. A summary of 37 experiments for the oxidation of ferrocene is superimposed on the dimensionless working curve of Figure 5. The data points were obtained at 6 double-band electrodes at scan rates between 0.010 and 20 V s^{-1} in a solution of $FeCp_2$ in acetonitrile containing 0.2 M TBAP supporting electrolyte. Although no prior knowledge of the width-to-gap ratio is necessary for a comparison to the simulated curve, this value ranged between 0.5 and 1 for the electrodes used here.

The conformal map simulation allowed us to evaluate previously published experimental data at double-band

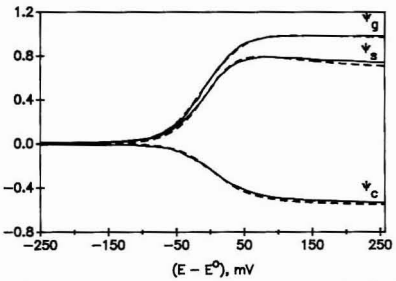

Figure 8. Oxidation of DPA at a double-band electrode. Solid line: experimental dimensionless single (Ψ_b), generator (Ψ_g), and collector (Ψ_c) currents. $w = 4.5$ μm, $g = 4.5$ μm, $v = 0.1$ V/s. Dashed line: simulation of experimental voltammograms. $w/g = 1.0$, $p = 0.123$.

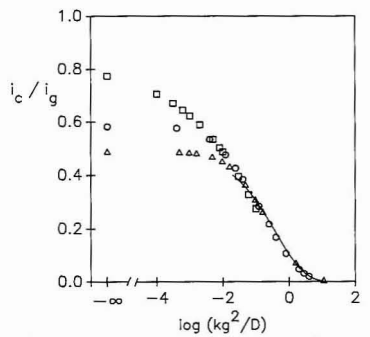

Figure 9. Collection efficiency as a function of log (kg^2/D) for the EC mechanism. Squares: $p = 0.005$, $w/g = 2$. Circles: $p = 0.10$, $w/g = 1$. Triangles: $p = 0.20$, $w/g = 0.5$. Solid line: collection efficiency calculated by eq 17. The abscissa at $-\infty$ indicates the simulation used involved chemically stable species.

electrodes. Figure 5 of ref 2 shows simulated and experimental data points for the collection efficiency as a function of gap width for several double-band electrodes. When these data were compared to those from the conformal map simulation described here, excellent agreement was found. Specifically, the coefficient of determination (*28*) between the conformal map simulation and the data was 0.93, whereas the coefficient of determination between the simulations used in that work and the data gave a value of 0.64 with the worst fit at low collection efficiencies. This clearly shows the improved agreement of simulations with experiments when the transformation of space is used to redefine the diffusion equation for the double-band electrode.

Chemical Kinetics at Paired Bands. To evaluate the utility of paired band electrodes in the study of chemical kinetics, the conformal map simulation was modified to incorporate the EC mechanisms as described in the Appendix sections, and the collection efficiency was evaluated as a function of log (kg^2/D). Working curves are shown in Figure 9. A working curve for the EC mechanism for this electrode geometry has previously been published (*3*); however, we show the work in Figure 9 because the published working curve did not indicate the dependence on the electrode width, the scan rate, or the collection efficiency in the absence of the chemical reaction. It is seen from Figure 9 that all of these parameters affect the collection efficiency. However, at low collection efficiencies, the curves appear to merge and approach the empirical limit

$$i_c/i_g = (1/2)\exp\{-(k/D)^{1/2}(\pi g/2)\} \qquad (17)$$

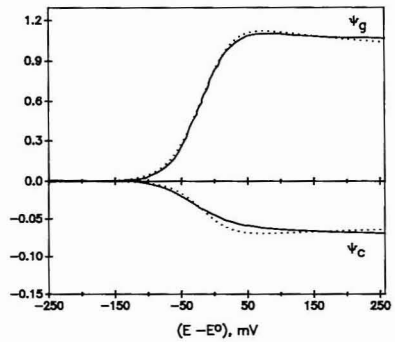

Figure 10. Oxidation of 0.5 mM DPA in the presence of 5 mM pyridine at a double-band electrode. Solid line: experimental generator and collector currents. w = 4.5 μm, g = 4.5 μm, v = 0.1 V/s. Dashed line: simulation of experimental voltammograms. w/g = 1.0, p = 0.123, k = 100 s^{-1}.

indicated by the solid line in the figure. Note this result is useful over at least 2 orders of magnitude. The working curves for the DISP1 simulations are identical but with the abscissa equal to log ($2kg^2/D$) (see Appendix II).

To test the DISP1 simulations, the anodic substitution reaction of pyridine with the DPA radical cation in acetonitrile containing 0.1 M (TBA)PF_6 was evaluated (*29*). The rate of the reaction was first determined with cyclic voltammetry at a disk electrode (r = 50 μm), and the resulting amplitude of the oxidation current was plotted as a function of scan rate. The data were obtained under conditions of linear diffusion, and the pseudo-first-order rate constant was evaluated with a conventional working curve (*30*). The paired band electrode was then used in the generator–collector mode in the same solution. A sample set of voltammograms, along with the simulated results, is shown in Figure 10. The rate constant used in the simulation, k = 100 s^{-1}, was that determined from the linear diffusion experiments, and excellent agreement is found. For four electrodes (w/g values of 0.7–1.0) in three different solutions (k = 83–112 s^{-1}), the simulated collection efficiencies fell within the experimental range.

It is apparent from Figure 9 that the double-band electrode can be used to determine the rates of the EC and DISP1 mechanism reactions successfully. However, the range of rate constants that can be determined at any given electrode depends on the amount of gain that can be used at the collector. In fact, very small numbers of molecules have been detected with devices of this type (*31*). The total range of rate constants that can be found with this technique can be improved through the use of several electrodes with different width-to-gap ratios.

CONCLUSIONS

The use of a conformal map has enabled an accurate solution to be obtained for the double-band electrode operated at steady state. In addition, the use of the conformal map approach has enabled more efficient digital simulation programs to be written, which results in considerably shorter run times. At conditions away from steady state, the grid lines of equal concentration do not follow those of the conformal map, but nevertheless, the map is advantageous over other configurations because it more closely approximates the actual grid. Experimental data are accurately predicted by the simulation that enables the utility of the double band to be evaluated in various applications. Thus, the use of conformal mapping procedures has significant advantages to model voltammetry at complex electrode geometries.

ACKNOWLEDGMENT

Helpful discussions with Royce Engstrom in the formulative stages of this work are gratefully acknowledged.

APPENDIX I

Derivation of Fick's Law for the Spherical Case. Starting with the definition of y ($y = (r - r_0)/r$), we can write

$$\frac{\partial C}{\partial r} = \frac{(1-y)^2}{r_0}\frac{\partial C}{\partial y}$$

Similarly

$$\frac{\partial C}{\partial t} = \frac{D(1-y)^4}{r_0^2}\frac{\partial^2 C}{\partial y^2}$$

which is identical with eq 3 with $D^* = D(1-y)^4/r_0^2$.

The current is obtained by evaluation of $i = -nF\int\int J(t)\,d\sigma$, where $d\sigma$ is the elementary surface area, and the integration is performed over the whole surface area.

The flux $J(t)$ of material is given by Fick's first law:

$$J(t) = \frac{-1}{d\sigma}\frac{dN}{dt}$$

where N is the number of molecules in a volume element $d\sigma$ dr at the electrode surface. In real space, $dN/dt = d\sigma\, dr\, dC/dt$, and the flux is $J(t) = -[(dr)^2/dt](dC/dr)_{r=r_0}$. Thus, the current is

$$i = nFAD(dC/dr)_{r=r_0}$$

In the transformed space, $dN/dt = d\sigma\, dy(dr/dy)(dC/dt)$ and the flux is $J(t) = -[(dy^2)/dt][(dC/dy)(dr/dy)]_{r=r_0}$. This can be rewritten with the use of D^* to be $J(t) = -[D^*(dC/dy)(r^2/r_0)]_{r=r_0}$. Integration over the electrode area gives

$$i = -nFA[-D^*(dC/dy)r^2/r_0]_{y=0}$$

which reduces to eq 4.

APPENDIX II

Diffusion Equations in the Conformal Space. To solve for the currents at a collector–generator pair, Fick's second law

$$\frac{\partial C_A}{\partial t} = D\left(\frac{\partial^2 C_A}{\partial x^2} + \frac{\partial^2 C_A}{\partial y^2}\right)$$

must be solved. The following boundary conditions define the reversible, diffusion-controlled case for the special case where the diffusion coefficients of the reactant (A) and product (B) are equal:

$t = 0;\quad y > 0,\quad -\infty < x < +\infty;\quad C_A = C^0,\quad C_B = 0$

$t > 0;\quad y = 0,\quad -[(g/2) + w] < x < -g/2;$
$C_B = C_A \exp[(nF/RT)(E - E^0)]$ generator

$y = 0,\quad g/2 < x < (g/2) + w;\quad C_A = C^0,$
$C_B = 0$ collector

$y = 0,\quad -g/2 < x < g/2,\quad x > (g/2) + w,$
$x < -[(g/2) + w];\quad [\partial C_A/\partial y]_{y=0} = 0$ insulator

The currents are defined by

$$i_g = \int_{-g/2}^{-(g/2)+w} nFDl(\partial C_A/\partial y)_{y=0}\,dx \quad \text{generator}$$

$$i_c = \int_{g/2}^{(g/2)+w} nFDl(\partial C_A/\partial y)_{y=0}\,dx \quad \text{collector}$$

The following dimensionless variables and parameters are introduced:

$$a = C_A/C^0; \quad b = C_B/C^0; \quad \tau = t(nFv/RT)$$

$$\alpha = g/w; \quad p = (g/2)(nFV/DRT)^{1/2}; \quad \xi = nF(E - E^0)/RT$$

In the conformal space, Fick's second law is

$$\partial a/\partial\tau = (1/p)^2[1/(\sinh^2 \Gamma + \sin^2 \theta)](\partial^2 a/\partial\Gamma^2 + \partial^2 a/\partial\theta^2)$$

The appropriate boundary conditions are

$\tau = 0$; $\quad \Gamma > 0$, $\quad 0 < \theta < \pi$; $\quad a = 1$, $\quad b = 0$

$\tau > 0$; $\quad 0 < \Gamma < \text{arg cosh}\,(1 + 2/\alpha)$, $\quad \theta = \pi$; $\quad b = ae^{\xi}$ generator

$0 < \Gamma < \text{arg cosh}(1 + 2/\alpha)$, $\quad \theta = 0$; $\quad a = 1$, $\quad b = 0$ collector

$\Gamma > \text{arg cosh}\,(1 + 2/\alpha)$, $\quad \theta = 0$ and $\theta = \pi$; $\quad da/d\theta = 0$ insulator

Except as noted, the grid for the double-band simulation in the conformal space had a high density of points near the collector to ensure high precision in the results. Preliminary results indicated that 200 points are needed along the Γ axis. The outer limit was determined as the extent of the diffusion layer at a single-band electrode, as described in our previous work (*17*). The portion of this axis occupied by each electrode comprises 120 points, with the same density of points extended to $1.25\Gamma_1$, where Γ_1 is the outer edge of each electrode. Along the θ axis, a double-scale grid is employed to give high resolution next to the generator, which is required except when the collection efficiency approaches unity. The region from 0.9π to π (nearest the generator) is defined by 80 points, and 70 points define the remainder. The initial dimensionless potential (ξ) is -10 ($E = E^0 + 257$ mV at 298 K), and the final value employed is 10. The voltammogram is generated with a maximum of 30 000 time iterations.

For collection efficiencies approaching unity, a grid was employed with equal spacing between points in the conformal space. The grid contained 150 points along the Γ axis and 50 points along the θ axis, with 50 points along each electrode. Typically 5000 time iterations were employed.

EC Kinetic Scheme. When a chemical reaction follows the interfacial electron transfer so that the electrochemical product, B, is consumed, an additional differential equation must be solved. In real space, the partial derivative equation relative to the B species is

$$\frac{\partial C_B}{\partial t} = D\left(\frac{\partial^2 C_B}{dx^2} + \frac{\partial^2 C_B}{\partial y^2}\right) - kC_B$$

where k is the first-order rate constant of the chemical reaction. The following additional boundary conditions are required:

At the generator, $b = ae^{\xi}$ and $(\partial a/\partial\theta)_{\theta=\pi} = -(\partial b/\partial\theta)_{\theta=\pi}$ and at the collector, $(\partial a/\partial\theta)_{\theta=0} = -(\partial b/\partial\theta)_{\theta=0}$ and $b = 0$.

DISP1 Kinetic Scheme. The DISP1 kinetic scheme is

$$A + e^- \rightarrow B$$

$$B \xrightarrow{k} C$$

$$B + C \xrightarrow{k'} A + D$$

The following differential equations describe the concentration of species A and B:

$$\frac{\partial C_A}{\partial t} = D\left(\frac{\partial^2 C_A}{\partial x^2} + \frac{\partial^2 C_A}{\partial y^2}\right) + k'C_BC_C$$

$$\frac{\partial C_B}{\partial t} = D\left(\frac{\partial^2 C_B}{\partial x^2} + \frac{\partial^2 C_A}{\partial y^2}\right) - k'C_BC_C - kC_B$$

If the rate of the last reaction is rapid, the steady-state approximation can be applied to species C:

$$\partial C_c/\partial t = 0 = kC_B - k'C_BC_C, \qquad C_C = k/k'$$

Substitution of this result gives

$$\frac{\partial C_A}{\partial t} = D\left(\frac{\partial^2 C_A}{\partial x^2} + \frac{\partial^2 C_A}{\partial y^2}\right) + kC_B$$

$$\frac{\partial C_B}{\partial t} = D\left(\frac{\partial^2 C_B}{\partial \lambda^2} + \frac{\partial^2 C_B}{\partial y^2}\right) - 2kC_B$$

Introduction of $C_u = 2C_A + C_B$ and combination of the preceeding equations give

$$\frac{\partial C_u}{\partial t} = D\left(\frac{\partial^2 C_u}{\partial x^2} + \frac{\partial^2 C_u}{\partial y^2}\right)$$

Solution of this equation in combination with the differential equation for B gives the current. These equations are equivalent to those employed in the EC kinetic scheme. The boundary condition of the electrode in this case is

$$C_u^0 = 2C_A^0 = [2\exp((E - E^0)F/RT) + 1]C_B^0$$

Thus, the wave shape only differs in the rising portion.

For both the EC and DISP1 simulations, the grid for the simulation had a high density of volume elements near the generator. This grid is optimal because of the chemical reaction which, in effect, impedes reagent B from diffusing to the collector electrode.

LITERATURE CITED

(1) Chidsey, C. E.; Feldman, B. J.; Lundgren, C.; Murray, R. W. *Anal. Chem.* **1986**, *58*, 601–607.
(2) Bard, A. J.; Crayston, J. A.; Kittlesen, G. P.; Varco Shea, T.; Wrighton, M. S. *Anal. Chem.* **1986**, *58*, 2321–2331.
(3) Varco Shea, T.; Bard, A. J. *Anal. Chem.* **1987**, *59*, 2102–2111.
(4) Hill, H. A. O.; Klein, N. A.; Psalti, I. S. M.; Walton, N. J. *Anal. Chem.* **1989**, *61*, 2200–2206.
(5) Bartelt, J. E.; Deakin, M. R.; Amatore, C. A.; Wightman, R. M. *Anal. Chem.* **1988**, *60*, 2167–2169.
(6) Niwa, O.; Morita, M.; Tabei, H. *Anal. Chem.* **1990**, *62*, 447–452.
(7) Harrington, M. S.; Anderson, L. B. *Anal. Chem.* **1990**, *62*, 546–550.
(8) Matsue, T.; Aoki, A.; Ando, E.; Uchida, I. *Anal. Chem.* **1990**, *62*, 407–409.
(9) Jones, E. T. T.; Chyan, O. M.; Wrighton, M. S. *J. Am. Chem. Soc.* **1987**, *109*, 5526–5528.
(10) Oldham, K.; Zoski, C. *J. Electroanal. Chem. Interfacial Electrochem.* **1988**, *256*, 11–19.
(11) Cassidy, J.; Ghoroghchian, J.; Sarfarazi, F.; Smith, J.; Pons, S. *Electrochim. Acta* **1986**, *31*, 629–636.
(12) Feldberg, S. W. *J. Electroanal. Chem. Interfacial Electrochem.* **1987**, *222*, 101–106.
(13) Heinze, J.; Strzbach, M. *Ber. Bunsenges. Phys. Chem.* **1986**, *90*, 1043–1048.
(14) Saito, Y. *Rev. Polarogr.* **1968**, *15*, 177–186.
(15) Amatore, C. A.; Fosset, B.; Deakin, M. R.; Wightman, R. M. *J. Electroanal. Chem. Interfacial Electrochem.* **1987**, *225*, 33–48.
(16) Amatore, C. A.; Deakin, M. R.; Wightman, R. M. *J. Electrochem. Chem. Interfacial Electrochem.* **1986**, *206*, 23–26.
(17) Deakin, M. R.; Wightman, R. M.; Amatore, C. A. *J. Electrochem. Chem. Interfacial Electrochem.* **1986**, *215*, 49–61.
(18) Michael, A. C.; Wightman, R. M.; Amatore, C. A. *J. Electroanal. Chem. Interfacial Electrochem.* **1989**, *267*, 33–45.
(19) Amatore, C. A.; Saveant, J.-M.; Tessier, D. *J. Electroanal. Chem. Interfacial Electrochem.* **1983**, *146*, 39–52.
(20) Aoki, K.; Morita, M.; Niwa, O.; Tabei, H. *J. Electroanal. Chem. Interfacial Electrochem.* **1988**, *256*, 269–282.
(21) Aoki, K. *J. Electroanal. Chem. Interfacial Electrochem.* **1989**, *270*, 35–41.
(22) Seddon, B. J.; Girault, H. H.; Eddowes, M. J. *J. Electroanal. Chem. Interfacial Electrochem.* **1989**, *266*, 227–238.
(23) Wylie, C. R.; Barrett, L. C. *Advanced Engineering Mathematics*, 5th ed.; McGraw-Hill, Inc.: New York, 1982; pp 1004–1006.

(24) Niwa, O.; Morita, M.; Tabei, N. J. Electroanal. Chem. Interfacial Electrochem. 1989, 267, 291-297.
(25) Abramowitz, M., Stegun, I. A., Eds.; Handbook of Mathematical Functions; Dover Publications: New York, 1970; pp 589-598.
(26) Baur, J.; Wightman, R. M. J. Electroanal. Chem. Interfacial Electrochem., in press.
(27) Shoup, D.; Szabo, A. J. Electroanal. Chem. Interfacial Electrochem. 1984, 160, 1-17.
(28) McClave, J. T.; Dietrich, F. H., II. Statistics, 2nd ed.; Dellen Publishing Co.: Santa Clara, CA, 1982; p 602.
(29) Manning, G.; Parker, V. D.; Adams, R. N. J. Am. Chem. Soc. 1969, 91 (16), 4584-4585.
(30) Wipf, D. O.; Wightman, R. M. Anal. Chem. 1988, 60, 2460-2464.
(31) Cammarata, V.; Talham, D. R.; Crooks, R. M.; Wrighton, M. S. J. Phys. Chem. 1990, 94, 2680-2684.

RECEIVED for review June 20, 1990. Accepted November 16, 1990. This research was supported by the National Science Foundation (CHE-8996213) and CNRS (U.A. 1110, "Activation Moleculaire"). Financial support from NATO (International Grants Division) is also acknowledged.

Expansion of Laser-Generated Plumes Near the Plasma Ignition Threshold

Laszlo Balazs

Central Research Institute for Physics of the Hungarian Academy of Sciences, P.O. Box 49, H-1525 Budapest 114, Hungary

Renaat Gijbels and Akos Vertes*

University of Antwerp (U.I.A.), Department of Chemistry, Universiteitsplein 1, B-2610 Wilrijk, Belgium

Expansion of laser-produced plumes on a solid–vacuum interface during and after the laser shot was investigated theoretically, incorporating several new features into our previous one-component one-dimensional hydrodynamic model. Time development of density, velocity, temperature, and pressure profiles was calculated at laser irradiances below and above the plasma ignition threshold. The estimated velocity of ions released from the plume was close to the measured values. The fast spreading of the blow-off material under the laser vaporization regime and the long lifetime of the relatively compact plasma core above the ignition threshold were predicted in agreement with experimental observations. Calculated surface recession due to evaporation provided a lower bound to the measured crater depth, whereas the calculated melt depth proved to be a realistic upper limit.

INTRODUCTION

When a high-power laser pulse is focused onto a solid surface, the irradiance in the focal spot can lead to rapid local heating, intense evaporation, and degradation of the material.

In analytical chemistry several exploited and potential uses of such processes exist. Most eminent among them is its application in mass spectrometry as an ion source in a vacuum environment (*1–3*). Further possibilities lie with the utilization as an optical emission source (*4*) or as a universal tool for sampling solids (*5–8*). Laser desorption and volatilization found their way to applications in interfacing thin-layer chromatography to gas chromatography (*9*) and to mass spectrometry (*10*).

The most attractive features of laser excitation are its capability to probe insulators—an area where most other methods encounter difficulties—and its cleanliness in depositing energy; i.e. no contamination from electrodes or plasma supporting gases can occur. Furthermore, short laser pulses (ranging routinely from picoseconds to nanoseconds) often offer advantages in analysis, like for example the application of time of flight ion analyzers. Easy tuning of the delivered energy amount and the possibility of localized sampling supplement the list of benefits.

The difficulty related to laser excitation is that the sample has to absorb the light at the particular wavelength, a prerequisite often met in the ultraviolet region. Further problems are the high cost and complexity of the laser systems and the poor understanding of laser-induced processes. Both of these shortcomings are likely to improve in the near future. In this paper we will try to unveil some of the underlying processes of laser–target interaction in a vacuum environment.

It is well-known from mass spectrometric investigations that the amount and ionization degree of the vaporized material depend on the energy deposited into the target. The different regimes of laser ionization, laser desorption, laser vaporization, and laser plasma ionization are characterized by the amounts of deposited energy. The different regimes require different descriptions, because each has its distinctive features determined by a dominating process or several competing processes.

The most common mechanism of laser desorption is a thermally activated process induced by surface heating of the sample (*11*). In this regime the amount of material transport across the surface is negligible (Figure 1a).

Laser heating of the solid surface and of the induced plume leads to the generation of different chemical species. Ion–molecule reactions are among the favored reaction channels for producing ions which contribute to the variety of important lines in the mass spectra (*12*). Protonation and alkalination reactions are often the sources of the most characteristic species in the ion cloud (*13*).

Increasing the energy deposition into the sample the surface temperature reaches a point where material transfer across the surface becomes significant (Figure 1b). In the experiments observable target erosion appears in the form of craters (*14*). In theoretical terms it means that the energy balance equation has to be supplemented by the balance equations for mass and momentum. The flow, the heating, and the expansion of the evaporated target material are governed by the equations of hydrodynamics (*15–17*). Solving the coupled partial differential equations of the conservation laws provides

* To whom correspondence should be addressed. Electronic mail: vertes@ccv.uia.ac.be.

0003-2700/91/0363-0314$02.50/0

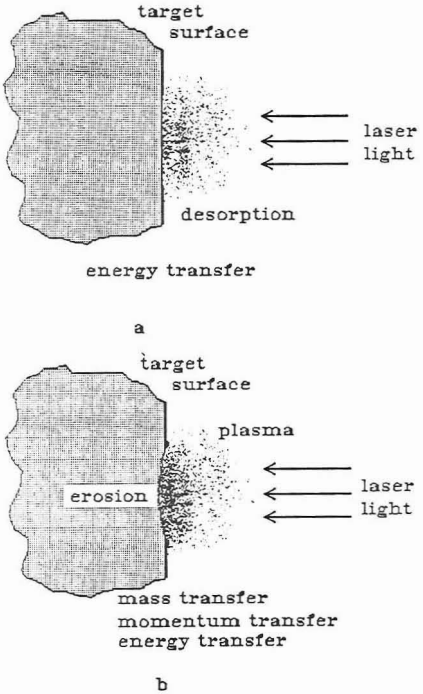

Figure 1. Different regimes of laser–target interaction under vacuum. In laser desorption (a) material transport across the surface is negligible. Laser volatilization (b) is characterized by considerable transport of mass, momentum, and energy and occasional plasma formation.

insight into the factors determining crater depth, cloud extension, ion yield, relative sensitivity factors, and ion kinetic energy distributions. Calculated and measured values of these quantities show promising correlations for different lasers and different types of materials (*15*).

In the present article we exclude the laser desorption regime from the discussion; i.e. we focus our attention to situations where material transport cannot be neglected. Naturally, this is the case in laser sampling experiments and both in mass and optical atomic spectroscopy applications (*18*).

In order to describe the fate of the laser energy during laser–solid interaction, several processes should be considered. Due to the character of the target, a fraction of the energy is absorbed from the laser pulse while the rest is reflected by the surface. The deposited part of the laser energy is converted into local heat instantaneously, which can in turn diffuse by heat conduction. An increase in temperature may induce appreciable changes in optical and thermal properties of the solid, thus influencing the rate of energy deposition and heat transfer. If the surface temperature is sufficiently high, phase change (melting) may occur and part of the absorbed laser power is expended into the latent heat of transition. Further heating results in the translation of the solid–liquid interface into the bulk, while the surface temperature continues to rise until evaporation commences. Part of the absorbed energy is devoted to the heat of vaporization. Although rapid vapor formation at high temperatures causes significant surface recession, vaporization is not the only and not even the most important crater formation mechanism in many cases. Hydrodynamic effects in which droplets and particulates are expelled from the molten surface layer and ejection of the melt caused by vapor recoil are among the mechanisms which contribute to the ablation of the target (*19*, *20*).

In the hot vapor excited species, ions and free electrons are generated which interact with the laser light, leading to further heating and ionization. This in turn leads to increased absorption. On the basis of the laser power, this feed-back mechanism may or may not result in a breakdown, i.e. the generation of a fully ionized plasma. In a previous paper we established a criterion for this plasma ignition threshold as a relation of the normal and plasma absorption coefficient (*21*).

After plasma ignition the laser energy is coupled to the strongly absorbing plume. Plasma temperature can reach extremely high values, and the plume, containing also multiply charged species, becomes luminous. The extremely high energy density of the medium fuels the plasma expansion, and the blow-off material continues its radiation for a long time even after the end of the laser pulse (*22*).

From the practical point of view, postpulse processes might be just as important. Expansion of the hot cloud of particles continues after laser heating has ceased, and the plume starts to cool down, leading to recombination (*23*, *24*). Atomic emission spectroscopy is based on the line emission emerging from radiative recombination and on other relaxation processes in the postpulse plume (*22*). Part of the ions detected in a mass spectrometer are also released during the late expansion phase of the plasma.

Vaporization due to Q-switched laser illumination proceeds on the 100-ns time scale. Some laser-induced processes, however, do not cease at this stage. Particulate formation may continue for as long as several hundred microseconds (*25–27*). Although particulates are very important in the explanation of laser sampling experiments, ion formation, essential in atom and ion sources, is more bound to the vaporization and plasma formation phase.

It is the aim of this paper to assess the importance of different processes taking place in the expanding vapor during and *after* the laser shot and to compare the temporal behavior of the cloud generated by laser vaporization and by plasma ionization.

METHODS OF CALCULATION

In order to study pulsed-laser heating and evaporation of solids, we constructed a one-dimensional model consisting of two parts: the first dealt with the heating and melting of the target and predicted the temperature, density, and flow velocity of the particles emerging on the liquid-vapor interface, whereas the second followed the expansion of the plume expelled from the surface. In the following sections we present the framework of the calculations.

(a) Heating, Melting, and Vapor Formation. Let us consider a pulsed laser beam impinging perpendicularly on the solid surface. If the beam diameter is much larger than the thermally affected thickness of the solid, the diffusion of the absorbed laser energy can be described by the one-dimensional heat conduction equation with a source term:

$$\frac{\partial T(x,t)}{\partial t} = \frac{\partial}{\partial x}\left[\left(\frac{K}{c_p\rho}\right)\frac{\partial T(x,t)}{\partial x}\right] + \frac{\alpha}{c_p\rho}I(x,t) \qquad (1)$$

where T denotes the temperature inside the solid, x is the position measured from the surface, t is the time, and K, c_p, α, and ρ stand for the thermal conductivity, heat capacity, absorption coefficient, and mass density, respectively. $I(x,t)$ is the laser irradiance which, assuming a homogeneous absorbing medium, can be written as

$$I(x,t) = I_0(t)(1 - R)\exp(-\alpha x) \qquad (2)$$

Here $I_0(t)$ is the incident laser irradiance and R is the reflectivity of the surface.

Reliable experimental data on the reflectivity of hot surfaces are rather scarce, although there is strong evidence that in the case of metals the infrared reflectivity drops sharply with increasing temperature whereas the change is less pronounced in the UV domain (*19, 20, 28*). It is usually assumed that for long wavelengths the temperature dependence of reflectivity can be related to that of the dc conductivity, $\sigma_0(T)$, through the following expression:

$$1 - R(T) = [1 - R(T_0)]\sigma_0(T_0)/\sigma_0(T) \quad (3)$$

where $R(T_0)$ and $\sigma_0(T_0)$ are the free-electron part of the reflectivity and the dc conductivity of the solid (*19*).

In order to deal with phase transitions during the heat transfer and to cope with temperature-dependent optical and thermal parameters, eq 1 had to be solved numerically. The finite difference method we employed was similar to the one described by several authors (*29–31*).

Assuming thermally activated surface vaporization, the flux of atoms crossing the liquid–vapor interface is determined by the actual surface temperature, T_s, and can be approximated by

$$j(T_s) = Ap(T_s)/\sqrt{2\pi MRT_s} \quad (4)$$

where M is the molecular mass of atoms, R is the gas constant, and $p(T_s)$ is the equilibrium vapor pressure (*19*). The sticking coefficient, A, is usually taken to be close to unity in the case of metals. An expression for the temperature dependence of the equilibrium vapor pressure can be obtained by integrating the Clausius–Clapeyron equation:

$$p(T_s) = p_0 \exp(\Delta H_{lv}(T_s - T_{lv})/RTT_{lv}) \quad (5)$$

where ΔH_{lv} stands for the heat of vaporization and T_{lv} is the boiling point at the ambient pressure p_0. The amount of heat devoted to the vaporization and the thickness of the layer evaporated during the time interval, Δt, are expressed as

$$\Delta Q_{evap} = j\Delta H_{lv}\Delta t \quad (6)$$

$$\Delta x_{evap} = \frac{jM\Delta t}{\rho} \quad (7)$$

The initial velocity distribution of particles which come off the surface can be regarded as a half-range Maxwellian; i.e. the velocity component normal to the surface can have nonnegative values only (*32*). The flow velocity of the vapor appearing above the liquid surface can be approximated by the average of the normal velocity component (*32*):

$$\hat{v}_x = \sqrt{2kT_s/\pi m} \quad (8)$$

where k is the Boltzmann constant and m is the mass of an atom.

The main source of positive ions at the onset of vaporization is the thermionic emission from the heated surface, generally described by the so-called Langmuir–Saha equation (*28*):

$$\frac{n_1}{n_0} \approx \exp\left(-\frac{E_1 - \phi}{kT}\right) \quad (9)$$

where n_0 and n_1 are the number densities of neutrals and singly charged ions, respectively, E_1 is the first ionization potential, and ϕ is the electronic work function.

(b) Vapor Expansion and Plasma Generation. As target heating continues and the plume develops with continuously increasing density and temperature, the collisions between particles become frequent enough that the hypotheses of *local thermal equilibrium* for the individual volume elements can be adopted. This means, that, in a sufficiently small region of the plume, thermal equilibrium is established between electrons, ions, and neutrals; that is, they can be characterized with a common temperature and the Saha–Eggert equation can be utilized for calculating electron, ion, and neutral densities. We consider a quasi-neutral plasma of one chemical element consisting of electrons, atoms, and ions with charge number z, ranging from $z = 1$ to $z = z_{max}$. Only thermal ionization due to energetic collisions in the plasma was considered, other processes like charge exchange, excitation, cluster formation, etc. were not included in the model.

Neglecting the possible depression in ionization potentials and the difference between the partition function of ions and neutrals, we can write for each ionization step an appropriate Saha–Eggert equation:

$$\frac{x_e x_z}{x_{z-1}} = \frac{1}{n}\left(\frac{2\pi m_e kT}{h^2}\right)^{3/2} \exp\left(-\frac{E_z}{kT}\right) \quad (10)$$

where h stands for the Planck constant and E_z is the ionization energy of the species with a charge number $z - 1$. The local number density, n, is given by $n = \rho/m$; ρ is the local mass density of the plasma, m_e is the electron mass, and x_z and x_e are defined as $x_z = n_z/n$ and $x_e = n_e/n$.

Supplementing eq 10 with the conservation of matter

$$x_0 + x_1 + x_2 + \ldots + x_{zmax} = 1 \quad (11)$$

and with the conservation of charge

$$x_1 + 2x_2 + \ldots + z_{max}x_{zmax} = x_e \quad (12)$$

we obtain a complete set of equations from which the local densities of each component can be obtained. The Newton–Raphson method (*33*) was used to solve this strongly nonlinear system of equations, ensuring fast and reliable convergence during the iteration.

For the sake of simplicity we neglect the radial thinning of the plume, which is a good approximation if the diameter of the laser focal spot is commensurable or especially if it is much larger than the distance left behind by the plume during the time of investigation. To follow the expansion of the vapor, we then have to solve the one-dimensional equations of hydrodynamics expressing the conservation of mass, momentum, and energy, respectively:

$$\frac{\partial \rho}{\partial t} = -\frac{\partial(\rho v)}{\partial x} \quad (13)$$

$$\frac{\partial(\rho v)}{\partial t} = -\frac{\partial}{\partial x}(p + \rho v^2) \quad (14)$$

$$\frac{\partial}{\partial t}\left[\rho\left(e + \frac{v^2}{2}\right)\right] = -\frac{\partial}{\partial x}\left[\rho v\left(e + \frac{p}{\rho} + \frac{v^2}{2}\right)\right] + \alpha\Phi - \epsilon_{rad} \quad (15)$$

Here p denotes the local pressure, ρe is the local internal energy density, Φ is the laser irradiance, and α and ϵ_{rad} are the linear light absorption coefficient and the radiation power loss emitted in the Bremsstrahlung process, respctively. If the electrons have a Maxwellian distribution of velocities, the total amount of energy emitted per unit volume per unit time is (*34*)

$$\epsilon_{rad} = \left(\frac{2\pi kT}{3m_e}\right)^{1/2} \frac{32\pi e^6}{3hm_e c^3} n_e \sum_z z^2 n_z g_z \quad (16)$$

where e is the electron charge, c is the velocity of light, and g_z stands for the Gaunt factor, which is usually close and has been taken equal to unity in our calculations. Assuming that the plasma follows the ideal gas rule, the relation of pressure and internal energy density to the state variables can be written in the form

$$p = (1 + x_e)\rho kT/m \quad (17)$$

$$\rho e = \frac{\rho}{m}\left[\frac{3}{2}(1 + x_e)kT + \sum_{w=1}^{z_{max}}(E_w \sum_{z=1}^{z_{max}} x_z)\right] \quad (18)$$

Table I. Thermophysical and Optical Parameters of Copper Used in Our Calculations

	solid	liquid
thermal conductivity, W/(m K)	380	170
specific heat, J/(kg K)	420	494
density, kg/m^3	8900	7800
mp, K	1356	
ΔH_{fusion}, kJ/mol	13.0	
ΔH_{iv}, kJ/mol		304.8
reflectivity at 300 K	0.975	
abs coeff, m^{-1}	7.44×10^7	7.44×10^7

where E_w is the wth ionization energy.

As it was mentioned earlier, transition between laser vaporization and plasma ignition shows threshold behavior and drastic differences can be observed in characteristic features (e.g. expansion velocities, temperatures, ion energies, etc.) of the plumes generated under the two different regimes. This threshold behavior can be explained by the onset of a feedback mechanism in the absorption of the plume which turns the almost completely transparent vapor into a strongly absorbing, opaque plasma.

Absorption of heated gases that have no molecular absorption bands can be attributed mainly to free–free transitions of electrons in the field of neutrals or ions. Photoionization of excited species may have important contribution only in the case of UV lasers and in the presence of species with low ionization potential (*35*). Preceding plasma ignition, the plume consisting of largely neutral atoms, interacts with the laser mainly through electron–neutral inverse Bremsstrahlung processes. For this process the absorption coefficient is given by

$$\alpha_{e,n} = [1 + \exp(-h\nu/kT)]Qn_e n_0 \qquad (19)$$

where ν is the laser frequency, T is the local plume temperature, n_e and n_0 are the electron and neutral number densities, and Q is the cross section of the photon absorption (*36*). As the vapor temperature and hence the number of charged particles increases, the electron–ion inverse Bremsstrahlung process becomes dominant. The absorption coefficient in this case can be written as follows (*34*, *36*):

$$\alpha_{e,i} = \left[1 - \exp\left(-\frac{h\nu}{kT}\right)\right]\frac{4e^6 n_e}{3hc\nu^3 m_e}\left(\frac{2\pi}{3m_e kT}\right)^{1/2}\sum_z z^2 n_z g_z \qquad (20)$$

Equations 5 and 8 completed with the assumption that the vapor temperature at the liquid–gas interface is equal to the actual surface temperature served as boundary conditions for the equations of hydrodynamics. Numerical solution of the problem was based on a finite difference approximation of eqs 13–15 utilizing the scheme of Godunov (*37*). Details of the algorithm were discussed elsewhere (*16*).

RESULTS AND DISCUSSION

Calculations were carried out for the ruby laser–copper interaction at 30 J/cm^2 and at somewhat higher, 36 J/cm^2, laser energy densities. The temporal intensity profile of the laser pulse, $I_0(t)$ in eq 1, was approximated by Gaussian distribution of 30-ns full width at half-maximum (see dashed curve in Figure 4). Although the numerical solution of eq 1 enabled the accurate temperature dependence of the thermophysical parameters to be considered, we made distinction only between the solid and the liquid phase, each characterized by one set of thermal parameters, as it is displayed in Table I.

In eq 15 the absorption coefficient, α, was approximated by the sum of the electron–neutral and electron–ion inverse Bremsstrahlung coefficients given by eqs 19 and 20. Surface

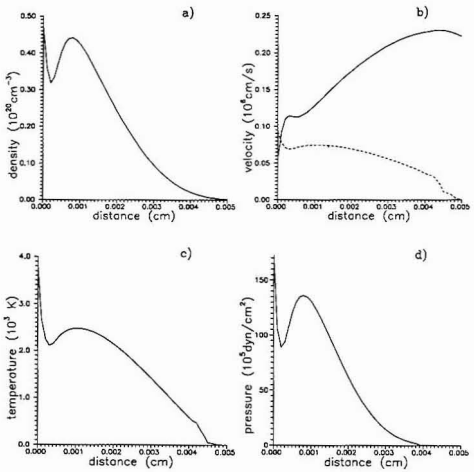

Figure 2. Calculated density (a), velocity (b), temperature (c), and pressure (d) profiles at 70 ns. The laser energy fluence was 30 J/cm^2. The dashed curve in b corresponds to the local sound velocity defined by eq 21.

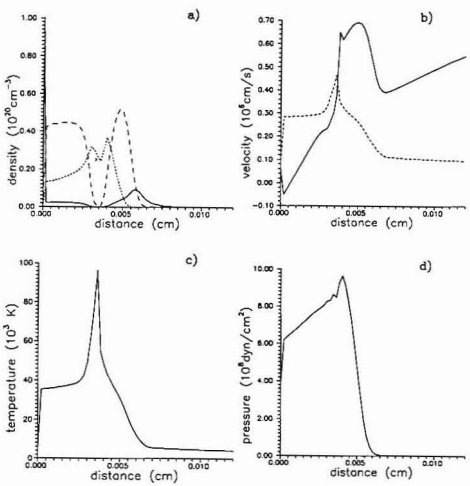

Figure 3. Calculated density (a), velocity (b), temperature (c), and pressure (d) profiles at 70 ns. The laser energy fluence was 36 J/cm^2. The different lines in a correspond to different species: (—) Cu^0; (– – –) Cu^+; (- - -) Cu^{2+}. The broken line in b represents the local sound velocity defined by eq 21.

reflectivity was calculated according to eq 3 on the basis of dc conductivity and on other data (*19*, *38–40*). In the plasma, formation of singly and doubly charged copper ions (ionization potentials $E_1 = 7.726$ eV and $E_2 = 20.29$ eV) were investigated.

Results referring to the trailing edge of the laser pulse (70 ns) are presented in Figures 2 and 3, for 30 and 36 J/cm^2 laser fluences. The conspicuous difference in the calculated density, velocity, temperature, and pressure profiles points to the difference in the position of energy deposition.

Below the plasma ignition threshold, the blow-off material remains transparent as long as the laser is on. Therefore the laser can reach the metal surface without appreciable attenuation where a fraction of its energy is absorbed while the rest

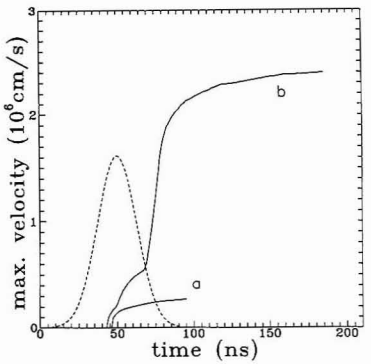

Figure 4. Calculated front velocities as a function of time at (a) 30 J/cm^2 and (b) 36 J/cm^2 laser energy densities. The dashed curve represents the temporal distribution of the laser pulse.

is reflected and lost as far as the laser ablation process is concerned. The temperature of the expanding plume never exceeds the surface temperature, and in the vapor thermal ionization is almost completely absent. The plume expands into the vacuum, and its flow becomes supersonic; i.e. the flow velocity exceeds the local velocity of sound, defined as

$$v_s = \sqrt{\gamma kT/m} \qquad (21)$$

where $\gamma = {}^5/_3$ for a gas consisting of atomic species.

In the high-fluence case, the energy delivered to the plume through electron–neutral inverse Bremmsstrahlung processes was enough to elevate the temperature close to the surface value, giving rise to high electron density as well as intense light absorption.

In Figure 4 the comparison of maximum flow velocities as a function of time indicates that streaming velocities were almost identical for low- and high-energy fluences until the onset of plasma formation.

In the high-fluence case, at about 50 ns a transition period starts leading to the rapid growth of the plasma, which is apparent from the steep rise in the flow velocity. After breakdown, the incident laser energy is completely deposited into the plasma, increasing its velocity to about 2.4×10^6 cm/s, whereas at 30 J/cm^2 the expansion velocity remains about one-eighth of this value due to the lack of direct plume heating. As it is apparent in Figure 3a and c, a highly ionized, hot layer is formed at the plasma front in which the temperature exceeds 10^5 K by the end of the laser pulse. These high temperatures result in the production of multiply charged ions. Depending on the local density and temperature the different regions are dominated by different species. Figure 3b and d illustrate the piling up of waves induced by laser heating in the absorption zone and the development of the shock wave driven by the dense, expanding plasma core.

Expansion of the plasma continues after the laser pulse has ceased, and plume properties change considerably during this additional flow. In order to elucidate some of these variations, we traced the expansion further in time.

Figures 5 and 6 show three selected stages of the evolution of density profiles for 30 and 36 J/cm^2 energy fluences, respectively. As time evolves the vapor detaches from the target and a bell-shaped density distribution develops, which drifts towards the vacuum. The motion of the blow-off material can be interpreted as the translation of the center-of-gravity accompanied by the expansion of the cloud.

The fast decay of the density distribution at 30 J/cm^2 and the persistence of a relatively compact core at the higher

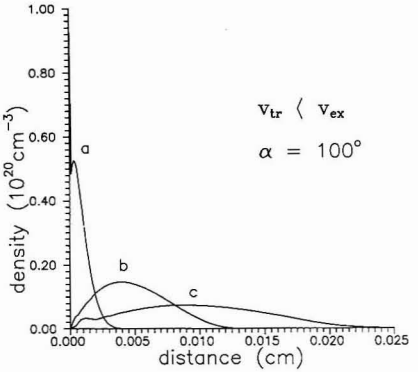

Figure 5. Density profiles at (a) 65 ns, (b) 95 ns, and (c) 125 ns. The laser fluence was 30 J/cm^2. Calculated translation and expansion velocities of the plume were $v_{tr} = 1.3 \times 10^5$ cm/s and $v_{ex} = 2 \times 10^5$ cm/s, respectively.

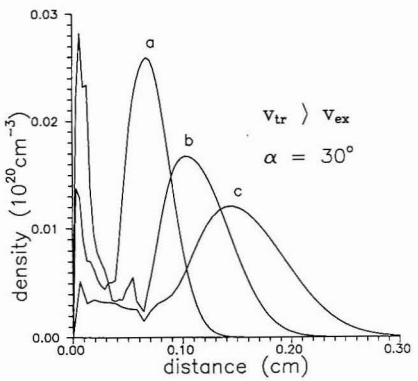

Figure 6. Density profiles at (a) 125 ns, (b) 155 ns, and (c) 185 ns. The laser fluence was 36 J/cm^2. Calculated translation and expansion velocities of the plume were $v_{tr} = 1.3 \times 10^6$ cm/s and $v_{ex} = 6.8 \times 10^5$ cm/s, respectively.

energy fluence reflect that the relation between the propagation and expansion velocities is different below and above the plasma ignition threshold. Translation velocities are 1.3×10^5 and 1.3×10^6 cm/s for the low- and high-fluence cases, respectively. The expansion velocities estimated at the half-maxima of the density distribution curves are 2×10^5 and 6.8×10^5 cm/s below and above the ignition threshold.

Another feature of the plume formation is that the ratio of propagation and expansion velocities does not change during the postpulse period. It is worth noting that this kind of behavior corresponds to a steadily growing spherical plume in three dimensions drifting along the target normal. The laser blow-off material occupies a conical annular region, and the opening angle is determined by the ratio of the expansion and translation velocities. This observation is justified by laser beam deflection experiments on laser-generated plumes (*41*). We indicated in Figures 5 and 6 the angle of a hypothetical cone in which a three-dimensional plume would be confined with the same expansion and translation velocities that were obtained in the calculations: $\alpha = 100°$ for the subthreshold situation, whereas $\alpha = 30°$ for the plasma ignition case.

Experimental evidence was adduced that laser-generated plasmas exhibit strong forward peaking; moreover, in certain

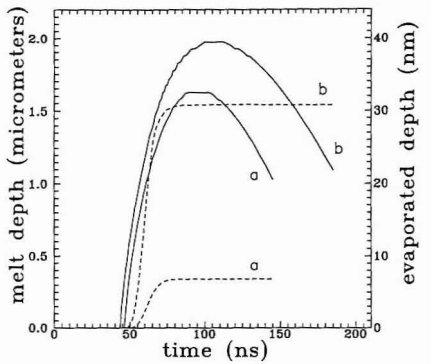

Figure 7. Evolution of melt depth (solid curve) and evaporated thickness (dashed curve) with time at (a) 30 J/cm^2 and (b) 36 J/cm^2 laser energy densities.

cases the plume is tightly confined to narrow cylindrical structures (*42*, *43*). In the light of the present calculations this phenomenon could be explained by assuming an essentially planar expansion at the very beginning of the laser–solid interaction accompanied by a significant increase in the velocity component normal to the target surface. Nevertheless, one must not overlook the fact that other factors, e.g. streaming of the vapor out of the crater created by the laser pulse, result also in the decrease of the expansion angle (*41*).

The agreement between calculated expansion velocities and the results of ion energy measurements is also reasonable. The energy distribution of multiply charged ions stemming from ruby laser–copper interaction were determined by means of a 127° electrostatic analyzer (*44*). The lowest irradiance limit of these measurements coincided with our 36 J/cm^2 calculation. In these experiments only two ionic species, Cu^+ and Cu^{2+}, were identified. The center of the measured energy distribution for Cu^{2+} ions was at 250 eV corresponding to 2.8×10^6 cm/s ion velocity, which is in good agreement with the calculated 2.4×10^6 cm/s terminal plasma front velocity.

Despite the promising correlation we would like to emphasize that this kind of comparison is always subject to ambiguity. Apart from the significant uncertainties in laser power density determinations, our model was designed to describe planar expansion which was obviously not the case in the aforementioned experiment. On the other hand we did not address the question how velocity distributions of different species change when the assumption of local thermal equilibrium ceases to hold. Furthermore we did not consider the effect of the external field penetration to the low-density regions of the plasma. Nevertheless, it is reasonable to assume that the terminal front velocity represents the mean velocity of ions even after the transition to collision-free flight.

Finally, we consider the problem of crater formation. The evolution of the melt depth with time along with the corresponding evaporated thickness is presented in Figure 7 for both laser fluences. One can observe that the melt front penetrates rapidly into the solid and, after having reached the maximum depth (1.63 μm for 30 J/cm^2 and 1.98 μm for 36 J/cm^2), it recedes back due to the resolidification with a somewhat lower velocity. Through the comparison of melt front histories with the shape of the laser pulse (see Figure 4), it is apparent that melting continues even after the incident laser pulse has been extinguished and a region thicker than 1 μm remains molten for almost 100 ns in both cases. In our model material removal is solely attributed to vaporization and, therefore, the thickness of the evaporated layer can be regarded as a lower bound to the crater depth. Subthreshold behavior resulted in low evaporated thickness, whereas in the higher fluence case the amount of material removed by evaporation was increased significantly due to the exponential dependence of evaporation rate on the surface temperature.

As it was discussed above, in pulsed-laser ablation experiments, the splashing of the melt due to vapor recoil is observed. If we assume that the melt is completely ejected before resolidification, the maximum and the melt depth curve serves as an upper limit for the measured value. This assumption is supported by measurements on copper where a 2.2 μm deep crater was produced by a 44 J/cm^2 irradiance Q-switched ruby laser pulse (*28*). Extrapolating our calculated maximum melt front position to this fluence, we obtain 2.6 μm, a fair estimate for the measured crater depth.

CONCLUSIONS

The diversity of phenomena occurring during laser ablation and the lack of reliable experimental data on the high-temperature behavior of solids compelled us not to make any pretense of describing laser–solid interaction in detail. We rather tried to find a simple model to account for pulse melting and vaporization of metals as well as for the absorption and ignition of the plume. The fair agreement between the calculated and measured ion velocities and the feasible upper and lower limits for the crater depth, as well as the prediction of the plume propagation confined in a conical spatial region, indicate that laser vaporization and plasma ionization can be treated in the framework of the presented model.

Nevertheless, the general formulation of the problem makes it difficult to account for all the events of practical and theoretical interest during the laser–solid interaction. The applicability of the model at high irradiances could be stretched by taking into account more ionization steps, employing a more realistic equation of state, and possibly considering critical phenomena.

LITERATURE CITED

(1) Conzemius, R. J.; Capellen, J. M. *Int. J. Mass Spectrom. Ion Phys.* **1980**, *34*, 197.
(2) Vertes, A.; Gijbels, R.; Adams, F. *Mass Spectrom. Rev.* **1990**, *9*, 71.
(3) Jansen, J. A. J.; Witmer, A. W. *Spectrochim. Acta* **1982**, *37B*, 483.
(4) Kagawa, K.; Matsuda, Y.; Yokoi, S.; Nakajima, S. J. *Anal. At. Spectrom.* **1988**, *3*, 415.
(5) Broekaert, J. A. C.; Leis, F.; Raeymaekers, B.; Zaray, Gy. *Spectrochim. Acta.* **1988**, *43B*, 339.
(6) Gray, A. L. *Analyst* **1985**, *110*, 551.
(7) Arrowsmith, P. *Anal. Chem.* **1987**, *59*, 1437.
(8) Adams, F.; Vertes, A. *Fresenius' J. Anal. Chem.* **1990**, *337*, 638.
(9) Zhu, J.; Yeung, E. S. *Anal. Chem.* **1989**, *61*, 1906.
(10) Li, L.; Lubman, D. M. *Anal. Chem.* **1989**, *61*, 1911.
(11) Vertes, A.; Juhasz, P.; Balazs, L.; Gijbels, R. *Microbeam Anal.* **1989**, *1989*, 273.
(12) Visvanadham, S. K.; Hercules, D. M.; Schreiber, E. M.; Weller, R. R.; Giam, C. S. *Anal. Chem.* **1988**, *60*, 2346.
(13) Vertes, A.; Juhasz, P.; Gijbels, R. *Fresenius' Z. Anal. Chem.* **1989**, *334*, 682.
(14) Chen, G.; Yeung, E. S. *Anal. Chem.* **1988**, *60*, 864.
(15) Vertes, A.; Juhasz, P.; De Wolf, M.; Gijbels, R. *Int. J. Mass Spectrom. Ion. Processes* **1989**, *94*, 63.
(16) Vertes, A.; Juhasz, P.; De Wolf, M.; Gijbels, R. *Scanning Microsc.* **1988**, *2*, 1853.
(17) Vertes, A.; Juhasz, P.; De Wolf, M.; Gijbels, R. *Adv. Mass Spectrom.* **1989**, *11*, 1638.
(18) Koppenaal, D. W. *Anal. Chem.* **1988**, *60*, 113R.
(19) von Allmen, M. *Laser-Beam Interactions with Materials*; Springer: Berlin, 1987; Chapters 2 and 5.
(20) Kelly, R.; Rothenberg, J. E. *Nucl. Instrum. and Methods Phys. Res.* **1985**, *B7/8*, 755.
(21) Vertes, A.; De Wolf, M.; Juhasz, P.; Gijbels, R. *Anal. Chem.* **1989**, *61*, 1029.
(22) Kim, Y. W. Fundamentals of Analysis of Solids by Laser-Produced Plasmas. In *Laser-Induced Plasmas and Applications*; Radziemski, L. J., Cremers, D. A., Eds.; Marcel Dekker, Inc.: New York, 1989; pp 327–346.
(23) Pitsch, P.; Rohr, K.; Weber, H. *J. Phys. D* **1981**, *14*, L51.
(24) Afanas'ev, Yu. V.; Rozanov, V. B. *Sov. Phys.—JETP* (*Engl. Transl.*) **1972**, *35*, 133.
(25) Huie, C. W.; Yeung, E. S. *Appl. Spectrosc.* **1986**, *6*, 863.
(26) Huie, C. W.; Yeung, E. S. *Anal. Chem.* **1986**, *58*, 1989.
(27) Kimbrell, S. M.; Yeung, E. S. *Spectrochim. Acta* **1988**, *43B*, 529.
(28) Ready, J. F. *Effects of High Power Laser Radiation*; Academic: New York, 1972; Chapters 3 and 4.

(29) Baeri, P.; Campisano, S. U.; Foti, G.; Rimini, E. *J. Appl. Phys.* **1979**, *50*, 788.
(30) Wood, R. F.; Giles, G. E. *Phys. Rev. B* **1981**, *23*, 2923.
(31) Jain, A. K.; Kulkarni, V. N.; Sood, D. K. *Appl. Phys.* **1981**, *25*, 127.
(32) Kelly, R. *J. Chem. Phys.* **1990**, *92*, 5047.
(33) See for example: *Numerical Analysis*; Burden, R. L., Faires, J. D.; Reynolds, A. C., Eds.; Prindle, Weber & Schmidt: Boston, 1978; pp 443-450.
(34) Spitzer, L. *Physics of Fully Ionized Gases*; Interscience Publishers: London, 1956; pp 147-149.
(35) Rosen, D. I.; Hastings, D. E.; Weyl, G. M. *J. Appl. Phys.* **1982**, *53*, 5882.
(36) Root, R. G. Modelling of Post-Breakdown Phenomena. In *Laser-Induced Plasmas and Applications*; Radziemski, L. J., Cremers, D. A., Eds.; Marcel Dekker, Inc.: New York, 1989; pp 69-103.
(37) Godunov, S. K.; Zabrodin, A. V.; Prokopov, G. P. *USSR Comput. Math. Math. Phys. (Engl. Transl.)* **1961**, *6*, 1020.
(38) *Handbook of Optical Constants of Solids*; Palik, E. D., Ed.; Academic: Orlando, F 1985; pp 280-286.
(39) *Tables of Physical and Chemical Constants*; Kaye, G. W. C., Laby, T. H., Eds.; Longman: London, 1973; p 102.
(40) *American Institute of Physics Handbook*, 3rd ed.; McGraw-Hill: New York, 1972; Section 4.
(41) Chen, G.; Yeung, E. S. *Anal. Chem.* **1988**, *60*, 864.
(42) Irons, F. E.; McWhirter, R. W. P.; Peacock, N. J. *J. Phys. B* **1972**, *5*, 1975.
(43) Doschek, G. A.; Feldman, U.; Burkhalter, P. G.; Finn, T.; Feibelman, W. A. *J. Phys. B* **1977**, *10*, 1977.
(44) Goto, T.; Kishi, K.; Okuda, T. *Kaku Yugo Kenkyu* **1982**, *47*, 592.

RECEIVED for review July 20, 1990. Accepted October 29, 1990. This work was partly supported by the Belgian Nationaal Fonds voor Wetenschappelijk Onderzoek (Belgian National Science Foundation). L.B. is indebted to The Soros Foundation—Hungary for financial support. This publication forms part of research results in a project initiated by the Belgian State—Prime Minister's Office—Science Policy Programming.

Evaluation of Three Zero-Area Digital Filters for Peak Recognition and Interference Detection in Automated Spectral Data Analysis

Fabian Janssens and Jean-Pierre François*
Limburgs Universitair Centrum, Department SBM, Universitaire Campus, B-3590 Diepenbeek, Belgium

An intermediate step in the automatic evaluation of complex spectra is the determination of positions and number of individual lines. In practice, peak analysis is often hampered by statistical noise, presence of a significant background, and influence of substantial interference. One possibility to avoid some of these peak detection problems consists in transforming the accumulated (spectral) data into another spectrum, by means of convolution. Transformed signals have a very characteristic shape, allowing recognition of peaks in an easier and more explicit way. Furthermore, by choosing the proper filter and its parameters, a resolution enhancement can be achieved. In the present work, the performance of square-wave, Gaussian, and triangular zero-area digital filters is compared when applied to single Gaussian lines, multiplets of Gaussian profiles, and Voigt profiles. In order to obtain a general overview of the properties of the filters just mentioned, analytical expressions for the convolution of a Gaussian profile with each of the filters are derived. It is proved in general that a linear background component of a signal is completely filtered out by an even zero-area digital filter as opposed to higher order components. The parameters that are looked at in the convolution signal are full-width at half-maximum, intensity at the position of the maximum, signal-to-noise ratio, second-order background contribution, and resolution enhancement as a function of some typical filter parameters. Besides its use for peak detection, the convolution signal can also provide some information about the presence of interferences. When combined with Zimmermann's method, digital filtering is able to detect most spectral interferences or can at least give a warning about irregularities in the original spectrum.

INTRODUCTION

In spectroscopical analysis, overlapping of lines is often encountered. For quantitative purposes, extraction of numerical information from the peak region is required. This process usually starts with a line detection procedure, followed by a resolution of multiplets into their components. It is often easy to detect a peak or a set of peaks visually, even in the presence of a noisy baseline. However, the presence of a substantial background or spectral interference can make it very tough for the operator, especially in those cases where quantitative work has to be done. To exclude any subjective influence from the operator, the just mentioned procedures are automated now for computer-aided data handling.

Line recognition can be based upon algebraic inequalities between single-channel contents or groups thereof in the registered spectrum. However, these methods are the first to fail in the presence of substantial noise and/or overlapping peaks.

One possibility to reduce peak detection problems consists in transforming the original spectrum into another one, where the lines can be recognized in an easy and more explicit way. The independence of this transformation for any background and/or noise contribution to the spectral intensities, would be an important advantage.

For this purpose cross-correlation has been used as early as 1950 (*1*) and later on in a lot of variations. Unlike the autocorrelation applied by Horlick (*1*), where the raw data are cross-correlated with a spectrum already containing the sought-for spectral features, Black (*2*) suggested a convolution technique (he called it cross-correlation) to isolate structures in a spectrum by sliding an appropriate function over the spectrum containing the raw data. In order to reduce the influence of noise and to eliminate the background, Robertson (*3*) used a so-called zero-area fold-in function. This is a symmetrical rectangular function, which resembles somewhat a typical line shape minus a constant in order to obtain a total zero area. Robertson showed that the signal-to-noise ratio (SNR), as he defined it, is maximal for equal functional forms of both the correlator and original signal. More recently, Taylor and Schutyser (*4*) used what they called a zero-area square-wave correlator, suggested by Op de Beeck (*5*), in their program for analyzing inductively coupled plasma optical emission spectra (ICP-OES). In order to achieve deconvo-

0003-2700/91/0363-0320$02.50/0

lution, Biermann (6) used an adjustable triangular digital filter of unit area.

The zero-area square-wave correlator of Taylor and Schutyser—also known as a top hat filter—will be called here the square-wave filter (SWF), whereas a triangular one (similar to Biermann's) will be referred to as the triangular filter (TF). The SWF and TF are compared with a filter which combines the advantages of Black's filter and Robertson's rectangular fold-in function, namely a Gaussian-shaped filter (GF).

It should be emphasized that in the present work all filters can be represented by an even (symmetrical) function and that they all posses a net zero area. Furthermore, it is proved in general that the linear background component of a signal is completely filtered out by an even zero-area digital filter, as opposed to the higher order components.

A more detailed, comparative study of these digital filters seemed appropriate in view of introducing this technique into a program for automated quantitative analysis of (ICP-OE) spectral data. However, the intension was not only to incorporate a single, fixed filter, as was done by Taylor and Schutyser, but also to conceive the program in such a way that it chooses the optimal parameters for the filter in order to achieve the maximal profit of the convolution operation.

THEORY

General Outline. The convolution $R(\tau)$ of two functions $f(t)$ and $g(t)$ is defined as

$$R(\tau) \equiv \int_{-\infty}^{\infty} f(t)\, g(\tau - t)\, dt \tag{1a}$$

which can be written equivalently as

$$R(\tau) = \int_{-\infty}^{\infty} g(t)\, f(\tau - t)\, dt \tag{1b}$$

The correlation or cross-correlation function $\mathcal{R}(\tau)$ of the two functions $f(t)$ and $g(t)$ is defined as follows:

$$\mathcal{R}(\tau) \equiv \int_{-\infty}^{\infty} f(t)\, g(\tau + t)\, dt \tag{2a}$$

which can also be transformed as

$$\mathcal{R}(\tau) = \int_{-\infty}^{\infty} g(t)\, f(t - \tau)\, dt \tag{2b}$$

It should be remarked that for the special case where $f(t)$ is an even function, convolution and cross-correlation become equivalent. More detailed treatments of convolution and cross-correlation can be found in a number of books (7).

For continuous functions, integrated over finite intervals (windows, with $2M$ being the window width), the convolution integral becomes

$$R(\tau) = \int_{\tau-M}^{\tau+M} f(t)\, g(\tau - t)\, dt \tag{3}$$

In many practical situations either one function or both functions are digitized data streams. Then, the integral is replaced by a summation, representing the discrete convolution

$$R(\tau) \equiv \sum_{t=0}^{2M-1} f(t)\, g(\tau - t) \tag{4a}$$

It can be seen that the image of the function $g(t)$ about the ordinate axis is taken first and then $g(-t)$ shifted by the amount τ.

An alternative form of the discrete convolution summation can be written as

$$R(\tau) = \sum_{t=\tau-M}^{\tau+M} f(t)\, g(\tau - t) \tag{4b}$$

If $f(t)$ represents the actual data stream and $g(t)$ some function to be convoluted with $f(t)$, application of eq 4a will cause a displacement of the output function $R(t)$ compared to the original one, $f(t)$. This shift can be compensated for by eq 4b.

For the special case where $f(t)$ is an even function, eq 4b can be rewritten as

$$R(\tau) = \sum_{t=\tau-M}^{\tau+M} f(t)\, g(\tau + t) \tag{4c}$$

which is also the discrete cross-correlation equation. Here the function $g(t)$ is only shifted by the amount τ.

Another interpretation of the eqs 4a and 4b is that they describe the convolution of an input signal $f(t)$ with a digital "transversal" filter $g(t)$. In the present work $g(t)$ will always be referred to as filter or digital filter whereas the operation (summation or integration) will be called convolution rather than cross-correlation, since both are only equivalent for an even $f(t)$.

A supplementary advantage of linear filters is that the output function is made up of individual convolution contributions $R_i(\tau)$. This property holds for continuous as well as for discrete data:

$$R(\tau) = \sum_{t=\tau-M}^{\tau+M} \left(\sum_i D_i(t)\right) g(\tau - t) = \sum_i \sum_{t=\tau-M}^{\tau+M} D_i(t)\, g(\tau - t) = \sum_i R_i(\tau) \tag{5a}$$

where $f(t)$ has been replaced by

$$f(t) = \sum_i D_i(t) \tag{5b}$$

In practical situations however, the individual peaks $D_i(t)$ consist of several parts, i.e. the real signal in which we are interested, the background, and some additional statistical noise. Generally, the background can be represented by a polynomial; it should be remarked that linear or quadratic functional forms suffice in most practical situations.

Computational Methods. In many cases, spectral line profiles can be approximated quite well by Gaussian distributions, although it is well-known that in general this is not the real functional form. In emission spectrometry for instance, the data should be represented by the so-called Voigt profile (Appendix 1). It has been shown frequently (4, 8, 9) that the central part of an emission line can be approximated by a Gaussian distribution; for an accurate description, especially of the line wings, the Voigt profile should be used.

In order to characterize the relationship between the original and the convolution data together with their typical parameters, such as intensity at the position of the maximum, full-width at half-maximum (FWHM), and signal-to-noise ratio (SNR), analytical expressions of the convolution signals are derived, for zero-area square-wave, Gaussian, and triangular-digital filters $C(\tau - t)$, assuming that the continuous data $D(t)$ can be represented quite correctly over a small window by a Gaussian profile and a quadratic background. The expression for $D(t)$ becomes thus

$$D(t) = S(t) + B(t) = I_{0,s} \exp\left[-\frac{1}{\sigma_s^2}(t - t_{0,s})^2\right] + a_0 + a_1 t + a_2 t^2 \tag{6}$$

where $S(t)$ is the Gaussian model function and $B(t)$ the quadratic background; σ_s is the standard deviation given in units of channels or distance between data points, $t_{0,s}$ is the position of the centroid, and $I_{0,s}$ is the intensity of the Gaussian distribution at $t_{0,s}$.

In Appendix 2 it is shown in general that the linear background component $a_0 + a_1 t$ of the signal $D(t)$ is completely filtered out by an even zero-area filter $C(\tau - t)$, as opposed to the higher order components ($a_n t^n$, $n \geq 2$).

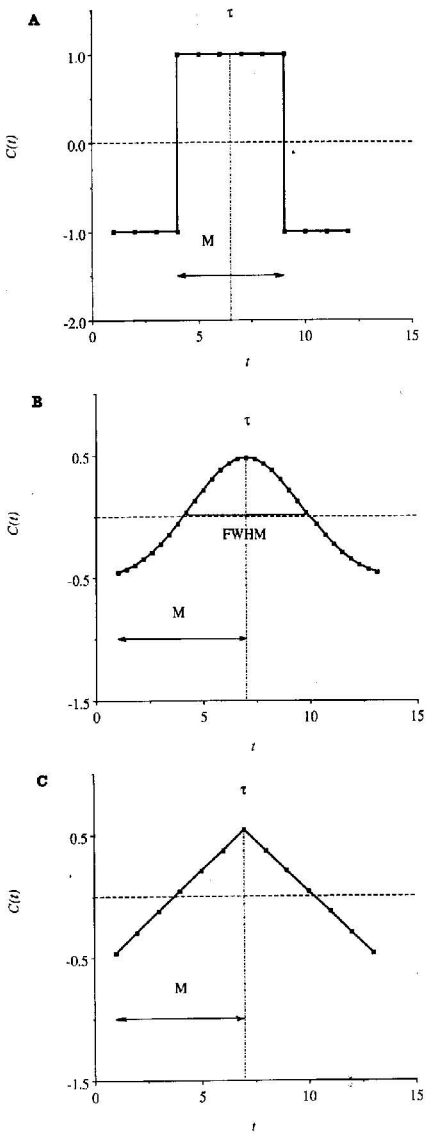

Figure 1. (A) Zero-area square wave filter (SWF). (B) Zero-area Gaussian filter (GF). (C) Zero-area triangular filter (TF).

Square-Wave Filter. The square-wave filter (SWF) was suggested in a discrete form by Op de Beeck (*5*) in γ-ray spectrometry, and adapted by Taylor and Schutyser (*4*) in their computer program for quantitative analysis of ICP-OE spectra. In fact, this filter is a symmetric rectangular (or square) fold-in function with unit intensity in both the positive central window and the negative side windows (Figure 1a). The convolution signal $R(\tau)$ for a continuous SWF can be obtained by means of

$$R(\tau) = -\int_{\tau-M}^{\tau-\frac{M}{2}} D(t)\,dt + \int_{\tau-\frac{M}{2}}^{\tau+\frac{M}{2}} D(t)\,dt - \int_{\tau+\frac{M}{2}}^{\tau+M} D(t)\,dt \quad (7)$$

where M represents the width of the filter.

Substitution of eq 6 into expression 7 gives after a number of intermediary steps

$$R(\tau) = \sqrt{\frac{\pi}{2}}\sigma_s I_{0,s}\left\{2\left[\operatorname{erf}\left(\frac{\tau - t_{0,s} + \frac{M}{2}}{\sqrt{2}\sigma_s}\right) - \operatorname{erf}\left(\frac{\tau - t_{0,s} - \frac{M}{2}}{\sqrt{2}\sigma_s}\right)\right] - \left[\operatorname{erf}\left(\frac{\tau - t_{0,s} + M}{\sqrt{2}\sigma_s}\right) - \operatorname{erf}\left(\frac{\tau - t_{0,s} - M}{\sqrt{2}\sigma_s}\right)\right]\right\} - \frac{1}{2}a_2M^3 \quad (8a)$$

$$\operatorname{erf} z \equiv \frac{2}{\sqrt{\pi}}\int_0^z e^{-t^2}\,dt \quad (8b)$$

It can be seen from eq 8a that the convolution signal is no longer Gaussian and that it only depends upon the correlator width and the quadratic background term (a constant or linear background is efficiently filtered out, due to the zero area of the correlator). By setting the derivative of eq 8a equal to zero, it is found that $R(\tau)$ becomes maximal when τ equals $t_{0,s}$.

$R(t_{0,s})$ without the background contribution ($a_2 = 0$) is given by

$$R(t_{0,s}) = \sqrt{2\pi}\sigma_s I_{0,s}(2\operatorname{erf} Y - \operatorname{erf} 2Y) \quad (9a)$$

$$Y \equiv \frac{M}{2\sqrt{2}\sigma_s} = \frac{\sqrt{\ln 2}M}{\mathrm{FWHM_s}} \quad (9b)$$

and $\mathrm{FWHM_s}$ represents the full-width at half-maximum of the original signal.

A maximal intensity enhancement of $\sqrt{2\pi}\sigma_s$ with respect to the original signal intensity $I_{0,s}$ can be achieved for M tending to infinity. It also found that the second-order background contribution lowers the convolution signal by $^1/_2a_2M^3$.

Gaussian Filter. Connelly and Black (*10*) indicated already that convolution has the tendency to select those structures out of the spectrum which correspond most nearly to the correlating function. Robertson (*3*) also confirmed this and showed that the signal-to-noise ratio of the correlation signal—as he defined it—is maximized when the functional forms of the signal and the correlator are the same.

The Gaussian filter, as it is used in the present work, can be represented by

$$C(\tau - t) = I_{0,c}\exp\left[-\frac{1}{2\sigma_c{}^2}(\tau - t)^2\right] - A \quad (10)$$

where $I_{0,c}$ stands for the intensity of the Gaussian distribution, σ_c is the standard deviation of the distribution, and A is a constant which is determined in such a way that the total net area of the filter is zero:

$$A = \frac{1}{2M}\int_{\tau-M}^{\tau+M} I_{0,c}\exp\left[-\frac{1}{2\sigma_c{}^2}(\tau - t)^2\right]dt = \sqrt{\frac{\pi}{2}}\frac{I_{0,c}\sigma_c}{M}\operatorname{erf}\left(\frac{M}{\sqrt{2}\sigma_c}\right) \quad (11)$$

This filter (Figure 1b) has two adjustable parameters, namely its width M and its own $\mathrm{FWHM_c}$ or σ_c.

The expression for the convolution signal $R(\tau)$ becomes then

$$R(\tau) = \int_{\tau-M}^{\tau+M} \left\{ I_{0,c} \exp\left[-\frac{1}{2\sigma_c^2}(\tau - t)^2 \right] - A \right\} D(t)\, dt \tag{12a}$$

and after some intermediary steps

$$\frac{R(\tau)}{I_{0,c}} = \sqrt{\frac{\pi}{2}} I_{0,s} \frac{\sigma_s \sigma_c}{\sqrt{\sigma_s^2 + \sigma_c^2}} \exp\left(\frac{1}{2} \frac{(\tau - t_{0,s})^2}{\sigma_s^2 + \sigma_c^2} \right) \times \left\{ \operatorname{erf}\left[\frac{\sigma_c^2(\tau - t_{0,s}) + (\sigma_s^2 + \sigma_c^2)M}{\sigma_s \sigma_c \sqrt{2(\sigma_s^2 + \sigma_c^2)}} \right] - \operatorname{erf}\left[\frac{\sigma_c^2(\tau - t_{0,s}) - (\sigma_s^2 + \sigma_c^2)M}{\sigma_s \sigma_c \sqrt{2(\sigma_s^2 + \sigma_c^2)}} \right] \right\} - \frac{\pi}{2} \frac{I_{0,s} \sigma_s \sigma_c}{M} \operatorname{erf}\left(\frac{M}{\sqrt{2}\sigma_c} \right) \left[\operatorname{erf}\left(\frac{\tau - t_{0,s} + M}{\sqrt{2}\sigma_s} \right) - \operatorname{erf}\left(\frac{\tau - t_{0,s} - M}{\sqrt{2}\sigma_s} \right) \right] + 2\sqrt{2} a_2 \sigma_c^3 \gamma\left(\frac{3}{2}, \frac{M^2}{2\sigma_c^2} \right) - \frac{1}{3}\sqrt{2\pi} a_2 \sigma_c M^2 \operatorname{erf}\left(\frac{M}{\sqrt{2}\sigma_c} \right) \tag{12b}$$

where $\gamma(a, x)$ is the usual notation (*11*) for the incomplete γ-function:

$$\gamma(a, x) \equiv \int_0^x e^{-t} t^{a-1}\, dt \tag{12c}$$

From eq 12b the following conclusions can be drawn: (a) the convolution spectrum has no Gaussian shape, even if the peak in the data spectrum and the functional form of the filter are Gaussian; (b) $R(\tau)$ reaches its maximum value for $\tau = t_{0,s}$; (c) the convolution signal depends upon two adjustable paramters, σ_c and M.

The reduced intensity at the maximum of the convolution signal can be shown to be

$$\frac{R(t_{0,s})}{I_{0,c}} = \sqrt{2\pi} I_{0,s} \frac{\sigma_s \sigma_c}{\sqrt{\sigma_s^2 + \sigma_c^2}} \operatorname{erf}\left(\frac{M\sqrt{\sigma_s^2 + \sigma_c^2}}{\sqrt{2}\sigma_s \sigma_c} \right) - \pi \frac{I_{0,s} \sigma_s \sigma_c}{M} \operatorname{erf}\left(\frac{M}{\sqrt{2}\sigma_s} \right) \operatorname{erf}\left(\frac{M}{\sqrt{2}\sigma_c} \right) + 2\sqrt{2} a_2 \sigma_c^3 \times \gamma\left(\frac{3}{2}, \frac{M^2}{2\sigma_c^2} \right) - \frac{1}{3}\sqrt{2\pi} a_2 \sigma_c M^2 \operatorname{erf}\left(\frac{M}{\sqrt{2}\sigma_c} \right) \tag{13}$$

Thus, the value of $R(t_{0,s})/I_{0,c}$ depends upon M and upon both the $\mathrm{FWHM_s}$ of the original signal and the $\mathrm{FWHM_c}$ of the filter. Here, the choice of $\mathrm{FWHM_c}$ will have some influence upon the intensity enhancement, in contrast to the SWF where $\mathrm{FWHM_s}$ and M are the only parameters that matter. A maximal intensity enhancement of $\sqrt{2\pi}\sigma_s\sigma_c/\sqrt{\sigma_s^2 + \sigma_c^2}$ with respect to the original signal $I_{0,s}$ can be obtained in this case, when the background contribution is neglected ($a_2 = 0$).

Triangular Filter. As introduced already by Biermann (*6*), another possible filter is given by a triangular fold-in function, with also two adjustable parameters, comparable to the Gaussian filter. However, Biermann's filter is not of the zero-area type but it is a discrete filter with an area normalized to 1. It can be understood quite easily that the terms, depending on a_0 and a_1 of the background, in the expression of the convolution signal will not disappear here, as it is for any zero-area filter (Appendix 2).

The triangular filter (TF), as it is constructed here, has only one adjustable parameter, namely its width M (Figure 1c). It can be represented by

$$C(\tau - t) = I_{0,c}\left(1 - \frac{|\tau - t|}{M} \right) - A \tag{14}$$

where

$$A = \frac{1}{2M} \int_{\tau-M}^{\tau+M} I_{0,c}\left(1 - \frac{|\tau - t|}{M} \right) dt = \frac{1}{2} I_{0,c} \tag{15}$$

represents a constant in order to realize a net area of zero. This filter, in its discrete form, is in fact very similar to that described by Biermann (*6*). The constant term A, which equals the area of the filter divided by the number of discrete points (filter window), can be shown to be $I_{0,c}M/(2M + 1)$. After a second parameter $\alpha_B = [I_{0,c}(M + 1) - 1]/2$ is introduced, the filter becomes

$$C(\tau - t) = \frac{2\alpha_B + 1}{2M + 1} - \frac{2\alpha_B + 1}{M(M + 1)}|\tau - t| \tag{16}$$

which is very similar to Biermann's filter.

The reduced convolution signal for TF is given by

$$\frac{R(\tau)}{I_{0,c}} = \frac{2 I_{0,s} \sigma_s^2}{M} \exp\left(-\frac{(\tau - t_{0,s})^2}{2\sigma_s^2} \right) \times \left\{ \exp\left(-\frac{M^2}{2\sigma_s^2} \right) \cosh\left[\frac{(\tau - t_{0,s})M}{\sigma_s^2} \right] - 1 \right\} - \sqrt{\frac{\pi}{2}} \frac{I_{0,s}\sigma_s}{M} (\tau - t_{0,s}) \left[2 \operatorname{erf}\left(\frac{\tau - t_{0,s}}{\sqrt{2}\sigma_s} \right) - \operatorname{erf}\left(\frac{\tau + M - t_{0,s}}{\sqrt{2}\sigma_s} \right) - \operatorname{erf}\left(\frac{\tau - M - t_{0,s}}{\sqrt{2}\sigma_s} \right) \right] + \frac{1}{2}\sqrt{\frac{\pi}{2}} I_{0,s}\sigma_s \left[\operatorname{erf}\left(\frac{\tau + M - t_{0,s}}{\sqrt{2}\sigma_s} \right) - \operatorname{erf}\left(\frac{\tau - M - t_{0,s}}{\sqrt{2}\sigma_s} \right) \right] - \frac{1}{6} a_2 M^3 \tag{17}$$

which shows that the convolution signal $R(\tau)$ is not Gaussian, and that its maximum value is reached for $\tau = t_{0,s}$. The intensity of the reduced convolution signal at the position of the maximum becomes

$$\frac{R(t_{0,s})}{I_{0,c}} = 2\frac{I_{0,s}\sigma_s^2}{M} \left[\exp\left(-\frac{M^2}{2\sigma_s^2} \right) - 1 \right] + \sqrt{\frac{\pi}{2}} I_{0,s}\sigma_s \operatorname{erf}\left(\frac{M}{\sqrt{2}\sigma_s} \right) - \frac{1}{6} a_2 M^3 \tag{18}$$

When the background contribution is neglected ($a_2 = 0$), a maximal intensity enhancement of $\sqrt{\pi/2}\sigma_s$ with respect to the original signal $I_{0,s}$ can be obtained. It is also seen that the second-order background contribution lowers the convolution signal by $^1/_6 a_2 M^3$.

From the foregoing it can be infered that all these zero-area filters have some properties in common. The most important property from the peak detection point of view is that the position of the convolution signal coincides exactly with that

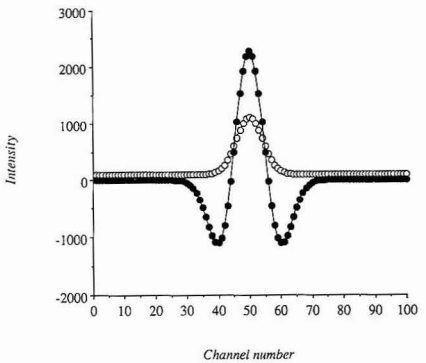

Figure 2. Gaussian profile (O) with I_s = 1000 counts/channel and σ_s = 4.25 channels ($FWHM_s$ = 10 channels) and the corresponding convolution signal (●) obtained with a Gaussian filter with $FWHM_c$ = 10 channels and M = 10 channels.

of the original spectral line. For single lines, there will thus be no need for a peak position correction, at least in the case of a continuous convolution signal.

RESULTS AND DISCUSSION

When a SWF and a TF, as well as a GF, operates upon a single line, the shape of the convolution signal resembles that of a smoothed, inverted pseudo second derivative of the original distribution. The very characteristic shape, with a strong positive central peak and negative side lobes is depicted in Figure 2. In general, the central intensity of the convolution signal is increased, whereas its line width is reduced with respect to the corresponding parameters in the original spectrum. In the present study, convolution spectra are calculated by using eqs 3 and 4b for continuous distributions and discrete data, respectively. For the GF some minor differences in the intensities between the continuous and the discrete convolution spectra can occur, due to round-off errors, but they are never really significant. The original discrete data are obtained with a computer program, developed for the simulation of Voigt profiles (see Appendix 1) according to Armstrong's procedure (*12*). The Gaussian distribution is only a special case of the Voigt profile when the Voigt parameter a equals zero. The convolution spectra for a Gaussian spectral shape are generated by using eqs 8, 12, and 17 for continuous profiles and eq 4b for discrete data. Statistical noise was introduced on the original spectral distributions by using a Gaussian pseudorandom generator, as described by Brent (*14*, *15*).

As there is only one adjustable parameter for the SWF and the TF, i.e. the filter width M, changing M with respect to $FWHM_s$ is the only way to study the effect of the filter on the convolution signal. On the other hand, the GF has two adjustable parameters that can be varied, namely the width M and the full-width at half-maximum of the filter, $FWHM_c$.

Digital Filtering on Single Gaussian Peaks. In order to obtain a general view of their properties and influence on spectral data, the different fold-in functions are first convoluted with single Gaussian lines. Various parameters can be considered now to characterize the resulting convolution signal.

A first parameter is the full-width at half-maximum of the convolution signal ($FWHM_{conv}$), which is defined here as the FWHM of the positive part of the convolution signal (the negative side lobes are neglected). As already mentioned, the line width or $FWHM_{conv}$ is usually reduced with respect to the FWHM of the original signal ($FWHM_s$). This reduction of the line width may result in a resolution enhancement,

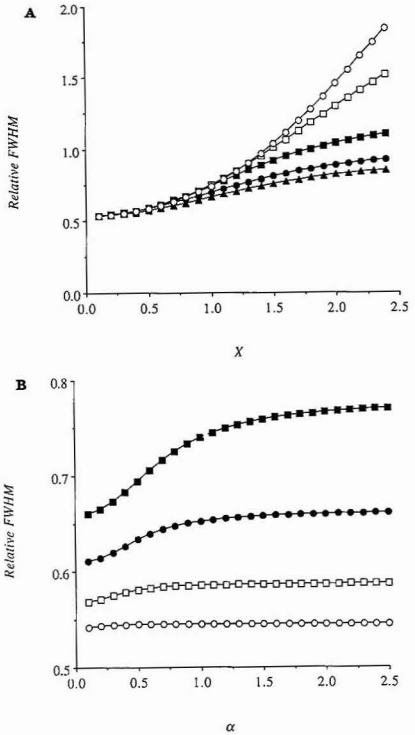

Figure 3. (A) Relative FWHM of the convolution signal ($FWHM_{conv}/FWHM_s$) as a function of X for various filters: SWF (O), TF (□), and GF with various α (α = 1.0 (■), α = 0.5 (●), and α = 0.1 (▲)). (B) Relative FWHM of the convolution signal ($FWHM_{conv}/FWHM_c$) as a function of α for various values of M (of the GF): X = 1.0 (■), X = 0.75 (●), X = 0.50 (□), and X = 0.25 (O).

which will be most important for small values of $FWHM_{conv}$.

As it was mentioned already, the properties of the square-wave and triangular filters depend only upon the value of M. It can be seen from Figure 3a that the relative FWHM ($FWHM_{conv}/FWHM_s$) versus X corresponds to a quadratic relationship. X is defined as

$$X \equiv M/FWHM_s \tag{19}$$

As long as X remains smaller than 1.5, the $FWHM_{conv}$ is also smaller than that of the original signal.

For a Gaussian filter we can look at $FWHM_{conv}$ in two different ways, i.e. as a function of X for various α, defined as

$$\alpha \equiv FWHM_c/FWHM_s \tag{20}$$

or as a function of α for various values of the filter basis M. These relationships are depicted in Figure 3a and b. The smallest values for the relative FWHM can be found with small values for X as well as for α. Since the smallest relative FWHM that can be obtained equals 0.533 channels, the full-width at half-maximum can maximally be reduced by a factor of 1.875. In the limit of zero filter widths, SWF, TF, and GF give the same resolution enhancement.

From Figure 3b it can be seen that the $FWHM_{conv}$ does not increase further, once α reaches a certain value. It can also be seen that a change in α has a lesser effect for small M

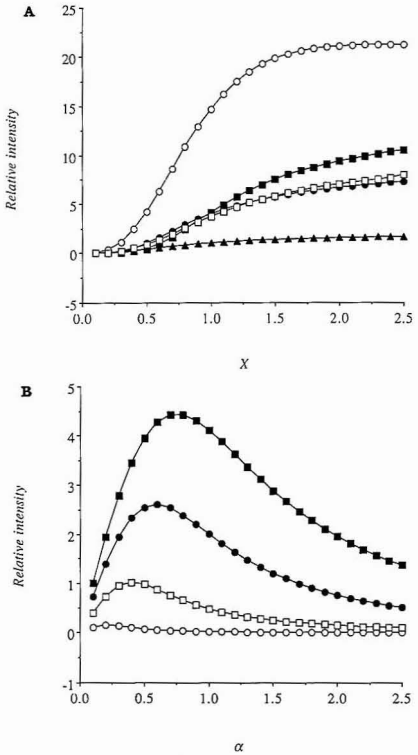

Figure 4. (A) Relative intensity of the convolution signal ($R(t_{0,s})/I_{0,s}$) at the position of the maximum as a function of X for various filters: SWF (○), TF (□), and GF with various α (α = 1.0 (■), α = 0.5 (●), and α = 0.1 (▲)). (B) Relative intensity of the convolution signal ($R(t_{0,s})/I_{0,s}$) at the position of the maximum as a function of α for various values of M (of the GF): X = 1.0 (■), X = 0.75 (●), X = 0.50 (□), and X = 0.25 (○).

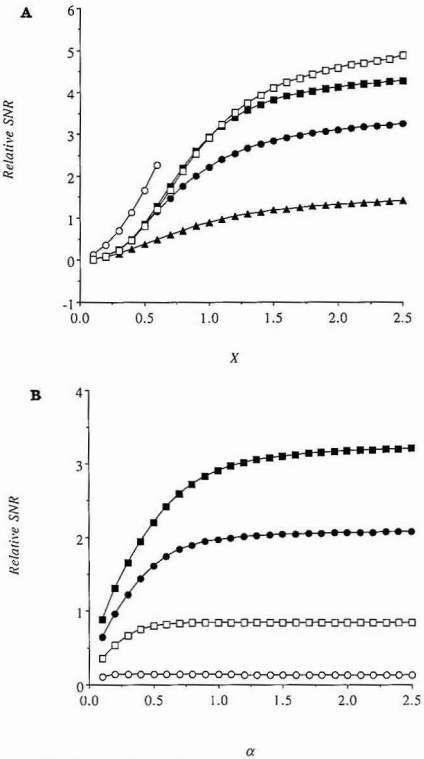

Figure 5. (A) Relative SNR of the convolution signal ($SNR_{conv}/SNR_{original}$) as a function of X for various filters: SWF (○), TF (□), and GF with various α (α = 1.0 (■), α = 0.5 (●), and α = 0.1 (▲)). (B) Relative SNR of the convolution signal ($SNR_{conv}/SNR_{original}$) as a function of α for various values of M (of the GF): X = 1.0 (■), X = 0.75 (●), X = 0.50 (□), and X = 0.25 (○).

values. For high α values, the width M determines the properties of the filter, whereas α is rather important in the case of a broad correlator (high M).

From eqs 8a, 12b, and 17, the position of the maximum in the convolution signal can be shown to be the same as in the original signal. Storing the first summation for discrete data into output channel number M, rather than in the first one, results in an exact coincidence of the maxima in the original and convolution signals. In the discrete SWF case, a typical shift of one channel can be found due to the fact that only an even number of channels can be used for the width (M) of this filter.

The relationship between the relative intensity of the convolution signal at the position of the maximum, $R(t_{0,s})/I_{0,s}$, and the relative width of the filter (X) is represented in Figure 4a. $R(t_{0,s})/I_{0,s}$ increases very fast for SWF with increasing X, compared to the cases of GF and TF. The maximal intensification of the convolution signal with respect to the original distribution is for the different filters as follows: $[R(t_{0,s})/I_{0,s}]_{max,SWF}$ = 21.310, $[R(t_{0,s})/I_{0,s}]_{max,TF}$ = 10.653, and $[R(t_{0,s})/I_{0,s}]_{max,GF}$ = 15.066 for σ_s = 8.5 channels and α = 1.0. The limiting value for the SWF can indeed be found back in Figure 4a, whereas the other values for the TF and GF are only reached for very large values of M (or X).

If $R(t_{0,s})/I_{0,s}$ is calculated as a function of α for various M, a maximum occurs, as can be seen from Figure 4b, indicating an optimal $FWHM_c$ with respect to $FWHM_s$. This optimum corresponds to a β value of 1.25, where β is defined as

$$\beta \equiv M/\mathrm{FWHM_c} \tag{21}$$

Another important parameter is the signal-to-noise ratio (SNR) of the convolution signal at the position of the maximum. The ratio is defined as

$$\mathrm{SNR} \equiv R(t_{0,s})/\sigma(R(t_{0,s})) \tag{22}$$

where $\sigma(R(t_{0,s}))$ is the standard deviation of the filtered signal (convolution signal) at the position of the maximum, which can be calculated via the error propagation rules. The relationship between the relative SNR ($SNR_{conv}/SNR_{original}$) and the filter parameters is depicted in Figure 5a and b. It can be seen that the relative SNR seems to increase until infinity for the SWF and that a limiting value exists for large X values in the case of the TF and for large X and α values in the case of the GF. From Figure 5b it appears that a change in α has a minor effect on the relative SNR for small M values.

Thus, the relative SNR clearly increases with increasing filter width, for all filter types. Soon, an important improvement can be found, indicating that a smoothing effect ($SNR_{conv} > SNR_{original}$) already starts for relatively small filters (small values of X or M). The values of X for which an improvement is achieved, are listed in Table I. It is also

Table I. Minimum Values of X and/or α for Which an Improvement of SNR Can Be Achieved

filter	α	X
SWF		0.40
GF	1.0	0.60
	0.5	0.60
	0.3	0.75
	0.2	1.00
	0.1	1.20
TF		0.60

clearly seen that high X values are required to obtain any improvement when using small α values.

Equations 8a, 12b, and 17 all show a dependence of the intensity of the convolution signal on the quadratic background term a_2, the width, and FWHM of the filter. The relative FWHM ($FWHM_{conv}/FWHM_s$), the relative intensity at the position of the maximum ($R(t_{0,s})/I_{0,s}$), and the relative SNR (SNR_{conv}/SNR_s) of the convolution signal are shown in Figure 6 for various percentages of a quadratic background contribution. The percentage of this quadratic background is calculated as the fraction of the background at the position of the original maximum. The values of the relative FWHM, intensity, and SNR without the presence of background have been taken as a reference.

As can be seen very clearly from Figure 6a and b, the SWF and TF convolution signals are influenced in a very similar way by the varying amount of quadratic background. Concerning FWHM, application of the GF results in rather broad peaks in the convolution signal, although a 10% background contribution does not cause more than ca. 2% broadening of the line. $R(t_{0,s})/I_{0,s}$, on the contrary, shows an intensification of the convolution signal as the quadratic background increases, when the GF is used. These two tendencies will compensate each other, and peak recognition will not be hampered. Furthermore, it can be seen that the relative SNR is less affected by the quadratic background contribution in the case of the GF, which makes it preferable for complex spectral data where a quadratic background becomes more and more probable.

Digital Filtering on Doublets of Gaussian Profiles. Resolution is a well-known concept in spectroscopy, as well as in chromatography, where the following definition is conventionally used

$$R \equiv \Delta x/2(\sigma_1 + \sigma_2) \tag{23}$$

Δx stands for the distance between the maxima of the peaks, σ_1 and σ_2 are the Gaussian standard deviations of the distributions. The minimum R value for quantitative separation of two peaks is considered to be 1.0, which corresponds to a Δx of 1.699 times the FWHM (for two identical lines). Usually, two lines are considered spectroscopically resolved as soon as their center separation Δx equals or exceeds 1.0 FWHM ($R = 0.589$). We could try now to calculate R for the convolution spectrum resulting from such an original signal and compare it to 0.589 in order to obtain the resolution enhancement (RE) after filtering. However, this procedure fails because there is a problem in finding the correct FWHM values of the lines in the composite convolution spectrum. Biermann (6) proposed therefore a procedure in which he calculated the relative indent

$$RI \equiv (I_{max} - I_{min})/I_{max} \tag{24}$$

of two identical peaks separated by one FWHM and tried to find the distance to which the convolution peaks could be pushed together in order to obtain the same relative indent. Here, I_{max} denotes the intensity of the apparent maxima and

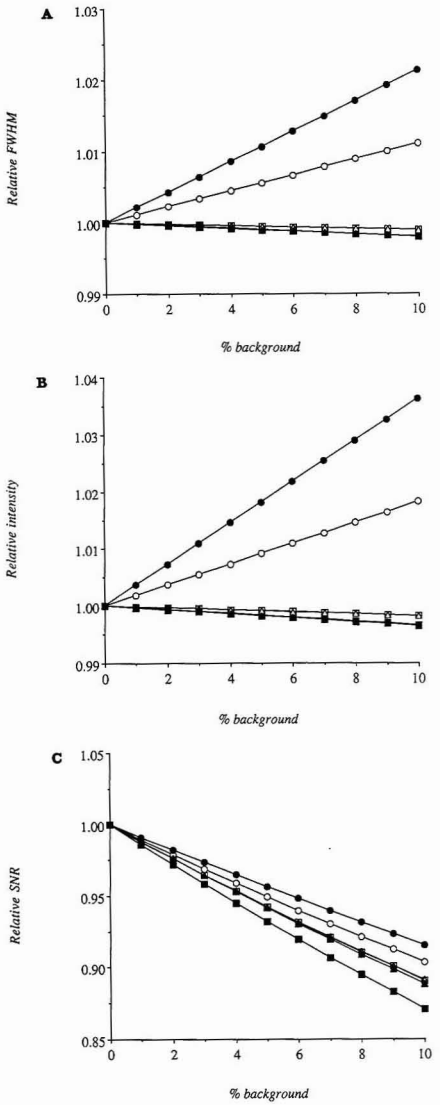

Figure 6. (A) Relative FWHM of the convolution signal ($FWHM_{conv}/FWHM_s$) as a function of the percentage of additional second-order background contributions for various filters and filter widths: SWF (X = 1.0 (■), X = 0.5 (□)), TF (X = 1.0 (▲), X = 0.5 (△)), and GF (X = 1.0 (●), X = 0.5 (○)). (B) Relative intensity of the convolution signal ($R(t_{0,s})/I_{0,s}$) at the position of the maximum as a function of the percentage of additional second-order background contributions for various filters and filter widths: SWF (X = 1.0 (■), X = 0.5 (□)), TF (X = 1.0 (▲), X = 0.5 (△)), and GF (X = 1.0 (●), X = 0.5 (○)). (C) Relative SNR of the convolution signal ($SNR_{conv}/SNR_{original}$) as a function of the percentage of additional second-order background contributions for various filters and filter widths: SWF (X = 1.0 (■), X = 0.5 (□)), TF (X = 1.0 (▲), X = 0.5 (△)), and GF (X = 1.0 (●), X = 0.5 (○)).

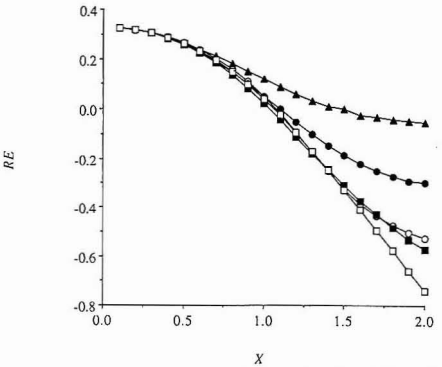

Figure 7. Resolution enhancement (RE) as a function of X, obtained with various zero-area filters: SWF (○), TF (□), and GF with various α (α = 1.5 (■), α = 1.0 (●), and α = 0.5 (▲)).

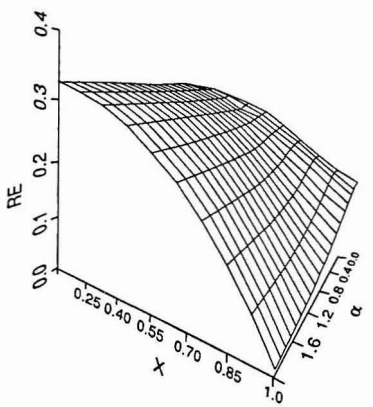

Figure 8. Resolution enhancement (RE) as a function of X and α, in a tridimensional representation, for the Gaussian filter.

I_{min} the intensity of the intermediate minimum. The RE is then defined as

$$RE \equiv 1 - P \tag{25}$$

where P denotes the new distance in the convolution signal in units of full-width at half-maximum.

It can be seen from Figure 7 that the RE calculated in this way decreases with increasing width X of the filter. This tendency is also found for RE as a function of α. Unlike Biermann's findings, there is no significant maximal RE corresponding to an optimal set of filter parameters. This probably results from the zero area of the filters which are used here. As soon as X becomes smaller than 0.5, RE becomes very similar for all filters. The similarity between the RE of the SWF and GF with α = 1.5 is very clear. Once again it can be concluded that α becomes more important as a filter property (or parameter) for large M values, whereas M is the limiting factor for RE when its value becomes small ($X < 0.25$).

For the GF a three-dimensional analysis (Figure 8) was made, using the DISPLA subroutines (running on the Cyber 930 computer, which is used in this study). The RE as a function of X and α does not possess a maximum as was already seen above. It is found that X values smaller than approximately 0.3 will never give a further resolution enhancement; it will only result in a worse SNR.

Table II. Ratio of the Intensities of the Negative Side Lobes (RSL) in the Convolution Signal as a Function of M for Various Doublets[a]

X	I	II	III	IV
1.00	1.3879	1.1143	1.0000	1.0430
0.75	1.5253	1.1656	1.0000	1.0974
0.50	1.6361	1.2311	1.0000	1.1298
0.45	1.6533	1.2415	1.0000	1.1312
0.40	1.6761	1.2519	1.0000	1.1383
0.25	1.7000	1.2740	1.0000	1.1507

[a] The four doublets of Gaussian profiles are characterized as follows: (I) $I_{0,s,1} = 2I_{0,s,2}$, $\sigma_{s,1} = \sigma_{s,2} = 8.5$ channels, and $t_{0,s,2} - t_{0,s,1} = 0.7\text{FWHM}_s = 14.0$ channels; (II) $I_{0,s,1} = 2I_{0,s,2}$, $\sigma_{s,1} = \sigma_{s,2} = 8.5$ channels, and $t_{0,s,2} - t_{0,s,1} = 0.5\text{FWHM}_s = 10.0$ channels; (III) $I_{0,s,1} = 2I_{0,s,2}$, $\sigma_{s,1} = \sigma_{s,2} = 8.5$ channels, and $t_{0,s,2} - t_{0,s,1} = 0.2\text{FWHM}_s = 4.0$ channels; (IV) $I_{0,s,1} = 10I_{0,s,2}$, $\sigma_{s,1} = \sigma_{s,2} = 8.5$ channels, and $t_{0,s,2} - t_{0,s,1} = 0.5\text{FWHM}_s = 10.0$ channels. A GF has been used with β = 1.5.

Digital Filtering on More Complex Spectral Data—Detection of Interference. Its good behavior in the presence of statistical noise and background, together with the resolution enhancement obtained by convoluting the original signal with a zero-area filter, makes digital filtering a useful tool for peak detection. However, if the "chromatographic" resolution becomes too small, two peaks cannot be separated, not even using the smallest possible filter. Two identical peaks separated only by 0.7 times their FWHM, are no longer detected as two individual lines in the original spectrum, and the apparent position is situated exactly between the correct positions. A Gaussian filter with X = 0.6 is not able to separate those peaks and will detect a single line on exactly the same position as the original signal. As soon as X equals 0.5 or less, two peaks appear in the convolution spectrum, and as X decreases, the positions approximate more and more the true ones. Finally, there is a deviation of only 1 channel. If the distance between the two peaks becomes still smaller (i.e. 0.6 FWHM, so that R = 0.353) the procedure described here cannot separate them anymore.

However, for two peaks appearing as a single envelope, the ratio of the intensities of the negative side lobes (RSL) can provide some additional information. Because of the symmetry of the filter, symmetric data should result in a symmetric convolution signal. This means that the RSL should equal unity. A different value for the RSL, indicates some kind of asymmetry, which will be due to an undetected and/or undetectable interference in the case of symmetrical data. The RSL will be defined as the ratio of the minimum at the left side to that at the right side, meaning that a RSL > 1.0 indicates an "interfering" peak at the right side of the detected peak, and vice versa. Indeed, the nondetected maximum of the interfering peak causes an enhancement of the intensity of the negative side lobe on the side of its appearance. A typical case where this technique fails is the presence of two perfectly identical peaks, where the RSL always equals unity. Problems can also arise in the presence of high levels of statistical noise, because in that case deviation from unity can be due to an asymmetrical peak or noise. For various interfered lines, the RSL has been determined for some X values (Gaussian filter width; β = 1.5) and the results are summarized in Table II. It can be seen that for two Gaussians, with an intensity ratio of $^1/_2$ and separated by more than 0.5 FWHM_s, the RSL is definitely different from unity. This effect is even more pronounced for small filter widths. When the second peak is 10 times less intense than the first one, it is also possible to detect the interfering peak by means of the RSL. Situations where two peaks are separated by no more than 0.2 FWHM_s with an intensity ratio of $^1/_2$, the RSL always equals unity, even for very small X values.

Table III. Digital Filtering on Complex Spectral Data[a]

positions p and intensities I in the simulated multiplets		peaks found in the simulated spectrum[b]	peaks found in the convolution spectrum	second derivative of Zimmermann
no.	$p_{1s}/p_{2s}/\ldots/p_{ns}$ $I_{1s}/I_{2s}/\ldots/I_{ns}$	$p_{1o}/p_{2o}/\ldots/p_{no}$	$p_{1c}/p_{2c}/\ldots/p_{nc}$	no. of peaks
1	40/48/56 1/1/0.50		40/48/56	
2	40/48/56 4/0.50/1		40/−/56	2[c]
3	40/48/56 1/0.50/0.50		40/−/56	2
4	40/48/56 0.50/1/0.50		39/48/−	3
5	40/50/60 1/1/1	40/50/60	39/50/61	
6	40/48/56 1/1/1	−/49/−	40/48/56	
7	40/46/52 1/1/1	−/46/−	41/−/50	2
8	40/48/58 1/0.75/1	42/−/57	40/−/58	3
9	40/48/58 1/0.50/1	41/−/57	40/−/58	3
10	40/48/58 1/0.25/1	40/−/57	40/−/58	2[c]
11	40/48/58 1/0.10/1	40/−/58	40/−/58	2[c]
12	40/48/58 0.75/0.75/1	−/45/57	40/46/58	
13	40/48/58 0.50/0.50/1	−/48/57	40/−/58	3
14	40/48/58 0.25/0.25/1	−/−/57	39/−/58	3
15	30/40/60/80 0.50/0.50/1/1	31/39/60/80	29/40/60/80	
16	40/50/60/80 0.50/0.50/1/1	41/−/60/80	39/49/60/80	
17	45/55/60/80 0.50/0.50/1/1	46/−/58/80	44/−/59/80	3[c]
18	55/60/65/80 0.50/1/0.50/1	−/60/−/80	−/60/−/80	3 (?)[c]
19	60/65/75/80 1/0.50/0.50/1	61/−/−/79	61/−/−/80	3 (?)

[a] $FWHM_s$ = 10 channels and GF with $M = FWHM_c$ = 3 channels. A noise level of 3% has been introduced on the original data. [b] Using a peak search routine based upon the algebraic inequality of the sums of three channel contents. [c] An abnormality (indicated by "?") can be found in the second derivative of the Zimmermann plot, without being recognized as an interference; however, a least-squares analysis indicated indeed a wrong number of peaks in the model function.

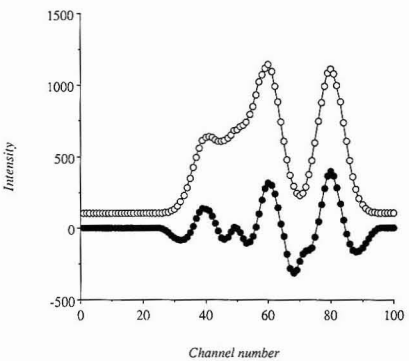

Figure 9. Original composite spectrum (O) (no. 16 in Table III) and the corresponding convolution signal (●).

Table III gives an overview of the parameters of some simulated complex spectra. Columns two and three represent the exact positioins and the intensities of the various profiles of the multiplets. All peaks have the same $FWHM_s$ of 10 channels, whereas the noise level equals 3%. On the other hand, the fourth column resumes the peak positions as they are found in the composed signal by a peak-search routine based upon the algebraic inequality of the sums of three channel contents. After the application of a Gaussian filter (GF) with $M = FWHM_c$ = 3 channels (a small filter width was used in order to obtain maximal RE), peaks are found in the convolution signal at the positions summarized in the fifth column. It can be seen from some of these examples that digital filtering can often separate peaks originally appearing as a single envelope. This is illustrated in Figure 9, representing the complex spectrum 16 in Table III.

The presence of more than one peak in the convolution spectrum unfortunately makes the use of the RSL impossible as an indication for interference. Indeed, a RSL different from unity can be caused by an undetected interference and also by the influence of two neighboring peaks on each other. This

Table IV. Effect of Noise Levels on the Ratio of the Intensities of the Negative Side Lobes in the Convolution Spectrum and on the Slope in Zimmermann's Plot for a Single Gaussian Profile[a]

noise level, %	RSL	global slope	corr coeff global slope	max dev from global slope, %
0	1.000	0.027 73	1.000	0.00
1	1.001	0.027 78	0.999	0.50
3	1.004	0.027 83	0.997	1.65
5	1.007	0.027 89	0.993	2.75
7	1.009	0.027 93	0.986	3.90
10	1.016	0.028 01	0.972	5.57

[a] The Gaussian profile is characterized by σ_s = 8.5 channels. A Gaussian filter (GF) with $X = 1.0$ and $\beta = 1.5$ has been used. The last column gives the maximal deviation between the global slope of Zimmermann's plot and any value of the slope, before and/or after the position of the maximum, using a window of five channels.

puts some limits on the use of digital filtering in the case of complex spectral data. Thus, a supplementary technique for the detection of hidden peaks—even in the convolution signal—would be very useful.

In a previous paper (*15*) we reported already about Zimmermann's method (*16*) for the linearization of the central Gaussian part of spectral lines, and its possibilities to detect interferences. In a Zimmermann graph the quantity

$$Q(t) = \ln \frac{S(t-1)}{S(t+1)} \tag{26}$$

is plotted versus t, where $S(t)$ denotes the background corrected intensity at channel number t. The interference then can be detected by means of a more or less noticeable "kink" in the $Q(t)$ vs t plot. This "kink" can be made visible in most cases by sliding a small window (3 or 5 channels) over the plot and by calculating each time the slope, resulting in a change of the slope at the inflection point of the Zimmermann plot. However, the use of this small window is rather sensible to statistical fluctuations, as can be seen from Table IV, which summarizes the effect of various noise levels on the RSL and

Table V. RSL and Zimmermann Slopes for Various Doublets of Gaussian Profiles[a]

I_1/I_2	$\Delta t/\mathrm{FWHM_s}$	$t_{0,\mathrm{conv}}$	RSL	slope I	slope II	slope III
1/1	0.7	57	1.000	0.021 56	0.009 15	0.021 07
	0.6	56	1.000	0.021 09	0.014 03	0.021 10
	0.5	55	1.000	0.021 57	0.018 18	0.021 57
	0.4	54	1.000	0.023 14	0.021 60	0.023 15
	0.3	53	1.000	0.024 71	0.024 27	0.024 71
	0.2	52	1.000	0.026 28	0.026 19	0.026 28
	0.1	51	1.000	0.027 35	0.027 34	0.027 35
2/1	0.7	52	1.388	0.025 35	0.017 59	0.012 12
	0.6	53	1.222	0.024 84	0.017 85	0.015 30
	0.5	53	1.114	0.024 66	0.020 09	0.018 58
	0.4	50	1.001	0.027 71	0.027 69	0.027 64
	0.3	50	1.016	0.027 25	0.026 79	0.026 04
	0.2	50	1.000	0.027 72	0.027 72	0.027 72
	0.1	50	1.003	0.027 42	0.027 39	0.027 36
10/1	0.7	50	1.168	0.027 38	0.025 84	0.017 97
	0.6	50	1.113	0.027 27	0.025 80	0.020 15
	0.5	51	1.068	0.027 18	0.025 73	0.022 37
	0.4	51	1.036	0.027 17	0.026 18	0.024 37
	0.3	50	1.016	0.027 25	0.026 79	0.025 94
	0.2	50	1.002	0.027 42	0.027 26	0.027 04
	0.1	50	0.999	0.027 63	0.027 60	0.027 57

[a] $\mathrm{FWHM_s}$ = 20 channels; centroid of the first Gaussian peak equals 50. No noise has been introduced. I_1/I_2 is the ratio of the intensities of both lines; $\Delta t/\mathrm{FWHM_s}$ is the distance between the individual lines in terms of $\mathrm{FWHM_s}$, and $t_{0,\mathrm{conv}}$, the position of the maximum in the convolution spectrum. The slopes in Zimmermann's plot are calculated as follows: the first five channels of the positive part (slope I), five channels around the position of the maximum (slope II), and the last five channels of the positive part in the convolution signal (slope III).

the slope of several parts of the Zimmermann plot, for a single Gaussian line. The global slope was calculated for that part of the Zimmermann plot corresponding to the positive part of the convolution signal. It can be seen that a noise level of 5% already causes a maximal deviation of 2.75%, if the slopes before and after the maximum are compared to the value of the global one. An increasing number of channels for the Zimmermann window will of course resist better to noise, but at the same time the change of the slope will be less pronounced.

The results for various doublets of Gaussian profiles have been summarized in Table V for several parameters (RSL, Zimmermann slopes, correlation coefficients, ...). The ratio of the intensities of both lines of the doublet are given in the first column, whereas in the second column $\Delta t/\mathrm{FWHM_s}$ represents the distance between the individual lines in terms of the FWHM of the signal. $\mathrm{FWHM_s}$ was set equal to 20 channels for all lines, and the position of the first peak equals 50. $t_{0,\mathrm{conv}}$ represents the position of the maximum in the convolution spectrum. The RSL was calculated as defined before. The slopes of the Zimmermann plot were calculated by using a window of 5 channels: part I is taken as the first 5 channels of the positive part of the convolution signal, part II is taken as 5 channels around the position of the maximum in the convolution spectrum, and part III is the last 5 channels of the positive part of the convolution signal. A rather broad filter (X = 1.0) was used in order to obtain smooth convolution spectra. Moreover, the peaks could not be separated unless extremely small filter widths were used (X = 0.3) which has to be avoided—as already indicated—in order to obtain a good SNR. A composite of two identidal peaks cannot be detected in practice by means of the RSL of the convolution signal since this value always equals unity. As long as the peaks are separated at least by 0.3 FWHM, a significant downward kink can be found in the Zimmermann plot. For two peaks with an intensity ratio of 10/1, the RSL can give an indication for interference until a separation of 0.4 FWHM is reached. The Zimmermann slope even decreases noticeably for a separation of 0.2 FWHM. It should be noted that no noise was introduced to the simulated profiles, which means that the same results can never be obtained for real spectral data. However, taking into account the overall noise level of a registered spectrum, the RSL and Zimmermann's method can often give a good indication for possible interference.

Because of the sensitivity of the slope of the Zimmermann plot to the noise level, the Zimmermann plot was smoothed (three points) and the first and second derivatives were calculated. Then, a kink in the Zimmermann plot results in a minimum in the first derivative and a sequence of a minimum and a maximum in the second derivative. As can be seen from Table III (column six), the analysis of these derivatives sometimes results in supplementary information about the number of peaks present in the original spectrum. The implementation of this technique into an automated routine will be hampered by the fact that an "abnormality" in the first or second derivative can often be recognized by an experienced operator, but not by an algebraic inequality. The "?" for the last two quadruplets in Table III indicates such a questionable indication of additional lines.

Some spectra showed such a more or less pronounced abnormality in the second derivative without being recognized as an interference by an automated routine. Nevertheless, a least-squares fit was made for some of them (indicated by footnote c in Table III), using the information provided by the automated routine. However, examination of a model parameter and the residuals of the fit indicated clearly a wrong number of peaks in the model function. If peaks were added to the model, better residuals were found and the χ^2_ν of the fit was reduced significantly.

Digital Filtering on Voigt Profiles. Although several kinds of spectral data can be represented quite correctly by a simple Gaussian distribution, the Gaussian filter has also been applied to various Voigt profiles in order to verify the previous conclusions. These convolution spectra have been calculated by using the discrete summation given by eq 4b, since the analytical expressions become too complex to derive. Some results are summarized in Table VI. The Gaussian filter has a width M = 10 channels, and β ($M/\mathrm{FWHM_c}$) equals 1.5. The original signal is characterized by $I_{0,s}$ = 1000 counts/channel, $t_{0,s}$ = 50, and σ_s = 4.25 channels. Although the

Table VI. Digital Filtering on Voigt Profiles with Various a[a]

Voigt parameter a	position min left	position min right	$R(t_{0,s})/I_{0,s}$	$\mathrm{FWHM_{conv}}$ channels	slope I	slope II	slope III
0.0	40	60	2.356	7.238	0.110 90	0.110 90	0.110 90
0.2	39	61	2.110	7.642	0.077 72	0.088 37	0.077 72
0.4	39	61	1.876	8.076	0.059 01	0.071 30	0.059 01
0.6	38	62	1.661	8.508	0.047 02	0.058 24	0.047 02
0.8	38	62	1.468	8.962	0.034 01	0.048 14	0.034 01

[a] The intensity of the original signal equals 1000 counts/channel, the Gaussian $\mathrm{FWHM_s}$ = 10 channels, and the position $t_{0,s}$ = 50. The slopes in Zimmermann's plots are calculated by using a window of five channels, before the position of the maximum (part I), around the maximum (part II), and after the maximum (part III).

increasing Voigt parameter a does not influence the position of the convolution signal with respect to the original position, the positions of the minima of the negative side lobes are displaced, indicating a broadening compared to a pure Gaussian peak ($a = 0.0$). The positive part of the convolution signal also increases as does $FWHM_{conv}$ with increasing a. Nevertheless, $FWHM_{conv}$ still remains smaller than the original $FWHM_s$ of 10 channels. $R(t_{0,s})/I_{0,s}$ decreases with increasing a but remains enhanced with respect to the original intensity by more than 40%. As a result, it can be expected that an increasing Voigt parameter will cause a less deconvoluted spectrum, so that strongly interfered lines will not be separated in the convolution signal, in contrast to the pure Gaussian situation.

Voigt profiles, as already mentioned, differ from pure Gaussian lines especially in the wings, which will also have some influence on the Zimmermann plot. Sliding a small window over the Zimmermann plot shows now an "upward kink" in the slope, corresponding to the broadening effect in the wings of the profile. Some results are shown in Table VI. The "upward kink" means that for single lines a proper distinction can be made between an interfering line and a Voigt profile by using the Zimmermann plot.

CONCLUSIONS

The performance of zero-area square-wave (SWF), Gaussian (GF), and triangular (TF) filters is compared when applied to single Gaussian lines, multiplets of Gaussian profiles, and Voigt profiles. Analytical expressions are given for the convolution of a Gaussian profile with each of these filters. It is proved that the linear background component of a signal is completely filtered out by an even zero-area filter as opposed to higher order components. The parameters, studied in the convolution spectrum, are full-width at half-maximum, intensity at the position of the maximum, signal-to-noise ratio, second-order background contribution, and resolution enhancement as a function of some typical filter parameters.

It is shown that digital filtering—as it is described here—can produce two totally different effects on the original data. First, there is a possible resolution enhancement which makes it particularly useful in peak detection routines. Second, as an opponent property, a smoothing effect can be created by choosing broad filters, which can be helpful in the treatment of rather noisy spectral data.

In practice, only discrete calculations of the convolution spectra can be used, due to the fact that only discrete data points are experimentally available for an "unknown" profile. For the SWF and TF there is only one adjustable parameter, namely the width M; for SWF only an even number of channels for the width M can be used. An advantage of the GF over the SWF and TF is the presence of two adjustable filter parameters. If a certain resolution enhancement (RE) has to be realized, both filter parameters should be considered. In the case of GF, a relatively large M value can be combined with a rather small α in order to obtain the desired RE level, while the large M can still produce a reasonably good SNR. The lack of a second adjustable parameter forces M to be very small when the SWF or TF is used, resulting in the desired RE but also in the loss of any smoothing effect.

It is shown that in the case of multiplets, composed of strongly overlapping lines, digital filtering fails as a peak detection method; however, some supplementary information can be obtained by means of the second derivative of the Zimmermann plot. It is not always possible to ensure the presence of a missing interfering line, but an indication about interference can often be found. From our study on Voigt profiles it appears that an increasing damping constant will cause in all cases a certain loss of information compared to pure Gaussian profiles.

Thus, the final choice of a digital filter can be based on personal preferences and/or on the problem to be handled. The SWF and TF as well as GF will do well, while the SWF is certainly a good choice when simple algorithms and minimal computing time are requested. In our opinion, the GF will give some more flexibility to fully automated routines and programs.

GLOSSARY

A	Constant term to obtain a zero-area for the Gaussian filter (GF) and triangular filter (TF)
a	Voigt parameter
$B(t)$	Background intensity at position t
$C(\tau - t)$	Filter function
$D(t)$	Spectral line intensity at position t, including background $B(t)$
$FWHM_c$	Full-width at half-maximum of the filter
$FWHM_{conv}$	Full-width at half-maximum of the convolution signal
$FWHM_s$	Full-width at half-maximum of the original signal
$I_{0,c}$	Central intensity of the Gaussian filter (GF)
$I_{0,s}$	Maximal intensity of the original signal (Gaussian profile)
M	Filter width
$Q(t)$	Zimmermann's function
R	Resolution (chromatographical definition)
$R(\tau)$	Convolution signal at position τ
$\mathcal{R}(\tau)$	Cross-correlation signal at position τ
RE	Resolution enhancement
RI	Relative indent
RSL	Ratio of the intensities of the negative side lobes of the convolution signal
$S(t)$	Net signal intensity at position t
SNR	Signal-to-noise ratio
$t_{0,s}$	Position of the maximum of the Gaussian signal profile
$t_{0,conv}$	Position of the maximum in the convolution spectrum
t	Channel number
X	$M/FWHM_s$
Y	$X\sqrt{(\ln 2)}$
GF	Zero-area Gaussian filter
SWF	Zero-area square-wave filter
TF	Zero-area triangular filter
α	$FWHM_c/FWHM_s$
β	$M/FWHM_c$
σ_c	Standard deviation of the Gaussian filter (GF)
σ_s	Standard deviation of the Gaussian signal profile

APPENDIX 1

The Voigt profile results from the superposition of an independent Lorentz and Gaussian (Doppler) line broadening. For an experimentally observable spectral line, the Gaussian profile is expressed as the convolution of the Doppler and instrumental profiles.

The Voigt profile is given by

$$V(x, a) = \frac{1}{\alpha_G}\sqrt{\frac{\ln 2}{\pi}}K(x, a) \qquad \text{(A1-1)}$$

where $K(x, a)$, the so-called Voigt function, is given by

$$K(x, a) \equiv \frac{a}{\pi}\int_{-\infty}^{+\infty}\frac{\exp(-u^2)}{a^2 + (x - u)^2}\,du \qquad \text{(A1-2)}$$

In eqs A1-1 and A1-2 the following symbols are introduced:

$$x = \frac{t - t_0}{\alpha_G}2\sqrt{\ln 2} \qquad \text{(A1-3)}$$

$$a = \frac{\alpha_L}{\alpha_G}\sqrt{\ln 2} \qquad \text{(A1-4)}$$

where α_L and α_G are the full-widths at half-maximum of the

Lorentzian and the Gaussian line profiles, respectively, t is the wavelength, and t_0 represents the wavelength at the center of the Voigt line profile. The quantity a is usually called the Voigt parameter or damping constant.

It can be shown that when $a = 0$, the Voigt profile is reduced to a Gaussian one:

$$\lim_{a \to 0} K(x, a) = e^{-x^2} \tag{A1-5}$$

α_G can be obtained from the quadratic summation of the Doppler width α_D and the instrumental spectral bandwidth α_{instr}:

$$\alpha_G^2 = \alpha_D^2 + \alpha_{instr}^2 \tag{A1-6}$$

where α_D is computed from the wavelength t_0, temperature T, and atomic mass M_A (c is the velocity of light).

$$\alpha_D = \frac{t_0}{c}\sqrt{\frac{8\,RT \ln 2}{M_A}} \tag{A1-7}$$

If the parameters are known, the Voigt profile can be composed by computing

$$I(t - t_0) = I_0\,(K(x, a)/K(0, a)) \tag{A1-8}$$

where $I(t - t_0)$ is the intensity at any distance from the peak position t_0 and I_0 is the intensity at t_0. The Voigt function has been tabulated by a large number of authors (see for instance refs 13, 17, and 18) and also a number of numerical procedures (*19*) and computer programs have been published (*12, 20*). The FORTRAN routine given by Armstrong (*12*) is used in our program for the simulation of discrete spectral data.

APPENDIX 2

Theorem. For an even zero-area filter $C(t)$, the constant (a_0) and linear ($a_1 t$) terms in the background distribution of the signal do not contribute to the convolution spectrum $R(\tau)$ as opposed to the higher order terms ($a_n t^n$, $n \geq 2$).

Proof. We start with the general expression for the convolution spectrum

$$R(\tau) = \int_{\tau-M}^{\tau+M} C(\tau - t)[S(t) + a_0 + a_1 t + a_2 t^2 + a_3 t^3 + \ldots]\,dt = \int_{\tau-M}^{\tau+M} C(\tau - t)S(t)\,dt + a_0\int_{\tau-M}^{\tau+M} C(\tau - t)\,dt + a_1\int_{\tau-M}^{\tau+M} tC(\tau - t)\,dt + a_2\int_{\tau-M}^{\tau+M} t^2C(\tau - t)\,dt + a_3\int_{\tau-M}^{\tau+M} t^3C(\tau - t)\,dt + \ldots \tag{A2-1}$$

Since, by assumption, $C(\tau - t)$ is an even zero-area filter, eqs A2-2 and A2-3 hold:

$$C(\tau - t) = C[-(\tau - t)] \tag{A2-2}$$

$$\int_{\tau-M}^{\tau+M} C(\tau - t)\,dt = \int_{-M}^{M} C(y)\,dy = 0 \tag{A2-3}$$

The third integral in eq A2-1 can be transformed in the following way:

$$\int_{\tau-M}^{\tau+M} tC(\tau - t)\,dt = \int_{-M}^{M} (\tau - y)C(y)\,dy = \tau\int_{-M}^{M} C(y)\,dy - \int_{-M}^{M} yC(y)\,dy = -\int_{-M}^{M} yC(y)\,dy = 0 \tag{A2-4}$$

The last integral in eq A2-4 equals zero since $yC(y)$ is an uneven function in y. This shows that the linear part of the background $a_0 + a_1 t$ does not contribute to the convolution spectrum. This is not the case for the higher order terms as can be easilty shown for $a_2 t^2$:

$$\int_{\tau-M}^{\tau+M} t^2C(\tau - t)\,dt = \int_{-M}^{M} (\tau - y)^2C(y)\,dy = \int_{-M}^{M} y^2C(y)\,dy - 2\tau\int_{-M}^{M} yC(y)\,dy + \tau^2\int_{-M}^{M} C(y)\,dy = \int_{-M}^{M} y^2C(y)\,dy \tag{A2-5}$$

The last integral is different from zero since $y^2C(y)$ is an even function in y. With an analogous reasoning it is easily verified that all higher order terms ($a_n t^n$, $n = 2, 3, 4, \ldots$) do contribute to $R(\tau)$, which completes the proof of the theorem.

LITERATURE CITED

(1) Horlick, G. *Anal. Chem.* **1973**, *45*, 319.
(2) Black, W. *Nucl. Instrum. Methods* **1969**, *71*, 317.
(3) Robertson, A. *Nucl. Instrum. Methods* **1972**, *100*, 317.
(4) Taylor, P.; Schutyser, P. *Spectrochim. Acta* **1986**, *41B*, 81.
(5) Op de Beeck, J. *At. Energy Rev.* **1975**, *13* (4), 743.
(6) Biermann, G. *Anal. Chem.* **1986**, *58*, 536.
(7) See for instance: Bracewell, R. N. *The Fourier Transform and Its Applications*; McGraw-Hill: New York, 1978. Champeney, D. C. *Fourier Transforms and Their Physical Applications*; Academic Press: New York, 1973. Brigham, E. O. *The Fast Fourier Transform and Its Applications*; Prentice-Hall: Englewood Cliffs, NJ, 1988.
(8) Human, H.; Scott, R. *Spectrochim. Acta* **1976**, *31B*, 459.
(9) Kawagushi, H.; Oshio, Y.; Mizuike, M. *Spectrochim. Acta* **1982**, *37B*, 809.
(10) Connelly, A.; Black, W. *Nucl. Instrum. Methods* **1970**, *82*, 141.
(11) Abramowitz, M., Stegun, I., Eds. *Handbook of Mathematical Functions*; National Bureau of Standards: Washington, DC, June 1964.
(12) Armstrong, B. *J. Quantum Spectrosc. Radiat. Transfer* **1967**, *7*, 61.
(13) Hummer, D. G. *Mem. R. Astron. Soc.* **1965**, *70*, 1.
(14) Brent, R. *Commun. Assoc. Comput. Mach.* **1974**, *17*, 704.
(15) François, J.-P.; Janssens, F. *Spectrochim. Acta* **1990**, *45B*, 177.
(16) Zimmermann, W. *Rev. Sci. Instrum.* **1961**, *32*, 1063.
(17) Posener, D. *Aust. J. Phys.* **1959**, *12*, 184.
(18) Young, C. *Tables for Calculating the Voigt Profile*; University of Michigan: ORA-05863, 1965.
(19) Whiting, E. *J. Quantum. Spectrosc. Radiat. Transfer* **1968**, *8*, 1379.
(20) Drayson, S. *J. Quantum Spectrosc. Radiat. Transfer* **1976**, *16*, 611.

RECEIVED for review July 31, 1990. Accepted October 29, 1990.

Luminescence Quenching Mechanism for Microheterogeneous Systems

E. R. Carraway[1] and J. N. Demas*

Chemistry Department, University of Virginia, Charlottesville, Virginia 22901

B. A. DeGraff*

Chemistry Department, James Madison University, Harrisonburg, Virginia 22807

Determining quenching mechanisms for luminescent species adsorbed or bound to a variety of heterogeneous systems (e.g., silicas, organic, inorganic, and biopolymers) is quite difficult in the absence of detailed information on system heterogeneity. A method for assessing the relative contributions of static and dynamic quenching in heterogeneous systems is presented. While the method does not provide direct information on the details of system heterogeneity, it requires no a priori information on the nature of the heterogeneity. This approach is based on a comparison of intensity quenching data with lifetime quenching data using a preexponential weighted lifetime, τ_M. τ_M is calculated by fitting the observed decay curves to a sum of a relatively small number (2–4) of exponentials. For time-correlated single-photon counting the parameters obtained from a statistically acceptable fit can be used to accurately estimate τ_M, even though the computed model may bear no resemblance to the true decay kinetics. Simulations confirm that the method works for a wide range of heterogeneous systems. The technique is applied to oxygen quenching of a luminescent metal complex on a silica surface.

INTRODUCTION

The study of microheterogeneous systems by luminescence is a relatively new and rapidly growing area (*1*, *2*). Such systems include surfactants, surfaces, polymers, and biosystems. In contrast to many homogeneous systems, heterogeneous media frequently give rise to complex decay kinetics that can be characterized as sums of several exponentials or as distribution functions of exponentials. Since decay data can frequently be fit equally well by several widely different decay models, mechanistic interpretation is hampered by the lack of a unique solution.

In microheterogeneous systems exhibiting luminescence quenching, even the simple question of whether quenching is dynamic or static has not been satisfactorily addressed. In homogeneous media with only a single-component exponential decay, the intensity and lifetime forms of the Stern–Volmer equations are

$$\tau_0/\tau = 1 + K_{SV}[Q] \quad (1a)$$

$$K_{SV} = k_2\tau_0 \quad (1b)$$

$$I_0/I = 1 + (K_{SV} + K_{eq})[Q] + K_{eq}K_{SV}[Q]^2 \quad (1c)$$

where [Q] is the quencher concentration, τ's are lifetimes, I's are intensities, K_{SV} and k_2 are the Stern–Volmer and bimolecular quenching constants, respectively, and K_{eq} is the association constant for binding of the quencher to the luminescent species. The subscript 0 denotes the value in the absence of quencher. If plots of τ_0/τ or I_0/I versus quencher concentration are linear and match, quenching is purely dynamic (i.e. $K_{eq} = 0$). If I_0/I is above τ_0/τ, static quenching is present. Fitting both intensity and lifetime curves then allows determining the static and dynamic quenching contributions.

In many microheterogeneous systems, the multiexponentiality of the decay curves and the uncertainty of the fitting model preclude evaluating a single-exponential τ for use in eq 1. We present a new method for analyzing luminescence decay curves in microheterogeneous media that allows assessing the contributions of static and dynamic quenching. The technique is shown by simulations to be insensitive to the nature of the true decay model. We demonstrate its utility by applying it to oxygen quenching of $Ru(phen)_3^{2+}$ (phen = 1,10-phenanthroline) adsorbed onto a silica surface.

THEORY

Consider a system consisting of a number of independently emitting species with different single-exponential lifetimes and relative contributions. The lifetime and Stern–Volmer quenching constant for each component are given by τ_i and K_{SVi}, respectively. The fraction of the total emission from the ith component in the absence of quencher is given by f_{0i}. The intensity form of the Stern–Volmer equation is

$$I_0/I = \left[\sum \frac{f_{0i}}{1 + K_{SVi}[Q]}\right]^{-1} \quad (2)$$

$$f_{0i} = I_{0i}/\sum I_{0i} \quad (3)$$

The impulse response of the system is described by

$$i(t) = \sum \alpha_i e^{-t/\tau_i} \quad (4)$$

where the preexponential weighting factors are α's and the lifetimes are τ's. The fractional contribution to the total emission for each component, f_{0i}, either under pulsed or steady-state conditions, is related to the α's and τ's by

$$f_{0i} = \alpha_i\tau_i/\sum \alpha_i\tau_i \quad (5)$$

To be able to compare intensity and lifetime quenching data, we define a new *preexponential weighted mean lifetime*, τ_M

$$\tau_M \equiv \sum \alpha_i\tau_i/\sum \alpha_i \quad (6)$$

In the absence of a quencher, the unquenched τ_M is τ_{M0} and is given by

$$\tau_{M0} = \sum \alpha_i\tau_{0i}/\sum \alpha_i \quad (7)$$

where the subscript 0 denotes the value in the absence of quencher. In the absence of static quenching the α's are the same for the quenched and unquenched sample. Assuming that each component obeys a normal Stern–Volmer equation (eq 1a), τ_M in the presence of quencher is

[1] Current address: Environmental Engineering Science, California Institute of Technology, Pasadena, CA 91125.

0003-2700/91/0363-0332$02.50/0

$$\tau_M = \frac{\sum \alpha_i \tau_i}{\sum \alpha_i} = \sum \frac{\alpha_i \tau_{0i} / \sum \alpha_i}{1 + K_{SVi}[Q]} \quad (8)$$

For microheterogeneous systems, we now define a lifetime Stern–Volmer equation using τ_M's rather than single-exponential lifetimes.

$$\frac{\tau_{M0}}{\tau_M} = \frac{\sum \alpha_i \tau_{0i} / \sum \alpha_i}{\sum \frac{\alpha_i \tau_{0i} / \sum \alpha_i}{1 + K_{SVi}[Q]}} = \left[\sum \frac{\alpha_i \tau_{0i} / \sum \alpha_i \tau_{0i}}{1 + K_{SVi}[Q]} \right]^{-1} = \left[\sum \frac{f_{0i}}{1 + K_{SVi}[Q]} \right]^{-1} \quad (9)$$

where the last form results from substituting f_{0i} from eq. 5. Comparison of eqs 2 and 9 shows that

$$I_0/I = \tau_{M0}/\tau_M \quad (10)$$

Thus, if we use τ_M's rather than single-exponential lifetimes in our Stern–Volmer equation, we can compare intensity and lifetime data in microheterogeneous systems to assess the presence of static quenching.

Attempts to use the analogous true mean lifetime or natural lifetime $\langle\tau\rangle_0/\langle\tau\rangle$ where

$$\langle\tau\rangle \equiv \sum \alpha_i \tau_i^2 / \sum \alpha_i \tau_i \quad (11)$$

fails to give lifetime and intensity expressions that are the same (*3*). Thus, the normally calculated $\langle\tau\rangle$ provides no insight whatsoever into static versus dynamic quenching processes.

IMPLEMENTATION

While theoretically correct, eq 10 still is not directly applicable to experimental data. The actual distribution of lifetimes is required to compute τ_M. What is needed is a way of accurately evaluating the τ_M's independent of knowledge of the true decay model. We describe a satisfactory way of evaluating τ_M's without any knowledge of the true model.

Our approach is based on the well-known fact that a wide variety of complex decay schemes can be accurately fit as the sum of a relatively small number of exponentials (*4*, *5*). This includes decays that are distribution functions or exhibit Förster energy transfer. However, satisfactory fitting of the decay curves with an incorrect model does not necessarily guarantee that computed parameters have physical significance. In particular, we cannot say a priori that τ_M's calculated from such an incorrect model are accurate. However, we will demonstrate that for a wide range of models and parameters, a fit of the data to a simple sum of two to four exponentials provides accurate estimates of τ_M's as long as the fit is statistically satisfactory. Once accurate τ_M's are obtained, intensity and lifetime quenching data can then be compared by eq 10 to assess the relative contributions of static and dynamic quenching.

We begin by fitting our decay curves using the impulse response that is a sum of exponentials given by eq 4. Both the α's and τ's are fit. In cases where the flash cannot be treated as a δ function, deconvolution is required to extract the decay parameters. The decay is fit with increasing numbers of exponentials until the fit is statistically acceptable as judged by the χ_r^2 test (i.e. near 1) and the weighted residuals plot. The τ_M and $\langle\tau\rangle$ are then calculated from eqs 6 and 11 with the best fit decay parameters, even though a sum of exponentials model may not resemble remotely the true decay scheme.

EXPERIMENTAL SECTION

The preparation of the $Ru(phen)_3^{2+}$ sample adsorbed onto Cab-O-Sil M5 fumed silica is described elsewhere (*3*, *6*). The steady-state measurements and the time-correlated single-photon decay time system are also described elsewhere (*3*, *7*).

Numerical simulations were performed on an AT class IBM PC clone with a math coprocessor. Programs were written in Turbo Pascal 5.

Decay models for unquenched samples were generated as single or double Gaussian distribution functions with different peak centers, τ_{peak}, and widths, σ. Each Gaussian distribution was approximated as a sum of 21 discrete single-exponential decays uniformly distributed over $\pm 3\sigma$. For the two Gaussian cases, we have

$$D(t) = \beta_1 \sum_{i=-10}^{10} \alpha_{i1} e^{-t/\tau_{i1}} + \beta_2 \sum_{i=-10}^{10} \alpha_{i2} e^{-t/\tau_{i2}} \quad (12a)$$

$$\alpha_{ij} = e^{-(\tau_{ij} - \tau_{jpeak})^2/2\sigma_j^2}; \qquad j = 1, 2 \quad (12b)$$

$$\tau_{ij} = \tau_{jpeak}(1 + 0.3i\sigma_j); \qquad j = 1, 2 \quad (12c)$$

where the β's are weighting factors for each Gaussian distribution. As defined, the relative total emission contribution from each Gaussian distribution is $\beta_j \tau_{jpeak}$. For the wider distributions, negative lifetimes were excluded. We also tested to see if the need to deconvolute data affected our analysis. For some of the simulations we first convoluted $D(t)$ with an excitation profile measured on our decay time system and then extracted the apparent α's and τ's by deconvolution (*7*).

Quenching of a distribution was simulated by calculating the new, quenched values of the contributing single-exponential lifetimes using eq 1 with the chosen quenching rate constant and quencher concentration. The α's in eq 12 are unchanged on dynamic quenching. The quenched decays were then calculated and summed. The decays were scaled to either 40 000 or, less commonly, 10 000 counts in the peak channel, and Poisson noise was added (*8*). An acquisition window of 0–4 μs was used, which matches that used for the majority of our data acquisitions. The contributing single-exponential decays and their associated weights were used to calculate the true τ_M and $\langle\tau\rangle$ for the noise-free distribution.

Decays were fit to a sum of exponentials (eq 4) by using a Marquardt nonlinear least-squares algorithm (*7–9*). For convoluted decays, the same program was used for deconvolution. A sum of up to four exponentials can be modeled and the success of the fit judged by the magnitude of the weighted χ_r^2, the appearance of the weighted residuals plot, and various goodness of fit indicators such as the Durbin–Watson parameter. The computed best fit α's and τ's were used to calculate τ_M and $\langle\tau\rangle$ from eqs 6 and 11.

In our simulations, τ_{peak} was varied from 0.1 to 1 μs with σ's as large as 100% of τ_{peak}. For the double-exponential cases, the relative contributions of each distribution to the total emission was varied by scaling the β's. Quenching rate constants and quencher concentrations were adjusted to simulate varying degrees of quenching.

RESULTS

We found that the optimum fitting procedure was to use no more exponentials than required to give a statistically acceptable χ_r^2. The use of more exponentials made for slow convergence, false minima, and program crashes. Two to four exponentials sufficed for all of the systems described here, although the broadest bimodal distributions would occasionally give χ_r^2 as large as 1.2 even with four exponentials.

We now demonstrate that our approach gives valid estimates of τ_M and $\langle\tau\rangle$ for a wide range of models. Note that our conclusions are independent of whether or not the data required deconvolution. Also, the results were similar for 10K and 40K peak counts data.

For narrow single-distribution functions ($\sigma \leq 0.3\tau_{peak}$), accuracy in τ_M and $\langle\tau\rangle$ was typically better than 1%. This is not surprising since, as the distribution becomes narrower, the system approaches a single exponential. A small systematic underestimation of $\langle\tau\rangle$ was observed for wider distributions with longer τ_{peak}'s. This underestimation is due to the low-amplitude tail on the decay that extends beyond our 4-μs measurement window and the sensitivity of the $\langle\tau\rangle$ calculation

Table I. Accuracy and Precision of Lifetimes of Gaussian Distributions[a]

simulation parameters, μs					fitted parameters, μs	
τ_{peak}	σ	β_2/β_1	τ_m	$\langle\tau\rangle$	τ_m (% error)	$\langle\tau\rangle$ (% error)
A. Single Gaussian Distribution						
0.7	0.7	0	0.886	1.24	0.884 ± 0.003 (0.25)	1.19 ± 0.004 (3.7)
B1. Double Gaussian Distribution						
0.7	0.7	7	0.222	0.707	0.228 ± 0.001 (2.8)	0.675 ± 0.005 (4.5)
0.1	0.1					

simulation parameters, μs				fitted parameters, μs	
[Q], M	β_2/β_1	τ	$\langle\tau\rangle$	τ_m (% error)	$\langle\tau\rangle$ (% error)
B2. Double Gaussian Distribution with Quenching (k_q = 1 M^{-1} μs^{-1})					
0.25	7	0.192	0.485	0.197 ± 0.003 (1.6)	0.475 ± 0.002 (1.9)
0.75	7	0.158	0.311	0.160 ± 0.003 (1.3)	0.308 ± 0.001 (1.2)
2.0	7	0.118	0.180	0.123 ± 0.0004 (4.1)	0.179 ± 0.0004 (0.7)
4.0	7	0.089	0.117	0.092 ± 0.0006 (2.9)	0.116 ± 0.0003 (0.5)

[a] n = 5, 6 where standard deviations are calculated. The time base is 4 μs. Fits are not deconvolutions and are from the data peak to the point at which intensity is negligible.

to longer lifetimes because of the τ^2 dependence in eq 11. Increasing the range of data acquisition corrects this problem, as shown by its absence for shorter lived distributions using the same measurement window. Even for the pathologically wide single-distribution functions where $\sigma = \tau_{peak}$, the errors are not large (Table I) and can be traced to too short a measurement window with some loss of data at long times. The important τ_M is accurate to 0.25%.

Errors are only slightly worse for the extremely wide double Gaussian distribution ($\sigma_1 = \tau_{1peak}$, $\sigma_2 = \tau_{2peak}$) where the contribution from both Gaussian parameters are equal (i.e., $\beta_1 = 1$, $\tau_{peak1} = 0.7$ μs, $\beta_2 = 7$, $\tau_{peak2} = 0.1$ μs) and the standard deviations equal their peak lifetimes. We will refer to this as the very wide double Gaussian system. Errors are <3% for τ_M and <5% for $\langle\tau\rangle$. $\langle\tau\rangle$ again exhibits the systematic underestimation because of the limited acquisition range and could easily be improved by using a wider data acquisition window. For double Gaussian distributions with narrower σ's, closer τ_{peak}'s, or larger differences in the areas under the two Gaussian curves, the errors become significantly smaller (≤1%).

As expected the very wide double Gaussian distribution with equal contributions from the two Gaussian parameters showed the worst errors. We focus on these results. Section B2 of Table I shows the effects of dynamic quenching. Errors are acceptably small over the entire quenching range. The errors in $\langle\tau\rangle$ decrease with increasing quencher concentration. We believe this effect is due to the loss of long-lived components on quenching. As the quencher concentration is increased, the distribution shifts to shorter lifetimes and the components that had fallen outside of the measurement window are brought into range.

Despite the systematic errors discussed above, our estimated τ_M's are very close to the true τ_M's for the quenched wide double Gaussian distribution. As with the unquenched wide double Gaussian distribution, even better agreement in quenched systems is obtained for narrower σ's, larger differences in the total contributions from the two components, or τ_{peak}'s that are not so widely separated.

To demonstrate the utility of eq 10 we computed a simulated Stern–Volmer quenching plot applied to the very wide double Gaussian distribution. The result is shown in Figure 1A with the true τ_{M0}/τ_M ($=I_0/I$) shown as a solid line along with the simulated results. The excellent agreement leads to the correct conclusion that quenching occurs by a purely dynamic mechanism.

These results also indicate that this method is applicable to a wide range of distributions, not just Gaussians. In dynamic quenching, longer lived components are more heavily quenched, resulting in a skewed, non-Gaussian distribution. The results for the quenched double Gaussian data of Table I and Figure 1A show our success in the treatment of this asymmetric bimodal distribution. Thus, the method can be applied to both symmetric and asymmetric distributions.

An alternative approach to our sum of several exponentials would be to deconvolute the data directly with an impulse response that is a single or double Gaussian or Lorentzian distribution. For systems that actually conform to such distributions, the calculated τ_M's computed from the fits will, of course, be correct. Further, the number of parameters is less than required by our sum of several exponentials as two exponentials require four parameters while a Gaussian distribution requires only three. However, without having the software for such deconvolution, we cannot comment on the relative computational speeds of the two approaches. Nor can we verify that the distribution function approach will yield reliable fits to distributions that do not conform to the fitting distribution (e.g. the quenched Gaussian distribution) without an excessive number of parameters. While we suspect that this alternative approach will work, its superiority over a sum of several exponentials, which we have shown will give satisfactory results for non-Gaussian distributions, still needs to be confirmed.

It should also be noted that at very high peak counts (100K–500K), there is a discernible difference between a Gaussian distribution and a sum of two exponentials. Thus, under such conditions, a distribution may be more accurate for computing decay parameters in some systems.

Some workers report $\langle\tau\rangle$ as a function of quencher concentration. We show $\langle\tau\rangle_0/\langle\tau\rangle$ Stern–Volmer plots in Figure 1A and 1B. For the broad double Gaussian distribution, there is clearly no correlation between this plot and the intensity plot, and any inferences drawn concerning the quenching mechanisms are meaningless. For all but a single-exponential decay, utilizing $\langle\tau\rangle$ is not useful.

Parts B and C of Figure 1 demonstrate another pitfall. Some workers fit their data to a sum of two or three exponentials and then examine the quenching behavior of the separate decays as though they were true single components. If the decays really were a sum of two or three exponential decays, then the resulting quenching plots would provide information about the discrete system components.

The hazards of this approach are shown in parts B and C of Figure 1, which give the extracted double- and triple-exponential parameters to our data for the very wide double Gaussian distribution. Plots of τ_{0i}/τ_i versus [Q] are shown

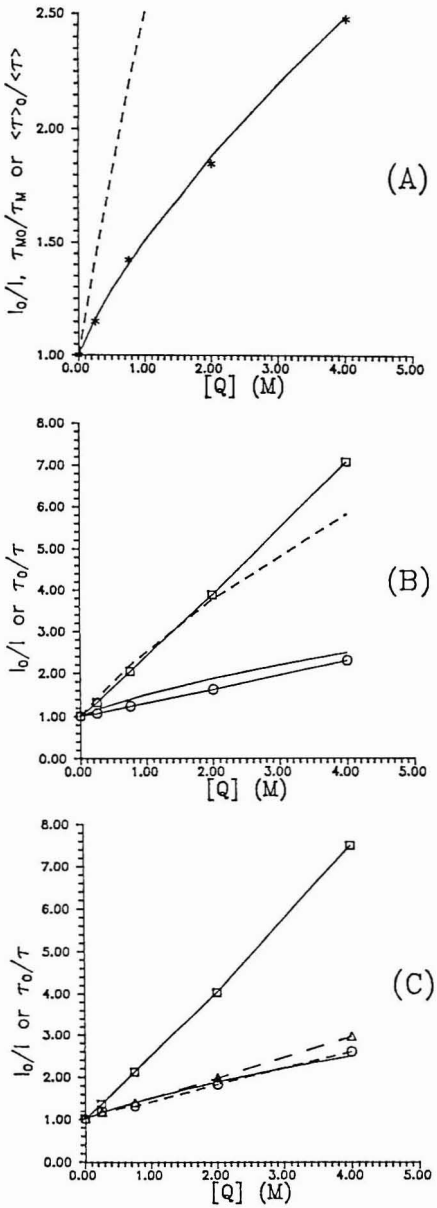

Figure 1. Calculated parameters for the quenched broad double Gaussian distribution (Table I, part B): (A) true τ_{M0}/τ_M or I_0/I (—), $\langle\tau\rangle_0/\langle\tau\rangle$ (---), and computed results (asterisks) using noisy data fit by the method of the text; (B) treatment of the data of part A assuming quenching of two independently emitting species (τ_0/τ for the long-lived (□) and short-lived (○) components, true τ_{M0}/τ_M or I_0/I (—) and $\langle\tau\rangle_0/\langle\tau\rangle$ (---)); (C) treatment of the data of part A assuming quenching of three independently emitting species (long-lived (□), medium-lived (△), and short-lived (○) components, true τ_{M0}/τ_M or I_0/I (—)).

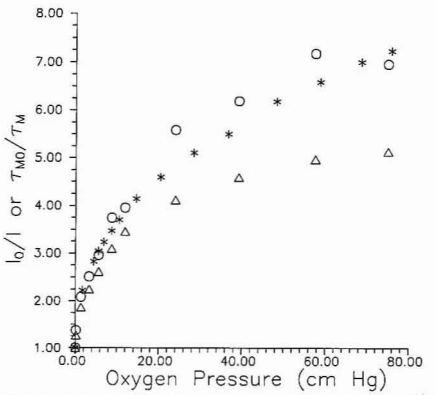

Figure 2. Intensity and lifetime oxygen quenching of $Ru(phen)_3^{2+}$ on a Cab-O-Sil disc: (asterisk) experimental I_0/I; (△) τ_{M0}/τ_M using a four-component fit with no baseline correction; (○) τ_{M0}/τ_M using a four-component fit with a baseline correction by omitting the ≈5-ns component.

for each of the "resolved" components. The Stern–Volmer quenching plots are nicely linear and can be interpreted by a plausible quenching model. This could lead the incautious to the totally erroneous conclusion that the system is a discrete two- or three-site one. As expected, none of the single-component quenching plots agrees satisfactorily with the true I_0/I data.

There can be warning that this discrete model is incorrect. The χ_r^2's (1.6–7.2) are significantly greater than 1.0 for single-photon counting data, which would lead to the rejection of a simple two-site fit. The deviations are not so large that the failure of a two-site model would be detected on most analog instrumentation. However, at 40 000 peak counts on a single-photon counting system the χ_r^2 (1.0–1.3) gives little warning of a failure of the three-site model. These results again emphasize the hazards of trying to draw detailed mechanistic conclusions based on discrete multiexponential fits to systems that may well be distribution functions.

In turning to real data, Figure 2 shows intensity and lifetime quenching plots for $Ru(phen)_3^{2+}$ adsorbed onto silica. In contrast to the simulated data, this system has several complexities. The emission is weak, and scatter and luminescence from the silica support are noticeable signal contributions, especially at short times. Because of the difficulty of reproducible sample placement in our gas cell, the fast background in the lifetime measurements cannot be accurately removed by simple blank subtraction.

Two τ_{M0}/τ_M versus [Q] plots are shown. The triangles show the data calculated without any attempt to remove the silicas scatter–fluorescence contribution. To reduce this error, however, we noted that the multiexponential fits consistently gave a very short-lived component (3–5 ns) that is uncharacteristic of the metal complex (typically >100 ns) but is present on the silica. We, therefore, assumed that the short-lived component was contributed from the silica, and we repeated the calculations discarding the short-lived component by omitting it in eqs 6 and 7. The corrected data are shown as circles. The excellent conformity between τ_{M0}/τ_M and I_0/I indicates that quenching in this system is virtually all dynamic. However, even if we use the uncorrected data, 80% of the emission is quenched dynamically at the highest oxygen concentration while 86% of the emission is quenched by all mechanisms; this leaves only 6% of the total quenching being static. Thus, the apparently large discrepancies between I_0/I and τ_{M0}/τ_M are actually not large at all. In conclusion,

on this silica support the dominant quenching mechanism is dynamic with a small or negligible static component.

We have applied our preexponential weighted mean lifetime to other metal complexes bound to silica systems (*3*, *6*) and to silicone polymer supported systems (*3*, *10*). For the other silica systems, dynamic quenching is the dominant, if not sole, quenching mechanism, although the need for the scatter–fluorescence corrections does not completely preclude a small static quenching component. For the more strongly emissive polymer systems, the scatter–fluorescence of the support is negligible, no short-lived component is required, and the systems are clearly quenched only by dynamic processes. Details on these systems are reported elsewhere (*3*, *6*, *10*).

While our method does not provide detailed micromechanistic information, it gives the relative contributions of static and dynamic quenching. For a general system having both static and dynamic quenching

$$I_0/I = (1/f_{\text{dynamic}})(1/f_{\text{static}}) = (\tau_{M0}/\tau_M)(1/f_{\text{static}}) \qquad (13)$$

where I_0/I is the observed intensity quenching ratio, f_{static} is the fraction of excited species that are not quenched statically, and f_{dynamic} is the fraction of excited molecules escaping static quenching, which are not quenched dynamically. Independent of model, $1/f_{\text{dynamic}}$ is given by τ_{M0}/τ_M. Thus, $1/f_{\text{static}}$ can be approximated from the measureable I_0/I and τ_{M0}/τ_M. From the τ_{M0}/τ_M and $1/f_{\text{static}}$, the researcher can then derive models to fit the observed results.

For data of the precision shown here, it will be necessary for the static contribution to exceed about 10% of the total intensity quenching for reasonable accuracy in the extraction and modeling of a static component to be possible.

For all of the systems under investigation in our laboratory, the differences between I_0/I and τ_{M0}/τ_M are so small that we have no evidence for static quenching, and we have been unable to apply the above approach to our data.

ACKNOWLEDGMENT

We thank S. W. Snyder for providing the deconvolution program and the reviewers for helpful suggestions.

LITERATURE CITED

(1) Kalyansundaram, K. *Photochemistry in Microheterogeneous Systems*; Academic Press: New York, 1987.
(2) Chemical, Biochemical, and Environmental Fiber Sensors. *Proceedings of SPIE—the International Society for Optical Engineering*; Lieberman, R. A., Wlodarczyk, M. T., Eds.; SPIE: Bellingham, WA, 1989; Vol. 1172.
(3) Carraway, E. R. Excited State Quenching of Immobilized Ruthenium(II) Complexes. Ph.D. Thesis, University of Virginia, 1989.
(4) James, D. R.; Liu, Yuan-Sheng; DeMayo, P.; Ware, W. R. *Chem. Phys. Lett.* **1985**, *120*, 460.
(5) Simiarczuk, A.; Ware, W. R. *J. Phys. Chem.* **1989**, *93*, 7609.
(6) Carraway, E. R.; Demas, J. N. Unpublished results.
(7) Snyder, S. W.; Demas, J. N. *Anal. Chem.* **1989**, *61*, 2704.
(8) Demas, J. N.; Demas, S. E. *Scientific Computing and Interfacing on Personal Computers*; Allyn & Bacon: New York, 1990.
(9) O'Connor, D. V.; Phillips, D. *Time-Correlated Single Photon Counting*; Academic Press: New York, 1984.
(10) Carraway, E. R.; Demas, J. N.; DeGraff, B. A.; Bacon, J. R. *Anal. Chem.* **1991**, *63*, 337–342.

RECEIVED for review August 3, 1990. Accepted November 1, 1990. We gratefully acknowledge the support of the National Science Foundation (Grants CHE 86-00012 and 88-17809).

Photophysics and Photochemistry of Oxygen Sensors Based on Luminescent Transition-Metal Complexes

E. R. Carraway[1] and J. N. Demas*

Chemistry Department, University of Virginia, Charlottesville, Virginia 22901

B. A. DeGraff*

Chemistry Department, James Madison University, Harrisonburg, Virginia 22807

J. R. Bacon*

Chemistry Department, Western Carolina University, Cullowhee, North Carolina 28723

A detailed study of the photophysics and photochemistry of polymer-immobilized luminescent transition-metal complex oxygen sensors is presented. Emphasis is on understanding the underlying origin of the nonlinear Stern–Volmer quenching response. Microheterogeneity is important in both photophysical and photochemical behavior, and the nonlinear quenching responses in RTV 118 silicone rubber can be adequately described by a two-site model, although detailed lifetime measurements suggest a more complex underlying system. Counterion studies with quenching counterions are shown to be useful probes of the structure of the complex in the polymer. While oxygen enhances photochemical instability, singlet oxygen is not directly implicated in sensor decomposition. In the photochemistry there is at least one reactive and one much less reactive site, although the photochemistry and quenching measurements probably sample different populations of sites. The existence of reactive sites suggests that stability can be enhanced by a preliminary photolysis to eliminate the more reactive sites.

INTRODUCTION

Luminescence-based optical sensors are becoming increasingly important, particularly in the area of fiber optic sensors (*1*). These sensors are frequently supported in polymers or gels or on surfaces. In contrast to more conventional homogeneous luminescences these supports are frequently heterogeneous on a microscopic scale and give rise to complex decay kinetics that can be characterized as sums of several exponentials or as distribution functions of exponentials (*2–6*). This complexity can frequently result in poorly understood sensors.

An important class of luminescence sensors is O_2-quenching sensors, which are based on the decrease of luminescent intensity and lifetime of the sensor material as a function of O_2 tension (*7–12*). In homogeneous media with only a single-component exponential decay, the intensity and lifetime forms of the Stern–Volmer equations with both static and dynamic quenching are

$$\tau_0/\tau = 1 + K_{SV}[Q] \quad (1a)$$

$$K_{SV} = k_2\tau_0 \quad (1b)$$

$$I_0/I = 1 + (K_{SV} + K_{eq})[Q] + K_{eq}K_{SV}[Q]^2 \quad (1c)$$

where [Q] is the quencher concentration, τ's are lifetimes, I's are intensities, K_{SV} and k_2 are the Stern–Volmer and bimolecular quenching constants, respectively, and K_{eq} is the association constant for binding of the quencher to the luminescent species. The subscript 0 denotes the value in the absence of quencher. If plots of τ_0/τ or I_0/I versus quencher concentration are linear and match, quenching is purely dynamic (i.e., $K_{eq} = 0$). If I_0/I is above τ_0/τ, static quenching is present.

However, in many microheterogeneous systems, the multiexponentiality of the decay curves and the uncertainty of the fitting model preclude evaluating a single-exponential τ for use in eq 1. Even the question of the relative contributions of static and dynamic quenching is difficult to address. Further, the I_0/I plots are downward curved, which makes more accurate calibration difficult.

We reported an O_2 sensor based on quenching of a transition-metal complex $Ru(Ph_2phen)_3^{2+}$ (Ph_2phen = 4,5-diphenyl-1,10-phenanthroline) in a silicone rubber (*12*). As with most quenching-based sensors, the response exhibits downward curvature. In view of the very long unquenched luminescence lifetimes of many transition-metal complex sensors (*13*, *14*), these complexes seemed ideal to explore the mechanisms of the nonlinear Stern–Volmer plots and to develop models for predicting sensor response.

Our goals were to examine in detail the photophysics and photochemistry of the quenching-based O_2 sensor by using RuL_3^{2+} where L is an α-diimine (2,2′-bipyridine, 1,10-phenanthroline, and their substituted analogues) in a silicone rubber. As we will show, quenching in these systems is purely dynamic, with the downward curvature resulting from site heterogeneity. Further, a very simple two-state model gives excellent fits to our experimental intensity-quenching results. The photochemistry also exhibits heterogeneity, which may prove useful for stabilizing sensors.

EXPERIMENTAL SECTION

Chemicals. Tris complexes, RuL_3^{2+}, of the following ligands were prepared by literature methods (*15*). The abbreviations for the ligands are bpy = 2,2′-bipyridine, phen = 1,10-phenanthroline, Ph_2phen = 4,7-diphenyl-1,10-phenanthroline, 5,6-Me_2phen = 5,6-dimethyl-1,10-phenanthroline, and 4,7-Me_2phen = 4,7-dimethyl-1,10-phenanthroline. The BPh_4^- salt of $Ru(4,7\text{-}Me_2phen)_3^{2+}$ was prepared by metathesis from the perchlorate salt (*16*). In addition, the *cis*-$Ru(phen)_2(CN)_2$ was prepared by literature methods (*17*).

The one-part RTV 118 and the two-part RTV 615 were from General Electric Corp. The one-part air-cured Dow Corning silicone was a Silastic medical adhesive tape, Catalog No. 891. Samples were prepared as described earlier (*12*) by using ≈1 mM solutions of the complex in CH_2Cl_2. Film thicknesses were typically 0.005–0.015 in. Earlier results showed behavior was independent of film thickness. The recommended slow evaporation procedure was used to improve film quality (*12*).

[1] Current address: Environmental Engineering Science, California Institute of Technology, Pasadena, CA 91125.

0003-2700/91/0363-0337$02.50/0

Absorption spectra for the RuL_3^{2+} species in RTV 118 showed no new bands or significant spectral shift. This, coupled with the similarity of the emission spectra in dilute solutions and in the films, indicates that aggregation is not significant.

Photophysical Measurements. Static dc luminescence measurements were made on a SPEX Fluorolog system (*18*). Luminescence lifetime measurements were made by using a homemade time-correlated single-photon-counting system (*19, 20*). Solution spectra were measured at ≈100 μM.

To survey different polymer–complex systems one-point intensity quenching data ($I_{nitrogen}/I_{air}$) were taken for several complexes. Different polymers and methanol were used as the solvents.

All measurements were made at room temperature (22 ± 2 °C). Air measurements used room air. Previous measurements have shown that the systems are not affected by variations in humidity that include putting the sample in water (*12*). For the pressure dependence studies, the gas was pure oxygen and the pressure was varied with a pump.

Photochemistry. Photochemical studies were performed by irradiating low optical density films in air in the Spex spectrofluorometer. Decomposition was monitored by following the emission intensity. Excitation bandwidth was set to the maximum of 16 nm to minimize photolysis times. Excitation was near the peak of the visible metal-to-ligand charge-transfer transition, and the emission was monitored at the wavelength of peak emission. Since emission intensity is directly proportional to concentration under our conditions and the only likely emitting species is the starting material, the decay of the emission intensity is directly proportional to the surviving concentration of the sensor material.

Photochemical decomposition curves (luminescent intensities vs time) were fit to a simple first-order decay

$$E(t) = K \exp(-k_{obs}t) \quad (2)$$

where $E(t)$ is the emission intensity as a function of time, K is a proportionality constant, and k_{obs} is the photochemical rate constant. In addition, since eq 2 did not give very good fits, we used a decaying exponential on a constant baseline:

$$E(t) = K[(1 - F) \exp(-k_{obs}t) + F] \quad (3)$$

where F corresponds to the fraction of the total emission that is not lost from extended photolysis.

We were also concerned that materials left in the polymer might be responsible for the degradation. To test this hypothesis, we exhaustively extracted a film in a Soxhlet extractor overnight with CH_2Cl_2. $Ru(phen)_3^{2+}$ sensors were constructed by using the virgin and extracted films and photolyzed.

Since our samples are optically dilute, the relative quantum yields were computed from

$$\phi_{photo} = k_{obs}/\epsilon \quad (4)$$

where ϵ is the molar extinction coefficient at the excitation wavelength.

Data Treatment. For ascertaining the relative contributions of static and dynamic quenching, we used the method described in the previous paper (*21*). The preexponential weighted mean lifetime, τ_M

$$\tau_M \equiv \sum \alpha_i \tau_i / \sum \alpha_i \quad (5)$$

was computed. The necessary α's and τ's were extracted from the decays by deconvolution assuming an impulse response that is a sum of exponentials; a Marquardt nonlinear least-squares algorithm was used (*19, 20, 22*). The success of the fit was judged by the magnitude of the weighted χ_r^2, the appearance of the weighted residuals plot, and various goodness of fit indicators such as the Durbin–Watson parameter. The number of components was varied until a statistically valid reduced χ^2 was obtained. The computed best fit α's and τ's were used to calculate τ_M from eq 5.

Even if no physical significance can be ascribed to the τ's and α's, the following is true if there is no static quenching:

$$I_0/I = \tau_{M0}/\tau_M \quad (6)$$

Thus, if we use τ_M's rather than single-exponential lifetimes in our Stern–Volmer equation, we can compare intensity and lifetime data in microheterogeneous systems to assess the presence of static quenching.

Table I. Sensitivity to Oxygen Quenching of Metal Complex–Polymer Systems

solvent/ support	$I_{nitrogen}/I_{air}$ Ru(4,7-Me_2phen)$_3$-$(ClO_4)_2$	Ru(4,7-Me_2phen)-$(Ph_4B)_2$	Ru(phen)$_2$-$(CN)_2$	Ru-$(Ph_2phen)_3$-$(ClO_4)_2$
methanol	6.7	6.7	14.7	19.6
RTV 118	5.6	4.3	4.0	7.4
Dow 891	3.6	1.3	2.1	5.6
RTV 615	2.4	1.0	2.6	1.26

Table II. Photochemical Decomposition Rates

complex	abs	exponential 10^5k_{obs}, s^{-1}	exponential plus baseline 10^5k_{obs}, s^{-1} (ϕ_{photo})	exponential plus baseline F
$Ru(bpy)_3(ClO_4)_2$[a]	0.15	1.65	9 (1.00)	0.73
$Ru(phen)_3(ClO_4)_2$[a]	0.036	4.0	13 (1.06)	0.55
$Ru(5,6\text{-}Me_2phen)_3(ClO_4)_2$[a]	0.06	7.0	22 (1.45)	0.43
$Ru(phen)_3(ClO_4)_2$[b]	0.1	3.5	14 (1.00)	0.61
$Ru(phen)_3(ClO_4)_2$[b,c]	0.1	2.3	11 (0.78)	0.55

[a] 450-nm excitation. [b] 420-nm excitation. [c] Exhaustive 10-h Soxhlet extraction with CH_2Cl_2 before forming sensor.

RESULTS

Figure 1 shows the emission spectra of the three complexes in different media. The emission spectra of $Ru(bpy)_3^{2+}$ is strikingly sensitive to media, $Ru(phen)_3^{2+}$ much less so, and $Ru(Ph_2phen)_3^{2+}$ is virtually media independent.

Figure 2 shows O_2 intensity-quenching data for $Ru(Ph_2phen)_3^{2+}$ along with the earlier reported intensity data. The current data extend to a full atmosphere of pure oxygen. Figure 3 shows intensity- and lifetime (τ_M)-quenching data for both $Ru(bpy)_3^{2+}$ and $Ru(phen)_3^{2+}$.

Table I gives the one-point intensity-quenching data ($I_{nitrogen}/I_{air}$). For homogeneous media such as methanol, the Stern–Volmer plots for these complexes are known to be linear, but no detailed studies were performed in the silicones.

Table II shows the results of photochemical decomposition studies using both a single-exponential model and a single-exponential plus a baseline model. ϕ_{photo} was normalized to 1.00 for $Ru(bpy)_3^{2+}$ for the 450-nm studies. For the extraction study of $Ru(phen)_3^{2+}$ at 420 nm, ϕ_{photo} was set to 1.00 for the sample that was not exhaustively washed.

The single exponential with a zero baseline gave very poor fits using 10^4-s photolyses. However, the deviations were much less obvious for our original 2000-s irradiations, and one might have been fooled into accepting the misleading results of the single-exponential fit (Table II). Acceptable fits with no obvious systematic errors were obtained with the exponential plus a baseline model for the 2000- and 10^4-s irradiations.

Figure 4 shows the intensity-quenching plots for $Ru(bpy)_3^{2+}$, $Ru(phen)_3^{2+}$, and $Ru(Ph_2phen)_3^{2+}$. The solid lines are best fits using model 2 described later. The estimated uncertainties on the I_0/I's are 1–2% based on the precision of the individual intensity measurements. These uncertainties also match the residuals in our modeling.

DISCUSSION

The luminescence of all the complexes arise from ligand to metal charge-transfer (MLCT) excited states where the emitting state is derived from a configuration involving promoting a metal d electron to a ligand π^* antibonding orbital. The long microsecond lifetimes arise from the emitting states containing a high degree of triplet character; however, to denote them as triplets and the emissions as phosphorescences is probably a misnomer. Due to the high atomic number of Ru, the emitting states are best described as spin–orbit states

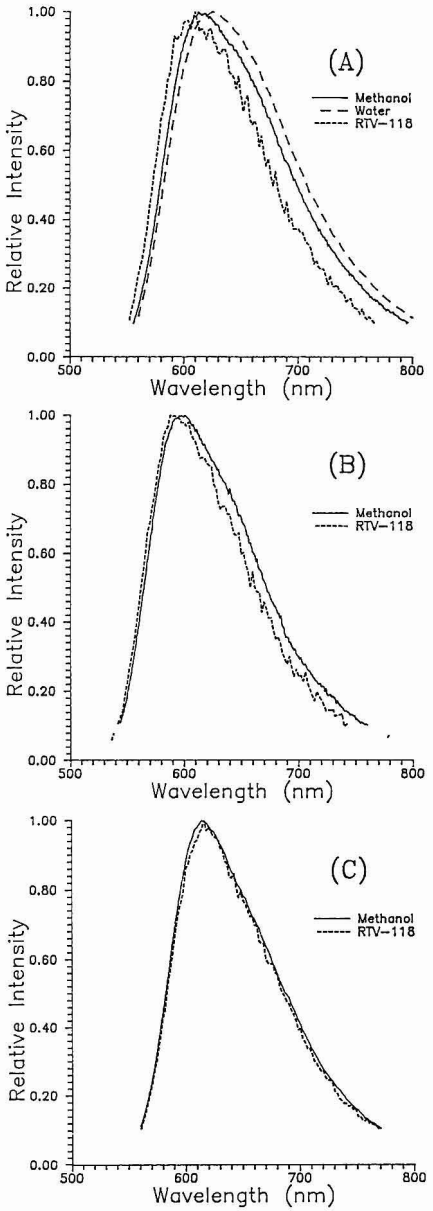

Figure 1. Emission spectra (450 nm) of $Ru(bpy)_3^{2+}$ (A), $Ru(phen)_3^{2+}$ (B), and $Ru(Ph_2phen)_3^{2+}$ (C) in different media.

rather than as either singlets or triplets (*23*).

The emissions can frequently show significant alterations with changes in solvent polarity or donor/acceptor properties due to the fact that the emitting states involve large radial changes in charge distribution. This is seen clearly for $Ru(bpy)_3^{2+}$ (Figure 1A). The solvent perturbations are strongly attenuated for $Ru(phen)_3^{2+}$ and all but eliminated for $Ru(Ph_2phen)_3^{2+}$. This decreasing sensitivity to solvent perturbation is a consequence of the excitation being localized in the metal α-diimine portion of the complex (–N=C–C=N–) (*24*). The more extended the complex, the greater the shielding of the excited portion and the smaller the solvent perturbations of the emission spectrum. In particular, the bulky phenyl groups are extremely effective at shielding the excited state from solvent perturbations. Similarly, micelles, surfactants, cyclodextrins, and intramolecular hydrocarbon tails can shield excited states of Ru(II), Os(II), and Re(I) complexes from solvent perturbations (*25–27*).

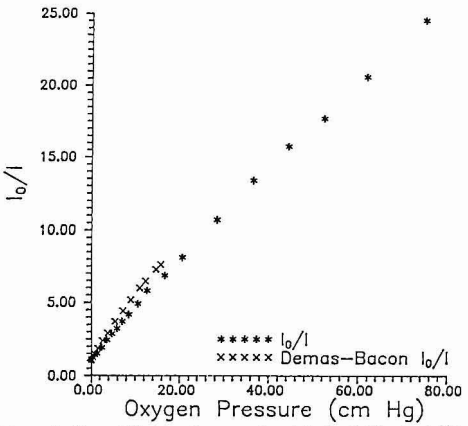

Figure 2. Current O_2 intensity-quenching data for $Ru(Ph_2phen)_3^{2+}$ in RTV 118 (asterisks) along with the earlier reported intensity (×) data (*12*).

It is difficult to put precise errors on the τ_{0M}/τ_M data, since they are so indirectly derived. The simulation of the previous paper suggests that good precision is possible. However, experimentally, with our data and instrumentation for a variety of systems, we find that experimental uncertainties, especially at high degrees of quenching exceed those of the simulations. On the basis of our observed noise levels for different systems, it appears that for the $Ru(bpy)_3^{2+}$ and $Ru(phen)_3^{2+}$ data of Figure 3, τ_{0M}/τ_M versus I_0/I can be considered within experimental error of each other, and O_2 quenching is essentially purely dynamic. The slight fall of the τ_M data for $Ru(phen)_3^{2+}$ is probably within experimental error. However, even if the fall-off is real, the total quenching is 79% at high O_2 concentrations while dynamic quenching is 75%. Static quenching, if present at all, could account for no more than a few percent of the total quenching.

The downward curvature of the Stern–Volmer plots necessitates a model more complex than a single species quenched bimolecularly. Microheterogeneity is required to explain these results. We evaluated two mechanistic models: (1) The complex exists in two distinctly different environments, with one being quenchable and the other being unquenched. (2) The complex exists in two distinctly different environments, with both being quenchable but with different rate constants.

Model 1 is the minimal dynamic model giving downward-curved Stern–Volmer quenching. It assumes two independent sites with only one having significant sensitivity to oxygen quenching. Model 2 is a more realistic two-site model that includes quenching of both sites. The basic equation for model 2 is

$$I_0/I = \frac{1}{f_{01}/(1 + K_{SV1}[Q]) + f_{02}/(1 + K_{SV2}[Q])} \quad (7)$$

where the f_{0i}'s are the fraction of the total emission from each

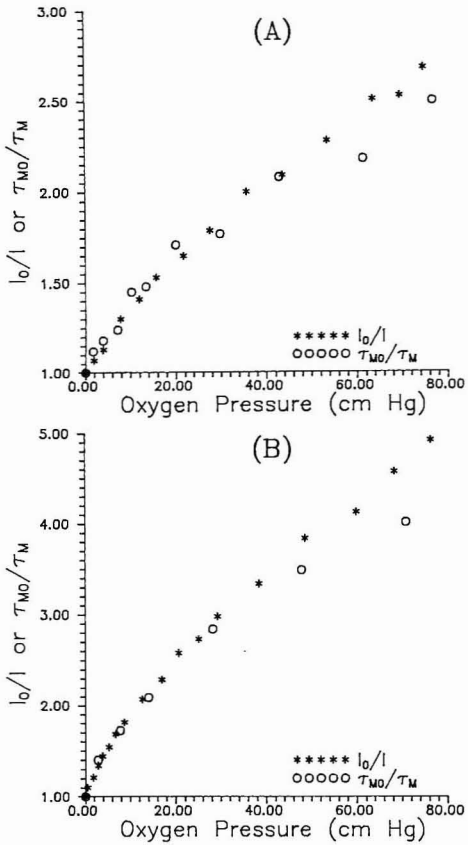

Figure 3. Intensity- (asterisks) and τ_M lifetime- (O) quenching data for both $Ru(bpy)_3^{2+}$ (A) and $Ru(phen)_3^{2+}$ (B).

Table III. Model 2 Oxygen-Quenching Fitting Parameters for RuL_3^{2+}

sample	f_{01}	K_{SV1}, $(cmHg)^{-1}$	f_{02}	K_{SV2}, $(cmHg)^{-1}$	χ^2
$Ru(bpy)_3^{2+}$					
film 1	0.57	0.070	0.43	0.0069	0.0074
film 2	0.61	0.056	0.39	0.0053	0.0046
$Ru(phen)_3^{2+}$	0.65	0.197	0.35	0.015	0.025
$Ru(4,7\text{-}Ph_2phen)_3^{2+}$	0.97	0.4	0.03	0.021	0.19

component under unquenched conditions and the K_{SVi}'s are the associated Stern–Volmer quenching constants for each component. Model 1 is a special case of model 2 with $K_{SV2} = 0$. The equation of model 1 has been used to generate calibration curves for luminescence sensors (*8*).

In addition, we also tested the widely used, but purely empirical, power law quenching model that accounts for the downward curvature of the Stern–Volmer plots.

$$I_0/I = 1 + K[Q]^m \quad (8)$$

where K and m are fitting parameters with no physical significance.

Model 1 was unacceptable compared to model 2. Model 1 gave distinctly inferior fits compared to model 2 with χ's

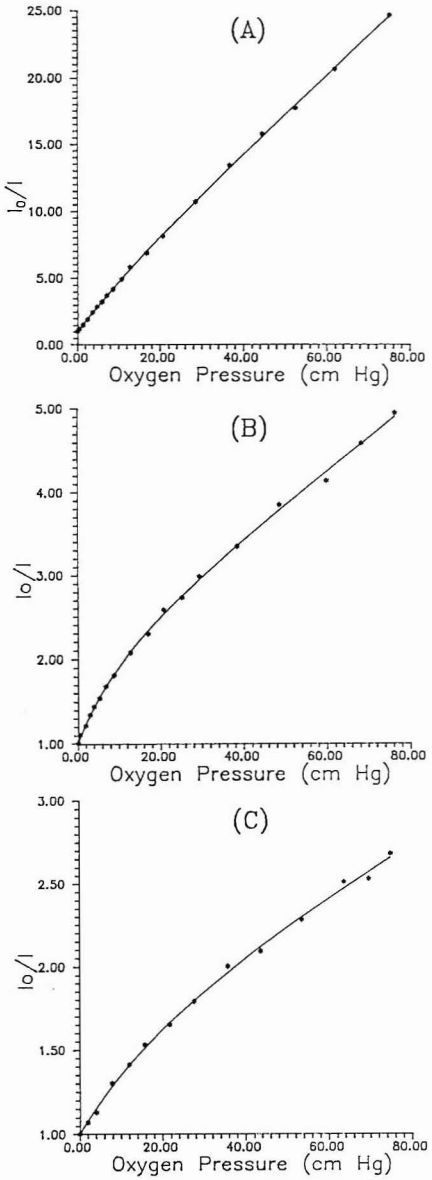

Figure 4. Intensity O_2-quenching data for $Ru(Ph_2phen)_3^{2+}$ (A), $Ru(phen)_3^{2+}$ (B), and $Ru(bpy)_3^{2+}$ (C) in RTV 118. The solid lines are the best fits using model 2.

that were 50–100% larger than for model 2. This result is physically reasonable, as it seems unlikely to have two species in a polymer with one being heavily quenched and the other virtually unquenched.

Table III summarizes the best fit parameters for model 2 with the three complexes. Figure 4 shows the best fits to the experimental data. Clearly, the data are fit within experi-

mental error. Similar fits were obtained with the lifetime data; due to much larger uncertainties in the τ_M's the results are less accurate (see Figure 3) and are not reported here (*5*).

Model 1 is inferior to the power law. Model 1 and the power law gave indistinguishable results for $Ru(bpy)_3^{2+}$; however, for the other two complexes, the χ^2 were 2–5 times larger than for the power law.

Model 2 was superior to the power law in all cases; the χ^2 for $Ru(phen)_3^{2+}$ was 4 times smaller. For $Ru(bpy)_3^{2+}$, χ^2 was 30% smaller. For the $Ru(Ph_2phen)_3^{2+}$, χ^2 was only 10% lower. However, this last case is not surprising as there is little curvature and the nonlinear corrections are minimal. Thus, model 2 provides superior fitting compared to the empirical power law or model 1.

In view of the ability of data described by complex decay kinetics to be fit by relatively simple decay schemes, it is quite possible that a two-component model can fit the data but not be correct. We address this question. If a two-component model is truly correct, the lifetime data should be fit by two exponentials and the lifetime and contributions should correlate with the parameters derived from the intensity-quenching data. For $Ru(bpy)_3^{2+}$ the decays for the entire oxygen concentration range were dominated by two components, which account for 96–99% of the total emission intensity. Further, both components are quenched in a chemically reasonable fashion; the degree of quenching for each component changes monotonically with oxygen pressure, and the rate constants are reasonable. However, the relative contributions of the short- and long-lived emissions to the total emission intensity are 16–31% and 65–80% over the oxygen pressure 0–1 atm, respectively. These deviate noticeably from the 40/60 ratio derived from the intensity data (Table III).

For $Ru(phen)_3^{2+}$ three lifetime components are required to account for about 90% of the emission; the components are not quenched in a monotonically decreasing fashion, and their contributions to the total emission intensity are inconsistent with a physically plausible model. Thus, while a two-site model may be a chemically reasonable model for $Ru(bpy)_3^{2+}$, it is certainly incorrect for $Ru(phen)_3^{2+}$. In view of the complexity of polymeric systems, it seems likely that the two-state model is also incorrect for $Ru(bpy)_3^{2+}$.

Even though the two-site model may be chemically incorrect, it is excellent for fitting intensity-quenching curves. The agreement is not surprising given the well-known ability of two exponentials to give excellent fits to complex decay curves made up of distribution functions of exponential decays especially at the count levels used on most single-photon-counting instruments. Thus, while the two-site model is not the full chemically correct model, it has excellent predictive and calibration properties, has a chemically sound basis, and (at least for inorganic complex sensors) is preferable to the less accurate power law calibration equation (*8*).

Our results demonstrate clearly that the lifetime data are more sensitive to subtleties of the micromechanistic photophysics. In this case we are able to establish inadequacies of model 2 that were not detected by intensity-quenching measurements only. It is also clear that resolution of the detailed mechanism in these complex polymer systems will require even better lifetime data than we are able to obtain with a conventional flashlamp-based time-correlated photon-counting system. Probably our largest source of error was the long tail on our 5-ns (fwhm) excitation source, which gave a contribution of fluorescence at long times and required deconvolution for all (including microsecond range) lifetimes and the relatively low peak counts ($\approx 10^4$) (*19*).

Photochemistry. We have observed a low-level decomposition of the $Ru(Ph_2phen)_3^{2+}$ complex under intense, protracted irradiation. The effect is enhanced in the presence of oxygen. Oxygen quenching of the complexes is an efficient source of singlet oxygen ($^1O_2$) in homogeneous (*28*) and heterogeneous media (*29*). Since $^1O_2$ is a well-known reactive species, it may attack and destroy the complexes. To test this possibility, we exploited the anticipated differences in reactivity of different complexes to $^1O_2$ attack. In 1,10-phenanthroline the bridging 5,6 double bond is much less aromatic than the fully aromatized pyridine rings, has much more double bond character and is, thus, a likely target of singlet oxygen attack. To test this hypothesis, we photolyzed $Ru(bpy)_3^{2+}$ (completely lacks the reactive double bond), $Ru(phen)_3^{2+}$ (has the bond without activating groups), and $Ru(5,6\text{-}Me_2phen)_3^{2+}$, which has a much more reactive double bond. For example, tetramethylethylene is an extremely reactive single-oxygen scavenger (*30*).

The k_{obs}'s of Table II for a decay without a baseline suggest that there is an increasing reactivity with activation of the double bond. However, this apparently rapid decay of the phen complexes relative to the bpy one is spurious; this is a consequence of the larger limiting photolysis levels for the bpy complex and not the higher reactivity of the other complexes. This is seen by examining the k_{obs}'s for the exponential plus baseline fits, which reveal that the k_{obs}'s differ by only a factor of 2.4. However, when corrected for the extinction coefficients of each complex, the ϕ_{photo} are 1.00:1.06:1.45, which shows no significant activation of the complexes on going from the bpy complex (no reactive double bond) to the $Ru(5,6\text{-}Me_2phen)_3^{2+}$ complex, which should be quite reactive towards singlet oxygen. We conclude that singlet oxygen is not the primary cause of sensor deactivation.

In the test of the unextracted and Soxhlet-extracted sensor films, the $Ru(phen)_3^{2+}$ photochemistry was very similar in both sensors with, perhaps, an $\approx$20% lower reactivity of the extracted film. Thus, if polymer components are responsible for the reactivity, they are not readily extractable.

The photochemical results do shed light on heterogeneity. If all sites were equally reactive, the simple exponential fit would apply, but this model does not give acceptable fits. An exponential plus a baseline gives satisfactory fits. These results demonstrate unequivocally that there is at least one reactive site and one much less reactive site. Interestingly, one of the biggest factors stabilizing the complexes is not k_{obs}, but F, the fraction of the unreactive form. Thus, the reactive fractions are 27%, 45%, and 57% for $Ru(bpy)_3^{2+}$, $Ru(phen)_3^{2+}$, and $Ru(5,6\text{-}Me_2phen)_3^{2+}$, respectively.

The F's do not appear to correlate with the fractions of the two forms in the quenching measurements. While f_{01} and F for $Ru(phen)_3^{2+}$ are similar, f_{01} for $Ru(bpy)_3^{2+}$ is slightly lower than for $Ru(phen)_3^{2+}$, but F is much higher. Thus, the evidence suggests that the two components in the quenching and the photochemical experiments do not represent the same population.

A corollary to the photochemical results is that most of the photochemistry occurs early. Therefore, to stabilize sensors, a preuse photolysis may destroy the more reactive component and leave only the more stable form.

Comparison of Complexes and Supports. Table I shows a number of interesting features. There is a wide range of behavior depending on complex and support. Note, in particular, the different behavior with different counterions for $Ru(4,7\text{-}Me_2phen)_3^{2+}$. The BPh_4^- systems have oxygen-quenching sensitivities much lower than those of the analogous ClO_4^- systems, and the differences are highly support dependent. In methanol there is no difference between the two species, while in RTV 615, the BPh_4^- salt is completely unquenched; this is in marked contrast to the perchlorate.

Tetraphenylborate is a quencher of the excited states of our metal complexes. Earlier, we exploited this fact to de-

termine whether the counterion was closely associated with the metal complex when the complex was bound to micelles. The closer the association, the more effective the counterion at quenching the complex (*16*). A similar argument would apply here. The less polar the environment, the more strongly the complex would ion pair with the quenching BPh_4^-, the shorter the lifetime, and the less the degree of oxygen quenching. Our results allow us to rank the polarity of the different polymers by their tendency to promote ion pairing.

In methanol, the solution is too dilute for the BPh_4^- to quench, and as expected, we see no differences between the perchlorate and BPh_4^- salts. In all the polymers, however, there is evidence for ion pairing; the $I_{nitrogen}/I_{air}$ values are always smaller for the BPh_4^- salts. The less polar the polymer the stronger the ion pairing and the poorer the O_2 quenching. Thus, experimentally, the polymer polarity decreases on going from RTV 118 to Dow 891 to RTV 615.

Even without BPh_4^-, there are large differences in polymer performance. RTV 615 has the poorest performance. This is a two-part polymer that is initiated with a free radical catalyst. We suspect that some of the catalyst persists in the polymer and quenches the sensor, thus degrading its performance. Even extended extraction with CH_2Cl_2 did not seem to reduce the quenching.

Also, one cannot use oxygen quenching in a homogeneous solvent such as methanol as a predictor of sensor performance in polymers. The methanol data would predict that $Ru(phen)_2(CN)_2$ would be markedly superior to $Ru(4,7\text{-}Me_2phen)_3^{2+}$, yet in all the polymer systems, the $Ru(4,7\text{-}Me_2phen)_3^{2+}$ is superior. Similarly, the methanol data predicts that $Ru(Ph_2phen)_3^{2+}$ will be the best sensor. While this is true in RTV 118 and Dow 891, $Ru(Ph_2phen)_3^{2+}$ is poorer than the other complexes in RTV 615.

ACKNOWLEDGMENT

We thank Seth Snyder for his assistance with the time-correlated single-photon lifetime system and with the deconvolution software.

LITERATURE CITED

(1) Chemical, Biochemical, and Environmental Fiber Sensors. *Proceedings of SPIE—the International Society for Optical Engineering*; Lieberman, R. A., Wlodarczyk, M. T., Eds.; SPIE: Bellingham, WA, 1989, Vol. 1172.
(2) Kalyansundaram, K. *Photochemistry in Microheterogeneous Systems*; Academic Press: New York, 1987.
(3) James, D. R.; Liu, Yuan-Sheng; DeMayo, P.; Ware, W. R. *Chem. Phys. Lett.* **1985**, *120*, 460.
(4) Simiarczuk, A.; Ware, W. R. *J. Phys. Chem.* **1989**, *93*, 7609.
(5) Carraway, E. R. Excited State Quenching of Immobilized Ruthenium-(II) Complexes. Ph.D. Thesis, University of Virginia, 1989.
(6) Carraway, E. R.; Demas, J. N. Unpublished results.
(7) Wolfbeis, O. S. *Chem. Anal. (N.Y.)* **1988**, *77*, 129.
(8) Peterson, J. I.; Fitzgerald, R. V.; Buckhold, D. K. *Anal. Chem.* **1984**, *56*, 62.
(9) Wolfbeis, O. S.; Posch, H. E.; Kroneis, H. W. *Anal. Chem.* **1985**, *57*, 2556.
(10) Lee, E. D.; Werner, T. C.; Seitz, W. R. *Anal. Chem.* **1987**, *59*, 279.
(11) Wolfbeis, O. S.; Weis, L. J.; Leiner, M. J. P.; Ziegler, W. E. *Anal. Chem.* **1988**, *60*, 2028.
(12) Bacon, J. R.; Demas, J. N. *Anal. Chem.* **1987**, *59*, 2780.
(13) Lees, A. J. *Chem. Rev.* **1987**, *87*, 711.
(14) Krause, R. A. *Structure and Bonding*; Springer-Verlag: Berlin, 1987; Vol. 67.
(15) Lin, C.-T.; Böttcher, W.; Chou, M.; Creutz, C.; Sutin, N. *J. Am. Chem. Soc.* **1976**, *98*, 6536.
(16) Hauenstein, B. L., Jr.; Dressick, W. J.; Gilbert, T. B.; Demas, J. N.; DeGraff, B. A. *J. Phys. Chem.* **1984**, *88*, 1902.
(17) Demas, J. N.; Turner, T. F.; Crosby, G. A. *Inorg. Chem.* **1969**, *8*, 674.
(18) Sacksteder, L.; Demas, J. N.; DeGraff, B. A. *Inorg. Chem.* **1989**, *28*, 1787.
(19) Snyder, S. W.; Demas, J. N. *Anal. Chem.* **1989**, *61*, 2704.
(20) O'Connor, D. V.; Phillips, D. *Time-Correlated Single Photon Counting*; Academic Press: New York, 1984.
(21) Carraway, E. R.; Demas, J. N.; DeGraff, B. A. *Anal. Chem.* **1991**, *63*, 332–336.
(22) Demas, J. N.; Demas, S. E. *Scientific Computing and Interfacing on Personal Computers*; Allyn & Bacon: New York, 1990.
(23) Mandel, K.; Pearson, T. D. L.; Krug, W. P.; Demas, J. N. *J. Am. Chem. Soc.* **1983**, *105*, 701.
(24) Krug, W. P.; Demas, J. N. *J. Am. Chem. Soc.* **1979**, *101*, 4394.
(25) Snyder, S. W.; Buell, S. L.; Demas, J. N.; DeGraff, B. A. *J. Phys. Chem.* **1989**, *93*, 5265.
(26) Reitz, G. A.; Demas, J. N.; Stephens, E.; DeGraff, B. A. *J. Am. Chem. Soc.* **1988**, *110*, 5051.
(27) Demas, J. N.; DeGraff, B. A. *J. Macromol. Sci., Chem.* **1988**, *A25*, 1189.
(28) Demas, J. N.; Harris, E. W.; McBride, R. P. *J. Am. Chem. Soc.* **1977**, *99*, 3547.
(29) Buell, S.; Demas, J. N. *J. Phys. Chem.* **1983**, *87*, 4675.
(30) Kearns, D. R. *Chem. Rev.* **1971**, *71*, 395.

RECEIVED for review August 3, 1990. Accepted November 1, 1990. We gratefully acknowledge the support of the National Science Foundation (Grants CHE 86-00012 and 88-17809).

Direct Analysis of Solid Powder Biological Samples Using a Magnetron Rotating Direct-Current Arc Plasma and Graphite Furnace Sample Introduction

David Slinkman[1] and Richard Sacks*

Department of Chemistry, University of Michigan, Ann Arbor, Michigan 48109

Solid powder samples deposited in a graphite tube furnace are vaporized and introduced into a magnetron rotating direct-current arc plasma. The arc plasma has the form of a radial current sheet that completely covers the end of the graphite anode. The sample vapor from the graphite furnace is forced to pass through the current sheet. This ensures adequate sample–plasma interaction and results in detection limits in the microgram/gram range. Analytical data will be presented for pure solid powder samples and for a number of NIST biological reference materials. Percent error values for the determination of various metallic elements using the method of standard additions ranged from 1.2% to 19.6%. Absolute detection limits at the subnanogram level are reported.

While most direct-current plasma (DCP) research has focused on solution sample analysis, recently there has been increased interest in the analysis of direct solid samples. The advantages of solid sampling include the saving of time and effort in the preparation of samples as well as the reduced risk of sample contamination and loss due to the sample preparation methods.

A number of authors (*1–3*) have used various forms of sample digestion and dissolution to determine various metals by DCP in complex matrices including animal tissue (*4*), plant tissue (*5*), aircraft lubricating oils (*6*), and environmental samples (*7*). While these methods produce adequate results, the complicated and time-consuming chemical pretreatments can be very cumbersome.

Fry and co-workers have investigated a variety of solid samples by nebulizing a slurry of suspended solids into the DCP (*8–10*). In this method, the solids are milled and suspended in a solution that is introduced into a clog-free Babington-type nebulizer. Laser ablation DCP spectrometry has been used by Sneddon and co-workers to sample metallic species in solid and pelletized powdered samples (*11*, *12*). In this work, a low-energy Nd:YAG laser ablates the sample, which is then carried to the DCP by a flow of Ar. Other forms of direct solid sampling include the introduction of a solid powder in a gas stream to a two-jet plasmatron (*13*) and the use of a ceramic nebulizer with a plastic spray chamber as a means of introducing dilute aqueous suspensions into a DCP (*14*).

Slinkman and Sacks (*15*, *16*) recently described a magnetron rotating DCP device that combines a hollow cylindrical graphite anode, a coaxial W/Th (4%) cathode wire, and a magnetic field parallel to the electrode axis to produce a rotation of the current channel in a motorlike fashion between the wire cathode and cylindrical anode. At sufficiently high rotational frequencies, the current channel assumes the form of a relatively uniform current sheet, which covers the end of the graphite tube anode. A tail flame extends for several millimeters above the current sheet. Sample is introduced by passing the aerosol or vapor through one end of the anode tube and forcing it to pass through the plasma tail flame at the other end of the tube.

The relatively short sample residence time in the high-temperature current sheet makes the device more useful for solution samples introduced from a graphite furnace (*17*) than for solutions nebulized into the plasma (*16*). The interface of the graphite furnace to the magnetron rotating DCP also makes possible the introduction of solids.

The analysis of solids has been carried out for years in graphite furnace atomic absorption spectrometry (*18–20*) with samples ranging from soil (*21*) to bovine liver (*22*). Electrothermal atomization has also been used to introduce solids into the ICP (*23–25*). An electrothermal atomizer has also been interfaced to a DCP to determine gold in solid algal cells (*26*).

This paper describes the application of the magnetron rotating DCP with graphite furnace sample introduction to the analysis of solid samples. Both pure metal powder samples and NIST biological reference materials were studied. Percent recovery data for both types of solid samples and detection limits for the determination of various metals in the NIST reference materials are presented.

EXPERIMENT DESIGN AND APPARATUS

Rotating Arc Design and Furnace Interface. The principle of operation of the magnetron rotating direct-current arc plasma has been presented in detail (*15*). Figure 1 shows a diagram of the magnetron rotating DCP, the graphite furnace, and the optical system used for this study. A radial electric field is generated in the arc plasma by the use of a cylindrical electrode geometry consisting of a W/Th (4%) wire cathode (W) and a coaxial graphite tube anode (A). The electrode axis is vertical, and an argon gas flow through the anode tube (Ar1) results in the arc forming between the cathode tip and the top inner edge of the anode tube. When this is combined with a coaxial magnetic field generated by a ceramic ring magnet (M), the $\mathbf{E} \times \mathbf{B}$ drift motion of the plasma electrons is in the azimuthal direction, and one end of the arc current channel rotates around the inner edge of the anode tube. The resulting plasma (P) is a diffuse, stable plume that covers the end of the anode cylinder. A ceramic insulator tube (T) prevents internal arcing. This system has been described in detail (*15*, *16*).

A graphite tube furnace (F) (Instrumentation Laboratory Model 555) was interfaced to the rotating DCP (*17*). A 7.5-cm-long, 3.0-mm-i.d. ceramic tube was placed in one end of the graphite furnace. Two pieces of Tygon tubing (9 cm long, 3-mm i.d.; and 6.5 cm long, 9-mm i.d.) connected the other end of the ceramic tube to the arc assembly. The sample was deposited into the furnace through the sample door (S). The argon sample vapor transport gas (Ar2) was introduced into the furnace chamber and flowed into the open end of the furnace to carry the sample vapor through the ceramic interface (I) and into the arc. The graphite furnace and DCP are powered by power supplies PS2 and PS1, respectively. Construction details and experimental conditions are found in Table I.

Optical and Electrical Monitoring. The monochromator conditions and the data collection procedure have been described previously (*17*). The electrode assembly was oriented with the

* Corresponding author.
[1] Present address: Nalco Chemical Co., Naperville, IL.

0003-2700/91/0363-0343$02.50/0

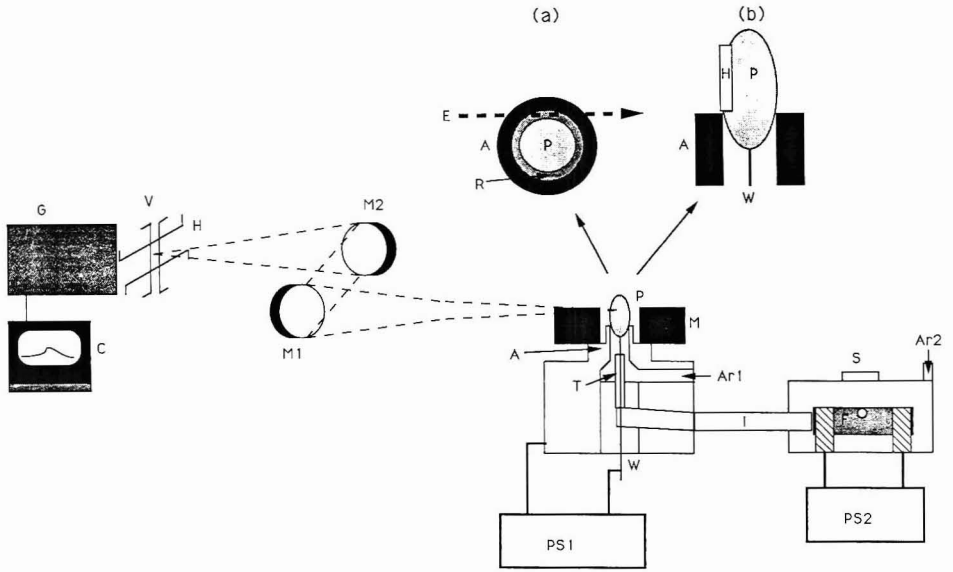

Figure 1. Schematic representation of instrumental setup. P, plasma; M, magnet; A, cylindrical hollow anode; T, ceramic insulator tube; W, W/Th cathode; Arl, Ar cooling gas; PS1, arc power supply; I, interface tube; F, graphite furnace; Ar2, Ar sample vapor transport gas; S, sample inlet; PS2, graphite furnace power supply; M1 and M2, over-and-under mirror configuration; V, spectrometer entrance slit; H, horizontal mask; G, monochromator; C, computer; R, analtye ring. inset on left (a) shows the view from above the arc and the horizontal viewing axis (E). Inset on right (b) shows the side view of the arc and the vertical observation window (H).

Table I. Construction Details and Experimental Conditions

rotating arc	
anode	graphite cylinder (Ultra Carbon Type UF/45), 5-mm i.d., 8-mm o.d., 13 mm long
cathode	W/Th (4%) rod, 1-mm diam
cathode insulator	Al_2O_3 tube, 3.0-mm i.d., 5.0-mm o.d., 25 mm long
current/voltage	12 A/74 V
gas flows	4.8 L/min Ar cooling gas, 1.0 L/min Ar sample vapor transport gas
magnet	ceramic alloy, 22-mm i.d., 60-mm o.d., 13-mm thick; peak field strength (vertical component) 0.90 kG
furnace	
tube	pyrolytic graphite, 5.0-mm i.d., 6.4-mm o.d., 38 mm long
gas flow	1.0 L/min Ar
interface	Al_2O_3 tube, 3.0-mm i.d., 5.0-mm o.d., 75-mm-long Tygon tube, 3-mm i.d., 9 cm long plus 9-mm i.d., 6.5 cm long

electrode axis in the vertical direction, parallel to the spectrometer slits. The image-transfer system used two 50-mm-diameter, 500-mm focal length spherical front-surface mirrors, M1 and M2, in an over-and-under configuration. The system had a lateral magnification of 2.0. The arc device was mounted on a translational stage, permitting the selection of both vertical and horizontal (normal to the optical axis) observation coordinates.

The plasma was viewed through a segment of the magnet that was cut out. The plasma was focused onto the vertical entrance slit (V) and the horizontal mask (H). The observation zones in the plasma are shown by the two insets. The side view of the arc (inset b) shows the vertical observation window (H), extending from the anode surface to 5 mm above the anode surface. The view from above the arc (inset a) shows the horizontal observation zone (E; optical axis). Previous studies (*16*) have shown that the sample appears to penetrate the plasma near the anode surface.

Table II. Furnace Temperature Program

element	ashing temp, °C	atomization temp, °C
Fe	1400	2400
Ni	1400	2500
Zn	700	1800
Cu	1000	2300
Mg	900	1700
Mn	1400	2200

The result is that the greatest analyte line intensities are found in a ring just above the inside anode wall. This is shown more clearly in inset a, where R represents the ring of greatest analyte emission.

Materials and Procedures. Both solid particle and solution residue samples were evaluated. Particle sizes of 5–10 and 20–30 μm of pure Mn and Ni were used for these studies. These size fractions are operationally defined as the portion of sieved powder retained by a specific size sieve and passed by another size sieve. The preparation of the NIST biological reference materials has been described in detail (27). The average particle size for these samples was reduced to less than 30 μm. Atomic absorption standards (1000 μg/mL, Aldrich, Milwaukee, WI) were used to prepare solution samples. Lower concentration solutions were prepared daily by serial dilution with distilled, deionized water.

The powder standards and NIST materials were weighed on a microbalance and suspended in 0.2% HNO_3. These suspensions were then mixed with an ultrasonic bath and a vortex mixer. Typically, 30-μL aliquots of suspensions were drawn and deposited into the graphite furnace while the suspension was still thoroughly mixed.

The furnace temperature program consisted of a 1.0-min desolvation step at 100 °C followed by a 5.0-s ashing step and a 5.0-s atomization step. The temperature value that resulted in the highest signal-to-background ratio for each element is listed in Table II. No visible condensation of analyte was observed along the transport lines. The initiation of the furnace heating cycle did not result in a major change in the plasma structure. The

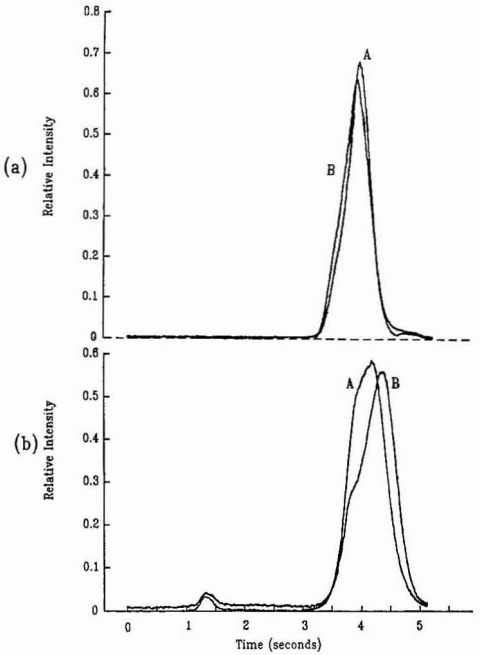

Figure 2. Emission wave forms for the Mn(II) 259.4-nm line (a) and the Ni(I) 305.0-nm line (b). All samples were present at the 1.2-μg level. In plots a, A is the signal from 20–30-μm Mn powder samples and B is from $Mn(NO_3)_2$ solution residue samples. In plots b, A is the signal from 20–30-μm Ni powder samples and B is from $Ni(NO_3)_2$ solution residue samples.

procedure for data manipulation has been described previously (*17*).

RESULTS AND DISCUSSION

Study of Pure Solids. Emission intensity vs time wave forms from pure solid powders were evaluated to test the ability of the furnace–DCP system to vaporize and excite the solids efficiently. Metal powders with particle sizes of 20–30 μm were vaporized in the furnace, and the emission wave forms were compared to wave forms from a corresponding amount of solution sample for the same metal. The emission wave forms are shown in Figure 2 where the relative intensity is plotted as a function of time for the Mn samples (a) and the Ni samples (b). The plots labeled A are for the solid powder samples, and plots labeled B are the signal from the solution samples. For both metals, the solution samples were prepared from the nitrate salts. The solid powder suspension and solution samples were prepared so that a 20-μL aliquot contained 800 ng of either Mn or Ni.

The Mn plots in Figure 2a show that the powder wave form and the solution wave form are very similar. The peak areas from 3 to 5 s show that the powder sample signal is only 1.3% larger than the solution signal. The Ni wave forms in Figure 2b show that the solid powder waveform A is symmetric, while the solution waveform B has a shoulder on the rising edge of the peak. The slight difference in peak structure could be an indication of different rates of atomization for the two sample forms. The peak area integrals from 3 to 5 s show that the signals are within 1% of each other.

These results also indicate that aqueous solution standards could be used in establishing calibration curves for the direct

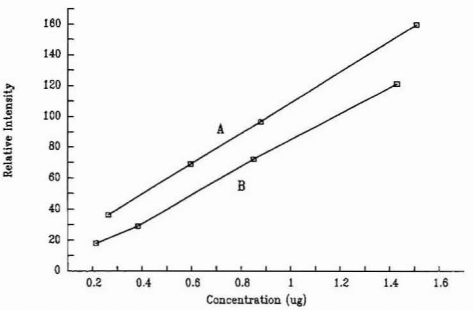

Figure 3. Analytical curves for Mn and Ni powder samples. In both cases, 5–10-μm powder samples were used. Each point represents the average peak area from four experiments.

elemental analysis of these solid powder samples. This would eliminate the need for using extremely small masses of powder samples and the errors due to powder-sampling statistics.

Analytical curves for both the Mn and Ni solid powder samples are shown in Figure 3. Particle sizes of 5–10 μm were used to reduce sampling errors. Each point is the average of at least four determinations. Correlation coefficients for both curves are greater than 0.999. The relative standard deviation (RSD) for most points was below ±8%; however, slightly larger values were obtained for the lower concentration samples.

Biological Sample Study. The rotating DCP–furnace technique was used for the analysis of six NIST solid powder biological reference materials, including pine needles (SRM 1575), oyster tissue (SRM 1566), bovine liver (SRM 1577), citrus leaves (SRM 1572), tomato leaves (SRM 1573), and rice flour (SRM 1568). These materials were chosen to represent a wide range of compositions.

Figure 4 shows the rotating DCP emission wave forms for an Fe(II) line in tomato leaves (a), pine needles (b), and bovine liver (c). Emission wave forms labeled A are average intensities from NIST reference materials, and wave forms labeled B are average intensities from equal amounts of Fe (with respect to the corresponding NIST reference material) present in aqueous solutions of $Fe(NO_3)_2$. In all cases, peak area values are larger for the solid powder sample than for the solution sample. The enhancement factors, defined as the ratio of the Fe signal in the solid powder sample to the signal in the solution sample, are 1.7, 1.5, and 2.0 for plots a, b, and c, respectively. The solid powder peaks not only are higher but are also wider than their corresponding solution peaks. All of the peaks are fairly symmetric except for the bovine liver sample in c where there is a significant decrease in the Fe(II) intensity from 3 to 3.5 s. This is probably the result of concomitant effects.

Previous work with the magnetron rotating DCP has shown that concomitant species can have a large effect on analyte signals (*28*, *29*). It has been shown that the addition of easily ionized elements (EIEs) to the rotating DCP can increase the temperature of the plasma up to 1000 K and can double the electron density (*28*). This results in an increase in the analyte signal for most elements (*29*). A decrease in the background intensity was also observed with the addition of an EIE.

The NIST reference materials used here all contain significant amounts of EIEs, and these elements are probably the cause of the results in Figure 4. The most prevalent concomitant species are K, Ca, and Na with weight percents nearing 5% for some of the samples. For the samples used in Figure 4, the tomato leaves contained 4.46% K and 3.00% Ca, the pine needles 0.41% Ca and 0.37% K, and the bovine liver 0.996% K and 0.243% Na. On the basis of previous work

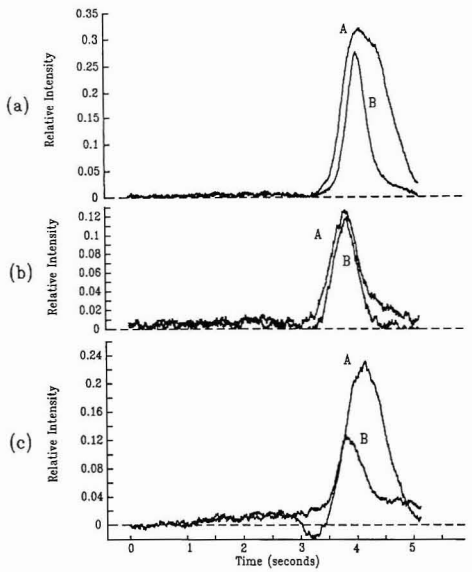

Figure 4. Emission wave forms from NIST reference materials for the Fe(II) 259.9-nm line. (a) Tomato leaves, (b) pine needles, (c) bovine liver. In all three sets, curve A is the emission wave form from Fe in the NIST reference material (solid powder), and curve B is the wave form from an equal amount of Fe as $Fe(NO_3)_2$.

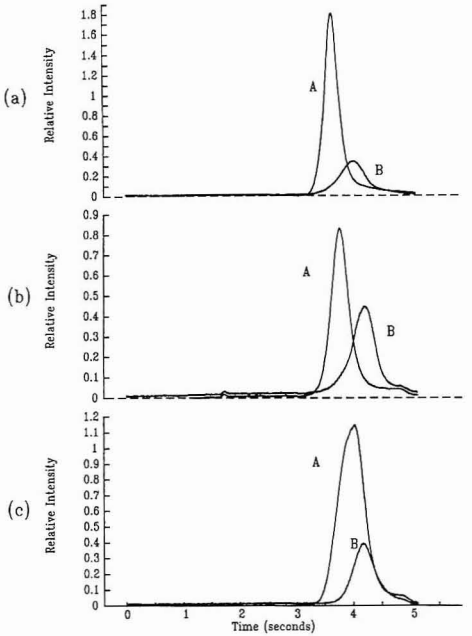

Figure 5. Emission wave forms from NIST reference materials for the Mg(II) 285.2-nm line. (a) Oyster tissue, (b) citrus leaves, (c) bovine liver. In all three sets, curve A is the emission wave form from Mg in the NIST reference material (solid powder), and curve B is the wave form from an equal amount of Mg as $Mg(NO_3)_2$.

(29), the concentrations of concomitant species in these samples could easily account for the enhancement effects as well as the decrease in background intensity observed.

Figure 5 shows Mg(I) wave forms for 1.0 μg/mL amounts of Mg in oyster tissue (a), citrus leaves (b), and bovine liver (c). Once again, the wave forms labeled A are average intensities from the NIST reference materials, and wave forms labeled B are average intensities from equal amounts of Mg present in aqueous solutions of $Mg(NO_3)_2$. The Mg(I) plots for the NIST samples also show large concomitant enhancement factors with values of 3.0, 1.5, and 3.6 for plots a, b, and c, respectively. The concomitant concentrations for oyster tissue are 0.15% Ca, 0.969% K, and 0.51% Na, and for citrus leaves, they are 3.15% Ca and 1.82% K.

Also note in Figure 5 that there is a temporal shift in the Mg(I) wave forms between the solid and solution samples. In all cases, the NIST reference material peak comes before the solution peak. This is seen dramatically in the oyster tissue (a) and the citrus leave (b) plots with the solid sample peak intensity value coming over 0.5 s before the corresponding solution sample peak intensity. A much smaller change occurs in the bovine liver (c) wave form. This suggests that the sample matrix is influencing the temporal release of the Mg during atomization in the furnace and acting as a matrix modifier in increasing the volatility of the Mg.

The matrix-effect data from Figures 4 and 5 as well as data from other elements in the NIST samples are presented in Table III. The lowest enhancement factor of 1.1 was obtained for Zn(I) in rice flour, while the highest enhancement factor of 3.6 was obtained for Mg(I) in bovine liver. Note that the concomitant concentrations in the rice flour are very low with only 0.112% K and 0.014% Ca.

These enhancement factors suggest that it would be difficult to use aqueous solutions as standards for the NIST reference materials. Two attempts were made to reduce the matrix enhancement effects so that it would be possible to use solution standards. The first attempt involved using the ashing step to volatilize selectively the concomitant species. The second involved matrix matching. It was found that most K solutions were volatilized with the ashing temperatures used; however, the Ca and Na solutions were not. The ashing

Table III. Concomitant Effects Obtained with Biological Samples

sample	element	λ, nm	concn, μg/mL	concomitant enhancement factor
oyster tissue SRM 1566	Zn(I)	213.8	2	2.4
	Mg(I)	285.2	1	3.0
	Mg(II)	279.5	1	2.6
	Fe(II)	259.9	1	2.7
bovine liver SRM 1577	Mg(I)	285.2	1	3.6
	Fe(II)	259.9	1	2.0
pine needles SRM 1575	Mn(II)	259.4	2	2.4
	Fe(II)	259.9	0.6	1.5
citrus leaves SRM 1572	Mg(I)	285.2	1	1.5
	Mg(II)	279.5	1	1.9
tomato leaves SRM 1573	Fe(II)	259.9	2	1.7
rice flour SRM 1568	Zn(I)	213.8	0.4	1.1

Table IV. Determination of Elements in NIST Reference Materials

sample	element line, nm	certified value, μg/g	found value, μg/g	% error
tomato leaves SRM 1573	Zn(I) 213.8	62 ± 6	73 ± 7.3	+17.7
	Mn(II) 259.4	238 ± 7	218 ± 15.8	−8.4
bovine liver SRM 1577	Zn(I) 213.8	123 ± 8	125 ± 3.4	+1.6
	Cu(I) 324.7	158 ± 7	189 ± 1.9	+19.6
	Mg(I) 285.2	600 ± 15	560 ± 23.5	−6.7
pine needles SRM 1575	Fe(II) 259.9	200 ± 10	192 ± 3.1	−4.0
	Mn(I) 259.4	675 ± 15	651 ± 41.7	−3.5
oyster tissue SRM 1566	Zn(I) 213.8	852 ± 14	865 ± 100.3	+4.7
citrus leaves SRM 1572	Mg(I) 285.2	5800 ± 174	5869 ± 255.2	+1.2

temperatures needed to clean the system of Ca and Na often lead to a major loss in the analyte as well.

Matrix matching was attempted with the NIST materials that had the lower concentrations of concomitant species. A bovine liver sample and a corresponding solution sample were made 0.04 M in Na and 0.001 M in Ca. These concentrations are over an order of magnitude higher than the concentrations in the solid sample so that any enhancement seen should be due almost entirely to the added matrix modifiers. The enhancement factors did decrease with the use of the matrix modifiers, but the values were not acceptable. Without the matrix modification, a Mg(II) line in bovine liver showed an enhancement factor of 2.8, and with the modified matrix, the enhancement factor decreased to 1.6. Similar decreases in the enhancement factor were observed for Cu(I) and Zn(I) lines; however, the values were still significantly greater than 1.0, suggesting that matrix effects are associated with the atomization processes in the furnace. These severe matrix effects also have been seen in the analysis of similar samples with graphite furnace ICP techniques (*24*).

Due to the observed matrix effects, determination of metallic elements in the NIST reference materials was carried out by the standard addition method. Table IV shows the results for standard additions of various elements in five NIST reference materials. Seven of the nine determinations have errors of less than 10%, with the largest error being about 20%. These percent error values compare favorably to similar determinations in biological samples using graphite furnace techniques (*18*, *21*) and graphite furnace ICP techniques (*23*, *24*). These encouraging results demonstrate that, even for difficult sample matrices, standard addition methods can be used with the rotating DCP to determine metallic elements in solid powder samples.

The limits of detection achieved for the NIST solid samples for various elements are listed in Table V. Detection limits are defined as the concentration producing a net analyte emission intensity equivalent to 3 times the standard deviation of background emission intensity. The detection limits are in the microgram/gram range with absolute detection limits in the nanogram and subnanogram range.

It is interesting to note that for both Mg(I) and Mn(II) there is an order of magnitude difference in detection limits in the different NIST reference materials, while the Zn(I) detection limits show very little dependence on the sample. The detection limits for Mn(II) in pine needles is 6.4 μg/g, and in

Table V. Detection Limits Obtained for NIST Reference Materials

sample	element	λ, nm	concn, μg/g	abs amt, ng
citrus leaves SRM 1572	Mg(I)	285.2	7.8	0.122
tomato leaves SRM 1573	Mn(II)	259.4	0.5	0.122
	Zn(I)	213.8	0.4	0.180
	Fe(II)	259.9	17.2	3.000
bovine liver SRM 1577	Mg(I)	285.2	4.3	0.090
	Cu(I)	324.7	0.7	0.300
	Zn(I)	213.8	0.8	0.300
pine needles SRM 1575	Mn(II)	259.4	6.4	1.000
	Fe(II)	259.9	5.3	1.320
oyster tissue SRM 1566	Mg(I)	285.2	0.2	0.010
	Zn(I)	213.8	2.8	0.210

tomato leaves, the value drops to 0.5 μg/g. The concomitant species concentrations in the tomato leaves are nearly an order of magnitude higher than in pine needles, and increased signal enhancement caused by the greater concentrations of EIE in the matrix could account for the improved detection limits. The invariance of the detection limits for Zn(I) could result from Zn not being as susceptible to matrix effects as the other elements. Previous work (*29*) with solution samples showed that Zn signals were relatively independent of the presence of an EIE while Mg and Mn signals showed relatively large EIE enhancements.

The detection limits achieved with the rotating DCP–furnace system compare very well with those obtained by other forms of solid sample introduction into the DCP. The 20 and 10 μg/g detection limits for Cu in laser ablation DCP (*12*) and by sample dissolution techniques (*1*), respectively, are significantly greater than the 0.7 μg/g limit achieved in this work. The 3 μg/g detection limit for Mn in the two-jet plasmatron (*13*) is close to the 6.4 μg/g limit obtained in this study. Detection limits as low as 10 ng/g have been obtained for Fe in a solid powder sample with an electrothermal ICP system (*25*); however, the significantly better detection limits achieved with the ICP may be offset in part by the lower initial and operating costs of the magnetron rotating DCP system.

The preliminary study presented here demonstrates that solid powder biological samples can be vaporized, atomized, and excited in the magnetron rotating DCP with graphite furnace sample introduction. With a few minutes of grinding as the only sample preparation needed, this method provides a rapid and direct method for trace and minor components analysis in a variety of biological materials. The ability to use solution standards with the standard addition method for the direct analysis of solids also eliminates the need for preparing powder standards, which can be difficult, time-consuming, and lead to significant sampling errors with low-concentration standards.

LITERATURE CITED

(1) Natansohn, S.; Czupryna, G. *Spectrochim. Acta* **1983**, *38B*, 317.
(2) Bankston, D. C.; Fisher, N. S. *Anal. Chem.* **1977**, *49*, 1017.
(3) Potter, N. M.; Vergosen, H. E., III. *Talanta* **1985**, *32*, 545.
(4) Frank, A.; Peterson, L. R. *Spectrochim. Acta* **1983**, *38B*, 207.
(5) Lajunen, L. H. J.; Kubin, A. *Talanta* **1986**, *33*, 265.
(6) Brown, J. R.; Saba, C. S.; Rhine, W. E.; Eisentraut, K. J. *Anal. Chem.* **1980**, *52*, 2365.
(7) Grogen, W. C. *Spectrochim. Acta* **1983**, *38B*, 357.
(8) McCurdy, D. L.; Wichman, M. D.; Fry, R. C. *Appl. Spectrosc.* **1985**, *39*, 984.
(9) Wichman, M. D.; Fry, R. C.; Hoffman, M. K. *Appl. Spectrosc.* **1986**, *40*, 351.
(10) Vien, S. H.; Fry, R. C. *Appl. Spectrosc.* **1988**, *42*, 381.
(11) Mitchell, P. G.; Sneddon, J.; Radziemski, L. J. *Appl. Spectrosc.* **1986**, *40*, 274.

(12) Mitchell, P. G.; Sneddon, J.; Radziemski, L. J. *Appl. Spectrosc.* **1987**, *41*, 141.
(13) Yudelevich, I. G.; Cherevko, A. S.; Engelsht, V. S.; Pikalov, V. V.; Tagiltsev, A. P.; Zheenbajev, Zh. *Spectrochim. Acta* **1984**, *39B*, 777.
(14) Derie, R. *Anal. Chim. Acta* **1984**, *166*, 61.
(15) Slinkman, D.; Sacks, R. *Appl. Spectrosc.* **1990**, *44*, 76.
(16) Slinkman, D.; Sacks, R. *Appl. Spectrosc.* **1990**, *44*, 83.
(17) Slinkman, D.; Sacks, R. *Anal. Chem.* **1990**, *62*, 1656.
(18) Rettberg, T. M.; Holcombe, J. A. *Anal. Chem.* **1986**, *58*, 1462.
(19) Langmyhr, F. J. *Analyst* **1979**, *104*, 993.
(20) L'vov, B. V. *Talanta* **1976**, *23*, 109.
(21) Vollkopf, U.; Grobenski, Z.; Tamm, R.; Welz, B. *Analyst* **1985**, *110*, 573.
(22) Chakrabarti, C. L.; Karwowska, R.; Hollobone, B. R.; Johnson, P. M. *Spectrochim. Acta* **1987**, *42B*, 1217.
(23) Blakemore, W. M.; Casey, P. H.; Collie, W. R. *Anal. Chem.* **1984**, *56*, 1376.
(24) Aziz, A.; Broekaert, J. A. C.; Leis, F. *Spectrochim. Acta* **1982**, *37B*, 369.
(25) Reisch, M.; Nickel, H.; Mazurkiewicz, M. *Spectrochim. Acta* **1989**, *44B*, 307.
(26) Greene, B.; Mitchell, P. G.; Sneddon, J. *Spectrosc. Lett.* **1986**, *19* (2), 101.
(27) Brewer, S. W., Jr.; Sacks, R. D. *Anal. Chem.* **1988**, *60*, 1769.
(28) Slinkman, D.; Sacks, R. *Appl. Spectrosc.*, in press.
(29) Slinkman, D.; Sacks, R. *Appl. Spectrosc.*, in press.

RECEIVED for review August 9, 1990. Accepted November 5, 1990.

Quantitation of Acidic Sites in Faujasitic Zeolites by Resonance Raman Spectroscopy

Robert D. Place[1] and Prabir K. Dutta*

Department of Chemistry, The Ohio State University, 120 W. 18th Avenue, Columbus, Ohio 43210

This paper examines the selective excitation of the Raman spectra of dye molecules adsorbed on acidic zeolite surfaces. By taking advantage of the strongly allowed transitions in these dye molecules (large extinction coefficients) and the different absorption maxima of the conjugate acid and base forms of the dye, selective enhancements of the Raman bands specific to each form can be obtained. The focus has been on the dye molecule, 4-(phenylazo)diphenylamine (PDA), adsorbed onto the faujasitic zeolite, NaY. A calibration curve of Raman intensity (peak area) versus number of protons in supercages was obtained. Because of the inner filter effect, at loadings significantly greater than 1 proton per supercage, the Raman intensity was found to decrease. The sensitivity of the Raman method at low proton loadings appears to be considerably better than the typical infrared methods used to estimate acidity on catalyst surfaces.

INTRODUCTION

The acidic properties of zeolites play a central role in their catalytic behavior in a wide variety of chemical- and petroleum-related processes (*1*, *2*). Considerable research has been done in developing methods for measurement of distribution of acidic functionalities in these and other solid materials. Amongst the classical methods for measuring acidic properties of solid acid surfaces are color changes of indicators adsorbed on surfaces and butylamine titration of the surface in the presence of Hammett indicators (*3*, *4*). Infrared spectroscopy of basic molecules such as ammonia and pyridine adsorbed onto the acidic sites also provides for quantitative estimation of Bronsted and Lewis acid sites (*5*). The attractive feature of the Hammett indicator method is that the distribution of acid strengths in zeolites can be studied by choosing indicators of various pK_a's. The cautionary aspect of this method is to choose dyes that can penetrate into the zeolite supercages through the 12-membered-ring openings (~7–8 Å). However, there are several shortcomings of the Hammett indicator approach. First, in order for the dyes to be successfully used, there must be a perceptible change in color, implying that the spectral shift between the acid and the base forms be significant. This is especially a problem with lower pK_a (<1) indicators. In addition, there is often a change in color due to adsorption effects alone (*6–8*). These problems can be circumvented to some degree by obtaining the electronic spectra of the solid (*9*, *10*). However, because of significant band broadening on the solid surfaces, often there is overlap in the electronic spectra between the acid and basic forms. New electronic bands may also appear in the spectrum, e.g., 4-nitrotoluene exhibits only one band at 380 nm in acidic solutions, but three bands were reported at 300, 340, and 500 nm on an acidic aluminosilicate surface (*11*).

We reasoned that it may be possible to use the resonance Raman effect in order to distinguish between the acid and base forms, as well as to quantitate the amount of acidic form (and hence the acidity of the solid surface) from the Raman signal. In this paper, we illustrate this principle by using the dye molecule 4-(phenylazo)diphenylamine (PDA, see below) and various loadings of protons for the acidic form of zeolite Y.

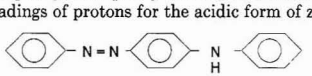

(PDA)

Resonance Raman spectroscopy involves excitation into an electronic band of the chromophore, which can result in enhancement of the Raman signal by orders of magnitude. Since the Raman spectrum is a vibrational signature of the chromophore and the Raman bandwidths are typically 10 cm^{-1}, this technique provides the potential for high selectivity and sensitivity (*12*). The latter can be particularly high in the case of dye molecules, since the extinction coefficient, or absorptivity, of these molecules is large and the resonance Raman intensity scales as the square of this parameter (transition moment terms in the numerator for the dipole-allowed transition in the *A* term) (*13*). In principle, this makes it possible to examine zeolite materials with low levels of acidity. In addition, since laser excitation is readily available in a continuously tunable fashion ranging from the near ultraviolet to the visible, the choice of dye molecules is also clearly no longer restricted (*14*). We illustrate below some of these features of resonance Raman spectroscopy using the dye

[1] Permanent address: Department of Chemistry, Otterbein College, Westerville, OH 43081.

0003-2700/91/0363-0348$02.50/0

molecule PDA and zeolite Y. The choice of this dye molecule was dictated by several factors: these include the size of this molecule (~7 × 24 Å), which allows it to penetrate into the zeolite cages, and also the fact that its acidic and basic forms have well-separated absorption maxima at 540 and 410 nm, respectively (*10*), and are therefore readily accessible with Ar and Kr ion lasers. The focus in this preliminary paper is primarily to illustrate that resonance Raman spectroscopy can be developed as a quantitative technique to examine acidic sites on solid surfaces in general.

EXPERIMENTAL SECTION

Zeolite Y was obtained from Union Carbide (LZY-52) and was ion-exchanged with ~1 M NaCl to ensure that all cationic sites were occupied by Na^+ ions and that excess OH^- ions were removed from the sample. These samples were then ion-exchanged with NH_4Cl to provide loadings of 0.61, 0.95, 1.3, 1.7, 3.5, and 6.4 protons per supercage as validated by analysis for Na^+ ions in the wash solutions using atomic emission spectroscopy. The choice of these loadings was made on the basis of the sensitivity of the pyridine IR method and is discussed in the Results and Discussion section. All other chemicals were used as received, including the dye, 4-(phenylazo)diphenylamine ($C_6H_5N_2C_6H_4NHC_6H_5$) from Aldrich.

Each of the different $NaNH_4Y$ samples was pressed into a 12-mm (125-mg) pellet at 3000 psi and was heated to 500 °C over a 2-h period. The sample was maintained at this temperature for 2.5 h under vacuum of 10^{-4} Torr in order to drive off NH_3 and replace each NH_4^+ with H^+ and generate the various proton loadings of NaHY. After 2 h at 500 °C, 1 atm of oxygen gas was added for 15 min to oxidize and vaporize impurities that were then evacuated. The sample treatment necessary to obtain Raman spectra from zeolites has been described in the literature (*15*). After the samples were cooled quickly to room temperature, pure ethanol was distilled onto and covered the pellet. The sample was allowed to equilibrate at room temperature overnight under 1 atm of nitrogen. This was done to ensure that ethanol was present through the zeolite, thus facilitating the movement of the dye. After this step, the zeolite sample was always maintained in a drybox or a sealed container until after the Raman and electronic spectra were recorded.

Each zeolite sample was pulverized under ethanol, and then 5 mL of 7.1×10^{-4} M solution of the indicator in ethanol was added for 1.5 h. The excess ethanol was then evaporated off, and as the last traces of ethanol were removed, the yellow zeolite samples turned to the final purple intensity in less than 1 min.

The zeolite was then reground, pressed into a pellet, cut in half, and clamped into a Raman cell along with half a pellet of KNO_3 of the same thickness, which acted as an external standard. The Raman cell was rotated at 30 rev/s while the spectrum was collected, thus ensuring that the laser sampled each half of the pellet about 50% ± 2% of the time. A number of scans were recorded with the laser focused on different positions of each pellet and then summed to produce the quantitative spectra.

The Raman spectra were collected by excitation with 514.5-nm radiation from an Ar ion laser (Spectra Physics 171) or 406.7 nm radiation from a Kr ion laser (Coherent Innova K100). The scattered light was filtered through a Spex 1403 double monochromator and detected with an RCA C31034 GaAs PMT. The diffuse reflectance electronic spectra were recorded on a Shimadzu (Model 265) spectrometer. The integrity of the zeolite sample throughout the experimental procedure was verified by powder diffraction patterns with a Rigaku D/Max-B diffractometer. The infrared spectra were obtained on self-supporting 20-mg wafers in a transmission anaerobic cell on a Perkin-Elmer 1600 FTIR spectrometer.

RESULTS AND DISCUSSION

Figure 1 shows the resonance Raman spectrum of the dye molecule in the free base (2% KBr pellet) and protonated forms (acidified with 1 M H_2SO_4 in methanol). Figure 2 shows the electronic spectra of these species and includes the excitation laser frequencies used to produce the resonance Raman spectra. Comparison of Figures 1 and 2 confirms clearly that the Raman spectra of the base and acid forms are distinct.

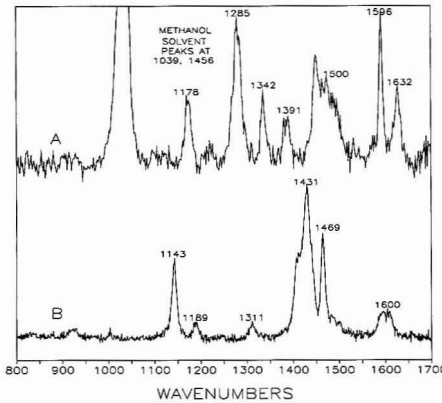

Figure 1. Resonance Raman spectra of PDA (A) in its acidic form (acidified methanol, excitation 514.5 nm) and (B) as a free base (2% KBr pellet, excitation 406.7 nm).

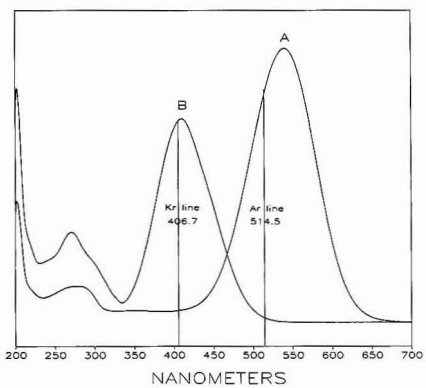

Figure 2. Electronic spectra of (A) acidic and (B) basic forms of the dye. (The Raman excitation lines are also shown in the figure.)

This is a reflection of the fact that the electronic structure of the molecule undergoes considerable changes upon protonation. In the basic form of the molecule, the electronic band at 410 nm has been assigned to a charge-transfer transition from the amino group to the azo group (*16*). Raman and IR data for a variety of azo compounds have been reported, along with band assignments (*17*). Two of the prominent bands at 1143 and 1431 cm^{-1} in Figure 1B (base form) are assigned to C—N and N=N stretches, respectively. The other bands at 1189, 1311, 1469, and 1600 cm^{-1} have been assigned to the phenyl ring modes. Considering the charge-transfer nature of this electronic band, it is not surprising that the most strongly enhanced Raman band is the N=N stretching of the azo group. Upon protonation, both the electronic and resonance Raman spectra exhibit considerable changes. There are two sites of protonation on this molecule, the azo group and the secondary amine. Primarily because of the long wavelength shift of the electronic band and the increase in absorptivity, the azo group has been thought to be more likely the center for protonation since resonance structures, such as drawn below, delocalize the positive charge (*18*).

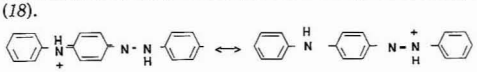

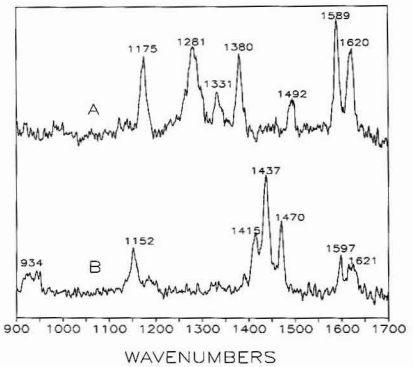

Figure 3. Resonance Raman spectra of PDA impregnated onto HY. Excitation at (A) 514.5 nm for the acid form and (B) 406.7 nm for the base form.

Resonance structures are not possible if the amino group is protonated. The disappearance of the N=N stretching band in the acid spectrum at 1434 cm^{-1} also supports this site for protonation. The new set of bands observed in the Raman spectra are also more appropriate for the charge-delocalized structure shown above. The band at 1632 cm^{-1} is typical for a C=N stretch, and the most prominent band at 1285 cm^{-1} is characteristic of quinone-like structures (*19*). The only major band that appears to remain close to the same frequency in both the acid and base forms is the band at 1596 cm^{-1} and is characteristic of monosubstituted benzene. It is quite clear from Figure 1 that, by selective choice of excitation wavelength, distinct resonance Raman spectra of acid and base forms can be readily observed.

In order to illustrate the selectivity of the Raman spectra on the zeolite surface, we treated a sample of zeolite HY with *excess* indicator. Figure 3 shows the resonance Raman spectra obtained at excitation wavelengths of 406.7 and 514.5 nm, in resonance with the basic and acidic forms of the indicator molecule, respectively. Comparison with Figure 1 will confirm that we are indeed observing separately both the basic and acidic forms of the molecule on the same zeolite sample simply by virture of choice of the excitation wavelength. Neither spectrum contains the Raman features assigned to the other form. Shifts of up to ~12 cm^{-1} are observed in some of the Raman bands upon interaction with the zeolite surface as compared to spectra in Figure 1 of the dye in solution or on the solid KBr.

The final part of this study concentrated on the ability to correlate the Raman intensities of the protonated form of the dye on NaHY to the amounts of acidic groups introduced into the zeolite. These acidic groups were introduced by partial exchange of Na^+ ions by NH_4^+ followed by calcination to generate NaHY. In order to exploit the sensitivity of resonance Raman spectroscopy, the loading levels were chosen to be in the range of 1 proton per supercage. At these loadings, the signals for the pyridinium ion in the conventional pyridine IR method is low. Figure 4 compares with the IR spectra for pyridine on completely exchanged HY and NaHY partially exchanged with a loading of 0.95 proton per supercage. The band at 1545 cm^{-1} due to protonated pyridine and indicative of Bronsted acidity is considerably weaker in the NaHY sample because of the low loading of protons (*20*). As a matter of fact, the NaHY intensity at 1545 cm^{-1} is the same as that of a totally unprotonated sample.

Since it is unlikely that more than one dye molecule can fit into a supercage, it was appropriate to keep the loading

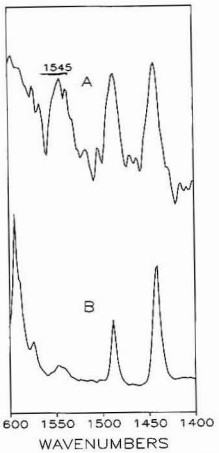

Figure 4. FTIR spectra of pyridine absorbed on (A) HY and (B) NaHY (0.95 proton per supercage).

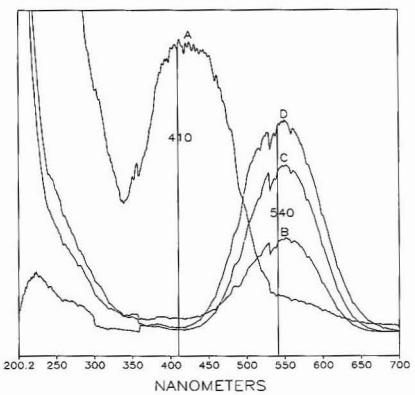

Figure 5. Diffuse reflectance electronic spectra of PDA adsorbed on NaHY. The proton loadings were (A) 0, (B) 0.61, (C) 1.7, and (D) 6.4 protons per supercage.

levels around 1 H^+ per supercage. However, the observations during the reaction of the dye with acidified zeolites indicate that the protons may have considerable mobility (*21*). For example, when ethanolic solutions of the dye are in contact with the NaHY sample, the zeolite retains the yellow color characteristic of the basic form of the dye. Only after all the ethanol is removed from the sample does the blue color of the protonated dye develop. This clearly indicates that the acidic sites generated at these low loadings (1 H^+ per supercage) are strong enough to protonate C_2H_5OH ($pK = 2.3$). The fact that the ethanol was indeed protonated was confirmed by replacing ethanol with benzene as solvent, in which case the purple color of the protonated dye was observed immediately after contact with NaHY. With benzene as a solvent, irregular intensities were observed for Raman bands, and that was the motivation for changing the solvent to ethanol. The reason for this is unclear but could relate to the difficult transport of the polar dye molecule in the strongly polar environment of the zeolite by the hydrophobic solvent, benzene. The protonation of ethanol and its subsequent migration through the zeolite system appears to result in more uniform reaction with the

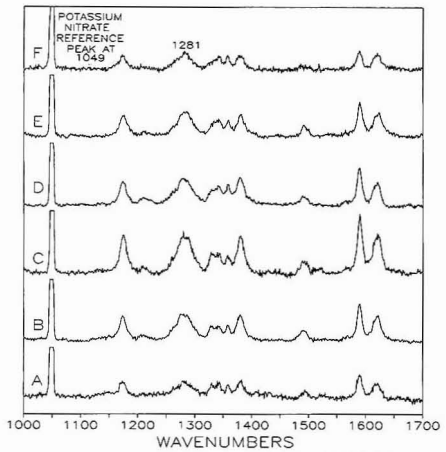

Figure 6. Resonance Raman spectra of PDA on NaHY. The spectra have all been normalized to the KNO_3 peak at 1049 cm^{-1}. The proton loadings are (A) 0.61, (B) 0.95, (C) 1.3, (D) 1.7, (E) 3.5, and (F) 6.4 protons per supercage.

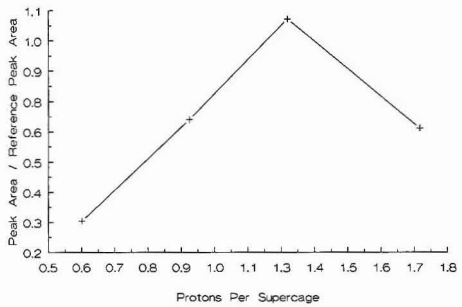

Figure 7. Plot of the integrated Raman peak area intensities of the 1281-cm^{-1} band versus proton loading.

dye molecules than in the case of benzene.

Figure 5 shows the diffuse reflectance spectra of the dye–zeolite system for NaHY with various degrees of protonation. In the absence of protons on the zeolite, the electronic spectrum resembles that of the free base form (Figure 2B), except that the 410-nm peak is considerably broadened and shifted slightly. With increasing H^+ concentration on the zeolite, the band at 540 nm due to the acidic form is observed and increases with increasing H^+ loading on NaHY. Figure 6 shows the resonance Raman spectra at various loadings. The peak at 1049 cm^{-1} is due to the NO_3^- ion, which is used as the external standard, and all of the spectra have been normalized to this peak. What is apparent from the Raman intensities of the acidic form is that they initially increase with the number of acidic sites in the zeolite. The integrated areas under the strongest Raman band (1281 cm^{-1}) as a function of the amount of acidic groups are plotted in Figure 7. The other bands show similar trends. Even though the electronic spectrum shows an increase in the intensity of the 540-nm band due to the acidic form of the dye, the decrease in Raman intensity beyond 1.3 protons per supercage arises from the self-absorption of the Raman scattered photon by the higher surface concentration of absorbing dye molecules. Quantitation by addition of an internal standard would alleviate this problem (22). However, since an activated zeolite is very reactive, the complications of interactions with the internal standard would have to be taken into consideration. We are presently examining such systems. However, the data in Figures 6 and 7 show that it is indeed possible to obtain selective resonance Raman spectra by choosing the proper excitation wavelength and use Raman intensities to construct calibration curves. Presently, efforts are underway to study dyes with lower pK_a's that exhibit significant overlap in the electronic spectrum before and after protonation, with particular emphasis on benzalacetophenone ($pK_a \sim -5.6$).

ACKNOWLEDGMENT

We thank Wayne Turbeville for his helpful assistance and ideas in the data collection and analysis. R. Place also thanks Otterbein College for a sabbatical leave which allowed time for this work to be completed.

LITERATURE CITED

(1) Olson, D. H.; Haag, W. O.; Lago, R. M. *J. Catal.* **1980**, *61*, 390.
(2) Ward, J. W. *Appl. Ind. Catal.* **1984**, *3*, 271.
(3) Benesi, H. A. *J. Phys. Chem.* **1957**, *61*, 970.
(4) Beaumont, R.; Barthomeuf, D. *J. Catal.* **1972**, *27*, 45.
(5) Ward, J. W. *J. Catal.* **1968**, *10*, 34.
(6) Deeba, M.; Hall, W. K. *J. Catal.* **1979**, *60*, 417.
(7) Deeba, A. K.; Curthoys, G. *J. Chem. Soc., Faraday Trans. 1* **1983**, *29*, 147.
(8) Kladnig, W. F. *J. Phys. Chem.* **1979**, *83*, 765.
(9) Drushel, H. V.; Sommers, A. L. *Anal. Chem.* **1966**, *38*, 1723.
(10) Anderson, M. W.; Klinowski, J. *Zeolites* **1986**, *6*, 150.
(11) Tape, J.; Tsuruya, T.; Sato, T.; Yoneda, Y. *Bull. Chem. Soc. Jpn.* **1972**, *45*, 3409.
(12) Long, D. A. *Raman Spectroscopy*; McGraw-Hill: New York, 1977.
(13) Albrecht, A. C.; Hutley, M. C. *J. Chem. Phys.* **1971**, *55*, 4438.
(14) Asher, S. A.; Johnson, C. R.; Murtaugh, J. *Rev. Sci. Instrum.* **1983**, *54*, 1657.
(15) Zaykoski, R.; Dutta, P. K. *Zeolites* **1988**, *8*, 179.
(16) Griffiths, J.; Roospeikar, B. *J. Chem. Soc., Perkin Trans. 1* **1976**, 42.
(17) Hacker, H. *Spectrochim. Acta* **1965**, *21*, 1989.
(18) Liler, M. *Adv. Phys. Org. Chem.* **1975**, *11*, 308.
(19) Lopex-Garriga, J. J.; Babcock, G. T.; Harrison, J. F. *J. Am. Chem. Soc.* **1986**, *108*, 7261.
(20) Liengne, B. V.; Hall, W. K. *Trans. Faraday Soc.* **1967**, *62*, 3232.
(21) Lohse, U.; Stach, J.; Thamm, H.; Schirmer, W.; Isirikjan, A. A.; Regent, N. I.; Dubinin, M. M. *Z. Anorg. Allg. Chem.* **1980**, *460*, 179.
(22) Shriver, D. F.; Dunn, J. B. R. *Appl. Spectrosc.* **1974**, *28*, 319.

RECEIVED for review August 21, 1990. Accepted November 16, 1990.

Influence of Carrier Molecules on the Intensity of Biomolecule Ions in Plasma Desorption Mass Spectrometry

A. Grey Craig* and Hans Bennich

Department of Immunology, Box 582, Uppsala University, S-75123 Uppsala, Sweden

The intensity of insulin and melittin singly charged molecule ions is suppressed when the sample is mixed with either a lysozyme carrier or bovine serum albumin (BSA) carrier. The suppression with a BSA carrier is shown to be dependent on the carrier concentration. In contrast, luteinizing hormone releasing hormone or glutathione when mixed with insulin or melittin does not result in suppression. These results suggest sample preparation procedures to increase the sensitivity with mass spectrometry.

INTRODUCTION

Plasma desorption mass spectrometry (PDMS) (*1*) and liquid secondary ion mass spectrometry (LSIMS) (*2*) have proven to be suitable techniques for the analysis of peptides and proteins (*3, 4*). This has led to a variety of situations where it is necessary to measure the mass spectrum of a peptide in the presence of another component, for example, the analysis of various molecular forms of a protein (*5, 6*) or the analysis of a peptide together with impurities (*7–9*). Alternatively, analysis may be required of purified peptides together with the products from enzymatic manipulation (*10–14*).

In the LSIMS experiment, kiloelectronvolt ions or atoms bombard the sample dissolved in a low volatility liquid, typically glycerol (*2*). A high primary ion flux ensures sufficient secondary ions to make LSIMS suitable for a variety of mass analyzers (*15*). The liquid matrix is important for reducing the effects of the damage caused by the high flux of primary ions (*15*). However, suppression of one component in a mixture of peptides has been observed (*10*). Since LSIMS analysis requires dispersion of the sample through the matrix or deposition of the sample on the surface of the matrix (*16*), the suppression has been attributed to a reduced relative surface concentration of the component (*10, 17, 18*). This selectivity has been correlated with the peptide's hydrophobicity/hydrophilicity (*19*). It has also been noted that the relative gas-phase basicity of the different molecules in a mixture correlates with the observed suppression (*20*).

PDMS uses high-energy ions, typically ^{252}Cf fission fragments, to bombard the solid sample placed on a thin metal film (*21*). The low flux of primary ions in PDMS essentially eliminates the problem of sample damage. However, because of the low flux, PDMS requires a high-transmission mass analyzer, such as the time-of-flight technique (*22*). Peptide samples prepared for PDMS are usually electrosprayed (*23*) alone or together with a coanalyte such as glutathione (*24*) or are applied to a nitrocellulose matrix (*25*). The sample applied to the nitrocellulose matrix can be contrasted with the coelectrosprayed glutathione in which the sample is dispersed. The yield of intact ions from large peptides is enhanced when applied to the nitrocellulose matrix rather than electrospraying either alone or with glutathione (*26*). This enhancement can be partially attributed to the nitrocellulose surface acting as an insulator (*27*). Another contribution may be the chemical interaction of the sample with the nitrocellulose. The binding of proteins to nitrocellulose is a feature of many biochemical procedures (*28*). In the PDMS experiment, the nitrocellulose surface has been shown to bind large peptides or proteins, allowing impurities that do not bind to the nitrocellulose to be rinsed away (*25*). Further enhancement has been reported by combining some features of both the nitrocellulose (*25*) and glutathione (*24*) sample preparation techniques (*29*). The absolute sensitivity with PDMS has previously been addressed (*30–33*).

The other components present in a sample for analysis surround the sample molecules and can be considered as a "carrier". Because PDMS ionizes a solid sample, the question of migration and/or surface activity of the carrier relative to the sample is avoided. The absence of migration with PDMS was therefore concluded to be one factor leading to the differences in the suppression observed with PDMS and LSIMS (*32*). However, it was only when low-mass peptides were electrosprayed rather than applied to nitrocellulose that the suppression by the carrier was not observed (*32, 34*). Although the feasibility of investigating a sample together with a carrier has been shown (*35*), the sensitivity limits for suppression of the sample by the carrier have rarely been addressed (*36*). In this report, we investigate the dependence of the molecule ion yield of bovine insulin and melittin in the presence of two peptide and two protein carriers.

EXPERIMENTAL SECTION

Measurements were made with a BIOION 20 mass spectrometer (Bio-Ion Nordic AB, Uppsala, Sweden). The instrument was operated at +16-kV accelerating potential. The instrument has a mass accuracy of ±0.1% and a resolution of ≈500 (*30*). Spectra were accumulated for 2 million primary ion counts. The spectra were calibrated with H^+ and Na^+. The nitrocellulose foils used were prepared by spin casting (*27*). The aluminized polyester foils were first rinsed with chloroform (reagent grade) and then ethanol (95%). A 50-μL aliquot of a 40% (w:v) solution of centrifuged nitrocellulose in acetone (reagent grade) was applied to a stationary foil that was then uniformly accelerated to 5000 rpm.

Luteinizing hormone releasing hormone (LHRH) was a gift from Novo Industri A/S, Denmark. Bovine insulin, honey bee melittin, oxidized glutathione, chicken lysozyme, and bovine serum albumin (BSA) (SDS mass marker grade purity) were purchased from the Sigma Chemical Co., St. Louis. All peptides and proteins were used without further purification. Distilled water was further purified on a Milli-Q system (Millipore, Bedford, MA). The stock solutions of bovine insulin (1 mM) and melittin (10 mM) and the dilution series (from 100 to 1 μM and 1 mM to 1 μM, respectively) were prepared in 0.1% aqueous trifluoroacetic acid (aqTFA). A separate series of dilutions were prepared from the same stock solutions by the addition of 100 μM solutions of glutathione, LHRH, or lysozyme in 0.1% aqTFA. Dilution series were also prepared from the same stock solutions with 100, 10, and 1 μM BSA solutions in 0.1% aqTFA. An aliquot (5 μL) of an insulin (100–1 μM) or melittin (1 mM–1 μM) solution was applied to a spin cast nitrocellulose foil and dried with a stream of nitrogen gas. The sample was analyzed and then withdrawn from the instrument. An aliquot (50 μL) of deionized H_2O was applied, which was then blown from the surface with a stream of nitrogen

*Author to whom correspondence should be directed at The Salk Institute, P.O. Box 85800, San Diego, CA 92186-5800.

0003-2700/91/0363-0352$02.50/0

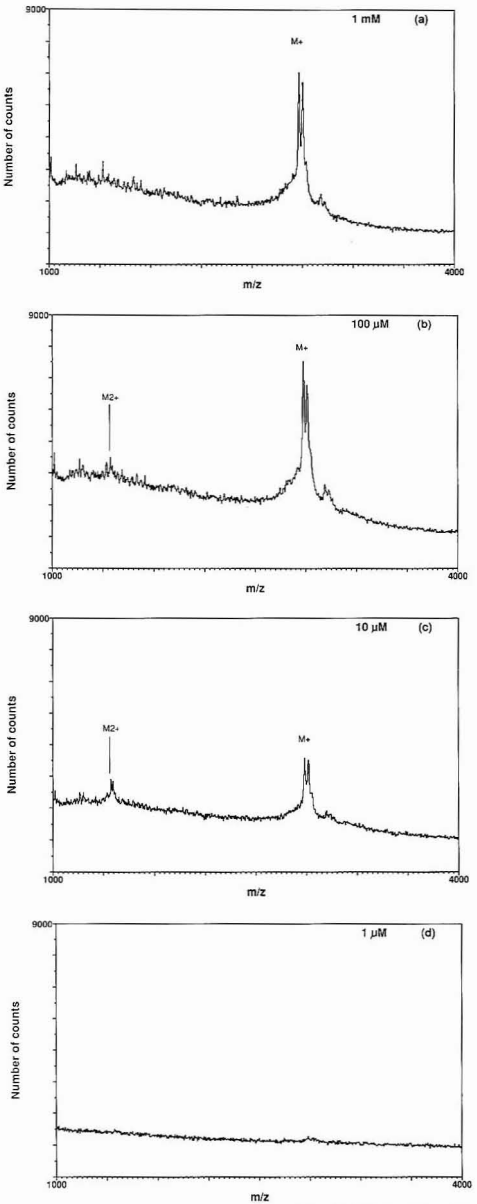

Figure 1. PDMS spectra of (a) 1 mM, (b) 100 μM, (c) 10 μM, and (d) 1 μM concentrations of melittin in 0.1% aqTFA prior to rinsing.

gas and the sample reanalyzed.

The term "molecule ion" (*33*) will be used to describe the intact species (which are presumed to correspond with the protonated molecule ion). In order to clarify the components of the sample in the PDMS experiment, the sample to be analyzed will be referred to as the "target". The target molecule ion peaks (Figures 1, 5, and 6a) will be identified by the symbol "M". The molecules present together with the target will be referred to as the "carrier". The lysozyme carrier molecule ion peaks in Figure 6b will be identified by the symbol "M(Lys)".

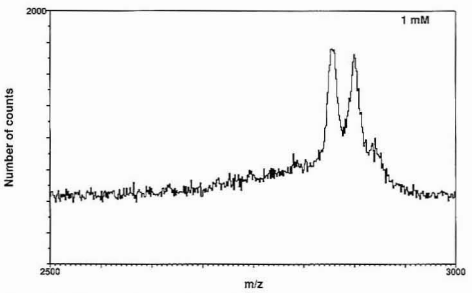

Figure 2. Molecule ion region of 1 mM melittin in 0.1% aqTFA prior to rinsing.

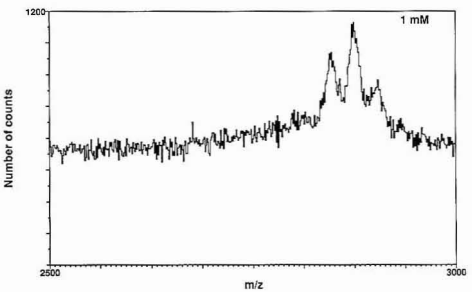

Figure 3. Molecule ion region of 1 mM melittin in 0.1% aqTFA after rinsing.

Reproducibility of Measurements. The uniformity of the preparation of the nitrocellulose surface spin cast foils (prepared as described above) was investigated. The yield of the singly charged molecule ion of the peptide LHRH was measured on eight spin cast foils. Each sample was measured six times prior to rinsing and six times after rinsing (prepared as described above). Each measurement accumulated secondary ions from 1 million primary ion counts without interruption of the high voltage or vacuum between the 2 sets of 48 individual measurements. The spectra were analyzed by using set positions for determining the peak area. The molecule ion intensity, prior to (46 182) and after rinsing (31 218), varied by ±2357 and ±5085 or 5% and 16%, respectively. Quantitating the results presented (Figures 4 and 7) required individual adjustments to compensate for the increased variation in background level and metastable decomposition in the spectra of insulin and melittin.

RESULTS

The reduction in intensity of the melittin singly charged molecule ion with concentration in the absence of a carrier is shown in Figure 1. In contast, the doubly charged ion, hidden by fragment peaks at 1 mM concentration, increases in intensity up to 10 μM concentration. At 1 μM concentration, the singly and doubly charged molecule ions are not observed. Figure 2 shows the expanded region between m/z 2500 and m/z 3000 of the 1 mM concentration sample. Intense peaks are observed at m/z 2847 and 2874, which correspond with the intact molecule ions of both the formylated (*37*) and unformylated analogues. Generally, before rinsing, the intensity of the singly charged unformylated melittin analogue was higher than the formylated analogue. However, after rinsing, the reverse was the case. Fragment ions are observed in the spectra that vary in intensity depending on the target molecule ion intensity and the carrier employed (*38*). The fragment ions of melittin or insulin will not be addressed in this article.

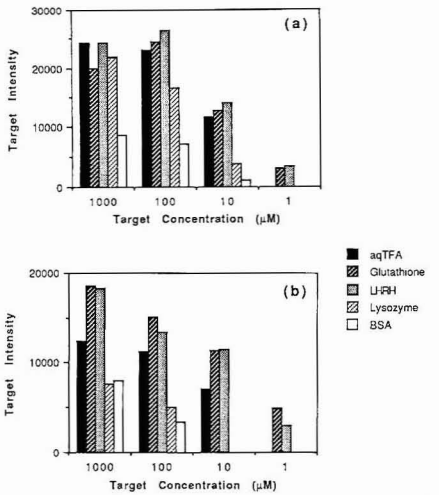

Figure 4. Plot of the melittin target peak intensity versus concentration when dissolved in 0.1% aqTFA, glutathione, LHRH, lysozyme, and BSA (a) prior to and (b) after rinsing.

Figure 3 shows the molecule ion region of the 1 mM spectrum after rinsing where three peaks are observed at m/z 2846, 2874, and 2902. A third component possibly with two formyl groups was present in addition to the formylated and unformylated analogues. The origin of this higher mass analogue of melittin is not known. Although this component was present prior to rinsing, its intensity relative to the formylated and unformylated analogues was significantly enhanced after rinsing. A similar behavior has been observed when purifying synthetic peptides that contain components which were not completely deprotected (*8*). The peaks corresponding with the partially deprotected peptides were more intense than expected based on chromatographic results (*8*). In the following discussion, all three components (unformylated, formylated, and higher mass) will be considered collectively as contributing to the molecule ion intensity, although variations in their relative intensities are observed.

The variation in the intensity of the singly charged molecule ion of melittin at concentrations of 1 mM to 1 μM in 0.1% aqTFA, glutathione, LHRH, lysozyme, and BSA is shown in Figure 4, (a) unrinsed and (b) rinsed. With the exception of the BSA carrier, comparable molecule ion yields were observed for the 1 mM sample with and without a carrier prior to rinsing. At lower concentrations, a difference was also observed between the lysozyme and peptide carriers. In the case of the lysozyme carrier, at 100 and 10 μM concentrations, the intensity of the molecule ion peaks was significantly reduced compared with the spectra measured in the absence of the carrier. The effect of rinsing the melittin in the lysozyme carrier samples was to further decrease the intensity of the singly charged melittin molecule ion. This decrease was significantly greater than observed in the absence of the lysozyme carrier. Figure 5 shows the 10 μM melittin in lysozyme spectrum prior to rinsing. No doubly charged ion is present, in contrast with the 10 μM sample without a lysozyme carrier. Figure 6 shows the rinsed spectra of (a) 1 mM and (b) 1 μM melittin in 100 μM lysozyme between 4 and 20 kDa. The lysozyme doubly charged molecule ion peak was observed at the 1 and 10 μM melittin target concentrations but was absent at higher target concentrations. The melittin dimer was observed at 1 mM but not at lower target concentrations.

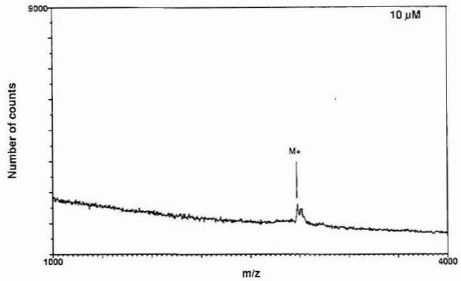

Figure 5. PDMS spectrum of 10 μM melittin in 100 μM lysozyme prior to rinsing.

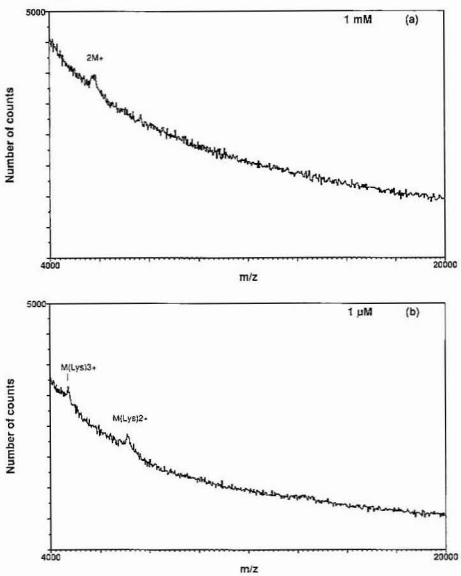

Figure 6. PDMS spectra of (a) 1 mM and (b) 1 μM melittin in 100 μM lysozyme after rinsing.

The BSA carrier when mixed with melittin had a more potent quenching effect than lysozyme, even the 1 mM concentration being significantly affected. Reducing the BSA carrier concentration from 100 to 10 μM significantly increased the intensity of the melittin molecule ion for the 1 mM target concentration sample (spectra not shown). When the BSA carrier concentration was further reduced from 10 to 1 μM, the intensity of the melittin molecule ion peak for the 1 mM target concentration was effectively the same as that observed with no carrier. The melittin molecule ion, absent at the 10 μM target concentration after rinsing, was not observed with the reduction in the carrier concentration. The 100 μM target concentration sample behaved somewhat between the 1 mM and 10 μM target concentration samples. The doubly charged melittin molecule ion was only observed at the 1 μM BSA carrier concentration. The BSA carrier molecule ions were not observed.

In contrast with the protein carriers, the LHRH and glutathione carriers did not reduce the intensity of the melittin molecule ion. The doubly charged molecule ions of melittin were present prior to and after rinsing (spectra not shown). The intensity of the LHRH carrier molecule ion peak in-

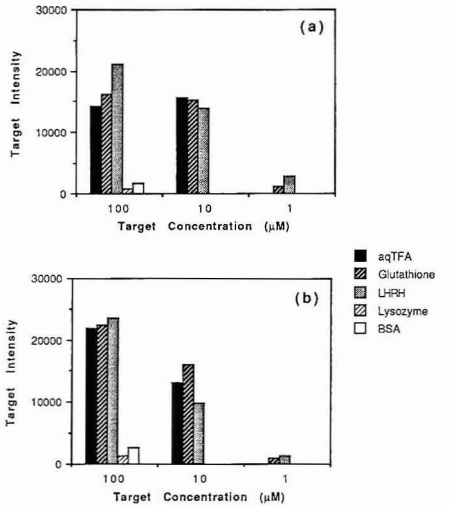

Figure 7. Plot of the insulin target peak intensity versus concentration when dissolved in 0.1% aqTFA, glutathione, LHRH, lysozyme, and BSA (a) prior to and (b) after rinsing.

creased to a maximum at 10 μM target concentration both before and after rinsing. The glutathione carrier peak, although significantly less intense than LHRH, increased with decreasing target concentration. The glutathione dimer peak was observed at the 1 μM target concentration.

The variation in the intensity of the singly charged molecule ion of insulin at concentrations of 100–1 μM in 0.1% aqTFA, glutathione, LHRH, lysozyme, and BSA is shown in Figure 7, (a) unrinsed and (b) rinsed. The insulin spectra reflect similar trends to those observed for melittin. For example, the insulin molecule ion intensity was not suppressed with either peptide carrier. In addition, the doubly charged insulin molecule ions were observed when insulin was mixed with either peptide carrier but absent with either protein carrier (spectra not shown). As observed for the melittin target, the LHRH carrier peak was significantly more intense than the glutathione carrier peak. Both the LHRH and glutathione molecule ion peaks increased with reduced insulin concentrations, and the effect of rinsing was to reduce the carrier peak intensity. Comparing Figures 4 and 7, the addition of either a lysozyme or BSA carrier had a more marked effect on insulin than melittin. Generally the insulin molecule ion intensity would increase with rinsing, both with peptide and protein carriers. The lysozyme molecule ion peaks are not observed with insulin as the target (spectra not shown).

The effect of the reduction in BSA carrier concentration on the insulin spectrum was more uniform than for melittin (spectra not shown). The 10 and 1 μM BSA carrier concentrations enable the 10 and 1 μM insulin singly charged ions to be observed, respectively. The doubly charged insulin molecule ion absent at the 100 μM target concentration in 100 μM BSA was observed with decreasing carrier concentration both before and after rinsing.

DISCUSSION

The intensity of the target molecule ions shows a significant dependence on both the concentration and the type of carrier molecule employed. Similarly, the intensities of the carrier molecule ions are dependent on both the concentration and the type of target. Although, the interdependence between target and carrier peak intensities is not easily reduced to convenient generalities, some distinct trends are observed. For both targets, the molecule ion intensity is reduced by a protein carrier and not reduced by a peptide carrier. In addition, the glutathione, LHRH, and lysozyme carrier molecule ion intensities increase with reducing target concentration.

Rinsing, with few exceptions, increases the intensity of the insulin molecule ion. In contrast, the melittin molecule ion is generally reduced. The increase in intensity for insulin suggests both a strong interaction with nitrocellulose and some positive action associated with the rinsing step. Previously, we have suggested the possibility of increased binding being responsible for the enhancement associated with rinsing (*33*). The interaction between a variety of proteins, including BSA and lysozyme, and nitrocellulose has been proposed to be of a hydrophobic nature (*39*). This is based on the observed inhibition of protein binding to nitrocellulose in the presence of a detergent (*39*). The increased binding may therefore result from the change in pH that accompanies the rinsing step, leading to an increased interaction of the hydrophobic regions of insulin with the nitrocellulose.

Since plasma desorption does not involve ionization from a liquid matrix, peptide hydrophobicity/hydrophilicity is not expected to result in suppression. The proposed dependence of target intensity on the relative gas-phase basicity of target and carrier (*20*) cannot be relegated in this manner. The correlation proposed between ion yield and peptide net charge (*32*) suggests that the gas-phase basicity does play a significant role in the PDMS ionization process. The reciprocal dependence of the carrier and target molecule ion intensities adds further support to this proposal. If gas-phase basicities were responsible for suppressing the formation of ions, then we would also expect this to be reflected in a high level of charge competition. The intensity of the doubly charged target molecule ion may be used as an indicator of the level of charge competition. In the absence of a carrier, the charge competition was reduced (observed as an intense M^{2+}) at low target concentrations for insulin and melittin (*30*, *33*). In this study, the protein carriers result in a significant reduction of the target M^{2+} at low target concentrations. Neither peptide carrier significantly reduced the target M^{2+} intensity. Apparently the protein carriers can substitute for the target in the charge competition event. However, at the same concentration, the peptide carriers cannot result in increased charge competition. Importantly, the increased charge competition is observed concordant with the suppression.

If the relative gas-phase basicity of the different molecules were responsible for the suppression effects, then the gas-phase basicities should follow the order carrier proteins > target molecules > carrier peptides. Unfortunately, gas-phase basicities are generally only known for small molecules (*40*). However, a high gas-phase basicity is usually reflected in a high solvent basicity (*40*). Since the isoelectric point of lysozyme (10.5–11.0) (*41*) is significantly higher than that of insulin, the suppression of insulin by lysozyme is consistent with this proposal. Melittin, which is also strongly basic (*42*), adds plausibility with regard to the reduced suppression of melittin when mixed with lysozyme (compared with insulin and lysozyme). The absence of suppression of melittin when mixed with peptide carriers would also be consistent with this proposal. There are, however, several problems with this scheme. For example, it does not address why insulin, which would not be expected to have a high gas-phase basicity, can compete with the peptide carriers. In addition, the low isoelectric point of serum albumin (5.9) (*43*) argues against a high gas-phase basicity for BSA. These discrepancies indicate that other factors must also be involved.

In analogy with the proposed nonuniform charge distribution on the surface of proteins in solution (*43*), the surface of a protein in the gas phase may contain regions of nonu-

niform gas-phase basicity. These regions may significantly affect the outcome of the charge competition phenomenon. Despite the low p*I* of insulin (and presumably low gas-phase basicity), some portions of the molecule may compete effectively with the peptide carriers for the charge in the desorbing cluster. The absence of the suppression of small peptide fragments when using the electrospray technique (*32*, *34*) may indicate a lower level of charge competition due to the physical constraints of sample preparation.

An additional consideration influencing the intensity of the target molecule ion peaks may be the nonspecific binding properties of the carrier proteins. The binding and transport of various substances (*44*, *45*) is one of the main functions of albumin in blood. It is suggested that the suppression observed with BSA may be due to binding between the BSA and the target molecule. It is envisaged that the interaction may retard the ion ejection from a desorbed cluster, resulting in delayed ionization at a reduced electric field potential. If the target and the carrier interacted for several nanoseconds, the distance traveled by the cluster would measurably shift the time of flight of a subsequently ejected ion (*46*). A longer time duration of target–carrier interaction would result in a metastable type peak (*46*).

The increased PDMS sensitivity for target molecules dissolved in peptide carriers (*29*) could be due to other parameters than reduced charge competition or the absence of nonspecific interaction with these peptides. Sokolowski and Wahlund investigating the retention of ammonium compounds using a variety of solid phases note an increased capacity ratio in the presence of diphenylacetic acid (*47*). The peptide carriers may function in a similar manner, increasing the target binding to nitrocellulose. Blotting buffers, containing small molecules such as glycine, are used to assist protein transfer from gels by the convection or mass flow of these carrier molecules (*28*). The peptide carriers may access the dendritic pores of the nitrocellulose, increasing the convection toward the protein accessible regions of the nitrocellulose. In this way, the peptide carriers may assist large target molecules to bind to the nitrocellulose.

CONCLUSION

It has been shown that the PDMS experiment is suited to the measurement of target and carrier molecules for determining sensitivity limits of mixtures. These experiments may be used to clarify the constraints the sample purity places on mass spectrometric analysis. The results indicate that for insulin and melittin the PDMS sensitivity may vary significantly depending on the nature of the carrier molecule. The introduction of a carrier peptide may be used to increase PDMS sensitivity. In contrast, procedures that involve the coanalysis of proteins and peptides may lead to reduced sensitivity.

ACKNOWLEDGMENT

We thank Jean Rivier and Peter Leach for helpful discussions. We also thank the referees for positive and constructive suggestions for the improvement of the presentation of these results.

Registry No. LHRH, 9034-40-6; insulin, 9004-10-8; melittin, 20449-79-0; lysozyme, 9001-63-2; glutathione, 70-18-8.

LITERATURE CITED

(1) Torgerson, D. F.; Skowronski, R. P.; Macfarlane, R. D. *Biochem. Biophys. Res. Commun.* **1974**, *60*, 616–621.
(2) Barber, M.; Bordoli, R. S.; Sedgwick, R. D.; Tyler, A. N. *J. Chem. Soc., Chem. Commun.* **1981**, 325–326.
(3) Gibson, B. W.; Yu, Z.; Burlingame, A. L.; Aberth, W. In *The Analysis of Peptides and Proteins by Mass Spectrometry*; McNeal, C. J., Ed.; John Wiley & Sons: New York, 1988; pp 217–237.
(4) Cotter, R. J. *Anal. Chem.* **1988**, *60*, 781A–793A.
(5) Lemaire, S.; Chouinard, L.; Denis, D.; Panico, M.; Morris, H. R. *Biochem. Biophys. Res. Commun.* **1982**, *108*, 51–58.
(6) Rinehart, K. L. J. In *Mass Spectrometry in Health and Life Sciences*; Burlingame, A. L., Castagnoli, N. J., Eds.; Elsevier Science Publishers B.V.: Amsterdam, 1985; pp 119–148.
(7) Roepstorff, P.; Nielsen, P. F.; Kamensky, I.; Craig, A. G.; Self, R. *Biomed. Mass Spectrom.* **1988**, *15*, 305–310.
(8) Lindeberg, G.; Engström, Å.; Craig, A. G.; Bennich, H. In *The Analysis of Peptides and Proteins by Mass Spectrometry*; McNeal, C. J., Ed.; John Wiley & Son: New York, 1988; pp 1–14.
(9) Chowdhury, S. K.; Chait, B. T. *Anal. Biochem.* **1989**, *180*, 387–395.
(10) Ciench, M. R.; Garner, G. V.; Gordon, D. B.; Barber, M. *Biomed. Mass Spectrom.* **1985**, *12*, 355–357.
(11) Chait, B. T.; Field, F. H. *J. Am. Chem. Soc.* **1985**, *107*, 6743–6744.
(12) Craig, A. G.; Engström, Å.; Bennich, H.; Kamensky, I. *Biomed. Mass Spectrom.* **1987**, *14*, 669–673.
(13) Caprioli, R. M.; Moore, W. T. In *The Analysis of Peptides and Proteins by Mass Spectrometry*; McNeal, C. J., Ed.; John Wiley & Sons: New York, 1988; pp 81–94.
(14) Klarskov, K.; Breddam, K.; Roepstorff, P. *Anal. Biochem.* **1989**, *180*, 28–37.
(15) Busch, K. L.; Cooks, R. G. *Science* **1982**, *218*, 247–254.
(16) Zhang, M.-Y.; Liang, X.-Y.; Chen, Y.-Y.; Liang, X.-G. *Anal. Chem.* **1984**, *56*, 2288–2290.
(17) Heine, C. E.; Holland, J. F.; Watson, J. T. *Anal. Chem.* **1989**, *61*, 2674–2682.
(18) Sunner, J. A.; Kulatunga, R.; Kebarle, P. *Anal. Chem.* **1986**, *58*, 1312–1316.
(19) Naylor, S.; Findeis, A. F.; Gibson, B. W.; Williams, D. H. *J. Am. Chem. Soc.* **1986**, *108*, 6359–6363.
(20) Sunner, J. A.; Morales, A.; Kebarle, P. *Int. J. Mass Spectrom. Ion Proc.* **1989**, *87*, 287–307.
(21) Sundqvist, B.; Macfarlane, R. D. *Mass Spectrom. Rev.* **1985**, *4*, 421–460.
(22) Cotter, R. J. *Biomed. Mass Spectrom.* **1989**, *18*, 513–532.
(23) McNeal, C. J.; Macfarlane, R. D.; Thurston, E. L. *Anal. Chem.* **1979**, *51*, 2036–2039.
(24) Alai, M.; Demirev, P.; Fenselau, C.; Cotter, R. J. *Anal. Chem.* **1986**, *58*, 1303–1307.
(25) Jonsson, G. P.; Hedin, A. B.; Håkansson, P. L.; Sundqvist, B. U. R.; Säve, G. S.; Nielsen, P. F.; Roepstorff, P.; Johansson, K.-E.; Kamensky, I.; Lindberg, M. S. L. *Anal. Chem.* **1986**, *58*, 1084–1087.
(26) Roepstorff, P.; Nielsen, P. F.; Sundqvist, B. U. R.; Håkansson, P.; Jonsson, G. *Int. J. Mass Spectrom. Ion Proc.* **1987**, *78*, 229–236.
(27) Säve, G.; Håkansson, P.; Sundqvist, B. U. R.; Jönsson, U.; Olofsson, G.; Malmquist, M. *Anal. Chem.* **1987**, *59*, 2059–2063.
(28) Gershoni, J. M.; Palade, G. E. *Anal. Biochem.* **1983**, *131*, 1–15.
(29) Jardine, I.; Scanlan, G. F.; Tsarbopoulos, A.; Liberato, D. J. *Anal. Chem.* **1988**, *60*, 1086–1088.
(30) Kamensky, I.; Craig, A. G. *Anal. Instrum.* **1987**, *16*, 71–91.
(31) Jonsson, G.; Hedin, A.; Håkansson, P.; Sundqvist, B. U. R. *Rapid Commun. Mass Spectrom.* **1988**, *2*, 154–156.
(32) Nielsen, P. F.; Roepstorff, P. *Biomed. Mass Spectrom.* **1989**, *18*, 131–137.
(33) Craig, A. G.; Bennich, H. *Anal. Chem.* **1989**, *61*, 375–382.
(34) Craig, A. G.; Engström, Å.; Bennich, H.; Kamensky, I.; Roepstorff, P.; Self, R.; Richter, W. J.; Raschdorf, F.; Salehpour, M.; Sundqvist, B. U. R. Presented at the 34th Annual Conference on Mass Spectrometry and Allied Topics, Cincinnati, OH, June 8–13, 1986.
(35) Sundqvist, B.; Hedin, A.; Håkansson, P.; Kamensky, I.; Salehpour, M.; Säve, G. *Int. J. Mass Spectrom. Ion Proc.* **1985**, *65*, 69–89.
(36) Bojesen, G. *Adv. Mass Spectrom.* **1988**, *11A*, 414–415.
(37) Jentsch, J. *Z. Naturforsch.* **1969**, *24B*, 264–265.
(38) Craig, A. G.; Bennich, H.; Derrick, P. J. Unpublished work.
(39) Lin, W.; Kasamatsu, H. *Anal. Biochem.* **1983**, *128*, 302–311.
(40) Sunner, J. A.; Morales, A.; Kebarle, P. *Anal. Chem.* **1987**, *59*, 1378–1383.
(41) Windholz, M. *The Merck Index*; Merck & Co., Inc.: Rahway, NJ, 1983.
(42) Habermann, E. *Science* **1972**, *177*, 314–322.
(43) Hearn, M. T. W.; Hodder, A. N.; Stanton, P. G.; Aguilar, M. I. *Chromatographia* **1987**, *24*, 769–776.
(44) Chignell, C. F. In *Handbook of Biochemistry and Molecular Biology*; Fasman, G. D., Ed.; CBC Publishing Inc.: Cleveland, OH, 1976; pp 554–582.
(45) Steinhardt, J.; Reynolds, J. A. *Multiple Equilibria in Proteins*; Academic Press: New York, 1969.
(46) Chait, B. T. *Int. J. Mass Spectrom. Ion Phys.* **1983**, *53*, 227–242.
(47) Sokolowski, A.; Wahlund, K.-G. *J. Chromatogr.* **1980**, *189*, 299–316.

RECEIVED for review April 24, 1990. Accepted November 19, 1990. This work was supported by grants from the Swedish Medical Research Council and the Swedish Board for Technical Development.

Noise Reduction of Gas Chromatography/Mass Spectrometry Data Using Principal Component Analysis

Terrence A. Lee, Lisa M. Headley, and James K. Hardy*

Department of Chemistry, The University of Akron, Akron, Ohio 44325

Principal component analysis has been evaluated as a digital filter to improve the overall quality of gas chromatography/mass spectrometry (GC/MS) data sets. Data are initially read into a matrix, scaled, and then processed by using the NIPALS algorithm, which is used to separate signal from the matrix. A new matrix is then reconstructed as the difference between the original and residual matrices, which is then rescaled and a new data file created. By use of a six-component solvent mixture with samples of from 0.5 to 150 pg of each component, significant improvements in mass spectral quality and spectral matches were observed. Signal to noise was improved by a factor of from 2 to 100 due to improved integration. Linearity and precision of chromatographic data were also improved.

INTRODUCTION

Mass spectrometers are relatively noisy in comparison to other gas chromatographic detectors. While to a high degree this is due to the inherent noise associated with the ion multiplier, quality can also be degraded as a result of changes in chromatographic conditions, such as carrier flow rate and column bleed, during an analysis. A number of investigators have reported filtering systems to improve the signal to noise ratio (S/N) (*1–10*). Hieftje summarized several instrumental methods for enhancing S/N (*1, 2*), and Doerfler and Campbell reported the use of an analog delay device for on-the-fly reduction of ion multiplier noise (*3*). The ability to postprocess gas chromatography/mass spectrometry (GC/MS) data sets allows for the use of software noise filters to improve signal to noise, peak shape, and spectral quality. Summing of several measurements is commonly used by GC/MS software to provide an initial smoothing of data (*4, 5*) though the actual approach taken will vary based on the analyzer type. The Hewlet-Packard approach for its mass selective detector (MSD) is to sum from 2 to 128 measurements at 0.1-amu intervals, whereas Finnigan's approach with its ion trap system is to add entire scans. Postprocessing for both systems is limited to either a moving average or Savitzky–Golay smoothing (*6*) of chromatographic data and simple averaging for mass spectra. The use of polynomial smoothing, measurement of noise variance, estimation of peak shape, and cross-correlation (*7–10*) has also been reported for enhancement of S/N for integrated signals.

Multivariate data analysis based on pattern recognition has been applied to a number of spectral and chromatographic methods. The typical goal of pattern recognition is to classify a new sample by comparing it to a reference set of predetermined ones. Derde and Massart reviewed a number of techniques and their application (*11*). Thomas and Haaland compared several least-squares methods and principal component analysis (PCA) for use in quantitative spectral analysis (*12*). With PCA, a data matrix can be decomposed into linear combinations of orthogonal vectors by diagonalization of the covariance matrix (*13*). This, however, requires that all components be determined simultaneously. The NIPALS algorithm can be used to determine a single component accounting for the greatest amount of variance in a data set (*14*). The matrix is degraded into a loading vector and a vector of scores (principal component or PC) and a matrix residual. Variables showing the highest degree of correlation are removed, being combined in the first PC, and their effect subtracted from the residual. Subsequent PCs will account for other sources of variance in decreasing order. Subsequent components can be determined with additional calls to the routine. Shah and Gemperline used PCA to classify near-infrared reflectance spectra (*15*), and it application to mass spectra of mixtures has also been reported (*16*). The approach has also been applied to chromatographic data to classify beverages, cheese, and soy sauce (*17–20*). Recently, PCA has been employed as a digital filtering method for reduction of artifacts in two-dimensional Fourier transform (2D FT) NMR data sets (*21*). Commonly, a plot of the first and second PC is used to determine whether or not underlying trends in the set exist. However, when applied to three-dimensional data sets such as 2D NMR or GC/MS data, the method can be used to separate noise and artifacts from signal.

EXPERIMENTAL SECTION

Instrumentation. A Hewlett-Packard capillary column gas chromatograph (Model 5890) interfaced by direct capillary inlet to a Hewlett-Packard MSD (Model 5970) was used for the production of all GC/MS data sets. Samples were introduced by using a Hewlett-Packard autoinjector (Model 7673A). The chromatographic conditions were sample size, 1 μL; sample split, 100:1; column, 25 m × 0.2 i.d. HP-1; and temperature program, T_{start} = 30 °C, t_I = 3.2 min, ramp 40 °C/min to 140 °C. The temperatures of the injection port and transfer line were set to 200 and 250 °C, respectively. The MSD was operated in a scan mode averaging 4 samples per scan, the HP default, with a mass range of 30–150 amu. Instrument control and data collection were accomplished by using a Hewlett-Packard Unix ChemStation (Model 59940) running version A.01.03 of the MSD software. After each analysis, data files were transferred to a Sun SPARCstation 1 workstation for postprocessing.

Samples. To evaluate the method, a mixture of low molecular weight solvents was used. This was done to assure that a significant portion of each substance's mass spectrum would occur in the low mass region, <50 amu, where noise is the greatest. A six-component solvent mixture consisting of 1% by volume each of dichloromethane, trichloromethane, tetrachloromethane, benzene, toluene, and ethylbenzene in methanol was prepared as a stock solution. Subsequent samples were prepared by dilution of the stock to produce samples ranging from 0.005% to 1% by volume.

Postprocessing. After data collection and transfer to the Sun SPARCstation, each data file was processed by using software written in-house in C using the compiler provided with the Sun system. The code initially read in mass spectra as raw ion intensities vs time from the HP data file. Since HP data files files maintain mass resolution values to the nearest 0.05 amu, data were initially converted to unit resolution where a mass in the range of −0.3 to +0.65 was rounded to the nearest whole amu in a manner similar to the current HP spectral averaging routine, which sums masses in the range of −0.3 to +0.7 (22). It was also determined that the HP scan algorithm allows more than a single mass spectral line to be recorded in a given amu range. To account for this, when multiple lines were detected, only the largest line

0003-2700/91/0363-0357$02.50/0

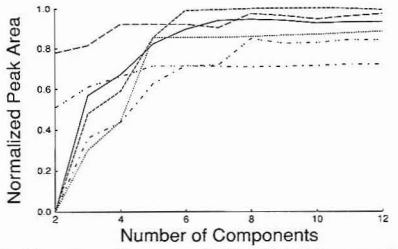

Figure 1. Chromatographic areas a a function of NIPALS passes. (—) Dichloromethane, (•••) trichloromethane, (- - -) benzene, (– • –) tetrachloromethane, (– – –) tetrachloromethane, (– •• –) toluene, (– –) ethylbenzene.

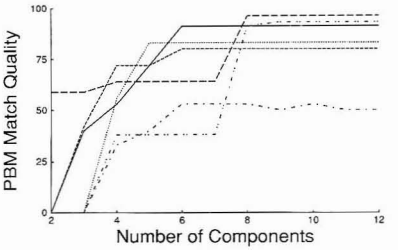

Figure 2. PBM match qaultiy as a function of NIPALS passes. (–) Dichloromethane, (•••) trichloromethane, (- - -) benzene, (– • –) tetrachloromethane, (– •• –) toluene, (– –) ethylbenzene.

was used. The resulting data matrix typically consisted of 130 variables (m/e) by 730 cases (scans) although this varied based on the actual range of masses detected and scans acquired. The entire matrix was then scaled to mean centered unit variance rather than scaling each variable. This assured that each set was treated with the same level of precision while avoiding problems with closure (*23*). After scaling, the matrix was subjected to PCA by using the NIPALS algorithm. When the variance change became relatively constant, a matrix was produced by subtracting the residual matrix from original and Hewlett-Packard readable GC/MS file for subsequent analysis. It was noted that processed files averaged about 70% of the original file size, indicating that a large number of spectral lines had been removed. All comparative tests were then accomplished by using the Hewlett-Packard ChemStation software. Each processed data file was compared to the original for mass spectral quality, changes in chromatographic integration areas and precision, and signal to noise for ethylbenzene, which was the last peak to elute.

RESULTS AND DISCUSSION

Initial Evaluation of the Algorithm. An initial investigation was made to determine what criteria should be used to determine when the majority of the mass spectral signal had been removed from the data matrix, leaving only the noise. Several approaches have been reported for estimating the number of significant components such as attempting to account for a fixed total variance and cross-validation and evaluating when the residual standard deviation equals the experimental error (*24–26*). Malinowski has proposed the use of an estimate of real error, RE, which is determined from the standard deviation of the residual, RSD (*13*)

$$\mathrm{RE} = \left[\frac{\sum_{j=n+1}^{j=c} \lambda_j^0}{r(c-n)} \right]^{1/2} \qquad (1)$$

where r and c represent the number of rows and columns in the matrix and λ_j^0 is the jth eigenvalue of the noise component. As components are removed from the residual, RE approaches a constant, indicating that all significant components have been determined. Malinowski also reports the use of intrinsic error and a Factor Indicator function to deduce the number of components (*27*). These, however, require that errors be relatively uniform throughout the data set. GC/MS data sets typically exhibit overall higher noise at lower masses, and high mass noise may increase during a temperature program, so noise was not expected to be uniform. Monitoring when real error becomes relatively constant should offer a reasonable approach. This can be determined by monitoring the rate of change of eigenvalues returned by the NIPALS algorithm and the use of an appropriate cutoff.

To determine the cutoff, each data file was processed for a fixed number of components and the resulting files were evaluated for chromatographic area and mass spectral match quality. Mass spectral quality was determined by using Hewlett-Packards's implementation of the Probability Based Matching (PBM) algorithm (*28*) with the NIST mass spectral library available for the ChemStation. Figures 1 and 2 show the effect of the algorithm for each chromatographic peak in a 0.005% by volume sample. As additional components are used, chromatographic areas and PBM quality both approach maxima and then remain constant. A cutoff value of 0.001 for the change in the eigenvector was found to give the best results for all data files evaluated.

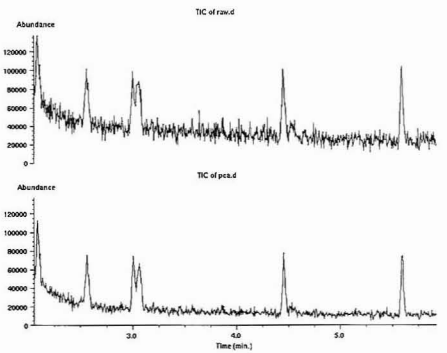

Figure 3. Representative chromatographic results of 0.005% by volume solvent sample. Original data, top; PCA processed data, bottom. Elution order: dichloromethane, trichloromethane, benzene, tetrachloromethane, toluene, ethylbenzene.

Evaluation of Chromatographic Quality. Figure 3 shows a representative chromatogram for unprocessed and PCA filtered data. As can be seen, there is a general improvement of peak quality and a reduction of background noise and base-line response. Table I lists integration results obtained for the data sets using an integration threshold of 16, which was the lowest value that resulted in integration of all six peaks for each sample. By reducing mass spectral noise, better integration results were observed as the ChemStation software was able to do a better job of properly locating the chromatographic peaks and calculating a base line. This improved integration is most evident for smaller peaks where areas might be overreported by as much as 100%. The AUTOSN macro provided with the HP ChemStation software was used to evaluate signal to noise (S/N) for the last chromatographic peak. This routine determined S/N by evaluating the maximum signal for the last peak in the chromatogram, ethylbenzene, and the average peak to peak noise for a region just prior to the peak. Table II lists the results obtained from this macro for raw, PCA-processed, and raw

Table I. Integration Results[a]

	peak area (% RSD)											
	dichloromethane		trichloromethane		benzene		tetrachloromethane		toluene		ethylbenzene	
sample	raw	PCA	raw	PCA	raw	PCA	raw	PCA	raw	PCA	raw	PCA
0.005	1.835	0.836	1.496	1.052	0.784	0.563	1.226	1.116	0.625	0.462	0.698	0.507
	(34.5)	(17.5)	(36.0)	(11.4)	(36.4)	(3.0)	(72.9)	(52.1)	(9.9)	(8.4)	(5.8)	(7.7)
0.010	1.861	1.714	2.315	2.040	1.350	1.157	2.605	1.970	1.292	1.044	1.267	1.093
	(6.5)	(5.8)	(14.0)	(9.9)	(11.8)	(10.0)	(14.4)	(5.6)	(4.4)	(4.8)	(4.5)	(3.9)
0.050	8.962	9.200	9.716	8.386	5.437	4.876	9.981	9.317	5.446	4.949	5.917	5.493
	(12.3)	(0.7)	(14.6)	(3.7)	(3.4)	(3.1)	(7.4)	(9.4)	(5.5)	(2.2)	(2.0)	(1.2)
0.100	18.35	17.30	18.13	15.95	10.16	9.541	19.10	17.72	10.12	9.602	11.53	10.81
	(1.4)	(0.2)	(8.3)	(0.4)	(4.2)	(0.3)	(5.2)	(0.2)	(1.6)	(1.4)	(1.6)	(7.5)
0.500	78.45	75.47	78.42	74.94	46.36	44.71	80.93	77.68	45.10	43.47	50.21	48.26
	(3.6)	(3.9)	(6.6)	(6.5)	(5.7)	(5.6)	(4.8)	(5.9)	(4.7)	(4.8)	(5.0)	(5.1)
1.000	133.5	129.1	138.0	132.8	83.66	82.32	148.1	140.8	80.67	77.82	89.63	83.59
	(0.9)	(0.8)	(6.5)	(6.5)	(4.5)	(3.7)	(6.7)	(7.2)	(6.5)	(6.5)	(5.2)	(0.3)
slope	134.4	130.2	138.3	133.7	83.87	82.64	147.8	141.0	80.90	78.27	89.94	84.35
Y intercept	3.19	2.76	2.98	2.09	1.35	0.929	2.65	2.29	1.42	1.17	1.58	1.55
CC	0.9967	0.9968	0.9980	0.9983	0.9987	0.9992	0.9990	0.9990	0.9985	0.9985	0.9984	0.9973

Table II. Signal-to-Noise Ratio for Ethylbenzene Peak. Average of Three Samples

sample	S/N_{raw}	$S/N_{smoothed}$	S/N_{PCA}	$S/N_{PCA/raw}$
0.005	20.9	35.6	39.2	1.88
0.010	39.9	97.3	97.2	2.44
0.050	179.7	372.5	457.0	2.54
0.100	368.0	996.1	1125.3	3.06
0.500	1793.3	3633.1	8873.0	4.95
1.00	2336.0	5276.2	284728.5	121.9

data that had been subjected to a 10-point Golay smooth (*6*). S/N improves by a factor of 1.88 for the 0.005% by volume samples after PCA. This compares favorably with smoothing, which only improves by a factor 1.70 for the 0.005% by volume samples. As concentration is increased, S/N steadily increases but takes a large jump for the 1% by volume samples. In these cases, it was observed that all spectral lines for each scan in the ethylbenzene peak were well above the scan threshold of 1000. ChemStation software will omit individual lines with intensities at or below the threshold, which introduces additional noise.

Mass Spectral Quality. Figures 4 and 5 show average mass spectra obtained by using the 0.005% by volume sample for the first and last peaks (dichloromethane and ethylbenzene). Upper spectra are for raw data sets and the lower represent PCA-processed spectra. Processed data show a substantial reduction in mass spectral noise with a subsequent improvement in spectral quality. To further evaluate mass spectral quality, each data set was evaluated to compare both raw and processed mass spectra by using the PBM search algorithm using HP defaults for each search. Average mass spectra were obtained by integration of each data file and taking the average spectra for the reported peaks. This assured that the spectra produced for both data sets were comparable and not subjected to the spectral summation routine currently employed by Hewlett-Packard, referred to as math with spectra (*4*). Table III lists PBM match probabilities obtained for all six peaks in each data set. By reducing the background noise, a general improvement in match quality is observed, through the greatest change occurs with lower concentration samples. Overall, 36.1% of the matches showed an improvement averaging 16.3%, whereas 18.5% showed a small degradation averaging 3.2%. For the lowest concentration sample, 15 of the 18 PBM values showed a net improvement with only 2 samples showing a degradation.

CONCLUSIONS

A digital filtering method for postprocessing of GC/MS data based on principal component analysis has been introduced.

Table III. PBM Search Match Quality

	PBM match quality											
	dichloromethane		trichloromethane		benzene		tetrachloromethane		toluene		ethylbenzene	
sample, % by vol	raw	PCA	raw	PCA	raw	PCA	raw	PCA	raw	PCA	raw	PCA
0.005	74	91	42	59	72	83	10	43	50	47	43	78
	72	72	50	83	72	74	38	83	80	86	90	93
	80	91	64	43	43	72	37	83	68	78	80	90
0.010	81	91	43	83	64	80	64	53	58	91	91	91
	64	72	72	90	56	90	40	83	91	90	91	91
	81	80	81	90	86	90	42	53	90	91	91	90
0.050	91	91	96	94	91	91	64	64	94	91	94	94
	91	91	96	93	91	91	64	64	95	91	94	94
	91	91	94	91	90	91	64	83	95	91	91	91
0.100	91	91	96	96	91	91	83	90	94	90	91	91
	91	91	94	97	91	91	64	64	95	90	91	91
	91	91	96	94	91	91	59	59	94	91	94	91
0.500	91	91	94	94	91	91	64	64	94	91	76	91
	91	91	96	96	91	91	64	64	94	90	90	91
	91	91	94	94	91	91	64	64	94	91	87	91
1.000	91	91	96	96	91	91	64	64	94	93	72	91
	91	91	96	96	91	91	59	84	94	94	87	91
	91	91	96	96	91	91	45	74	94	94	59	91

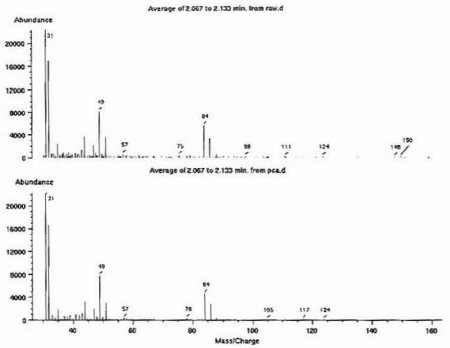

Figure 4. Average mass spectrum of dichloromethane, 0.005% by volume sample. Original data, top; PCA processed data, bottom.

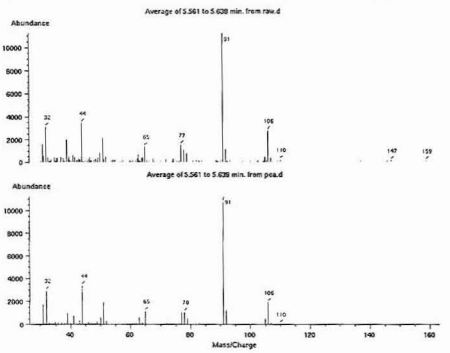

Figure 5. Average mass spectrum of ethylbenzene, 0.005% by volume sample. Original data, top; PCA processed data, bottom.

By monitoring the change in variance accounted for with each pass through the NIPALS algorithm, a routine has been developed that can determine the optimal number of iteations required to achieve the best overall results. Little user interaction beyond file selection is required. After processing, the resulting chromatographic peaks show improved iterations and signal-to-noise ratios. By removal of mass spectral noise, a significant improvement in spectral quality and PBM match probabilities is also observed. Another advantage of the routine is that data file size is reduced by an average of 30% due to removal of noise-related spectral lines.

LITERATURE CITED

(1) Hieftje, G. M. *Anal. Chem.* **1972**, *44*, 81A.
(2) Hieftje, G. M. *Anal. Chem.* **1972**, *44*, 69A.
(3) Doerfler, D. L.; Campbell, I. M. *Anal. Chem.* **1978**, *50*, 1018.
(4) *HP 59940A MS ChemStation Manual (HP-US series)*; Hewlett-Packard Co.; Palo Alto, CA, 1989.
(5) *Ion Trap Detector Operation Manual*; Finnigan MAT: San Jose, CA, 1986.
(6) Savitzky, A.; Golay, M. J. E. *Anal. Chem.* **1964**, *36*, 1927.
(7) Enke, C. G.; Nieman, T. A. *Anal. Chem.* **1976**, *48*, 705A.
(8) Duursma, R. P. J.; Smit, H. C. *Anal. Chim. Acta* **1981**, *133*, 67.
(9) Laeven, J. M.; Smit, H. C. *Anal. Chim. Acta* **1985**, *176*, 77.
(10) Lam, R. B.; Sparks, D. T.; Isenhour, T. L. *Anal. Chem.* **1982**, *54*, 1927.
(11) Derde M. P.; Massart, D. L. *Anal. Chim. Acta* **1986**, *191*, 1.
(12) Thomas, E. V.; Haaland, D. M. *Anal. Chem.* **1990**, *62*, 1091.
(13) Malinowski, E. R. *Anal. Chem.* **1977**, *49*, 606.
(14) Geladi, P.; Kowalski, B. R. *Anal. Chim. Acta* **1986**, *185*, 1.
(15) Shah, N. K.; Gemperline, P. J. *Anal. Chem.* **1990**, *62*, 465.
(16) Ritter, G. L.; Lowry, S. R.; Isenhour, T. L.; Wilkins, C. L. *Anal. Chem.* **1976**, *48*, 591.
(17) Van der Voet, H.; Doornbos, D. A. *Anal. Chim. Acta* **1978**, *103*, 201.
(18) Headley, L. M.; Hardy, J. K. *J. Food Sci.* **1989**, *54*, 1351.
(19) Aishima, T.; Nakai, S. *J. Food Sci.* **1987**, *52*, 939.
(20) Aishima, T. *J. Food Sci.* **1982**, *47*, 1562.
(21) Hardy, J. K.; Rinaldi, P. L. *J. Magn. Reson.* **1990**, *88*, 320.
(22) Micknovich, J. Hewlett-Packard Scientific Instrument Development, Palo Alto, CA, April 1990, personal communications.
(23) Johanson, E.; Wold, S.; Sjodin, K. *Anal. Chem.* **1984**, *56*, 1685.
(24) Wold, S. *Technometrics* **1978**, *20*, 397.
(25) Castro, P. E.; Lawton, W. H.; Sylvestre, E. A *Technometrics* **1986**, *28*, 329.
(26) Weiner, P. H.; Howery, D. G. *Anal. Chem.* **1972**, *44*, 1189.
(27) Malinowski, E. R. *Anal. Chem.* **1977**, *49*, 612.
(28) McLafferty, F. W.; Hertel, R. H.; Villwock, V. I. *Org. Mass Spectrom.* **1974**, *9*, 690.

RECEIVED for review June 19, 1990. Accepted November 19, 1990.

Multiphoton Ionization of Laser-Desorbed Neutral Molecules in a Fourier Transform Ion Cyclotron Resonance Mass Spectrometer

Jeffrey A. Zimmerman,[1] Clifford H. Watson,[2] and John R. Eyler*

Department of Chemistry, University of Florida, Gainesville, Florida 32611-2046

Resonant multiphoton ionization of laser-desorbed nonvolatile samples has been achieved in a Fourier transform ion cyclotron resonance (FTICR) mass spectrometer. The detection of iron at the 100 ppm (parts per million) doping level in an InP compound semiconductor sample and the production of molecular ions for a hexapeptide have been observed in a modified FTICR analyzer cell. A unique three-laser experiment has been devised in which infrared multiphoton dissociation of dipeptide ions, formed by resonant multiphoton ionization of laser-desorbed neutrals, is performed.

INTRODUCTION

Multiphoton ionization (MPI) (*1–3*) of neutral molecules has been widely studied in recent years as high-powered pulsed lasers with tunable output in the ultraviolet wavelength range have become commercially available. Both resonant (REMPI) and nonresonant MPI can be used to ionize species of interest, with the former yielding wavelength-selective formation of (primarily) parent ions at low laser power and increasing the number of fragment ions as the laser power is increased. At high laser powers, nonresonant MPI can be used to produce ionization from all molecules present in the focal volume of the laser, although wavelength selectivity is sacrificed and far fewer parent ions are usually formed (*4, 5*). The use of MPI to ionize neutral molecules which have been desorbed from solid surfaces has been shown to be a powerful analytical technique by several groups. In this approach, the ability to separate the desorption and ionization steps and the advantages of MPI outlined above have resulted in unique capabilities for analysis of solid samples.

All earlier experiments have utilized time-of-flight (TOF) mass spectrometers for mass analysis, because these pulsed instruments couple well with the pulsed lasers used for laser desorption and MPI. The groups of both Grotemeyer and Schlag (*6, 7*) and Lubman (*8, 9*) have used a supersonic expansion to entrain CO_2 laser-desorbed neutrals before MPI. This approach helps to provide a spatially well-defined beam of neutrals prior to ionization (enhancing the sensitivity and mass resolution when using TOF mass analysis) and at least partially cools the internal degrees of freedom of the neutral molecules, thus increasing the number of molecules in the states accessed by the MPI laser. A wide range of compounds, including many of biological interest, has been studied by these groups. Zare and co-workers (*10, 11*) have recently used a similar approach, but without supersonic expansion of the laser-desorbed neutrals, to analyze carbonaceous deposits in meteorites.

Our laboratory has been actively engaged (*12–15*) in coupling lasers to Fourier transform ion cyclotron resonance (FTICR) mass spectrometers (*16–20*) for a number of years. Of particular interest are the direct formation of ions by CO_2 laser desorption (*14, 21–23*) and the use of a second laser to induce fragmentation of these ions via infrared multiphoton dissociation (IRMPD) (*14, 21*). Since FTICR utilizes pulsed ion formation and detection, it should couple with (pulsed) laser desorption of neutral molecules followed by (pulsed) multiphoton ionization in as facile a manner as does TOF mass analysis.

At least two additional advantages should be realized when using FTICR mass analysis to study ions formed by MPI of laser-desorbed neutrals. The first is much higher resolution than is possible with TOF mass spectrometers, even those equipped with reflectrons (*24*). FTICR has routinely demonstrated the highest mass resolution (*25*) of any type of mass spectrometer, and such high resolution can often be valuable in distinguishing ion structures of the same nominal mass or in separating different isotopes of certain elements which overlap in mass. A second advantage of FTICR mass analysis is the ability to subject trapped ions to further analysis, studying their reactivity in ion/molecule reactions (*26*), and/or inducing fragmentation by collisional (*27*) or photon (*28*) activation.

While to our knowledge no group has demonstrated MPI of laser-desorbed neutrals in an FTICR mass spectrometer, several have reported MPI of molecules introduced into the ICR mass spectrometer directly in the gaseous state (*29–31*). Laser-desorbed neutrals have been ionized by methods other than MPI, such as electron impact (*32*) and chemical ionization (*33*). We report here the successful MPI formation of ions from laser-desorbed neutral molecules in a FTICR mass spectrometer. Ions formed in this way can be detected by using the high mass resolution capabilities of the FTICR technique. We have also exploited the ability to subject the ions produced and trapped in this manner to laser photodissociation in a unique three-laser experiment in which a third (gated continuous-wave (cw) CO_2) laser has been used to dissociate small oligopeptide ions.

EXPERIMENTAL SECTION

The Fourier transform ion cyclotron resonance mass spectrometer used in this work consisted of a Nicolet (now Extrel FTMS, P.O. Box 4508, Madison, WI 53711) FTMS-1000 data system, a prototype Nicolet 2.0-T magnet, and a home-built/assembled vacuum system (this system is described in detail in ref 34). The main vacuum chamber was a 15-cm inside diameter (i.d.) stainless steel cylinder that was mounted inside the 20-cm bore of the 2.0-T superconducting magnet. Two oil diffusion pumps (Alcatel Vacuum Products, 40 Pondpark Rd, Hingham, MA 02043), with pumping speeds of 700 and 300 L/s were used to evacuate the vacuum chamber. Several windows were mounted on each end flange to facilitate various laser-related experiments.

Several modifications to the existing FTMS-1000 analyzer cell were necessary in order to permit entry of the beams from more than one laser (see Figure 1). In all experiments, an excimer laser (Lumonics Model 860-4 excimer laser, 105 Schneider Road, Kanata, ON K2K 1Y3 Canada) modified with infrared (IR) optics and operating in the pulsed CO_2 mode (10.6-μm wavelength, pulse length ca. 1 μs, approximately 0.75 mJ/pulse entering the vacuum chamber) was used to desorb a solid sample mounted on a probe tip (cf. Figure 2 of ref 14). The laser beam passed through a ZnSe

[1] Present address: IBM Technology Laboratory, Dept T37, P.O. Box 8003, Endicott, NY 13760-5553.
[2] Present address: Bruker Instruments, Inc., Manning Park, 19 Fortune Dr, Billerica, MA 01821.

0003-2700/91/0363-0361$02.50/0

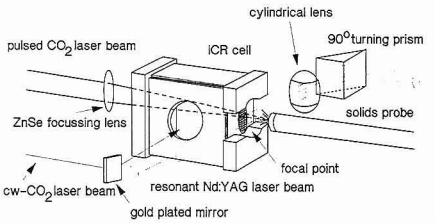

Figure 1. ICR cell modified to permit three laser experiments.

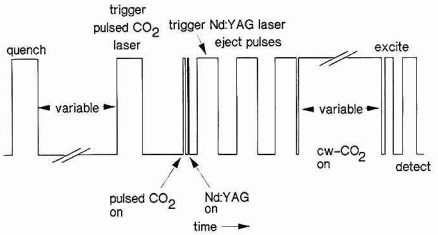

Figure 2. Experimental pulse sequence employed in the FTICR experiments. The cw CO_2 photodissociation step was eliminated when only LD/REMPI was desired.

window into the vacuum chamber and was focused by a 7.62-cm focal length ZnSe lens. The focused beam entered a small hole in the front trap plate of the FTICR cell, traversed the cell, and exited the back trap plate through a 1-cm-diameter mesh-covered opening, then irradiating the sample. Postionization of the neutrals desorbed by the first laser was achieved by using the fourth harmonic, 266 nm, of a Nd:YAG laser (Continuum, 390 Reed St, Santa Clara, CA 95050) or by the tunable output of a dye laser pumped by the second harmonic of the Nd:YAG laser. The output from rhodamine dyes 610 and 590 (Exciton, P.O. Box 31126, Overlook Station, Dayton, OH 45431) was doubled to obtain wavelengths in the range 305–280 nm. The UV beam entered the vacuum chamber through a 1-cm sapphire window and for the majority of the studies passed through a 90° fused quartz turning prism. The beam was then focused by a 2.54-cm focal length cylindrical lens through a cut-out section of the machinable ceramic cell support/insulator at the solids probe end of the cell. This positioned the focal point several millimeters from the probe tip and directly between the tip and the cell. Alternatively, some early studies were performed by passing the unfocused beam through 1-cm-diameter holes in the excite plates (similar to the cw-laser pathway shown in Figure 1), thus allowing the beam to travel through the center of the cell. Typical UV laser pulse energies were on the order of 50–100 mJ/pulse at 266 nm and 5–10 mJ/pulse for the (tuned) wavelengths from 280 to 305 nm. The output of the third laser, a gated cw CO_2 laser (Apollo Lasers, Inc., 9201 Independence Ave, Chatsworth, CA 91311), also entered the vacuum chamber through a ZnSe window and was turned by a plated gold mirror mounted to one of the excite plates. The beam entered the cell through a 1.25-cm hole and was reflected from the opposite (parallel) plate, giving a second pass of this laser beam through the cell.

The FTICR pulse sequence employed is shown schematically in Figure 2. It was necessary to adjust the pulse sequence to a period of 989.5 ms in order to conform to the triggering requirements of the Nd:YAG laser. Coupling of the FTICR electronics and the Nd:YAG laser was accomplished by a home-built microcomputer interface (*35*). Using this program, it was possible to trigger the laser q-switch every ninth firing of the flashlamps, thus allowing a lower FTICR pulse repetition rate (ca. 1 Hz as opposed to the normal 10-Hz laser firing rate) and permitting greater freedom in designing the pulse sequence shown in Figure 2.

The pulsed CO_2 laser was triggered by the "beam event" pulse directly after a quench pulse expelled all ions from the cell but due to internal timing constraints did not fire until an additional 44.1 ms after triggering. After pulsed laser desorption of neutral molecules, the Nd:YAG laser was fired a variable time period, 5–50 μs, later. The time between the two laser pulses was monitored by using the sync output from the CO_2 laser and the signal from a fast photodiode which picked up scattered light from the Nd:YAG laser pulse. Timing between the two laser pulses experienced jitter of ± 4 μs.

Because of timing restrictions, the Nd:YAG laser was not triggered during the pulse sequence in which it fired but instead during the *preceding* sequence and was "wrapped around" to the next pulse sequence. In the three-laser experiments, the cw CO_2 laser was gated on for a variable time after a series of three ejection events to remove unwanted ions, thus irradiating the trapped ions of interest that were formed by MPI of laser-desorbed neutrals. Following this, the usual FTICR excitation and detection process took place.

For most experiments, the mass spectrometer was operated in its standard broad-band (10 kHz to 2.67 MHz) mode using frequency chirp excitation. Heterodyne detection of the transient signal was used when required for accurate mass analysis. Typically, 10–50 transient signals, each generated by ions from 1 laser pulse and consisting of 16 384 data points, were acquired and averaged. The averaged time-domain transient was apodized (*36*) and zero-filled once prior to Fourier transformation. The number of data points collected for each transient signal was increased from 16K to 64K as necessary to increase the mass resolution. Only positive ions were observed following multiphoton ionization, and a trapping voltage of 2 V was used for most experiments. The trapping voltage was reduced to 0.5 V during heterodyne detection experiments.

A clean stainless steel probe tip was used to generate the Fe signal in initial experiments and an InP wafer doped with Fe to the 100 ppm level was used in subsequent experiments. Coronene (Aldrich) and peptide samples (Chemical Dynamics Corporation) were used without additional purification. Sample purity was assessed by using broad-band laser desorption mass spectrometry. The cororene and peptide samples (0.5–5 mg) were mixed with methanol (3–5 mL), and a small portion of the resulting slurry was deposited on a stainless steel probe tip by using a micropipet. The sample coating typically appeared opaque and was much thicker than that normally used for laser desorption. The probe tip was mounted such that rotation of the probe exposed a fresh surface for laser desorption of neutrals. Depending on sample preparation, a single spot produced a signal for 100–500 laser pulses.

RESULTS AND DISCUSSION

Postionization of Laser-Desorbed Neutrals in the FTICR. The first attempts at multiphoton ionization of laser-desorbed neutrals were made with coronene. Care was taken to use sufficiently low desorption laser power to avoid direct ion production. Postionization was achieved with an unfocused (frequency doubled) dye laser beam of 300-nm wavelength (solution λ_{max} of coronene is 302 nm (Sadtler Standard Spectra; Sadtler Research Laboratories, Inc., 1976)), which passed through the center of the cell in a path similar to that shown for the cw CO_2 laser beam in Figure 1. A maximum signal for the $m/z = 300$ parent ion was observed when the delay between the desorption and ionization lasers was set to 60 μs, but ions were still formed when the delay time was as long as 150 μs.

Multiphoton ionization of laser-desorbed iron atoms was performed by using a similar procedure and experimental configuration to that for coronene. Iron and other neutrals were desorbed from a 304 stainless steel probe tip with postionization achieved by 302.1-nm light, the first photon resonant with the $y\mathrm{D}^5_4 \leftarrow a\mathrm{D}^5_4$ transition and the second exciting into the ionization continuum. Light of several other wavelengths corresponding to transitions originating from the $a\mathrm{D}^5_4$ state (298.4, 296.7, and 293.7 nm) also produced ionization. However, no signal could be produced from other higher lying $a\mathrm{D}^5_J$ states. This indicates that significant populations of even low-lying excited states (0.05 and 0.11 eV above the ground

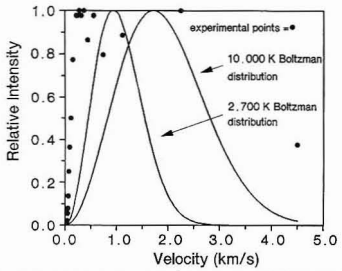

Figure 3. Relative intensity of Fe^+ formed by REMPI (302.1 nm) of laser-desorbed neutral Fe from a 304 stainless steel probe tip as a function of velocity, assuming all neutrals were desorbed during the 1-μs pulse duration of the CO_2 desorbing laser. Also plotted are the Boltzmann velocity distributions at 2700 K (boiling point of stainless steel) and 10 000 K.

state) of the Fe atoms either were not produced or were quenched en route to the cell center. These results are quite different from the resonant ionization lines observed in a glow discharge (37), where numerous examples of excitation from the higher excited states were observed. Figure 3 shows the Fe^+ signal produced by 302.1-nm resonant, two-photon ionization as a function of the velocity the neutral iron atoms would achieve if desorbed from the surface during the desorption laser beam pulse. The experimental distribution does not fit the Boltzmann velocity distributions at either 2700 °C (ca. the boiling point of 302 stainless steel) or 10 000 °C. A substantial signal is observed at velocities much slower than neutrals desorbed at 2700 °C would acquire and much faster than those formed at a temperature of 10 000 °C would acquire. This indicates either that the iron atoms are desorbed with a wide (non-Boltzmann) distribution of kinetic energies or that the desorption process proceeds gradually with atoms emitted tens of microseconds after the laser energy has been deposited.

Significant iron signals were also produced when the doubled dye laser beam was focused by the cylindrical lens and ionization took place quite close to the probe tip. At a distance between the probe tip and ionization laser focal point of approximately 2 mm, the strongest ion signals were found at a laser delay of 7 μs, but no observable signal was seen at either 4 or 10 μs. Jitter in the timing prevented a detailed study of neutral velocities; however, the narrow spatial distribution of desorbed iron atoms found close to the probe tip (as opposed to a wide distribution seen at the cell center, cf. Figure 3) indicates a virtually instantaneous desorption process with the resulting atoms desorbed with a wide range of velocities.

The ultimate intent of these atomic postionization experiments with FTICR mass analysis was to detect trace impurities while taking advantage of the technique's high resolution. Iron at a 100 ppm doping level in an InP substrate was observed by using the experimental configuration discussed above. The signal was maximized at a 10-μs delay time between the two lasers (slightly longer than with Fe from the stainless steel substrate) at a 2-mm probe to focal point distance, which permitted a major portion of the desorbed neutrals to be intersected by the focused ionization laser. The FTICR mass spectrum obtained is shown in Figure 4. A maximum mass resolution of 11 400 using 64K data points was obtained. This resolution, which is much lower than is normally experienced by using FTICR, may result from the high translational energy these ions possess (in addition to a wide distribution of translational energies) and the inability to thermalize the ions with a neutral gas because of resulting loss of signal strength. However, the mass resolution attained is still substantially higher than that demonstrated by commercial TOF reflectron instruments (a FWHH resolution of 5000 at m/z = 78 is obtained on a TOF1 relectron mass spectrometer, Bruker Instruments, Inc., Manning Park, Billerica, MA 01821), which use laser ionization. A small In^+ peak is also seen at m/z = 115 in Figure 4, since it was difficult to produce desorption without the formation of In^+. Given the signal-to-noise ratio (ca. 100:1) seen in Figure 4, analysis of samples with much lower levels of Fe (in the few ppm range) should be possible.

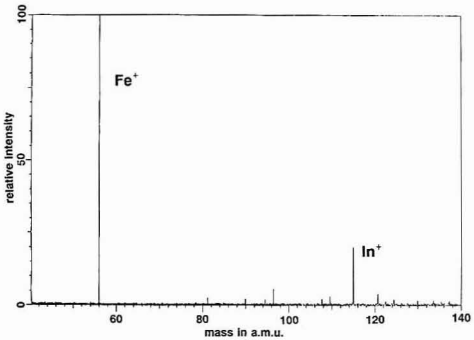

Figure 4. REMPI spectrum of iron-doped (100 ppm) InP. Resolution (FWHH) of the Fe^+ peak is 11 400. A small In^+ ion signal is also observed and is formed by the desorbing laser.

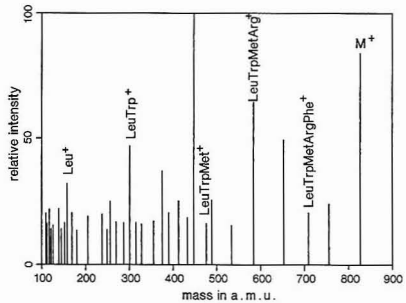

Figure 5. LD/REMPI (REMPI at 266 nm) spectrum of hexapeptide LeuTrpMetArgPheAla.

We have successfully demonstrated laser postionization of larger species, including the hexapeptide LeuTrpMetArgPheAla. This molecule undergoes facile ionization when irradiated with 266-nm light to produce a molecular ion and numerous fragment ions. These ions provide useful molecular weight and structural information. An abundant fragment peak is observed for each of the possible sequence ions, as shown in Figure 5. The labeled peaks represent fragmentation from the C-terminus end of the molecule. Additional fragment ions resulting from N-terminus cleavages and loss of side alkyl groups are present in lesser abundance.

Infrared Multiphoton Dissociation (IRMPD) of Oligopeptide Ions. Under proper conditions, laser desorption can be a "soft" ionization technique, in which pseudomolecular ions are formed by attachment of a cation such as K^+ or Na^+ to intact neutral molecules. Unfortunately, the main fragmentation pathway observed for these species with IRMPD is quite often the structurally uninformative loss of the neutral molecule

$$(M + K)^+ + nh\nu \rightarrow M + K^+$$

Such behavior is not seen when working with laser-desorbed negative ions, where $(M - H)^-$ ions are the pseudomolecular

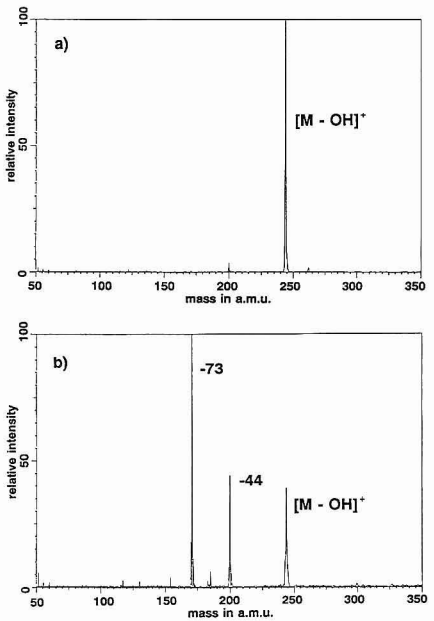

Figure 6. (a) LD/REMPI spectrum of TrpGly (all ions under $m/z = 150$ are ejected). (b) LD/REMPI/IRMPD spectrum of TrpGly showing losses of 44 and 73 amu neutral fragments.

ions most often formed, but it can be quite limiting when examining positive ions. Production of such pseudomolecular ions is particularly undesirable when using laser desorption and IRMPD to study oligopeptide ions, where cleavage of amide linkages instead of $M - K^+$ bonds is sought.

On the basis of the results of other workers (*8*, *9*) using low-powered laser desorption and multiphoton ionization for ion production in time-of-flight investigations, peptides can provide an abundance of ions that are potentially useful for structure identification. Peptides containing a strongly UV absorbing amino acid residue, such as phenylalanine (λ_{max} = 268 nm), tyrosine (λ_{max} = 272.7 nm), tryptophan (λ_{max} = 286.0 nm), or histidine (λ_{max} = 250.0 nm), are easily ionized by resonant multiphoton ionization, often producing a characteristic radical molecular or pseudomolecular ion.

Although the amount of fragmentation observed following MPI can sometimes be influenced by varying the energy of the ionization laser, quantitative control of fragmentation is often quite difficult. One answer to this problem is to irradiate ions trapped in the FTICR analyzer cell with infrared radiation. The laser desorption/multiphoton ionization mass spectrum of the dipeptide L-tryptophylglycine (TrpGly) is shown in the upper half of Figure 6. All ions below m/z = 150, including a fragment ion of m/z = 130, have been ejected prior to recording the spectrum. This dipeptide forms a pseudomolecular ion m/z = 244 ($[M - OH]^+$ as determined by exact mass analysis). This ion dissociates when irradiated with a gated pulse of light from a cw CO_2 laser, forming two fragment ions at m/z = 200 and 171. Double resonance experiments (m/z = 200 is ejected during the cw CO_2 laser pulse) confirm this to be a competing and not a sequential (m/z = 244 → m/z = 200 → m/z = 171) reaction. The amount of fragmentation is easily controlled by varying either the cw CO_2 laser power or the length of the irradiation period. A plot of

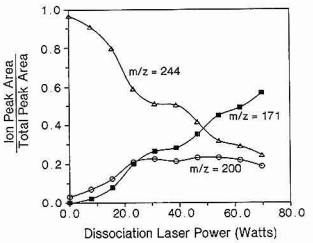

Figure 7. Dependence of ion peak area on cw CO_2 power for the photodissociation of $[M - OH]^+$ formed by LD/REMPI of TrpGly.

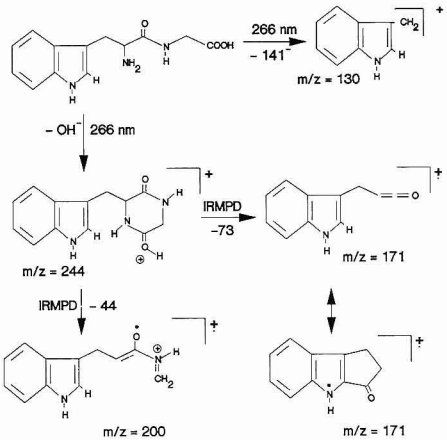

Figure 8. Possible ionization/dissociation scheme for the LD/REMPI/IRMPD of TrpGly.

the normalized abundance for the parent and daughter ions as a function of the cw CO_2 laser power (laser on for 50 ms) is shown in Figure 7. The daughter ion intensity increases monotonically as the amount of IR irradiation increases.

TrpGly has been shown to form a cyclodipeptide (*38*) (with elimination of water), but this occurred only when a thick sample was subjected to laser desorption followed by REMPI in a similar approach to this study (where sample thickness is estimated at 0.5-1 mm). However, exact mass analysis has shown that the m/z = 244 peak in our experiment is $[M - OH]^+$, differing by 1 amu from the mass-to-charge ratio for $[M - H_2O]^+$. As shown in Figure 8, a protonated cyclodipeptide is a quite reasonable structure for the $[M - OH]^+$ ion. The subsequent losses of 44 and 73 amu fragments, induced by IRMPD, can be explained by the ring-cleavage processes shown. We cannot explain why an $[M - OH]^+$ fragment, apparently with a protonated cyclodipeptide structure, is formed in our experiment, while quite similar conditions in an earlier work (*38*) resulted in an $[M - H_2O]^+$ cyclodipeptide. We note, however, that $[M - OH]^+$ ions were reported in one earlier publication (*39*).

The LD/REMPI of several dipeptides gave rise to intact molecular ions that were then subjected to IRMPD. The molecular ion of ProPhe (MW = 262) underwent photodissociation to form m/z = 70 [pyrrole - 1]$^+$ (see Figure 9a). A protonated ArgPhe ion (MW = 322) is apparently formed in the LD/REMPI process by a mechanism not yet understood. Photodissociation produces fragment ions at m/z = 305 (loss of neutral OH), m/z = 245 (loss of the phenyl group), m/z = 263 (loss of $NHCNH_2NH_2$), and m/z = 158 (cleavage of the

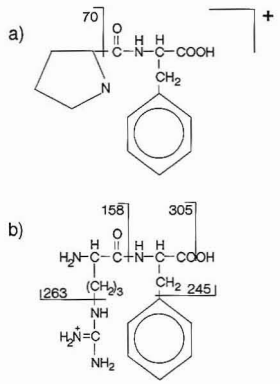

Figure 9. Ions formed by LD/REMPI of (a) ProPhe and (b) ArgPhe. Bond cleavages produced by IRMPD are indicated by solid lines, and the *m/z* ratio of the fragment ions is formed.

amide bond with the charge remaining on the arginine fragment), all consistent with protonation on the arginine side chain as shown in Figure 9b. These fragments provide practical information that is useful in structure elucidation. Thus, the promising results produced by the LD/REMPI/IRMPD technique suggest that it may be extended to more biologically significant oligopeptides/proteins of higher molecular weight in which direct laser desorption does not produce useful information.

CONCLUSIONS

Multiphoton ionization of neutral molecules formed by laser desorption has been carried out successfully in a Fourier transform ion cyclotron resonance mass spectrometer. At least two advantages of using FTICR mass spectrometric detection have been realized: high mass resolution and the ability to subject ions formed by MPI to infrared laser dissociation while they are trapped in the FTICR cell. Extensions of this technique to larger peptides, to other biological samples, and to lower concentrations of dopants or contaminants in semiconductor samples are in progress.

ACKNOWLEDGMENT

We thank Joseph Shalosky for constructing the modified FTICR analyzer cells, K. R. Williams for numerous helpful comments, and T. J. Anderson for providing the Fe-doped InP sample.

LITERATURE CITED

(1) Antonov, V. S.; Letokhov, V. S. *Appl. Phys.* **1981**, *24*, 89–104.
(2) Gedanken, A.; Robin, M. B.; Kuebler, N. A. *J. Phys. Chem.* **1982**, *86*, 4096–4107.
(3) Gobeli, D. A.; Yang, J. J.; El-Sayed, M. A. *Chem. Rev.* **1985**, *85*, 529–554.
(4) Schueler, B.; Odom, R. W. *J. Appl. Phys.* **1987**, *61* (9), 4652–4661.
(5) Pallix, J. B.; Gillen, K. T.; Becker, C. H. *Nucl. Instrum. Meth. Phys. Res.* **1988**, *B33*, 912–917.
(6) Grotemeyer, J.; Boesl, U.; Walter, K.; Schlag, E. W. *J. Am. Chem. Soc.* **1986**, *108*, 4233–4234.
(7) Grotemeyer, J.; Boesl, U.; Walter, K.; Schlag, E. W. *Org. Mass Spectrom.* **1986**, *21*, 595–597.
(8) Liang, L.; Lubman, D. M. *Appl. Spectrosc.* **1988**, *42* (3), 411–417.
(9) Liang, L.; Lubman, D. M. *Int. J. Mass Spectrom. Ion Proc.* **1989**, *88*, 197–210.
(10) Hahn, J. H.; Zenobi, R.; Zare, R. N. *J. Am. Chem. Soc.* **1987**, *109*, 2842–2843.
(11) Hahn, J. H.; Zenobi, R.; Bada, J. L.; Zare, R. N. *Science* **1988**, *239*, 1523–1525.
(12) Baykut, G.; Watson, C. H.; Weller, R. R.; Eyler, J. R. *J. Am. Chem. Soc.* **1985**, *107*, 8036–8042.
(13) Watson, C. H.; Baykut, G.; Battiste, M. A.; Eyler, J. R. *Anal. Chim. Acta* **1985**, *178*, 125–136.
(14) Watson, C. H.; Baykut, G.; Eyler, J. R. *Anal. Chem.* **1987**, *59*, 1133–1138.
(15) Moini, M.; Eyler, J. R. *Int. J. Mass Spectrom. Ion Proc.* **1987**, *76*, 47–54.
(16) Comisarow, M. B.; Marshall, A. G. *Chem. Phys. Lett.* **1974**, *25*, 282–283.
(17) Marshall, A. G. *Acc. Chem. Res.* **1985**, *18*, 316–322.
(18) Baykut, G.; Eyler, J. R. *Trends Anal. Chem.* **1986**, *5*, 44–49.
(19) Watson, C. H.; Baykut, G.; Eyler, J. R. In *Fourier Transform Mass Spectrometry*; Buchanan, M. V., Ed.; ACS Symposium Series 359; American Chemical Society: Washington, DC, 1987; pp 140–154.
(20) Wilkins, C. L.; Chowdhury, A. K.; Nuwaysir, L. M.; Coates, M. L. *Mass Spectrom. Rev.* **1989**, *8*, 67–92.
(21) Watson, C. H.; Baykut, G.; Mowafy, Z.; Katritzky, A. R.; Eyler, J. R. *Anal. Instrum.* **1988**, *17*, 155–172.
(22) Katritzky, A. R.; Watson, C. H.; Dega-Szafran, Z.; Eyler, J. R. *J. Org. Mass Spectrom.* **1989**, *24*, 1017–1021.
(23) Bach, S. B. H.; Eyler, J. R. *J. Chem. Phys.* **1990**, *92*, 358–363.
(24) Boesl, U.; Walter, K.; Schlag, E. W. *Int. J. Mass Spectrom. Ion Proc.* **1986**, *71*, 309–313.
(25) Bamberg, M.; Allemann, M.; Wanczek, K. P. *35th ASMS Conference on Mass Spectrometry and Allied Topics*, Denver; American Society for Mass Spectrometry: East Lansing, MI, 1987; pp 1116–1117.
(26) Van der Hart, W. J.; De Koning, L. J.; Nibbering, N. M. M.; Gross, M. L. *Int. J. Mass Spectrom. Ion Proc.* **1986**, *72* (1–2), 99–114.
(27) Cody, R. B.; Burnier, R. C.; Freiser, B. S. *Anal. Chem.* **1982**, *54*, 96–101.
(28) Dunbar, R. C. in *Gas Phase Ion Chemistry*; Bowers, M. T. Ed.; Academic Press: New York, London, 1984; Vol. 3, p 129.
(29) Irion, M. P.; Bowers, W.D.; Hunter, R. L.; Rowland, F. S.; McIver, R. T., Jr. *Chem. Phys. Lett.* **1982**, *93* (4), 375–379.
(30) Sack, T. M.; McCrery, D. A.; Gross, M. L. *Anal. Chem.* **1985**, *57* (7), 1290–1295.
(31) Kuo, C. H.; Beggs, C. G.; Kemper, P. R.; Bowers, M. T.; Leahy, D. J.; Zare, R. N. *Chem. Phys. Lett.* **1989**, *163* (4–5), 291–296.
(32) Sherman, M. G.; Kingsley, J. R.; Dahlgren, D. A.; Hemminger, J. C.; McIver, R. T., Jr. *Surf. Sci.* **1985**, *148*, L25.
(33) Amster, I. J.; Land, D. P.; Hemminger, J. C.; McIver, R. T., Jr. *Anal. Chem.* **1989**, *61*, 184–186.
(34) Zimmerman, J. A.; Bach, S. B. H.; Watson, C. H.; Eyler, J. R. *J. Phys. Chem.*, in press.
(35) Moini, M.; Eyler, J. R. *J. Chem. Phys.* **1988**, *88*, 5512–5515.
(36) Harris, F. J. *IEEE* **1978**, *66*, 51.
(37) Hess, K. R.; Harrison, W. W. *Anal. Chem.* **1986**, *58*, 1696–1701.
(38) Li, L.; Lubman, D. M. *Rapid Comm. Mass Spectrom.* **1989**, *3*, 12–16.
(39) Tembreull, R.; Lubman, D. M. *Anal. Chem.* **1987**, *59*, 1003–1006.

RECEIVED for review June 28, 1990. Accepted November 16, 1990. This work was supported in part by the Office of Naval Research and by the Florida SUS Advanced Materials and Microelectronic Processing DARPA Initiative.

Ultrasonic Time-of-Flight Method for On-Line Quantitation of in Situ Generated Arsine

Jorge L. Valdes* and Gardy Cadet

AT&T Bell Laboratories, Murray Hill, New Jersey 07974

An ultrasonic time-of-flight method is described for continuous concentration monitoring of in situ electrochemically generated arsine. The method is based on accurate measurements of the speed of sound, which is a sensitive function of the composition of a binary gas mixture, particularly with gases of disparate molecular weights, i.e. arsine and hydrogen. Speed of sound measurements made on flowing streams of argon–helium and arsine–hydrogen at ambient temperature and pressure are in excellent agreement with values predicted by using an acoustic model based on ideal gas theory. Highly repeatable calibration curves are obtained for each binary gas mixture analyzed over the entire range (0–100%) of compositions. The calibration was found to be independent of the volumetric flow rate of the gas mixture over the range of pressures 0–30 psig. The ultrasonic method offers a practical solution to accurate and reliable concentration monitoring of a wide range of gas-phase reagents used in the fabrication of devices.

INTRODUCTION

Control over the concentration of electronic reagents is critical for the growth of compound semiconductor materials by molecular beam epitaxy (MBE), hydride vapor-phase epitaxy (H-VPE), and metal organic chemical vapor deposition (MOCVD) processes. Current technology relies on feedstream compositions that are fixed by the prevailing contents of the cylinder containing the reagent. Control of the concentration at a different desired value is achieved by mixing the reagent stream with a diluent gas, such as hydrogen, using a mass flow controller (MFC). In a recent paper, we described a process for electrochemical generation of arsine for electronic applications (*1*). This on-demand generator offers delivery of a wide range of arsine concentrations (2–90% AsH_3 in H_2) at variable pressures and flow rates. For this more versatile and safer arsine source, knowledge of the extant reagent concentration permits precise replication of this experimental variable, which allows for a higher degree of reproducibility in growth conditions and thus material properties.

The composition of a gas mixture can be measured by a variety of techniques such as mass spectrometry and gas chromatography. Ultrasonic methods (*2–6*) have been used recently to measure acoustic velocities of gas mixtures in flow systems. The acoustic velocity is an intensive property of the gas that is related to its composition. For the case of a binary or pseudobinary gas, the acoustic velocity of the mixture depends on the mole fraction of each gas and their respective pure component properties. Acoustic velocities can be measured by using time-of-flight and continuous-wave cavity resonance techniques. In this work, we employ the former technique to assess the feasibility of soundspeed measurements for on-line reagent concentration monitoring of in situ generated arsine process streams.

THEORETICAL SECTION

The acoustic velocity (V_s) of a single-component gas stream is given by the following relationship (*7*)

$$V_s = \sqrt{\frac{RT}{M}\left(-\frac{V^2}{RT}\left(\frac{\partial P}{\partial V}\right)_T + \frac{R}{C_V}\left[\frac{V}{R}\left(\frac{\partial P}{\partial T}\right)_V\right]\right)} \quad (1)$$

where R is the universal gas constant, M is the molar mass of the gas, P is the pressure, V is the volume, and C_V is the specific heat at constant volume. A consistent use of SI units in eq 1 yields the acoustic velocity in units of meters per second. In this treatment, we consider 1 mol of an ideal gas whose thermodynamic behavior is described by the following equation of state

$$PV = RT \quad (2)$$

Substituting eq 2 into eq 1 and performing the indicated differentiations yields the following expression for the acoustic velocity of an ideal gas

$$V_s = \sqrt{\gamma RT/M} \quad (3)$$

where $\gamma \equiv C_P/C_V$ is the ratio of the specific heat capacities at constant pressure to the value at constant volume, respectively. The acoustic velocity predicted by eq 3 is generally in good agreement with experimentally measured values for noble gases (He, Ne, Ar, etc.), atmospheric diatomic gases, low molecular weight gases, and gases at sufficiently low pressures (i.e. <10 atm).

Although the acoustic velocity given by eq 3 applies strictly to pure component systems, binary and pseudobinary gas mixtures can also be described by the same functional relationship provided suitable values for γ and M, representative of the mixture, are adopted. In this work, we consider a binary gas mixture to be adequately described as a linear function, by mole fraction, of the pure component physical properties. The ratio of specific heats in a binary gas mixture, $\bar{\gamma}$, is given by

$$\bar{\gamma} = \frac{XC_{P,1} + (1-X)C_{P,2}}{XC_{V,1} + (1-X)C_{V,2}} \quad (4)$$

where X refers to the mole fraction of gas 1 and the subscripted quantities refer to those of the pure components. For an ideal gas, $C_P = C_V + R$, and thus eq 4 can be rewritten in a more conventional form as

$$\bar{\gamma} = 1 + \left(\frac{X}{\gamma_1 - 1} + \frac{1-X}{\gamma_2 - 1}\right)^{-1} \quad (5)$$

where γ_1 and γ_2 are the pure component specific heat ratios. Similarly, the mole fraction average weight, $\bar{M}$, of the binary gas mixture is given by

$$\bar{M} = XM_1 + (1-X)M_2 \quad (6)$$

The acoustic velocity of a binary mixture is then represented by

$$V_s = \sqrt{\bar{\gamma} RT/\bar{M}} \quad (7)$$

with $\bar{\gamma}$ and $\bar{M}$ given by eqs 5 and 6, respectively. At a given temperature T, the measured acoustic velocity can be used along with eq 7 to determine the composition of the gas mixture provided the pure component parameters (i.e. γ and

0003-2700/91/0363-0366$02.50/0

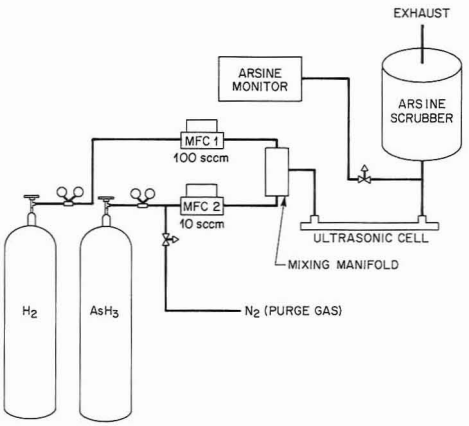

Figure 1. Experimental configuration for ultrasonic measurements.

M) are known. Once the mole fraction is determined, the partial pressure of component 1, P_1, can be calculated from the total pressure P by

$$P_1 = xP \tag{8}$$

EXPERIMENTAL SECTION

Acoustic velocity measurements were performed on the inert gas mixture argon/helium, prior to executing experiments with arsine/hydrogen. The acoustic velocity was measured by using a Model 6068 ultrasonic flow cell and a microprocessor-based acoustic spectrum analyzer (Panametrics, Waltham, MA). The experimental apparatus and configuration are shown in Figure 1. Cylinders of the appropriate pure component gases (research grade, >99.99% purity) were used, and the flow of each gas was precisely metered by using mass flow controllers (MKS Instruments, Andover, MA) to obtain the desired composition. The pure gases were mixed downstream in a manifold and then introduced into the ultrasonic cell in a flow-by configuration. Experiments involving arsine were conducted in a properly exhausted gas cabinet, and every precaution was followed to ensure maximum safety. Additionally, the exit stream of the ultrasonic cell was passed through an activated carbon-filled scrubber to remove arsine. Experiments were conducted at ambient temperature (23 ± 0.1 °C), and it was found that consistent and repeatable results could be achieved without requiring additional temperature control of the cell.

The ultrasonic flow cell consists of two titanium transducers (Model 91, also from Panametrics) placed at a fixed distance apart (0.314 3250 m) and in direct contact with the gas stream. Each transducer resides in a 1-in. pipe fitting located at either end of a 12 in. long by 0.375 in. diameter stainless steel tube. This arrangement provides uniform gas flow patterns around each transducer for proper transmission of the acoustic wave into the gas stream. Transducers are excited by ±60 V and nominally operate at 100-kHz frequency. Each transducer can operate as a transmitter and a receiver. In this manner, it is possible to measure both the upstream and downstream time-of-flights. The average of the upstream and downstream time-of-flights necessarily cancels the effect of flow-induced Doppler shifts in the frequency and thus yields higher accuracy acoustic velocities. Acoustic spectra were recorded on a digital oscilloscope, and the time-of-flight was determined by the acoustic spectrum analyzer, which uses an 8-MHz clock.

RESULTS AND DISCUSSION

It is often convenient in ultrasonic measurements to display the acoustic spectrum of the receiving transducer on an oscilloscope. The measured acoustic signal depends on the interaction of the ultrasonic wave with the gas mixture. In Figures 2 and 3 are shown the acoustic spectra measured for

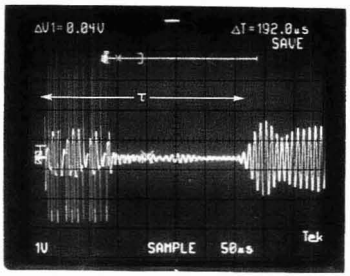

Figure 2. Acoustic spectrum for pure helium at ambient temperature and 1-atm pressure.

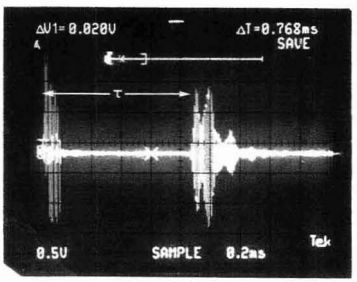

Figure 3. Acoustic spectrum for pure argon at ambient temperature and 1-atm pressure.

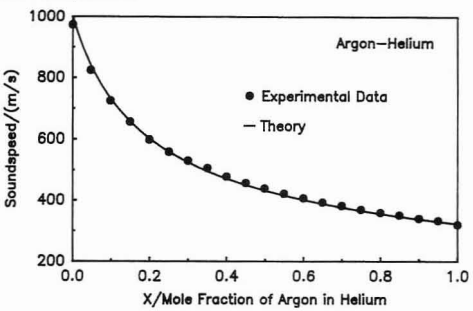

Figure 4. Comparison of experimental (●) and theoretical (—) soundspeed vs mole fraction of argon for the argon/helium system.

pure helium and pure argon, respectively, at ambient temperature and pressure. The ultrasonic wave that propagates through the gas medium is recognized by the double-humped region. The onset of this wave defines the time-of-flight, τ. The measured time-of-flights for helium and argon are τ = 322.7 μs and τ = 982.3 μs, respectively. At short times (<150 μs), the acoustic spectrum exhibits the propagation of sound through the stainless steel flow cell itself. The speed of sound in 316 stainless steel is 3070 m/s for a time-of-flight (~100 μs) consistent with the measured acoustic spectrum.

In Figure 4 are shown the measured acoustic velocities (●) for the argon/helium system as a function of the mole fraction of argon at ambient temperature and 1-atm pressure. The acoustic velocity predicted by eq 7 by using ideal gas theory and the pure component parameters is shown by the solid curve. Specific heat capacity ratios, γ_{Ar} = 1.669 and γ_{He} = 1.630, were used in eq 7 for argon and helium, respectively (8). The predicted (shown by the solid curve) and measured velocities are in excellent agreement. In addition, soundspeed vs mole fraction data for the argon/helium system obtained

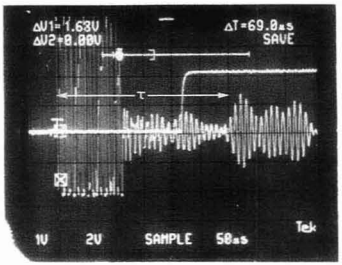

Figure 5. Acoustic spectrum for a binary mixture consisting of 0.019 mole fraction arsine in hydrogen.

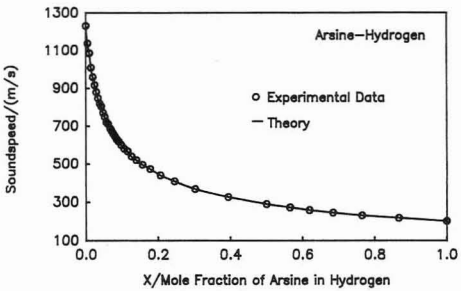

Figure 6. Comparison of experimental (O) and theoretical (—) soundspeed vs mole fraction of arsine for the arsine/hydrogen system.

by starting with either pure helium or argon and mixing increasing amounts of the diluent gas are highly repeatable. The measured soundspeed is also found to be independent of the volumetric gas flow rate through the ultrasonic cell. Consequently, a single calibration curve for the concentration can be employed to measure process streams with variable flow rates.

The acoustic spectrum for a mixture of arsine in hydrogen (0.019 mole fraction AsH_3) is shown in Figure 5. The measured time-of-flight is $\tau = 272.4$ μs for an acoustic velocity corresponding to 1154 m/s. In Figure 6 are shown the measured acoustic velocities for the arsine/hydrogen system as a function of the mole fraction of arsine. The soundspeed vs mole fraction data are in excellent agreement with the acoustic model based on ideal gas theory. Specific heat capacity ratios, $\gamma_{AsH_3} = 1.269$ and $\gamma_{H_2} = 1.405$, were used for arsine and hydrogen, respectively, in the acoustic model (*8*).

Despite the excellent agreement observed between the measured and theoretically predicted soundspeed for both systems studied here, there exist a number of possible sources for error in acoustic measurements. Acoustic velocity errors can arise from uncertainties in the separation or acoustic path length between the two transducers, the time-of-flight measurement itself, and the temperature of the gas. For a given flow cell, the acoustic path length can be determined accurately by using a reference gas with a precisely known acoustic velocity. The time-of-flight error can be minimized by having the clock frequency as high as possible. In this work, a timing clock mechanism operating at 8-MHz frequency was used in conjunction with acoustic spectrum correlation to yield time-of-flight measurements with accuracies of ±10 ns. Given this kind of uncertainty in the time-of-flight, the error in determining the composition of the binary gas mixture, δX, is given by

$$\delta X = \delta V_s/(\partial V_s/\partial X) \tag{9}$$

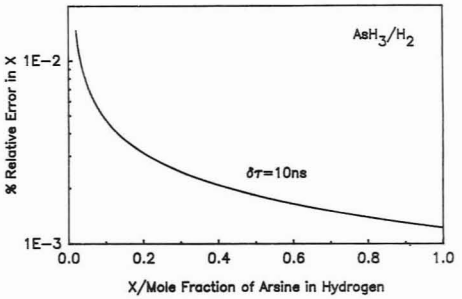

Figure 7. Relative percent error in concentration from the measured time-of-flight for arsine/hydrogen mixtures.

where $(\partial V_s/\partial X)$ is the derivative of the soundspeed vs concentration curve and δV_s is the error in the soundspeed measurement. The soundspeed and time-of-flight (τ) are connected through the acoustic path length L by

$$V_s = \frac{L}{\tau} \tag{10}$$

For this analysis we will assume that the path length is known with sufficient accuracy so as to incur minimal error in the soundspeed. Differentiating eq 10 and substituting into eq 9, one can derive the following expression for the error in concentration

$$\delta X = \frac{V_s^2}{L}\left(\frac{\partial V_s}{\partial X}\right)^{-1}\delta\tau \tag{11}$$

where $\delta\tau$ is the uncertainty associated with the time-of-flight measurement.

As an example of the error incurred in this acoustic measurement, we consider the arsine–hydrogen system. The partial derivative in eq 11 is performed with the aid of eq 7 by using the pure component specific heat capacity ratios for arsine and hydrogen. The relative error in the measured concentration from the time-of-flight measurement is given by

$$\left(\frac{\delta X}{X}\right)_\tau = \frac{V_s^2}{L}\sqrt{\frac{4}{RT}}\left[\frac{(\gamma_1-\gamma_2)(\bar\gamma-1)^2}{(\bar M\bar\gamma)^{1/2}(\gamma_1-1)(\gamma_2-1)} + \frac{(M_2-M_1)\bar\gamma^{1/2}}{\bar M^{3/2}}\right]^{-1}\frac{\delta\tau}{X} \tag{12}$$

The percent relative error in the concentration is shown in Figure 7 as a function of mole fraction. As one would expect, the relative error in the soundspeed and thus concentration decreases as the measured time-of-flight increases. As evident from Figure 7, this applies to higher mole fractions of arsine where the soundspeed of the gas mixture is lower. For most practical systems of interest, the concentration of arsine in hydrogen used is ≥0.02 mole fraction arsine. The relative error in concentration attributed to the time-of-flight measurement is then ≤±0.01%.

A rigorous error analysis of the ultrasonic method must also consider the effect of temperature on soundspeed and thus concentration. From eq 7, the soundspeed of a binary gas mixture depends on $T^{1/2}$. The temperature of the incoming gas mixture and ultrasonic flow cell can be maintained constant to better than ±0.02 °C by using an appropriate temperature control system. We have found that configuring the acoustic flow cell and gas lines in a standard exhausted gas cabinet provides constancy in the temperature of the entire

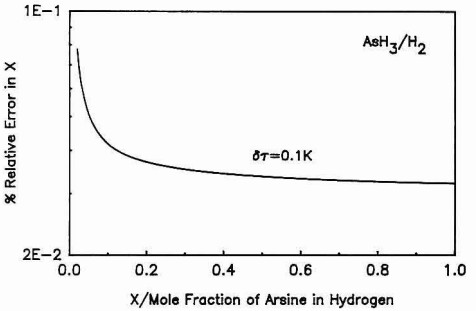

Figure 8. Relative percent error in concentration from thermal effects for arsine/hydrogen mixtures.

system to within ±0.1 °C. The error in concentration from an uncertainty in the temperature of the gas stream, δT, can be obtained from the following differential

$$\frac{\partial X}{\partial T} = \frac{\partial V_s}{\partial T}\left(\frac{\partial V_s}{\partial X}\right)^{-1} \tag{13}$$

The derivative of soundspeed with respect to temperature is evaluated with the aid of eq 7. The relative error in concentration can be expressed as

$$\left(\frac{\delta X}{X}\right)_T = \frac{1}{2}\frac{V_s}{T}\left(\frac{\partial V_s}{\partial X}\right)^{-1}\frac{\delta T}{X} \tag{14}$$

The relative percent error in the measured concentration assuming a temperature uncertainty of ±0.1 °C is shown in Figure 8 for arsine/hydrogen. The thermally derived error in concentration is about 1 order of magnitude larger and less composition dependent than the error in the time-of-flight measurement. A precision of ±0.03% in the mole fraction of arsine/hydrogen is obtained over most of the range of compositions. This precision exceeds requirements for on-line concentration determinations of arsine/hydrogen streams for MBE, H-VPE, and MOCVD processes.

CONCLUSIONS

An ultrasonic method is described for on-line determination of in situ generated arsine in process streams. For on-line monitoring of dangerously toxic gases, an ultrasonic method has proven to be superior to other techniques. Accurate, noncontaminating, real-time determinations of arsine in hydrogen have been accomplished. Highly repeatable experimental calibrations are in excellent agreement with theoretical predictions based on an appropriate acoustic model. The acoustic time-of-flight method was also found to be insensitive to pressure and volumetric gas flows. For these reasons, it is a versatile and practical tool for monitoring a broad range of binary gas flow streams of reagents used for device fabrication.

LIST OF SYMBOLS

C_P	specific heat capacity at constant pressure, J/(mol K)
C_V	specific heat capacity at constant volume, J/(mol K)
L	acoustic path length, m
M	molecular weight of gas, kg
$\bar{M}$	molar average molecular weight of binary gas mixture, kg
P	pressure, N/m^2
R	universal gas constant, 8.314 J/(mol K)
T	absolute temperature, K
V	volume of gas, m^3
V_s	acoustic velocity, m/s
X	mole fraction of component 1, dimensionless
$\delta\tau$	uncertainty in the time-of-flight measurement, s
δT	uncertainty in the temperature of the gas, °C
δV_s	error in the acoustic velocity, m/s
δX	error in the mole fraction
γ	specific heat capacity ratio for pure component
$\bar{\gamma}$	specific heat capacity ratio for the binary mixture
τ	time-of-flight

LITERATURE CITED

(1) Valdes, J. L.; Cadet, G.; Mitchell, J. W. On-Demand Electrochemical Generation of Arsine, unpublished work.
(2) Stagg, J. P. *Chemtronics* **1988**, *3*, 44–49.
(3) Capik, R. J.; Miller, A. High Speed High Sensitivity Ultrasonic Method for Determination of Matal–Alkyl Partial Pressures. Materials Research Society: San Diego, 1989; Extended Abstract No. A3.7.
(4) Tallman, C. R. *ISA Trans.* **1977**, *17*, 97–104.
(5) Hallewell, G. D.; Crawford, G.; McShurley, D.; Oxobey, G.; Reif, R. *Nucl. Instrum. Methods Phys. Res.* **1988**, *A264*, 219–234.
(6) Thorpe, P. L. *J. Phys. E.* **1969**, *2*, 1073.
(7) Bird, R. B.; Stewart, W. E.; Lightfoot, E. N. *Transport Phenomena*; John Wiley & Sons: New York, 1960; p 391.
(8) Braker, W.; Mossman, A. L. *Matheson Gas Data Book*, 6th ed.; Matheson Gas Products: New Jersey, 1980.

RECEIVED for review July 16, 1990. Accepted November 16, 1990.

Stable Carbon Isotope Analysis of Amino Acid Enantiomers by Conventional Isotope Ratio Mass Spectrometry and Combined Gas Chromatography/Isotope Ratio Mass Spectrometry

J. A. Silfer and M. H. Engel*

School of Geology and Geophysics, The University of Oklahoma, 100 E. Boyd Street, Norman, Oklahoma 73019

S. A. Macko

Department of Environmental Sciences, The University of Virginia, Charlottesville, Virginia 22903

E. J. Jumeau

VG Isotech Limited, Aston Way, Middlewich, Cheshire CW10 0HT, U.K.

The application of a combined gas chromatography/isotope ratio mass spectrometry (GC/IRMS) method for stable carbon isotope analysis of amino acid enantiomers is presented. This method eliminates the numerous preparative steps integral to the isolation of amino acids and amino acid enantiomers from protein hydrolyzates that precede $\delta^{13}C$ analysis by conventional isotope ratio mass spectrometry. Unlike hydrocarbons, amino acids require derivatization prior to GC/IRMS analysis. Replicate $\delta^{13}C$ analyses of trifluoroacetyl (TFA) isopropyl ester derivatives of 22 amino acids by IRMS revealed that the derivatization process is reproducible, with an average error (1 standard deviation) of 0.10‰ ± 0.09‰. The average analytical error for analysis of amino acid derivatives by GC/IRMS was 0.26‰ ± 0.09‰. In general, absolute differences between IRMS and GC/IRMS analyses were less than 0.5‰. The derivatization process introduces a distinct, reproducible isotopic fractionation that is constant for each amino acid type. The observed fractionations preclude direct calculation of underivatized amino acid $\delta^{13}C$ values from their respective TFA isopropyl ester $\delta^{13}C$ compositions through mass balance relationships. Derivatization of amino acid standards of known stable carbon isotope compositions in conjunction with natural samples, however, permits computation of the original, underivatized amino acid $\delta^{13}C$ values through use of an empirical correction for the carbon introduced during the derivatization process.

INTRODUCTION

Conventional stable carbon isotope analyses of bulk organic fractions from terrestrial and extraterrestrial samples continue to provide information concerning the origin and significance of organic matter in the geologic record. A diverse spectrum of applications has evolved in recent years, including elucidation of Precambrian biological evolution (*1*), evaluation of dinosaur trophic levels (*2*), determination of paleodietary trends in hominids (*3*), and assessment of the origin of organic compounds in carbonaceous meteorites (*4*). The interpretation of stable isotope data for composite samples remains complex, however, because the preserved isotopic signal for a given bulk sample represents an average value for a multitude of compounds, some of which may be contaminants or alteration products of the original material. Fundamental isotopic trends may therefore be obscured.

* Corresponding author.

The stable isotope analysis of individual organic compounds, particularly amino acids from living systems and fossils, is a powerful method for probing modern (*5–8*) and ancient (*9*) biochemistries. Comparison of the stable isotope compositions of amino acid enantiomer pairs, furthermore, has been suggested as an independent method to assess amino acid indigeneity in fossils (*10, 11*) and carbonaceous meteorites (*12, 13*). Stable isotope values for individual amino acids and their respective enantiomers in modern and fossil systems are rarely reported, however, because of the difficulties inherent in isolating individual components from complex mixtures for stable isotope analysis by conventional combustion methods (e.g., ref 14).

The recent development of combined gas chromatography/isotope ratio mass spectrometry (GC/IRMS) systems (*15, 16*) has permitted the direct stable carbon isotope analysis of individual, volatile organic compounds (i.e., hydrocarbons) in chemically complex samples (*17, 18*). The application of this method to amino acid analysis, however, is complicated by the fact that amino acids are nonvolatile, multifunctional molecules that require derivatization prior to analysis. The derivatization process introduces additional carbon atoms and the potential for isotopic fractionation; consequently, alteration of the original stable carbon isotopic composition of the amino acids occurs. The relationship between the $\delta^{13}C$ of amino acid derivatives and the $\delta^{13}C$ of the underivatized amino acids must be established before GC/IRMS analysis of these compounds can assume any practical value.

In this paper, we report the effects of derivatization on amino acid $\delta^{13}C$ compositions as determined by both conventional isotope ratio mass spectrometry and GC/IRMS. Specifically, $\delta^{13}C$ values of trifluoroacetyl isopropyl esters of biologically significant amino acids and an amino acid that is present in carbonaceous meteorites were determined by conventional IRMS in order to establish the reproducibility of the derivatization method and to confirm $\delta^{13}C$ values obtained by GC/IRMS. Additionally, IRMS and GC/IRMS analyses of five racemic amino acids were performed to determine whether amino acid enantiomers with identical stable carbon isotope compositions retained their isotopic integrity during derivatization and analysis. The results of these studies and the implications for GC/IRMS analyses of amino acids in natural materials are presented below.

EXPERIMENTAL SECTION

Standards and Reagents. Standard solutions (0.05 M) of individual amino acid enantiomers and racemic amino acids were prepared by dissolving appropriate amounts of crystalline amino acids (Sigma, St. Louis, MO) in distilled 0.1 N HCl. The solutions were stored at 4 °C. Acidified (2.8 M HCl) 2-propanol was

0003-2700/91/0363-0370$02.50/0

prepared in an ice bath by the addition of 250 μL of acetyl chloride (99+%, Aldrich, Milwaukee, WI) per milliliter of 2-propanol (HPLC grade, Fisher Scientific, Fairlawn, NJ). The acidified alcohol was used within 48 h of preparation. Trifluoroacetic anhydride (99+%, Pierce Chemical Co., Rockford, IL) was used for acylation. Reagents of the same lot numbers were used for all derivatizations.

Derivatization Procedure. For conventional IRMS analysis, 200-μL aliquots (10^{-5} mol) of the amino acid standard solutions were dispensed into individual 4-mL screw cap vials with Teflon cap liners. Three separate samples of each amino acid enantiomer were prepared. The samples were evaporated to dryness under a stream of N_2 at 40 °C. For GC/IRMS analysis, 100-μL aliquots of each standard solution were prepared in an identical manner.

The dried samples were esterified with 0.5 mL of the acidified 2-propanol for 1 h at 110 °C. After 1 h, the reaction was quenched by placing the vials in a freezer. Next, 0.25 mL of each sample was pipeted into a 20-cm × 7-mm-i.d. Pyrex tube. The solvent was removed by evaporation under a gentle stream of N_2 at 25 °C. Two successive 0.25-mL aliquots of CH_2Cl_2 were placed in each tube and evaporated to remove excess 2-propanol and water.

The remaining portions of the esterified samples were evaporated to dryness under N_2, redissolved in CH_2Cl_2, and dried again. The amino acid isopropyl esters were acylated with 0.5 mL of trifluoroacetic anhydride (TFAA) and 0.5 mL of CH_2Cl_2 for 10 min at 110 °C. Next, the vials were chilled in a freezer and then placed in an ice bath where the excess TFAA and CH_2Cl_2 were removed by evaporation under N_2. The derivatives were redissolved in 0.25 mL of CH_2Cl_2 and evaporated at 0 °C to remove residual traces of TFAA and trifluoroacetic acid. The derivatives were then dissolved in 0.5 mL of CH_2Cl_2, transferred to Pyrex tubes, and evaporated to dryness under N_2.

Conventional Isotope Ratio Mass Spectrometry. The amino acid isopropyl esters and the amino acid trifluoroacetyl isopropyl esters were transferred to individual Pyrex tubes (20 cm × 7 mm i.d.) as previously described. Five grams of copper oxide wire was added to each tube. The tubes and copper oxide wire were preheated (to 550 and 850 °C, respectively) and then cooled to room temperature just prior to loading the samples. The tubes were evacuated, sealed, and combusted at 550 °C for 2.5 h. The resultant CO_2 gas of each combusted sample was cryogenically purified and analyzed for its stable carbon isotope composition as previously described (*19*).

Stable carbon isotope data are presented by using the standard convention

$$\delta N_E‰ = [R_{sample}/R_{standard} - 1]10^3$$

where N is the heavier stable isotope of the element E and R is the abundance ratio of the heavy to light isotopes of the element. The standard for carbon is the Peedee Belemnite (PDB) that has been assigned a $\delta^{13}C$ value of 0.0‰. For routine measurement, samples are analyzed against a laboratory working standard tank of pure CO_2 gas that has been calibrated against NBS reference materials.

Gas Chromatography/Isotope Ratio Mass Spectrometry. Several of the TFA isopropyl esters of the individual enantiomers and racemic amino acids were analyzed directly for their stable carbon isotope compositions by using the VG Isochrom GC/IRMS system. The GC/IRMS system consists of a Hewlett-Packard 5890 gas chromatograph interfaced to a VG SIRA isotope ratio mass spectrometer via a combustion furnace/water trap. Details concerning the system hardware and software have been previously reported (*15*). In this study, the gas chromatograph was equipped with a 50-m × 0.25-mm-i.d. fused silica capillary column coated with an optically active stationary phase (Chirasil-Val; Alltech Assoc., Deerfield, IL) capable of resolving the TFA isopropyl esters of amino acid enantiomers (*20*). The CO_2 combustion products of the compounds eluting from the capillary column are introduced directly into the mass spectrometer ion source: this instrument configuration permits stable carbon isotope analysis at nanomole levels.

RESULTS AND DISCUSSION

$\delta^{13}C$ Analysis of Amino Acid Derivatives. The preparation of TFA isopropyl ester derivatives is, as previously discussed, a two-step process that alters the original stable carbon isotope compositions of the amino acids. In order to correct for the introduction of carbon during derivatization, it is necessary to establish the isotopic reproducibility of the derivatization method. The $\delta^{13}C$ values of 17 amino acids and their respective isopropyl esters and TFA isopropyl esters as determined by conventional IRMS are presented in Table I. In general, the esterification of three separate samples of each amino acid was accomplished with a reproducibility (1 standard deviation) of less than 0.3‰, with the exception of D-lysine (0.41‰). The average experimental error for the preparation and IRMS analysis of amino acid isopropyl esters was 0.12‰ ± 0.11‰. Similarly, the complete derivatization of the amino acids resulted in an experimental error of less than 0.2‰, with the exceptions of D-phenylalanine (0.25‰) and D-lysine (0.33‰). The average reproducibility for the preparation and IRMS analysis of the TFA isopropyl esters was 0.10‰ ± 0.10‰. The average experimental error for the preparation and IRMS analysis of the five racemic amino acid derivatives was 0.08‰ ± 0.03‰ (Table II). These reproducibilities are well within the the error reported for GC/IRMS $\delta^{13}C$ determinations of compounds that do not require derivatization prior to analysis (*16*).

The $\delta^{13}C$ compositions of TFA isopropyl ester derivatives of selected amino acids and amino acid enantiomers were also

Table I. Stable Carbon Isotopic Compositions of Amino Acids, Amino Acid Isopropyl Esters, and N-TFA Isopropyl Esters

	$\delta^{13}C$		
amino acid	underiv amino acid[a,b]	amino acid isopropyl ester[a-c]	amino acid N-TFA isopropyl ester[a-c]
α-Aiba[e]	−28.19	−27.87	−31.94
		0.05	0.09
D-Ala	−26.23	−25.99	−29.93
		0.17	0.08
L-Ala	−20.26	−23.12	−28.02
		0.06	0.07
D-Val	−31.47	−31.13[d]	−32.69
		0.10	0.04
L-Val	−25.97	−26.53	−29.65[d]
		0.23	0.23
Gly 1[f]	−32.67	−28.38	−32.42[d]
		0.01	0.29
Gly 2[f]	−25.85	−25.66	−30.43
		0.08	0.17
D-Leu	−25.25	−25.82	−28.76[d]
		0.09	0.04
L-Leu	−23.69	−24.83	−27.90
		0.22	0.02
D-Asp	−21.04	−23.81	−27.20
		0.08	0.01
L-Asp	−24.46	−25.18	−28.43
		0.02	0.01
D-Glu	−23.19	−24.25	−27.09
		0.03	0.11
L-Glu	−27.68	−26.45	−28.94
		0.05	0.03
D-Phe	−31.89	−30.84	−32.40
		0.08	0.25
L-Phe	−27.68	−27.63	−29.79[d]
		0.12	0.06
D-Lys	−22.62	−24.30	−29.44
		0.41	0.33
L-Lys	−11.48	−16.98	−24.47
		0.29	0.13

[a] Stable carbon isotopic compositions reported in per mil relative to PDB. [b] $\delta^{13}C$ determined by static combustion and conventional IRMS analysis. [c] Values represent means and standard deviations for three separate samples unless specified otherwise. [d] Average of two samples and their range. [e] α-Aminoisobutyric acid. [f] Gly 1 and Gly 2 represent glycines from two different commercial sources.

Table II. Stable Carbon Isotopic Compositions of Amino Acids and Their Respective N-TFA Isopropyl Esters Determined by IRMS and GC/IRMS Analysis

	$\delta^{13}C$				
amino acid	underivatized amino acid[a,b]	amino acid N-TFA isopropyl ester[a-c]	amino acid	amino acid N-TFA isopropyl ester[a,d,e]	Δ[g]
α-Aiba	−28.19	−31.94 0.09		−32.33 0.08	0.39
D-Ala	−26.23	−29.93 0.08		−30.10 0.14	0.17
L-Ala	−20.26	−28.02 0.07		−27.52 0.17	−0.50
D-Val	−31.47	−32.69 0.04		−32.62[f] 0.08	−0.07
L-Val	−25.97	−29.65 0.23		−29.75[f] 0.03	0.10
Gly 1	−32.67	−32.42 0.29		−32.09[f] 0.45	−0.33
D,L-Ala	−25.45	−29.82 0.05	D-Ala	−30.17 0.32	0.27
			L-Ala	−30.00 0.31	
D,L-Val	−26.99	−30.20 0.11	D-Val	−31.01 0.28	0.75
			L-Val	−30.88 0.40	
D,L-Leu	−24.93	−28.48 0.05	D-Leu	−29.13 0.20	0.39
			L-Leu	−28.61 0.26	
D,L-Asp	−22.32	−27.47 0.08	D-Asp	−28.47 0.29	0.90
			L-Asp	−28.27 0.25	
D,L-Glu	−23.59	−27.39 0.06	D-Glu	−28.22 0.29	0.73
			L-Glu	−28.01 0.33	

[a] Stable carbon isotopic compositions reported in per mil relative to PDB. [b] $\delta^{13}C$ determined by static combustion and conventional IRMS analysis. [c] Values represent means and standard deviations for three separate samples except for L-Val, Gly 1, and D,L-Ala, for which the mean and range for two samples is reported. [d] $\delta^{13}C$ determined by GC/IRMS analysis. [e] Values represent means and standard deviations for a minimum of three analyses of the same sample unless specified otherwise. [f] Values represent the mean and range for two analyses of the same sample. [g] IRMS $\delta^{13}C$ − GC/IRMS $\delta^{13}C$; note that for the racemic amino acids the average $\delta^{13}C$ value of the D- and L-enantiomers was used to compute the differences.

determined by GC/IRMS analysis. The results of these analyses are presented in conjunction with the $\delta^{13}C$ values for the derivatives determined by IRMS (Table II). The analytical error obtained for replicate GC/IRMS analyses of the same sample ranged from 0.08‰ to 0.40‰ and averaged 0.26‰ ± 0.09‰. The average error for GC/IRMS analysis of amino acid derivatives is consistent with analytical errors previously reported for other volatile organic compounds (*16*).

Following consultations with Sigma Chemical Co. (St. Louis, MO), it was concluded that the stable carbon isotope compositions of the individual enantiomers of their racemic amino acids should be identical, in the absence of stereospecific fractionation effects. The results of the GC/IRMS analyses confirm that, within the margin of analytical error, the $\delta^{13}C$ values of the enantiomers are in fact nearly indistinguishable (Table II).

The $\delta^{13}C$ values determined by GC/IRMS in general compare favorably with the stable carbon isotope compositions obtained by conventional IRMS analysis. The absolute differences between the $\delta^{13}C$ values obtained by the two analytical methods are less than 0.5‰ and in three instances are less than 0.2‰, for all amino acids except D,L-valine, D,L-aspartic acid, and D,L-glutamic acid. The presence of trace contaminants from the amino acid standards or the derivatizing reagents or side products resulting from derivatization could have influenced the IRMS analyses, whereas the chromatographic separation employed by GC/IRMS would have effectively removed these trace components.

Isotopic Fractionation during Derivatization. Theoretically, the amino acid isopropyl esters and N-TFA isopropyl esters should exhibit $\delta^{13}C$ compositions that reflect the relative contributions of carbon from each component and their respective $\delta^{13}C$ values. The generalized stoichiometric mass balance relationship for amino acid isopropyl esters, for example, may be written as

$$\delta^{13}C_{ESTER} = X\delta^{13}C_{AA} + (1 - X)\delta^{13}C_{ISO} \quad (1)$$

where $\delta^{13}C_{ESTER}$, $\delta^{13}C_{AA}$, and $\delta^{13}C_{ISO}$ represent the stable carbon isotope compositions of the isopropyl ester, the underivatized amino acid, and the 2-propanol, respectively, and X and $1 - X$ are the mole fractions of carbon from each of the sources. Similarly, the $\delta^{13}C$ composition of the TFA isopropyl derivatives, which contain additional carbon from trifluoroacetic anhydride, can be expressed as

$$\delta^{13}C_{DER} = X\delta^{13}C_{AA} + Y\delta^{13}C_{ISO} + (1 - X - Y)\delta^{13}C_{TFAA} \quad (2)$$

where $\delta^{13}C_{DER}$ and $\delta^{13}C_{TFAA}$ represent the stable carbon isotope compositions of the TFA isopropyl derivative and TFAA, respectively, and X, Y, and $1 - X - Y$ represent the mole fractions of carbon from each component. Comparison of the stable carbon isotope compositions of amino acid isopropyl esters and TFA isopropyl esters determined by IRMS analysis and the respective values predicted by mass balance consid-

Table III. Stable Carbon Isotopic Compositions of Amino Acid Isopropyl Esters and N-TFA Isopropyl Esters versus $\delta^{13}C$ Mass Balance Predictions for Each

	$\delta^{13}C$			$\delta^{13}C$		
amino acid	amino acid isopropyl ester[a,b]	predicted isopropyl ester[c]	Δ[d]	amino acid N-TFA isopropyl ester[a,b]	predicted N-TFA isopropyl ester[c]	Δ[d]
α-Aiba	−27.87	−27.34	−0.53	−31.94	−28.63	−3.31
D-Ala	−25.99	−26.22	0.23	−29.93	−27.96	−1.97
L-Ala	−23.12	−23.24	0.12	−28.02	−25.72	−2.30
D-Val	−31.13	−29.50	−1.63	−32.69	−30.23	−2.46
L-Val	−26.53	−26.06	−0.47	−29.65	−27.48	−2.17
Gly 1	−28.38	−28.79	0.41	−32.42	−30.05	−2.37
Gly 2	−25.66	−26.07	0.41	−30.43	−28.09	−2.34
D-Leu	−25.82	−25.57	−0.25	−28.76	−26.94	−1.82
L-Leu	−24.83	−24.53	−0.30	−27.90	−26.09	−1.81
D-Asp	−23.81	−24.14	0.33	−27.20	−25.64	−1.56
L-Asp	−25.18	−25.51	0.33	−28.43	−26.78	−1.65
D-Glu	−24.25	−24.84	0.59	−27.09	−26.10	−0.99
L-Glu	−26.45	−26.88	0.43	−28.94	−27.83	−1.11
D-Phe	−30.84	−30.47	−0.37	−32.40	−30.85	−1.55
L-Phe	−27.63	−27.31	−0.32	−29.79	−28.14	−1.65
D-Lys	−24.30	−23.82	−0.48	−29.44	−26.67	−2.77
L-Lys	−16.98	−16.39	−0.59	−24.47	−21.52	−2.95

[a] Stable carbon isotopic compositions reported in per mil relative to PDB. [b] $\delta^{13}C$ determined by static combustion and conventional IRMS analysis. [c] 2-Propanol $\delta^{13}C = -26.21‰$; TFAA $\delta^{13}C = -33.10‰$. [d] Analytical $\delta^{13}C$ − predicted $\delta^{13}C$.

erations, however, reveals that an apparent isotopic fractionation occurs during each derivatization step (Table III).

In general, amino acid esterification produces relatively small isotopic discrepancies that, with the exception of D-valine, range from +0.59‰ to −0.59‰. For amino acid isopropyl esters in which 2-propanol contributes more than 50% of the carbon (e.g., glycine, aspartic acid, glutamic acid), the predicted $\delta^{13}C$ values are light relative to the values measured by IRMS and GC/IRMS. In contrast, for the isopropyl esters in which 2-propanol contributes less than 50% of the carbon (e.g., valine, phenylalanine), the mass balance predictions are consistently heavier than the analytical values. The discrepancy between the predicted and analytical $\delta^{13}C$ values for alanine isopropyl esters, for which alanine and 2-propanol contribute identical moles of carbon, is approximately zero. The stable carbon isotope compositions of the TFA isopropyl esters determined by IRMS, however, are consistently depleted relative to the $\delta^{13}C$ values predicted from mass balance considerations. The isotopic discrepancies between the analytical and predicted values for the amino acid derivatives range from −0.99‰ to −3.31‰ (Table III).

The observed isotopic fractionations are consistent for each amino acid type and are independent of differences in original $\delta^{13}C$ compositions (Table III). For example, although glycine 1 and glycine 2 (1 and 2 designate the two commercial suppliers) differ by nearly 7‰, the observed fractionation for preparation of the glycyl isopropyl esters was 0.41‰ for both samples. The preparation of the N-TFA glycyl isopropyl esters resulted in a fractionation of −2.37‰ for glycine 1 and −2.34‰ for glycine 2. Similarly, the original $\delta^{13}C$ values for D-lysine and L-lysine prior to derivatization differ by approximately 11‰, yet the differences between the analytical and predicted values for the isopropyl esters were −0.48‰ and −0.59‰ and for the TFA isopropyl ester derivatives were −2.77‰ and −2.95‰, respectively. For the amino acids investigated, the isotopic fractionations observed for each amino acid type differ by no more than 0.16‰ for esterification (D-glutamic acid, L-glutamic acid) and 0.33‰ for preparation of the TFA isopropyl esters (D-valine, L-valine) and in most instances are less.

Origin of the Isotopic Fractionation. The origin of the isotopic discrepancies between the analytical and predicted $\delta^{13}C$ compositions of the amino acid derivatives is not apparent at present. The conditions employed for esterification and acylation have been demonstrated to produce quantitative derivatization of the amino acids investigated (*20* and references therein). Assuming that the reactions were quantitative, it is possible that a kinetic fractionation occurs during the acylation step, whereupon isotopically lighter reagent molecules react preferentially and deplete the derivative $\delta^{13}C$ value beyond that predicted by mass balance (eq 2). The fractionations for esterification, however, range from +0.59‰ to −0.59‰, with the exception of D-valine, and apparently cannot be ascribed simply to kinetics.

Variations of the magnitudes of the fractionations may result from differences in amino acid reactivity. Future detailed investigations of the effects of reagent $\delta^{13}C$ compositions, reaction time and temperature, reagent:amino acid molar ratios, and alternative derivatization methods on the magnitude of the isotopic fractionations should provide indirect evidence of their origin(s).

Calculation of Amino Acid $\delta^{13}C$ Values from Derivative $\delta^{13}C$ Values. The carbon isotope fractionation that occurs during derivatization precludes direct calculation of the $\delta^{13}C$ values of amino acids in natural samples by stoichiometric mass balance relationships (e.g., eq 2). The constancy of the derivatization fractionation effect observed for each amino acid, however, implies that original amino acid stable carbon isotope compositions ultimately can be derived from TFA isopropyl ester $\delta^{13}C$ values. To this end, the series of mass balance equations relating the $\delta^{13}C$ values of the amino acid derivatives to the stable isotope compositions and stoichiometric contributions of carbon from the amino acid, 2-propanol, and TFAA were modified:

$$\delta^{13}C_{DER} = X\delta^{13}C_{AA} + (1 - X)\delta^{13}C_{ISO,TFAA} \quad (3)$$

In essence, the mole fractions of carbon contributed to the amino acid derivative by 2-propanol and TFAA were summed and the variable $\delta^{13}C_{ISO,TFAA}$ was defined as the "effective" stable carbon isotope composition of the 2-propanol and trifluoroacetic acid introduced during derivatization. $\delta^{13}C_{ISO,TFAA}$ incorporates the observed isotopic fractionation for each amino acid type and is not related to the actual carbon isotope compositions of the two reagents. Consequently, $\delta^{13}C_{ISO,TFAA}$ must at the present time be determined empirically for each amino acid from standards of known stable

Table IV. Calculated $\delta^{13}C$ Values for Racemic Amino Acids

amino acid	$\delta^{13}C$ underivatized amino acid[a,b]	$\delta^{13}C$ calcd amino acid[c]
D,L-Ala	−25.45	−25.49
D,L-Val	−26.99	−26.78
D,L-Leu	−24.93	−24.75
D,L-Asp	−22.32	−21.70
D,L-Glu	−23.59	−23.81

[a] Stable carbon isotopic compositions reported in per mil relative to PDB. [b] $\delta^{13}C$ determined by static combustion and conventional IRMS analysis. [c] Calculated from respective N-TFA isopropyl ester $\delta^{13}C$ values determined by IRMS analysis and eq 3.

carbon isotope compositions. By use of the IRMS $\delta^{13}C$ values for the TFA isopropyl esters and underivatized amino acids from Table I, the empirical corrections for the carbon introduced during the derivatization process were derived for each amino acid enantiomer. The average $\delta^{13}C_{ISO,TFAA}$ for each amino acid type was then calculated from the separate enantiomer values.

To assess the accuracy of this method, the $\delta^{13}C$ compositions of the underivatized racemic amino acids D,L-alanine, D,L-valine, D,L-leucine, D,L-aspartic acid, and D,L-glutamic acid were calculated from their respective IRMS TFA isopropyl ester $\delta^{13}C$ values. The $\delta^{13}C_{AA}$ values were computed by substituting the $\delta^{13}C_{DER}$ compositions from Table II and the appropriate $\delta^{13}C_{ISO,TFAA}$ correction factors into eq 3. The analytically determined $\delta^{13}C$ values and the calculated $\delta^{13}C$ values for the five amino acids are presented in Table IV. The calculated $\delta^{13}C$ values of the racemic amino acids are, with the exception of D,L-aspartic acid, within 0.25‰ of the original, underivatized $\delta^{13}C$ compositions determined by IRMS. These data suggest that, at present, the most suitable method to determine amino acid $\delta^{13}C$ compositions in natural samples is to establish empirical correction factors for each amino acid by derivatization of amino acid standards of known stable isotope composition.

SUMMARY AND CONCLUSIONS

The effects of derivatization on the stable carbon isotope compositions of amino acids were investigated by conventional IRMS and GC/IRMS. The following conclusions can be drawn:

(1) Preparation and IRMS analysis of isopropyl esters and TFA isopropyl esters of 22 amino acids revealed that the derivatization process is reproducible. The average error for preparation and analysis of three separate samples of each amino acid was 0.12‰ ± 0.11‰ for isopropyl esters and 0.10‰ ± 0.09‰ for TFA isopropyl esters of individual enantiomers and racemic amino acids.

(2) The average analytical error for replicate analyses of a given amino acid derivative by GC/IRMS was 0.26‰ ± 0.09‰. In general, $\delta^{13}C$ compositions of amino acid derivatives determined by IRMS compared favorably with GC/IRMS $\delta^{13}C$ values. With three exceptions, the absolute differences between the two methods was less than 0.5‰. The exceptions may have resulted from incomplete derivatization and consequent elimination of impurities from the bulk samples by the chromatographic separation employed in the GC/IRMS system.

(3) The derivatization procedures introduce distinct but reproducible fractionations that presently preclude direct computation of the original, underivatized amino acid $\delta^{13}C$ compositions by stoichiometric mass balance. However, derivatization of amino acid standards of known stable carbon isotope composition in conjunction with natural samples permits computation of the original, underivatized amino acid $\delta^{13}C$ values through use of an empirical correction for the carbon introduced during the derivatization process.

ACKNOWLEDGMENT

We thank E. C. P. Gillyon and N. Crossley for permitting us to use the GC-IRMS system at VG Isotech.

LITERATURE CITED

(1) Schidlowski, M. *Nature* **1988**, *333*, 313–318.
(2) Ostrom, P. H.; Macko, S. A.; Engel, M. H.; Silfer, J. A.; Russell, D. *Org. Geochem.*, in press.
(3) Ambrose, S. H.; DeNiro, M. J. *Nature* **1986**, *319*, 321–324.
(4) Epstein, S.; Krishnamurthy, R. V.; Cronin, J. R.; Pizzarello, S.; Yuen, G. U. *Nature* **1987**, *326*, 477–479.
(5) Abelson, P. H.; Hoering, T. C. *Proc. Natl. Acad. Sci. U.S.A.* **1961**, *47*, 623–632.
(6) Winters, J. K. Ph.D. Thesis, The University of Texas, Austin, 1971.
(7) Macko, S. A.; Estep, M. L. F.; Hare, P. E.; Hoering, T. C. *Yearbook–Carnegie Inst. Washington* **1983**, *82*, 404–410.
(8) Macko, S. A.; Estep, M. L. F.; Engel, M. H.; Hare, P. E. *Geochim. Cosmochim. Acta* **1986**, *50*, 2143–2146.
(9) Hare, P. E.; Estep, M. L. F. *Yearbook–Carnegie Inst. Washington* **1983**, *82*, 410–414.
(10) Engel, M. H.; Macko, S. A. *Anal. Chem.* **1984**, *56*, 2598–2600.
(11) Engel, M. H.; Macko, S. A. *Nature* **1986**, *323*, 531–533.
(12) Pillinger, C. T. *Nature* **1982**, *296*, 802.
(13) Engel, M. H.; Macko, S. A.; Silfer, J. A. *Nature* **1990**, *348*, 47–49.
(14) Serban, A.; Engel, M. H.; Macko, S. A. *Org. Geochem.* **1988**, *13*, 1123–1129.
(15) Freedman, K. H.; Gillyon, E. C. P.; Jumeau, E. J. *Am. Lab.* (*Fairfield, Conn.*) **1988**, June, 114–119.
(16) Hayes, J. M.; Freeman, K. H.; Ricci, M. P.; Studley, S. A.; Merritt, D. A.; Brzuzy, L.; Brand, W. A.; Habfast, K. 37th ASMS Conference on Mass Spectrometry and Allied Topics, Miami Beach, FL, 1989; pp 33–34 (abstract).
(17) Freeman, K. H.; Hayes, J. M.; Trendel, J.-M.; Albrecht, P. *Nature* **1990**, *343*, 254–256.
(18) Kennicutt, M. C.; Brooks, J. M. *Org. Geochem.* **1990**, *15*, 193–197.
(19) Engel, M. H.; Maynard, R. J. *Anal. Chem.* **1989**, *61*, 1996–1998.
(20) Engel, M. H.; Hare, P. E. In *Chemistry and Biochemistry of the Amino Acids*; Barrett, G. C., Ed.; Chapman and Hall: New York, 1985; pp 462–479.

RECEIVED for review August 2, 1990. Accepted November 16, 1990. This work is supported by the National Science Foundation, Division of Earth Sciences (Grant No. EAR-8904215).

Ion Spray Liquid Chromatography/Ion Trap Mass Spectrometry Determination of Biomolecules

Scott A. McLuckey,* Gary J. Van Berkel, and Gary L. Glish

Analytical Chemistry Division, Oak Ridge National Laboratory, Oak Ridge, Tennessee 37831-6365

Eric C. Huang and Jack D. Henion*

Drug Testing and Toxicology Diagnostic Laboratory, New York State College of Veterinary Medicine, Cornell University, 925 Warren Drive, Ithaca, New York 14850

The first on-line coupling of microbore high-performance liquid chromatography (HPLC) with an ion trap mass spectrometer equipped for sampling ions formed by electrospray ionization at atmospheric pressure is reported. A pneumatically assisted electrospray (ion spray) liquid chromatograph/mass spectrometer interface was used to couple reversed-phase, linear solvent gradient separations of biologically important compounds, including peptides and proteins, with the ion trap mass spectrometer. Initial gradient HPLC conditions consisting of 95% aqueous 0.15% trifluoroacetic acid in acetonitrile maintained at a flow of 40 μL/min were used with the system. Useful ion current profiles for levels down to 2.5 pmol per component of tryptic peptides and 0.3 pmol of injected human serum albumin (HSA) were obtained under these conditions. Full-scan mass spectra of multiply protonated molecules are shown for the target compounds at these levels. On-line HPLC/mass spectrometry (MS) molecular weight determinations for cytochrome *c*, HSA, and myoglobin are shown as well as LC/MS^2 and LC/MS^3 determinations of selected tryptic peptides in a protein tryptic digest. These applications demonstrate the analytical potential for the ion trap mass spectrometer combined with HPLC through its high detection sensitivity and MS^n capability.

INTRODUCTION

The combination of mass spectrometry (MS) with on-line separation methods for mixtures in solution is playing an increasingly important role in the characterization of biomolecules. Mass spectrometry has long been recognized for its high specificity and high sensitivity. However, its use as a detector for on-line separations of condensed-phase analytes has been limited due to the inherent incompatibility of vacuum systems with solvents commonly used for separations. Current state-of-the-art interfaces for liquid chromatography/mass spectrometry (LC/MS), such as thermospray (*1*, *2*) and particle beam (*3*, *4*), have significantly improved the performance of the LC/MS combination, particularly for relatively small molecules (MW < 500). These interfaces, however, have been less successful for the analysis of samples containing relatively large biomolecules due, in large part, to the difficulties associated with forming gas-phase ions from large polar molecules. Promising results in this area have recently been obtained with continuous-flow fast atom bombardment ("flow FAB") (*5–7*), but its use with routine reversed-phase separations of large biomolecules, such as proteins, has enjoyed limited success.

Another promising approach to interfacing liquid separation techniques for biomolecules with mass spectrometry has appeared as a result of the demonstration by Fenn et al. (*8–10*), and later by Henion et al. (*11*, *12*) and Smith et al. (*13*, *14*), that gas-phase ions of large biomolecules present in solution may be formed by electrospray (ES). A particularly significant aspect of these observations is the multiple charging typically observed for large biopolymers, which makes their mass analysis possible with mass analyzers with relatively modest mass/charge range (m/z 1 to <4000). Another important feature of ES is that essentially no fragmentation accompanies ionization of peptides or proteins. Molecular weight determination may be uncompromised by fragment ions, and for molecules that show a propensity for multiple charging, precision is enhanced by the possibility for multiple mass measurements from a single mass spectrum (*9*, *11*). The utility of ES-based interfaces for coupling on-line condensed-phase separations with mass spectrometry has already been demonstrated with capillary zone electrophoresis (*14–17*), capillary isotachtophoresis (*18*), high-performance liquid chromatography (HPLC) (*19–21*), and ion chromatography (*22*).

HPLC addresses a wide range of separation problems and is widely employed for separating mixtures of biological compounds (*23*). The flows (20 μL/min to 2 mL/min) and high water composition of eluents frequently employed with many reversed-phase HPLC separations, however, are not compatible with "pure" ES. Pure ES, which is meant to imply ES without the use of additional measures to assist nebulization, is most effective at eluent flows less than 5 μL/min and with solvents of relatively high organic content (>50%). One proposed approach to this problem is to split the post-column flow and to subject only a fraction of the eluent to ES (*8*). This might be done in conjunction with the "sheath flow" technique (*15*), which is used to control independently the liquid composition at the ES needle tip. Such an approach, however, has yet to be demonstrated with conventional HPLC. Another approach is to couple HPLC with pneumatically assisted electrospray (*19*, *24*), frequently referred to as ion spray (*19*), which was developed to address the problems with higher flow rate and high aqueous content eluents. Since its introduction, ion spray has been demonstrated with a variety of analytical applications involving capillary zone electrophoresis (*17*), ion chromatography (*22*), and HPLC (*19–21*, *24–26*).

As a consequence of the fact that ES is a very gentle ionization process and generally yields no fragment ions, the ES mass spectrum provides no structural information. Fragmentation is only observed when energy is added to the ions after they are desolvated. Collision-induced dissociation (CID) of ions formed by ES has been effected both prior to mass analysis (*27–29*), viz., in a declustering region prior to a mass analyzer, and in between stages of mass spectrometry (*20*, *21*, *24*, *28–32*). Mass spectrometry/mass spectrometry (MS/MS), the latter approach, is well-known for the structural information it can provide, particularly in conjunction with soft ionization techniques (*33*, *34*). MS/MS has already been shown to provide structural information from ES-derived ions and has been used in conjunction with on-line separations by HPLC (*20*, *21*, *24–26*). These studies have clearly demon-

0003-2700/91/0363-0375$02.50/0

strated the analytical utility of coupling on-line separations with ES and MS/MS.

By far, most electrospray data have been acquired with quadrupole-based instruments, i.e., quadrupole mass filters or triple quadrupole mass spectrometers. Recently, pure ES has been coupled with a quadrupole ion trap (three-dimensional quadrupole) capable of multiple stages of mass analysis (*32*). The quadrupole ion trop was shown to hold particular promise as an analyzer for ions formed via ES due to its potentially high sensitivity, its MS^n capabilities, and its tendency to minimize clustering. A variety of other attractive features of the quadrupole ion trap as an analytical mass spectrometer have also been demonstrated in recent years, and it is still undergoing rapid development (*35*). For these reasons, the quadrupole ion trap may enjoy an important role in analytical applications of ES.

The motivation behind the work reported here was to combine on-line HPLC separations and the ion spray LC/MS interface with ion trap technology. In particular, our experience with injecting ions into ion traps (*36*) would allow us to evaluate the potential of the ion trap for HPLC/MS and $HPLC/MS^n$ applications. Major emphasis was placed on the separation and analysis of peptides and proteins due to their importance in biochemistry and biotechnology. However, some effort also went into analyzing physiological extracts containing drugs, and these results are also described briefly herein. The major objectives of this work were to demonstrate improved sensitivity and the MS^n capability of the ion trap in an on-line HPLC separation of a protein tryptic digest and to evaluate the performance of the present ion trap system in combination with ion spray LC/MS techniques. The present "interface" between the ion trap and atmosphere is the hardware for an atmospheric sampling glow discharge ionization (ASGDI) source (*37*), which was not designed for ES. Nevertheless, promising results have been obtained with peptides and proteins under pure ES conditions (*32*). In these latter studies, ions were formed from solutions composed predominantly of methanol at flows of roughly 1 μL/min. An important unknown, however, was the performance of this interface, which employs no intentionally added drying or declustering gases, under ion spray conditions (viz., a flow rate of 40 μL/min with solvent composition as high as 95% water).

EXPERIMENTAL SECTION

Materials. The peptides used in this work, fibrinopeptide A, bradykinin, and substance P, and the proteins, bovine cytochrome *c*, horse heart myoglobin, and human serum albumin, were obtained from Sigma Chemical Co. (St. Louis, MO) and used without further purification. Human hemoglobin normal β-chain was obtained from Beckman Research Institute (Duarte, CA). The enzyme used to digest the human hemoglobin was trypsin treated with L-1-tosylamide-2-phenylethyl chloromethyl ketone (TPCK) and was also obtained from Sigma. Sequencing-grade trifluoroacetic acid (TFA) was obtained from Aldrich Chemical Co. (Milwaukee, WI), HPLC-grade acetonitrile was obtained from J. T. Baker Inc. (Phillipsburg, NJ), and HPLC-grade water was obtained from Fisher Scientific (Rochester, NY).

Enzymatic Digestion. Human hemoglobin normal β-chain was digested with trypsin treated with TPCK for 16–20 h at 37 °C with a substrate-to-enzyme ratio of 50:1 (w/w) in 50 mM ammonium bicarbonate buffer solution at pH 8.5 (the pH of the buffer solution was adjusted with 1 M ammonia). The digestion solution was then lyophilized and redissolved in water containing 3 mM TFA with an approximate protein concentration of 0.5–1 mg/mL. A sample size of 5 μL was typically injected on-column for all on-line HPLC/MS analyses.

Microbore Liquid Chromatography. The preferred microbore HPLC column used for all work reported herein was 1-mm internal diameter, 10-cm length, and packed with 5-μm LC-308 packing material (bonded with C-8 stationary phase, 300-Å pore size) generously provided by Supelco, Inc. (Bellefonte, PA). The micro-HPLC system consisted of a Model 140A dual-syringe solvent delivery system generously loaned by Applied Biosystems, Inc. (Foster City, CA). The only modification to this system was replacement of the standard 250-μL mixing "T" incorporated in the plumbing system with a 52-μL mixer bed volume to ensure adequate mixing of the solvent components. Sample injection was accomplished with a Model 9125 biocompatible syringe-loading injector with a 5-μL external sample loop (Rheodyne, Cotati, CA). The mobile phase was composed of 0.15% TFA/H_2O as solvent A and 0.15% TFA/CH_3CN as solvent B. All separations were accomplished by applying a linear solvent gradient from 5% solvent B to 70% solvent B over a time period of 60 min unless otherwise stated. With this gradient program, the HPLC run times were typically less than 40 min. The HPLC column flow was maintained at 40 μL/min throughout these experiments. The exit of the analytical column was connected directly to the pneumatically assisted electrospray (ion spray) interface. There was no presplit (before the column) or postsplit (after the column, before entering the ion spray HPLC/MS interface) of the mobile phase.

Pneumatically Assisted Electrospray (Ion Spray) HPLC/MS Interface Conditions. The interface used for coupling the microbore HPLC system with the atmospheric sampling glow discharge ion trap mass spectrometer system has been described elsewhere (*19–22*). The HPLC/MS interface sprayer can be floated at ±3–4-kV potential. The polarity of this potential is dependent upon the operational mode (i.e., positive-ion or negative-ion detection) of the mass spectrometer. In the present study, the mass spectrometer was operated in the positive-ion mode of detection. Analyte ions formed from the ion spray HPLC/MS interface were sampled into the mass spectrometer through the 100-μm orifice in the flat plate on the atmosphere side of the ASGDI system. Neither a drying gas nor electrical declustering in the interface region was used in these experiments.

Ion Injection. The mass spectrometer is based on the Finnigan-MAT (San Jose, CA) ion trap mass spectrometer (ITMS), which has been modified to allow for ion injection from external ion sources. Details of ion injection into the ITMS from the ASGDI source (*36*) and from ES via the ASGDI source hardware (*32*) have been reported. Note that no glow discharge is employed with either ES or ion spray. The conditions used for ion injection from ion spray were essentially identical with those used for ES. These conditions are described only briefly here with reference to Figure 1. A small, unknown fraction of the ion spray "plume" of HPLC effluent was drawn through a 100-μm aperture in plate A1 and into a region evacuated to a pressure of 0.3 Torr, which contains lens elements AL1 and AL2. Plate A2, which is 1.9 cm from plate A1, contains an 800-μm aperture that is directly in-line with the aperture in A1 and the aperture in the entrance end-cap of the ion trap. For the peptides, A1, AL1, and AL2 were held at +150, +130, and +150 V, respectively. For the protein mixture, A1, AL1, and AL2 were held at +40, +30, and +40 V, respectively. Plate A2 was held at ground potential for all experiments described in this work.

Ions that issued from the aperture in A2 were focused through the aperture in the ion entrance end-cap via the three-element lens system comprising L1, L2, and L3. L2 consists of two half-plates and serves as an ion beam deflector for gating the ions into the ion trap. During ion injection, L1, both halves of L2, and and L3 were held at −20, −60, and −100 to −200 V, respectively. At all other times, one of the L2 half-plates was held at −420 V to prevent ions from entering the ion trap. Helium was admitted into the ion trap vacuum housing to a pressure of 2–3 mTorr for all experiments.

The position of the ion spray LC/MS interface relative to the 100-μm inlet aperature was found to be an unimportant variable. Similar data were acquired with the spray directed onto A1 roughly 0.5 cm to one side of the inlet aperture and with the spray aimed directly onto the aperture. This is in contrast to ion spray used on a triple quadrupole system equipped with a single-stage conical ion sampling orifice in which the best performance is observed when the spray is aimed 0.5–1.0 cm off-axis from the inlet aperture (*19*). However, it was found that the use of an infrared heat lamp directed at A1 was needed to prevent solvent droplets from periodically obstructing the inlet aperture.

Ion Trap Mass Spectrometry. Two types of signals were applied to the electrodes of the ITMS during these experiments.

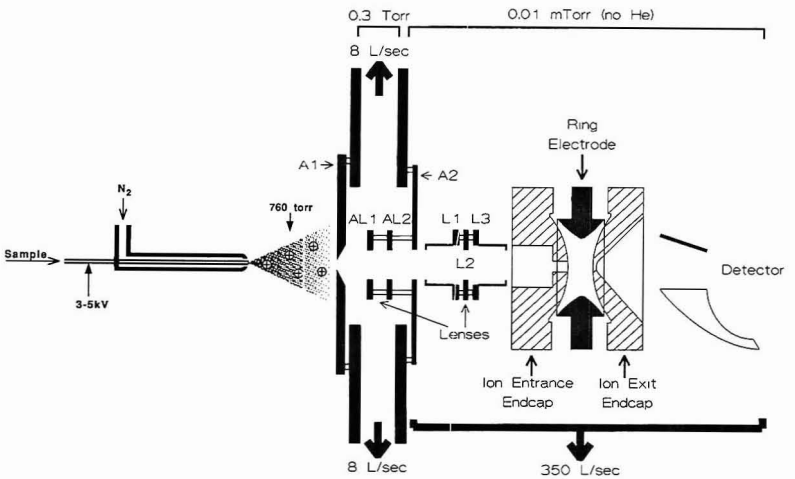

Figure 1. Cross-sectional view of the ion spray liquid chromatograph interface coupled with an ion trap mass spectrometer. Drawing is not to scale.

The most important signal was the radio-frequency (rf) signal applied to the ring electrode, which established the trapping field (*38*). This is a fixed frequency signal (1.1 MHz) that can be varied in amplitude from 0 to 7500 V zero to peak (0–p). The amplitude of the signal determines the mass/charge range of the ions that maintain stable trajectories in the trapping volume. When the ring electrode rf amplitude is increased, ions from low m/z to high m/z become sequentially unstable in the axial direction, i.e., the direction between the end-caps. As ions reach the rf amplitude value at which they become unstable, they exit the ion trap through the end-cap apertures. The ions that exit through the exit end-cap aperture are then detected with an electron multiplier (see Figure 1). The mass spectrum is obtained by scanning the ring electrode amplitude upwards from a value sufficiently low to trap the ions of interest to a value sufficiently high to eject those ions. This ion trap scanning method is referred to as the mass-selective instability mode of operation (*39*, *40*).

A distinct rf voltage was sometimes applied across the end-caps of the ion trap, the frequency of which was chosen to coincide with a characteristic frequency of motion of an ion of a particular mass-to-charge ratio. This frequency is referred to as the fundamental secular frequency of the ion in the axial dimension. Ions can be kinetically excited in the axial dimension by applying sine waves to the end-caps of opposite phase but of equal amplitude and (appropriate) frequency (*38*). The frequency is, to a first approximation, dependent upon mass/charge, the ring electrode rf amplitude and frequency, and the radius of the ring electrode (1.0 cm) (*32*, *38*).

The application of an rf signal to the end-caps was used for one of two purposes in these studies. First, a low amplitude signal (0.3–2.2 V p–p) was used *prior* to scanning the ring electrode amplitude to effect collision-induced dissociation (CID) (*41*). When used for this purpose, the rf signal applied to the end-caps is referred to herein as a "tickle voltage". Second, a relatively large signal (15 V p–p) was used *during* the scan of the ring electrode rf amplitude to extend the mass/charge range of the ion trap beyond its normal mass/charge range of m/z 650 (*42–44*). When used for this purpose, the rf signal applied to the end-caps is referred to herein as the "resonance ejection" signal to distinguish it from tickle voltage. In both cases, the rf signal applied to the end-caps is used to excite kinetically the ions in the axial dimension, but for different purposes. In the former application, the purpose is to induce energetic collisions without ejecting the precursor ions, whereas in the latter application the purpose is to eject ions from the ion trap at lower ring electrode rf amplitudes than are normally required. The 15-V p–p resonance ejection signal is obtained by passing the output of the end-cap rf signal provided by the ion trap electronics, which gives a maximum amplitude of 6 V p–p, through a power amplifier (Model 2100L, Electronic Navigation Industries, Rochester, NY).

The combined sequence, duration, and values of the signals applied to the ion trap electrodes during the experiment, along with other coordinated events, such as ion injection, are referred to as the scan function. Every scan function includes an ion injection period to accumulate ions and a scan of the ring electrode rf amplitude (with resonance ejection) to mass analyze the ions. Some scan functions also include one or more periods in which a tickle voltage is employed prior to scanning the ring electrode rf amplitude to effect CID. The latter scan functions are used for MS/MS and MS^n studies. Unique scan functions were designed for each type of experiment and are described below.

HPLC/MS Analysis of the Synthetic Peptide Mixture. All of the data shown for the synthetic peptide mixture were acquired with a 1270-V 0–p rf signal applied to the ring electrode (low mass/charge cut-off = 110) during the ion injection period. The ion injection period was 800 ms and the total time to acquire a spectrum, which included ion injection and mass analysis, was 906 ms. This gave a duty cycle, defined as the percentage of the total time to acquire a spectrum in which ions can be accumulated for analysis, of 88%. The duty cycle of the mass spectrometer is an important factor in determining how efficiently the molecules that elute from the column are detected. For beam-type scanning mass spectrometers, the duty cycle is determined by the percentage of the total scan time that the mass spectrometer spends on a peak. For a peak width of 1 m/z unit and a scan range of 1100, the typical scan range for these studies, the duty cycle would be 0.09%. The advantage in duty cycle of the ion trap over a scanning mass spectrometer is, in this case, roughly 3 orders of magnitude.

The mass/charge range of the ion trap was doubled by using resonance ejection. This caused ions with mass/charge ratios of 100 and greater to exit the ion trap at ring electrode rf amplitudes one-half those ordinarily required to eject the ions. Doubling the mass range compromises the mass assignment by reducing the number of data points per dalton from six to three. Furthermore, the data system software assigns an integer value to the ion mass, thereby introducing a rounding error. Mass assignments are therefore uncertain by at least ±2 Da in all of the synthetic peptide mixture data and tryptic digest data (see below).

HPLC/MS Analysis of the Tryptic Digest. The scan function used to obtain the chromatographic and mass spectral data for the tryptic digest of human hemoglobin normal β-chain included an ion injection period of 1.0 s with 1270-V 0–p applied to the ring electrode (low mass/charge cut-off = 110). The total time to acquire a single spectrum was 1.114 s (duty cycle = 90%). Resonance ejection was used during the ring rf amplitude scan

to double the mass range of the ion trap.

HPLC/MS Analysis of the Tryptic Digest. The pseudomolecular ions from four major compounds observed in the LC/MS total ion chromatogram were selected for MS/MS. A single scan function was used for all of the precursor ions. The scan function included an ion injection period of 800 ms (low mass/charge cut-off = 110) followed by four tickle periods of 20 ms each. The frequencies of the tickle voltages were chosen to excite kinetically the ions observed at m/z 477, m/z 658, m/z 1031, and m/z 892, in that order. The rf amplitude level for all of these periods was 1731 V 0–p (low mass/charge cut-off = 150). Resonance ejection was used during the scan of the ring electrode rf amplitude to double the mass/charge range of the ion trap. The total time of the scan was 0.989 s (duty cycle = 81%). Note that the scan function employed no changes in the ring electrode rf amplitude to effect ion isolation. The chromatographic separation provided the ion trap with ions of one mixture component, and the mass/charge dependence of the tickle voltage frequency ensured that only the targeted precursor ion was subjected to collisional activation.

Some "tuning" is usually required to obtain optimum conditions for collisional activation in the ion trap using a single tickle voltage frequency (*41*). Important variables are the ring electrode rf amplitude, the amplitude of the tickle voltage, and the time over which the tickle voltage is applied. Typically, the precursor ion of interest is used to adjust these parameters to maximize fragmentation and/or MS/MS efficiency. Tuning the MS/MS conditions is not presently an automated process with the ITMS. It is, therefore, difficult to tune MS/MS conditions "on the fly" as a peak elutes from the chromatograph. For these studies, only a minimal tuning procedure was employed. The ring electrode rf amplitude and the tickle voltage duration were chosen arbitrarily and were not varied. The tryptic digest mixture was "infused" through the ion spray LC/MS interface, and the frequency and amplitude of the tickle voltage for each of the selected precursor ions were adjusted so that the precursor ion intensity was noticeably diminished. No effort was made to isolate the precursor ions of interest from the complex mass spectrum resulting from ion spray of the mixture, and no effort was made to identify product ions during the tuning procedure.

HPLC/MS^3 Analysis of the Tryptic Digest. The doubly charged precursor ion at m/z 477 in the tryptic digest was chosen for MS/MS/MS analysis. The scan function used for the MS/MS study described above was modified by adding a step after the four tickle periods to remove all ions of $m/z < 650$ followed by a fifth 20-ms tickle period. During the fifth tickle period, the product ion observed at m/z 717 in the MS/MS spectrum of the ion at m/z 477 was subjected to collisional activation. The tuning procedure for this experiment involved infusing the digest mixture by using the modified scan function of the MS/MS experiment and adjusting the frequency and amplitude of the tickle voltage to significantly reduce the signal at m/z 717.

HPLC/MS Analysis of the Synthetic Protein Mixture. The scan function used to obtain the chromatographic and mass spectral data from the synthetic protein mixture included an ion injection period of 250 ms at a ring electrode rf amplitude of 1270 V 0–p (low mass/charge cut-off = 110) and an overall single spectrum acquisition time of 355 ms (duty cycle = 70%). A 5-ms ramp of the ring electrode rf from 1270 V 0–p to 7500 V 0–p while a relatively low amplitude (1 V p–p) fixed frequency rf signal was applied to the end-caps was used after ion injection but before the analytical scan. This ramp is sometimes necessary to complete desolvation of protein-derived ions within the ion trap (*45*). The ramp serves to bring all of the ions sequentially into resonance with the end-cap rf signal frequency, thereby exciting them. Collisions with background helium serve to decluster ions that may retain solvent. Resonance ejection was used during the ring electrode amplitude scan to extend the mass/charge range by a factor of 6.

RESULTS AND DISCUSSION

The initial work with the ES/ion trap system used what was referred to as a "figure of merit" to evaluate the system with regard to the quantity of analyte required to obtain a mass spectrum using continuous infusion (*32*). The figure of merit was defined as the product of the flow rate, the concentration of the solution, and the ion injection time (or the total time of data acquisition when scans were averaged). It was noted during the present study that the figure of merit for bradykinin, solutions of which were continuously infused periodically to tune the mass spectrometer, was about 2 orders of magnitude greater when using ion spray with the ion trap system than when using pure ES. Some of this difference may be due to the finite sampling capacity of the inlet aperture. However, a much smaller difference in response is typically observed between ion spray and ES on a triple quadrupole system, which employs a significantly different interface for sampling ions formed at atmospheric pressure (*19*). This observation, and others described below, suggests that the present interface used with the ion trap may be further from optimum for ion spray than it is for pure ES.

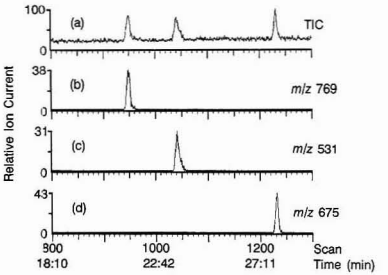

Figure 2. (a) LC/MS total ion chromatogram for a 1-μL injection of the synthetic peptide mixture (100 pmol) and the selected ion chromatograms for (b) fibrinopeptide A, (c) bradykinin, and (d) substance P, respectively.

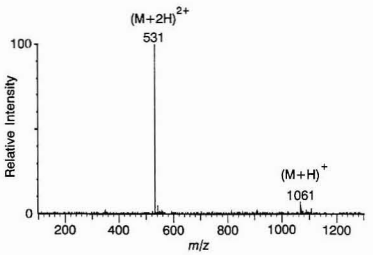

Figure 3. Mass spectrum obtained for bradykinin at the peak maximum in the selected ion chromatogram of Figure 2c.

The experiments designed to evaluate the combination of HPLC, ion spray, and the quadrupole ion trap for the analysis of peptides and proteins can be conveniently divided into three studies, viz., HPLC/MS of a synthetic peptide mixture, HPLC/MS and HPLC/MS^n of a tryptic digest, and HPLC/MS of a synthetic protein mixture. Each of these studies is described in turn below.

HPLC/MS Analysis of the Synthetic Peptide Mixture. The initial HPLC/MS experiments were performed on a synthetic peptide mixture containing fibrinopeptide A (MW = 1536), bradykinin (MW = 1060), and substance P (MW = 1348), each present in solution at a concentration of 50 pmol/μL in water. Part a of Figure 2 shows the total ion chromatogram from a 1-μL injection of the peptide mixture, and parts b–d of Figure 2 show the respective single-ion chromatograms that show separation of peptides with the maintenance of good chromatographic integrity in the elution order fibrinopeptide A:bradykinin:substance P. Chromatographic peak widths at the bases are roughly 20 s so that each peak is defined by roughly 20 data points (0.9 s/spectrum). Figure 3 is the mass spectrum obtained for bradykinin at the

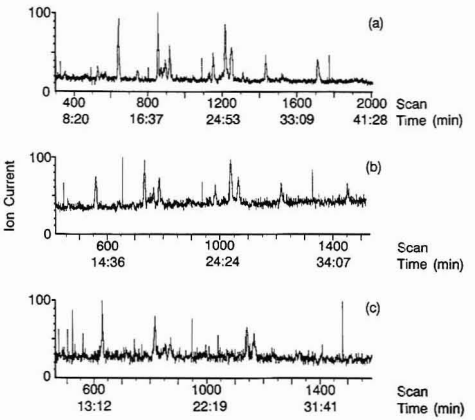

Figure 4. LC/MS total ion current profiles for (a) 100 pmol, (b) 25 pmol, and (c) 2.5 pmol of on-column injected sample quantities from the tryptic digest of normal β-chain hemoglobin.

peak maximum in which the diprotonated molecule $(M + 2H)^{2+}$ at m/z 531 is predominant with a much less abundant signal due to $(M + H)^+$ at m/z 1061. The mass spectra of fibrinopeptide A and substance P both showed doubly protonated species exclusively at m/z 769 and m/z 675, respectively. The signal/noise ratio in Figure 3 suggests that lower levels or more dilute solutions of the peptide mixture could be analyzed. However, no attempt was made to determine the minimim injectable quantity with this mixture.

HPLC/MS Analysis of Human Hemoglobin Normal β-Chain Tryptic Digest. One of the goals of this work was to determine whether microbore HPLC/MS on the ion trap mass spectrometer could provide improved sensitivity for the analysis and characterization of peptides in enzymatic digests. From our earlier work with ion spray HPLC/MS analyses of tryptic digests using a triple quadrupole mass spectrometer equipped with an atmospheric pressure ionization source and 1-mm-i.d. HPLC column (*21*), we find a practical detection limit for full scan MS in the neighborhood of 50 pmol per component in tryptic digests. Routine HPLC/MS results from this latter system are possible from 50–100 pmol of material, but meaningful results from lower levels are tenuous. In addition, full scan LC/MS/MS results on the triple quadrupole system typically require between 100 and 200 pmol per component. An added software limitation for older triple quadrupole systems limits the full scan mass range in the single MS and tandem MS modes such that only a few scans are obtained across the chromatographic peak. Since the chromatographic peaks may be only 15–30 s wide, the slow scan rate of these older systems limits the number of scans available across the peak. The combination of trace analyte levels and variation of sample quantity across the chromatographic profile sometimes produces unsatisfactory results from such studies.

Provided ions can be injected into the ion trap with efficiencies in excess of about 1%, the ITMS system should provide improved sensitivity, especially in the MS/MS mode, and its inherently shorter spectrum acquisition time should effectively deal with the problem of defining the chromatographic peaks with the relatively fast time scale of the modern HP liquid chromatograph. To test these concepts on a real sample and evaluate the feasibility of using the ITMS for on-line ion spray HPLC/MS, we analyzed a tryptic digest of human hemoglobin normal β-chain at three different levels. Figure 4a–c shows the total ion current (TIC) profiles for the

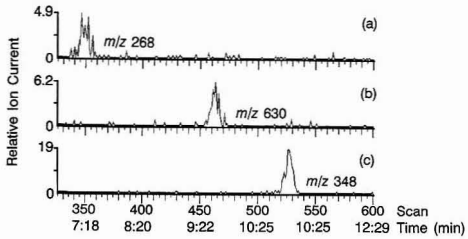

Figure 5. LC/MS extracted ion current profiles for ions that appear at (a) m/z 268, (b) m/z 630, and (c) m/z 348 in the 100-pmol tryptic digest injection.

analysis of this digest with 100, 25, and 2.5 pmol, respectively, injected onto the 1-mm × 10-cm C-8 microbore HPLC column. The separation was accomplished by applying a linear solvent gradient from 5% B to 70% B in 60 min (see Experimental Section for solvent composition). From these data, it is evident that the faster scan rate of the ITMS system provides good chromatographic fidelity for the gradient microbore HPLC separation of this tryptic digest. In addition, the symmetric chromatographic peak shape observed suggests the ion formation and sampling features of this system are performing satisfactorily. The occasional "spikes" observed in the TIC base line are of unknown origin although they were eliminated in later work when the ion spray interface was rebuilt during this study using a combination of concentric fused silica rather than stainless steel capillaries.

Inspection of Figure 4a reveals at least 16 chromatographic peaks detected when 100 pmol of the tryptic digest was analyzed under the described conditions. Thus, the electrospray mass spectra for each of these components may be inspected and, based upon the charge state and m/z ratio, the molecular weight for each component determined (*11*). Once the mass-to-charge ratios of these components are known, their corresponding extracted ion current profiles may be obtained and their plotted mass spectra presented. The ability to obtain mass spectral information from relatively weak ion current peaks in this TIC is demonstrated in Figure 5. The scan region between scans 300 and 600 in Figure 4a shows only weak evidence for chromatographic components, yet the extracted ion current profiles for m/z 268, m/z 630, and m/z 348, respectively, show these ions to be readily detected as evident in Figure 5. More importantly, the mass spectra avilable from these latter components (not shown here) are of sufficient quality to allow interpretation without resorting to background subtraction or other spectrum-enhancing techniques. Note that none of these ions corresponds to an ion of an expected tryptic fragment. They probably result from unspecific enzyme cleavage products and are probably not present at the 100-pmol level. For example, the ion at m/z 268 may be due to Thr-Phe (sequence numbers 84, 85) or Phe-Thr (sequence numbers 122, 123).

Inspection of the TIC for the on-column injection of 25 pmol of the tryptic digest of human hemoglobin normal β-chain (Figure 4b) reveals fewer chromatographic peaks. Those peptides that have a reduced response under these ion spray HPLC/MS experimental conditions are lost in the TIC base line when lower levels of material are introduced into the system. Again, however, the presence of weak or suspected components may be detected via their extracted ion current profiles and their mass spectra obtained to determine the molecular weight of the tryptic peptides.

In this work, the lowest level of injected tryptic digest sample analyzed was 2.5 pmol. Figure 4c shows the ion spray HPLC/MS TIC from this analysis. This represents a level below that which we have ever obtained data with our triple

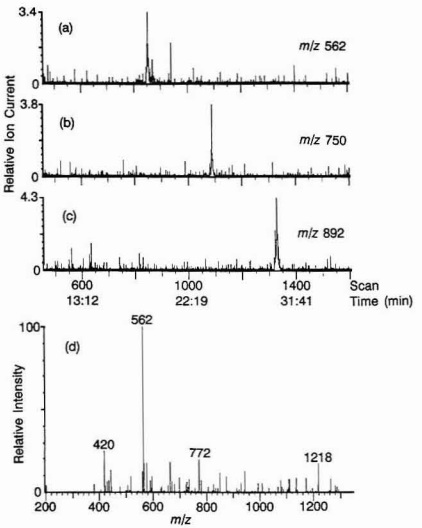

Figure 6. LC/MS extracted ion current profiles of ions that appear at (a) m/z 562, (b) m/z 750, and (c) m/z 892 in the 2.5-pmol on-column tryptic digest injection along with the mass spectrum (d) obtained for the ion at m/z 562 in the extracted ion current profile of (a).

quadrupole system using the same 1-mm-i.d. packed column. The TIC in Figure 4c is noisy with fewer than 10 chromatographic peaks discernible. However, as described above, the ability to use the data system to plot extracted ion current profiles allows one to obtain useful analytical information from this sample. For example, Figure 6 shows the extracted ion current profiles for the ions at m/z 562, m/z 750, and m/z 892 which elute in a region in the TIC base line observed in Figure 4c where there is weak evidence for chromatographic peaks. However, these and other ions characteristic of the tryptic peptides may be detected and their mass spectra viewed. Figure 6d shows the mass spectrum obtained from the m/z 562 extracted ion current profile shown in Figure 6c. This mass spectrum was obtained without background subtraction and readily reveals the m/z 562 ion, indicating a molecular weight of 561 from a singly protonated tryptic peptide or a molecular weight of 1122 from a doubly protonated tryptic peptide. This ion is probably due to the doubly protonated tryptic fragment Leu-His-Val-Asp-Pro-Glu-Asn-Phe-Arg. Although the TIC and corresponding ion current profiles resulting from the analysis of this 2.5-pmol sample of tryptic digest are weak, meaningful analytical data may be gleaned. It seems likely that improved data and lower levels may be accessible on an optimized atmospheric ion sampling interface for the ITMS system.

HPLC/MS/MS data were acquired for 100-pmol, 25-pmol, and 2.5-pmol injected sample quantities for the ions observed in the HPLC/MS study at m/z 477, m/z 658, m/z 1031, and m/z 892. The same scan function was used for all of the precursor ions as described in the Experimental Section. The same scan function was also used for all sample quantities except that the amplitude of the tickle voltage for the m/z 477 precursor ion was increased from 2.0 V p–p to 2.2 V p–p for the 2.5-pmol injection. The data for the m/z 477 precursor ion are used here as an illustration. Figure 7a shows the mass spectrum acquired at the peak maximum in the TIC observed for the mixture component that elutes at about 12.5 min (see Figure 4a, scan 640) for a 100-pmol sample injection. Ions

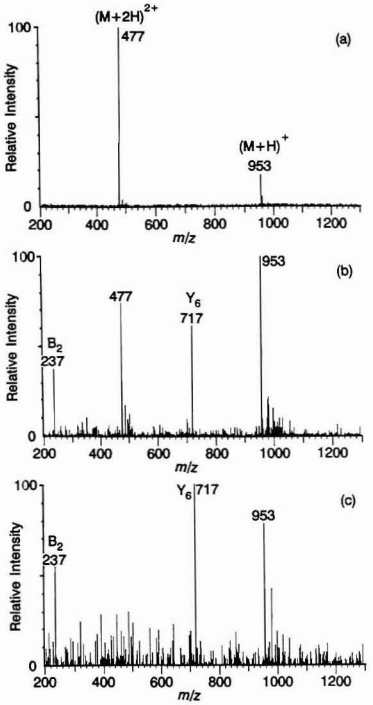

Figure 7. (a) Mass spectrum obtained at the peak maximum of the component that elutes at ~12.5 min in the TIC profile of Figure 4a and (b) the LC/MS/MS spectrum of the ion that appears at m/z 477 in (a). (c) LC/MS/MS spectrum of the same ion obtained under identical conditions except that a 2.5-pmol sample was injected onto the column.

are observed at m/z 477 and m/z 953 and are likely to correspond to $(M + 2H)^{2+}$ and $(M + H)^{+}$, respectively, for a tryptic peptide of molecular weight 952. This mass corresponds to the expected tryptic fragment from human hemoglobin normal β-chain with the sequence Val-His-Leu-Thr-Pro-Glu-Glu-Lys. Figure 7b shows the LC/MS/MS spectrum acquired for the ion at m/z 477 under conditions identical with those for acquisition of the spectrum of Figure 7a except that application of a tickle voltage frequency matching the secular frequency of the ion at m/z 477 was added to the scan function. Note that the ion at m/z 953 appears in this spectrum but is not a CID product of the ion at m/z 477. The ion at m/z 953 appears due to the absence of a precursor ion isolation step in the scan function (see Experimental Section). Major product ions are observed at m/z 717 and m/z 237, which are equidistant in mass-to-charge from the precursor ion. This suggests that both product ions are formed from the same dissociation reaction. It also indicates that the precursor ion is multiply charged and that it carries an even number of charges. This spectrum, therefore, further supports the conclusion that the m/z 477 ion is the doubly protonated tryptic peptide shown above. Assuming this to be the case, the m/z 717 and m/z 237 ions correspond to, in terms of the conventional peptide fragment shorthand (*46*), the Y_6^+ and B_2^+ fragments expected from this peptide. Figure 7c shows the LC/MS/MS spectrum of the m/z 477 precursor ion obtained under conditions identical with those used to acquire Figure 7b except that a 2.5-pmol sample quantity was injected

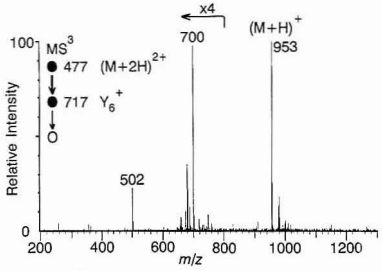

Figure 8. LC/MS^3 spectrum obtained from the ion at m/z 477 formed from the mixture component that eluted at ~12.5 min (see Figure 4a). The precursor ion sequence was m/z 477 → m/z 717 → ?. These data were acquired with an injected sample quantity of 100 pmol.

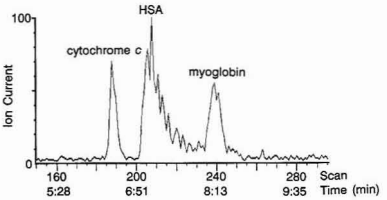

Figure 9. LC/MS total ion chromatogram obtained for a synthetic protein mixture consisting of cytochrome c, human serum albumin (HSA), and myoglobin, with mixture component quantities of 5.5 pmol, 1.3 pmol, and 3.8 pmol, respectively.

onto the column and a slightly larger tickle voltage amplitude was employed (2.2 V p–p versus 2.0 V p–p). The signal/noise is poorer, but the major product ions are still clearly evident. The larger tickle voltage amplitude used to acquire the spectrum of Figure 7c is responsible for the significantly reduced precursor ion intensity relative to that observed in the MS/MS spectrum of Figure 7b.

These results indicate that, at least for some tryptic digest components, LC/MS/MS spectra can be obtained from sample quantities as low as 2.5 pmol of injected material. Given that little effort was expended optimizing CID conditions for maximum efficiency and maximum structural information (i.e., maximizing the number of different product ions), it is probably not justified to draw firm conclusions regarding the limits of LC/MS/MS with an ion trap for tryptic peptides. These data, as well as data for other peptides, indicate that MS/MS efficiencies in excess of 20% can easily be obtained. However, MS/MS efficiencies approaching 100% are typically not observed. All of the LC/MS/MS spectra acquired in this study showed structurally characteristic product ions, but none of these data provided complete sequence information. On the other hand, for peptides of similar size, we have observed extensive structurally characteristic fragmentation when MS/MS conditions are tuned to maximize energy deposition (*47*).

More complete structural information than is available from the MS/MS spectrum might be obtainable from further stages of MS. To demonstrate this capability with an on-line analysis of a tryptic digest, we subjected the precursor ion observed at m/z 477, from a 100-pmol sample injection, to MS^3. Figure 8 shows the ion spray LC/MS^3 spectrum for the sequence m/z 477 → m/z 717 → ?. Note that the signal at m/z 953 is not due to a product ion but is simply the $(M + H)^+$ ion for this tryptic peptide that remains in the ion trap throughout the analysis. The two major second generation product ions from the ion at m/z 717 are observed at m/z 700 and m/z 502. Again, making the reasonable assumption that the ion at m/z 477 is the doubly protonated tryptic peptide Val-His-Leu-The-Pro-Glu-Glu-Lys, the MS^3 experiment can be interpreted as shown in Scheme I. The ion at m/z 700 probably results

Scheme I

$$(M + 2H)^{2+} \rightarrow B_2^+ + Y_6^+$$

$$Y_6^+ \rightarrow m/z\ 700\ (-NH_3), \quad m/z\ 251\ (Y_4^+)$$

from the loss of ammonia, a fragmentation that we have frequently observed from other peptide cations. (With the uncertainty in the mass assignment with the current system, however, we cannot preclude water loss.) The ion at m/z 251 corresponds to the Y_4^+ ion from $(M + 2H)^{2+}$. These data therefore confirm that further structurally characteristic fragmentation can be obtained from additional stages of mass spectrometry, which is a relatively straightforward procedure with the ITMS. Complete sequence determination in this case would indeed require further stages of mass spectrometry. The routine application of MS/MS and MS^n to on-line analyses of unknowns, however, requires further development in optimizing tuning conditions on the fly.

HPLC/MS Analysis of a Synthetic Protein Mixture. One of the most remarkable features of ES as an ionization method for mass spectrometry is its ability to ionize biopolymers, such as proteins, by imparting multiple charges to the molecule. It is the multiple charging characteristic of ES that makes the characterization of high mass molecules possible with two- and three-dimensional quadrupoles, which typically have an upper mass/charge limit of < 4000. As the original report discussed, however, the present operation of the ITMS system electronics prevents the ITMS from providing its inherent mass resolution and mass accuracy for high mass, multiply charged ions (*32*). Briefly, this is due to the fact that the normal mass/charge range of the ion trap (m/z 650) must be extended, using resonance ejection, for analysis of the high mass, multiply charged ions. In doing so, the number of data points per dalton decreases, thereby compromising mass accuracy, and the scan speed in daltons/second increases, which decreases resolution. The software used to acquire the data reported here further compromises mass assignment in that peaks are assigned an integral mass/charge. An uncertainty in mass/charge assignment of one unit, as displayed by the software, translates to an uncertainty of 72 Da when the mass range of the ion trap is extended by a factor of 6 and for an ion with a charge state of 12. In principle, however, the three-dimensional quadrupole should provide mass resolution and mass accuracy comparable to those provided by the quadrupole mass filter.

Despite the handicaps imposed on the present ion trap system for mass measurement of high mass, multiply charged ions, a synthetic protein mixture was subjected to HPLC/MS analysis to determine the relative accuracy for mass measurement under HPLC/MS conditions. The mixture consisted of bovine cytochrome c, horse heart myoglobin, and human serum albumin (HSA) at concentrations of 5.5, 3.8, and 1.3 pmol/μL, respectively, in 2:1 water/acetonitrile. Figure 9 shows the total ion chromatogram obtained under microbore LC/MS conditions with injected sample quantities of 5.5, 3.8, and 1.3 pmol of cytochrome c, myoglobin, and HSA, respectively. The separation was accomplished by applying a linear solvent gradient from 20% B to 100% B in 15 min with a hold at the final conditions for another 15 min. The TIC profile shows good chromatographic separation of the tryptic components and good signal/noise for each.

Figure 10a–c shows the mass spectrum of each component obtained by averaging several scans acquired over the corresponding chromatographic peak. All of the mass spectra were acquired by using resonance ejection to extend the mass/charge range of the ion trap by a factor of 6 (i.e., to m/z 3900).

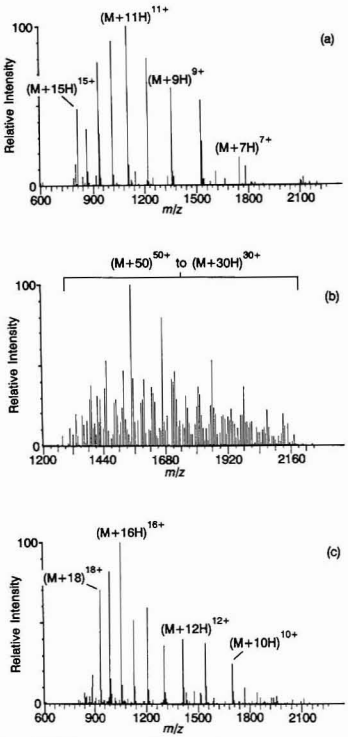

Figure 10. LC/MS spectra of (a) cytochrome *c*, (b) HSA, and (c) myoglobin obtained by averaging several scans over the corresponding peaks in the TIC profile shown in Figure 9.

Mass measurements could be made for cytochrome *c* [MW_{avg} = 12 200 (*48*), measured MW_{avg} = 12 200 ± 22] and for myoglobin [MW_{avg} = 16 951 (*48*), measured MW_{avg} = 16 936 ± 23], which typically show well-resolved charge states in their ES/ion trap mass spectra. The procedure for making a molecular weight determination of a high mass molecule with a distribution of charge states using an ion trap is analogous to that used with a quadrupole mass filter (*9*, *11*). Some corrections must be made to the mass/charge assignments of the data system when the mass range is extended by resonance ejection (*32*). The major sources of uncertainty in these measurements arise from the limited number of data points per peak and from the integral mass assignment made by the software.

Unlike the cytochrome *c* and the myoglobin cases, a molecular weight determination for HSA cannot be made from the mass spectrum shown in Figure 10b. The peak maxima for the charge states of HSA (MW_{avg} = 66 000) cannot be assigned reliably, which introduces uncertainty for determining the charge state and, hence, the mass. Two of the reasons why the masses of the HSA ions are measured less reliably than those of, for example, cytochrome *c* are that the charge states are closer together in m/z and each charge state is composed of a wider range of masses, which results in broader peaks. These factors lead to poorer resolution of the charge states. A third factor that may come into play with the ion trap is the degradation of resolution due to space charging. This is a well-known phenomenon in ion trapping instruments (*38*). In the quadrupole ion trap, peak broadening is typically the

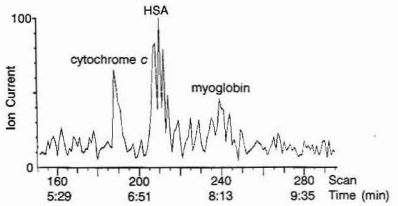

Figure 11. LC/MS total ion chromatogram for the protein mixture containing cytochrome *c*, HSA, and myoglobin with mixture component quantities of 1.1 pmol, 0.3 pmol, and 0.8 pmol, respectively.

first symptom observed when the space charge becomes significant. A shift in peak position can also occur. Empirically, we observe loss of resolution due to space charge at shorter injection times for HSA ions than for either myoglobin or cytochrome *c* ions when solutions of equal concentrations are subjected to ES via infusion. This may be due to the fact that the HSA ions are more highly charged or to greater ionization/sampling/detection efficiency for HSA ions or to both. We have not performed studies to separate these effects, but we have observed evidence that both factors could contribute to the shorter injection time onset of space charge effects for HSA ions. The fact that conditions necessary for space charge effects are more readily achieved for HSA ions than for the ions of cytochrome *c* and myoglobin and the fact that all ions were analyzed by using the same scan function lead to the possibility that space charge was significant for the HSA ions whereas it was not for the ions of cytochrome *c* and myoglobin.

The mass accuracy limitations imposed by the present data system must be addressed before the quadrupole ion trap can be expected to measure the molecular weights of proteins in excess of several tens of kilodaltons. Provided adequate improvements are made, the ion trap holds promise for this application due to the relatively low levels of injected analyte necessary to obtain mass spectra with adequate S/N ratios. Figure 11, for example, shows the TIC of the protein mixture acquired from the injection and HPLC/MS analysis of 1.1, 0.8, and 0.3 pmol, respectively, of cytochrome *c*, myoglobin, and HSA. The fact that each component is clearly observable in the TIC is encouraging in light of the minimal effort that went into optimizing the analysis conditions.

HPLC/MS Analysis of Physiological Extracts Containing Drugs. The detection and identification of drugs present in extracts of physiological fluids is another important application for HPLC/MS. We made several attempts at the on-line analysis of LSD and etorphine (a highly potent stimulant) with the ion spray LC/ITMS system. We found the system to be insensitive to these compounds. Etorphine was not detected up to injected sample quantities of 5 ng. LSD was only clearly detectable with an injected sample quantity of 100 ng. Neither of these compounds showed strong signals when delivered to the ion spray via infusion. Furthermore, neither compound showed strong signals when they were subjected to pure ES from methanol solutions. They have, on the other hand, shown strong signals with ion spray on our commercial triple quadrupole instrument equipped with an atmospheric pressure ionization source (*26*).

These observations appear to point to a shortcoming of the ASGDI hardware as an atmospheric ion sampling interface. The region between A1 and A2 (see Figure 1) is not collision-free, and extensive scattering can occur prior to ion exit through the aperture in A2. Scattering is most likely for ions of relatively low mass, such as the ions derived from LSD ($(M + H)^+$ appears at m/z 324) and etorphine ($(M + H)^+$ appears at m/z 412). Scattering losses in the interface region are expected to be less important as the ions become more

massive. This explains, in part, the excellent performance noted for the proteins. In some cases, excellent performance has also been noted for relatively low mass ions with pure ES with this ITMS system (*32*). There is strong evidence, however, that at least some of these ions are highly solvated upon injection into the ion trap and are therefore relatively massive in the interface region. This does not appear to be the case for the ions derived from LSD and etorphine.

CONCLUSIONS

This work has highlighted several shortcomings of the present ion injection/ITMS system as the mass spectrometer for on-line HPLC/MS analyses. Fortunately, all of these shortcomings are, in principle, correctable. Mass accuracy can be improved by reducing the scan speed and increasing the number of data points per peak. Improved atmospheric ion sampling designs should provide greater ion transmission through the interface, particularly for low mass ions. The automation of MS/MS and MS^n for on-line analyses requires some rather extensive improvements to the present ITMS software. Efforts are already being made in this direction (*49*). Until these changes are made, however, this system cannot be applied routinely for LC/MS and LC/MS^n determinations.

Despite the problems noted herein, these studies indicate that the ion spray liquid chromatography/quadrupole ion trap combination shows great promise for the determination of biomolecules. Even with a nonoptimized atmospheric ion sampling interface, ion spray LC/MS data for a tryptic digest could be obtained at levels 10–50 times lower than those normally required for a triple quadrupole system. The advantage for LC/MS/MS is even greater. We have also demonstrated the use of LC/MS^3 in an on-line analysis of a tryptic digest. Data can also be obtained at subpicomole levels for proteins as high in mass as 10–20 kDa. Provided the improvements discussed above are made, the quadrupole ion trap should prove to be a powerful analyzer for ions derived via ES with on-line separation of biomolecules.

ACKNOWLEDGMENT

We thank Richard Ludwig of Supelco, Inc., for providing the microbore C-8 HPLC column used in this work. We also thank Terry Lee of Beckman Research Institute, City of Hope, for providing the human hemoglobin normal β-chain sample. J.D.H. thanks Applied Bioanalytical Systems, Inc., for the loan of the Model 140A micro-HPLC pump used in this work.

LITERATURE CITED

(1) Vestal, M. L. In *Mass Spectrometry in the Health and Life Sciences*; Burlingame, A. L., Castagnoli, N., Jr., Eds.; Elsevier: Amsterdam, 1985; p 99.
(2) Stachowiak, K.; Wilder, C.; Vestal, M. L.; Dyckes, D. F. *J. Am. Chem. Soc.* **1988**, *110*, 1758.
(3) Willoughby, R. C.; Browner, R. F. *Anal. Chem.* **1984**, *56*, 2626.
(4) Winkler, P. C.; Perkins, D. D.; Williams, D. K.; Browner, R. F. *Anal. Chem.* **1988**, *60*, 489.
(5) Caprioli, R. M. *Biochemistry* **1988**, *27*, 513.
(6) Caprioli, R. M. *Anal. Chem.* **1990**, *62*, 477A.
(7) Ashcroft, A. E. *Org. Mass Spectrom.* **1987**, *22*, 754.
(8) Whitehouse, C. M.; Dreyer, R. N.; Yamashita, M.; Fenn, J. B. *Anal. Chem.* **1985**, *57*, 675.
(9) Mann, M.; Meng, C. K.; Fenn, J. B. *Anal. Chem.* **1989**, *61*, 1702.
(10) Fenn, J. B.; Mann, M.; Meng, M. K.; Wong, S. F.; Whitehouse, C. M. *Science* **1990**, *246*, 64.
(11) Covey, T. R.; Bonner, R. F.; Shushan, B. I.; Henion, J. D. *Rapid Commun. Mass Spectrom.* **1988**, *2*, 249.
(12) Henion, J. D.; Covey, T. R.; Muck, W.; Huang, E. C. Presented at the 37th Annual Conference on Mass Spectrometry and Allied Topics, Miami Beach, FL, 1989; p 1014.
(13) Smith, R. D.; Olivares, J. A.; Nguyen, N. T.; Udseth, H. R. *Anal. Chem.* **1988**, *60*, 436.
(14) Loo, J. A.; Udseth, H. R.; Smith, R. D. *Anal. Biochem.* **1989**, *179*, 404.
(15) Smith, R. D.; Barinaga, C. J.; Udseth, H. R. *Anal. Chem.* **1988**, *60*, 1948.
(16) Lee, E. D.; Covey, T. R.; Muck, W.; Henion, J. D. *J. Chromatogr.* **1988**, *458*, 313.
(17) Lee, E. D.; Muck, W.; Covey, T. R.; Henion, J. D. *Biomed. Environ. Mass Spectrom.* **1989**, *18*, 844.
(18) Udseth, H. R.; Loo, J. A.; Smith, R. D. *Anal. Chem.* **1990**, *61*, 228.
(19) Bruins, A. P.; Covey, T. R.; Henion, J. D. *Anal. Chem.* **1987**, *59*, 2642.
(20) Lee, E. D.; Covey, T. R.; Henion, J. D. *J. Microcol. Sep.* **1989**, *1*, 14.
(21) Huang, E. C.; Henion, J. D. *J. Am. Soc. Mass Spectrom.* **1990**, *1*, 158.
(22) Conboy, J. J.; Henion, J. D.; Martin, M. W.; Zweigenbaum, J. A. *Anal. Chem.* **1990**, *62*, 800.
(23) Dong, M. W.; Gant, J. R.; Larsen, B. R. *Biochromatography* **1989**, *4*, 19.
(24) Bruins, A. P.; Weidolf, L. O. G.; Henion, J. D.; Budde, W. L. *Anal. Chem.* **1987**, *59*, 2647.
(25) Weidolf, L. O. G.; Lee, E. D.; Henion, J. D. *Biomed. Environ. Mass Spectrom.* **1988**, *15*, 283.
(26) Huang, E. C.; Wachs, T.; Conboy, J. C.; Henion, J. D. *Anal. Chem.* **1990**, *62*, 713A.
(27) Loo, J. A.; Udseth, H. R.; Smith, R. D. *Rapid Commun. Mass Spectrom.* **1988**, *2*, 207.
(28) Smith, R. D.; Barinaga, C. J.; Udseth, H. R. *J. Phys. Chem.* **1989**, *93*, 5019.
(29) Smith, R. D.; Loo, J. A.; Barinaga, C. J.; Edmonds, C. G.; Udseth, H. R. *J. Am. Soc. Mass Spectrom.* **1990**, *1*, 53.
(30) Barinaga, C. J.; Edmonds, C. G.; Udseth, H. R.; Smith, R. D. *Rapid Commun. Mass Spectrom.* **1989**, *3*, 160.
(31) Siu, K. W.; Gardner, G. J.; Berman, S. S. *Org. Mass Spectrom.* **1989**, *24*, 931.
(32) Van Berkel, G. J.; Glish, G. L.; McLuckey, S. A. *Anal. Chem.* **1990**, *62*, 1284.
(33) McLafferty, F. W., Ed. *Tandem Mass Spectrometry*; Wiley: New York, 1983.
(34) Busch, K. L.; Glish, G. L.; McLuckey, S. A. *Mass Spectrometry/Mass Spectrometry: Techniques and Applications of Tandem Mass Spectrometry*; VCH Publishers: New York, 1988.
(35) Nourse, B. D.; Cooks, R. G. *Anal. Chim. Acta* **1990**, *228*, 1.
(36) McLuckey, S. A.; Glish, G. L.; Asano, K. G. *Anal. Chim. Acta* **1989**, *225*, 25.
(37) McLuckey, S. A.; Glish, G. L.; Asano, K. G.; Grant, B. C. *Anal. Chem.* **1988**, *60*, 2220.
(38) March, R. E.; Hughes, R. J. *Quadrupole Storage Mass Spectrometry*; John Wiley and Sons: New York, 1989.
(39) Stafford, G. C.; Kelley, P. E.; Syka, J. E. P.; Reynolds, W. E.; Todd, J. F. J. *Int. J. Mass Spectrom. Ion Proc.* **1984**, *60*, 85.
(40) Stafford, G. C.; Kelley, P. E.; Stephens, D. R. U.S. Patent 4 540 884, 1985.
(41) Louris, J. N.; Cooks, R. G.; Syka, J. E. P.; Kelley, P. E.; Stafford, G. C., Jr.; Todd, J. F. J. *Anal. Chem.* **1987**, *59*, 1677.
(42) Hemberger, P. H.; Moss, J. D.; Kaiser, R. E.; Louris, J. N.; Amy, J. W.; Cooks, R. G.; Syka, J. E. P.; Stafford, G. C., Jr. Proceedings of the 37th ASMS Conference on Mass Spectrometry and Allied Topics, Miami Beach, FL, May 21–26, 1989; p 60.
(43) Kaiser, R. E., Jr.; Cooks, R. G.; Moss, J.; Hemberger, P. H. *Rapid Commun. Mass Spectrom.* **1989**, *3*, 50.
(44) Kaiser, R. E.; Louris, J. N.; Amy, J. W.; Cooks, R. G. *Rapid Commun. Mass Spectrom.* **1989**, *3*, 225.
(45) McLuckey, S. A.; Glish, G. L.; Van Berkel, G. J. Proceedings of the 38th ASMS Conference on Mass Spectrometry and Allied Topics, Tuscon, AZ, June 3–8, 1990; p 512.
(46) Roepstorff, P.; Fohlman, J. *Biomed. Mass Spectrom.* **1984**, *11*, 601.
(47) Glish, G. L.; McLuckey, S. A.; Van Berkel, G. J. Proceedings of the 38th ASMS Conference on Mass Spectrometry and Allied Topics, Tuscon, AZ, June 3–8, 1990; p 922.
(48) Dayhoff, D. O., Ed. *Atlas of Protein Sequence and Structure*; National Biomedical Research Foundation: Silver Springs, MD, 1972.
(49) Todd, J. F. J.; Penman, A. D.; Thorner, D. A.; Smith, R. D. *Rapid Commun. Mass Spectrom.* **1990**, *4*, 108.

RECEIVED for review August 20, 1990. Accepted November 19, 1990. E.C.H. thanks the Eastman Kodak Company for financial support during the course of his postdoctoral studies. S.A.M., G.V.B., and G.L.G. acknowledge research sponsorship by the U.S. Department of Energy, Office of Basic Energy Sciences under Contract DE-AC05-84OR21400 with Martin Marietta Energy Systems, Inc.

Analysis of Drugs in the Presence of Serum Albumin by Liquid Chromatography with Eluents Containing Surfactants

Ralph A. Grohs,[1] F. Vincent Warren, Jr.,[2] and Brian A. Bidlingmeyer*

Waters Chromatography Division, Millipore Corporation, 34 Maple Street, Milford, Massachusetts 01757

Surfactant-containing eluents are evaluated for possible application to direct serum injection using conventional reverse-phase columns. Serum albumin was quantitatively eluted at the column void volume by using surfactant concentrations below or above the critical micelle concentration, and organic solvents could be used in proportions as high as 40% (w/w). Surfactant choice, pH, and salt effects were also evaluated.

INTRODUCTION

The analysis of drugs from biological fluids is an important problem in pharmaceutical research, clinical chemistry, and pharmacokinetics which is frequently accomplished by methods based on liquid chromatography (LC). These LC methods generally require a time-consuming sample preparation step to remove proteinaceous sample components that would otherwise degrade system performance through deposition on the chromatographic packing. Protein precipitation, ultrafiltration, liquid/liquid extraction, and solid-phase extraction have all been used for sample preparation prior to injection into LC systems. All are labor-intensive techniques, although the solid-phase extraction approach can be automated through the application of laboratory robotics (*1*) or column switching (*2*). The relative merits of these alternatives have been discussed elsewhere (*3*).

In an effort to avoid the sample preparation step entirely, the direct injection of serum samples has been practiced by a number of laboratories. In some cases, these efforts have involved the use of column packings that are designed to minimize the adsorption of serum proteins (*4–8*). Certain eluent restrictions are associated with the use of these columns to ensure that serum components remain in solution, and these columns are generally used with a guard column, which is changed regularly to keep the system back-pressure at normal levels (*6, 7*). A related approach for the direct injection of serum samples is the use of a protein-coated packing (*9*). In this approach, a conventional reverse-phase column is modified in situ by the injection of serum and/or solutions containing bovine serum albumin (BSA). A variation on this technique is the pretreatment of bare silica columns with serum prior to their use in direct serum injection applications (*10*).

The primary alternative to the use of specially prepared columns employs conventional LC column packings and eluents capable of solubilizing serum proteins. This approach allows the chromatographer to work with familiar column packings and eluents. For example, Weinberger and Chidsey (*11*) analyzed theophylline by direct serum injection using phosphate buffer (pH 3.65) and a cation-exchange column and guard column. More than 500 serum samples were analyzed with no apparent degradation of chromatographic performance, provided that the guard column was changed after each 30–40 injections. More recently, Bui and French (*12*) used silica packings with triethylammonium acetate buffers for the analysis of several β-blockers by direct serum injection.

Micellar eluents have been used with reverse-phase LC columns to analyze a variety of solutes by direct serum injection (*13–16*). By definition, these eluents contain a surfactant at a concentration above the critical micelle concentration (CMC). Sodium dodecyl sulfate (SDS) is the most commonly used surfactant for this approach, but nonionic surfactants have also been employed successfully (*3*). In the preparation of micellar eluents for direct serum injection, it is necessary to avoid eluent conditions that are unfavorable for (1) micelle formation or (2) serum protein solubilization. For this reason surfactant concentration is maintained at or above the CMC, and organic solvent composition is kept relatively low in micellar eluents (*16*).

This report describes our efforts to understand the range of surfactant and organic solvent compositions which will permit direct serum injection. Conventional reverse-phase LC packings are used, and both micellar and nonmicellar eluents are considered. Surfactant concentration is allowed to vary above and below the CMC, and organic solvent compositions up to 80% methanol (w/w) are tested. An aqueous solution of bovine serum albumin (BSA) is used as the model serum for these preliminary studies, permitting a more direct focus on the surfactant/protein interactions required for successful direct serum injection.

EXPERIMENTAL SECTION

Instrumentation. The chromatographic system from Waters Chromatography Division of Millipore Corp. (Milford, MA) included a WISP 712 autoinjector, a Model 510 solvent delivery system, a Model 441 fixed-wavelength UV/vis detector equipped with a 214-, 254-, or 280-nm filter kit, and a Model SE120 dual-pen chart recorder. Automated runs were controlled by a Model 840 chromatography control station, with data collected and autoarchived to a Model 860 networking chromatography station for processing and storage.

Unless otherwise noted in the text, a μBondapak C_{18} column (Waters) was used for all of the work described. Either a steel column (0.39 × 15 cm) or radially compressed cartridge (0.8 × 10 cm) was used. The cartridges were housed in an RCM-100 or RCM-8 × 10 radial compression module (Waters). Except where noted, a fresh column or cartridge was used for testing each new eluent. Other columns used were Protein-Pak SP-5PW (steel, 0.75 × 7.5 cm) and Nova-Pak Phenyl (steel, 0.39 × 7.5 cm, or cartridge, 0.8 × 10 cm), both from Waters. When necessary, the time equivalent to the void volume was determined by injection of a dilute solution of uracil.

Reagents and Eluents. Purified water was obtained from a Milli-Q system (Millipore Corp., Bedford, MA). Liquid chromatography grade methanol, 2-propanol, and acetonitrile were obtained from J. T. Baker (Phillipsburg, NJ). Bovine serum albumin was purchased from Sigma (St. Louis, MO) and stored at 4 °C. Carbamazepine (CBZ), sodium desoxycholate, CHAPS, Nonidet-P40, and Brij-35 were obtained from Sigma. Cetyltrimethylammonium bromide was obtained from Alfa Products (Danvers, MA). Sodium dodecyl sulfate (BioChemica Microselect grade) was obtained from Fluka (Ronkonkama, NY). Sodium decyl sulfate and sodium pentadecyl sulfate were obtained from Lancaster Synthesis Ltd. (Windham, NH), and carbamazepine

[1] Present address: Institute for Applied Physical Chemistry, University of Saarland, Saarbrucken, Germany.
[2] Present address: Bristol-Myers Squibb Pharmaceutical Research Institute, One Squibb Drive, New Brunswick, NJ 08903-0191.

0003-2700/91/0363-0384$02.50/0

10,11-epoxide (CBE) was purchased from Alltech/Applied Science (Deerfield, IL).

Model serum consisted of 50 mg of BSA/mL of water. Once prepared, model serum was stored at 4 °C. Aliquots required for injections were stored at room temperature for no more than a few hours, as we observed differences in peak areas when 2-day-old samples were used. Stock solutions of CBZ and CBE (10 mg/mL) were prepared in methanol, stored at 4 °C, and used as necessary for the preparation of spiked model serum.

Eluents were filtered through a 0.45-μm cellulose acetate filter under vacuum, using a solvent clarification accessory (Waters) just prior to addition of the surfactant. To avoid excessive foaming as well as regassing of the eluent, the surfactant was slowly dissolved with gentle stirring. If necessary, eluents could be refiltered after blending.

Measurement of Adsorbed Surfactant. Upon initial exposure of a column to a surfactant-containing eluent, the adsorption process was monitored by recording the response of a differential refractometer using a procedure similar to the one described previously (*17*). A manually operated six-port valve (Rheodyne, Cotati, CA) was installed at the column inlet, allowing the incoming solvent to bypass the column (when necessary) and flush the reference cell of the differential refractometer. Prior to exposing each new column to surfactant-containing eluent, both the column and reference cell were thoroughly flushed with eluent containing no surfactant. A zero level was established for the detector output. The valve was then set to the column bypass position, and the system (including the reference cell) was flushed with surfactant-containing eluent. The detector output would rise or fall to a new level, and the chart recorder was adjusted to keep this signal on scale. Finally, the valve was switched, allowing eluent to enter the column. The output of the differential refractometer was monitored until the trace returned to the previously established zero level, indicating that surfactant-containing eluent was present in both the sample and reference cells of the detector. From the strip chart record, the total volume of solvent required to equilibrate the system was determined. The void volume was subtracted, and the result was multiplied by the surfactant concentration to determine the adsorbed amount.

Determination of Protein Recovery. Two methods were used to test for protein mass recovery. First, the Bradford assay (BioRad, Richmond, CA) was used according to the manufacturer's instructions. Identical injections of BSA were made with and without a column in place, and fractions containing the resulting peak were collected. The Bradford assay response was measured for each fraction, and this value was multiplied by the volume of the collected fraction to yield an adjusted assay response. Agreement between the adjusted assay response determined with and without the use of a chromatographic column was accepted as evidence of quantitative elution of BSA.

It was noted that the Bradford assay response tended to drift during the measurement period, possibly due to the presence of SDS at a level (1 mM) close to the upper limit recommended by the manufacturer (0.1% w/v). For this reason, a second approach using direct UV assay at 280 nm was done to confirm the Bradford assay results. Fractions containing the peak resulting from a 10-μL injection of model serum were collected in a 2-mL volume. The UV absorbance at 280 nm was measured relative to an eluent blank, and values obtained with and without the use of a chromatographic column were compared.

RESULTS AND DISCUSSION

Work with size-exclusion chromatography (SEC) and other techniques for the analysis and purification of proteins indicates that surfactant concentrations below the CMC can effectively elute serum protein components. For example, the addition of 0.1% w/w SDS (equivalent to 3.2 mM) to aqueous phosphate buffers was shown to alter the elution times for various proteins in SEC systems in a manner consistent with their denaturation to a random coil formation (*18*). Surfactants have also been used at concentrations below the CMC in eluents designed for hydrophobic interaction chromatography (*19*), particularly when membrane proteins and other hydrophobic species are to be separated. In addition, elution buffers for SDS-PAGE (polyacrylamide gel electrophoresis) typically contain SDS at a concentration below the CMC (*20*).

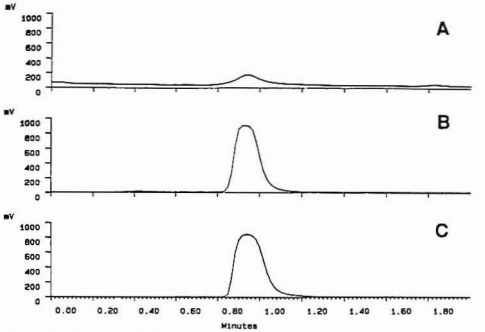

Figure 1. Effect of SDS concentration on the elution of bovine serum albumin (BSA). Conditions: column, μBondapak C_{18} (steel, 0.39 × 15 cm); eluents, (A) water, (B) aqueous 1 mM SDS, (C) aqueous 20 mM SDS; detection, at 280 nm.

Among existing approaches to direct serum injection, micellar LC is particularly attractive due to its compatibility with conventional reverse-phase column packings. However, the eluents typically used for micellar LC may represent only a subset of the surfactant-containing eluents that will permit direct serum injection.

Our goal in working with surfactant-containing eluents was to understand the range of surfactant and organic solvent compositions that can be used in the design of successful eluents for direct serum injection onto reverse-phase columns. For example, eluents having surfactant concentrations below the CMC might still be useful for direct serum injection. In addition, if the stabilization of micellar aggregates is not required, relatively high organic solvent compositions might be acceptable. Either of these cases would broaden the range of eluents that can be used in combination with conventional reverse-phase columns for direct serum injection applications (*21*).

In order to test candidate eluents for their ability to permit direct serum injection in reverse-phase systems, studies were conducted with model serum consisting of an aqueous 50 mM solution of bovine serum albumin (BSA). This serum albumin concentration is near the level found in normal human serum (*22*). The use of the relatively simple model serum matrix permits a clearer focus on the interactions between surfactant and protein that are expected to be critical to the performance of successful eluents for direct serum injection. Depending upon the results of the studies with model serum, additional testing with bovine serum (and ultimately human serum) will be required to verify the suitability of a given eluent.

Elution of BSA. To study the effect of SDS concentration on the elution of serum albumin, a set of eluents containing 0, 1, 5, 10, or 20 mM SDS was prepared. A fresh μBondapak C_{18} column containing packing from the same manufacturing batch was equilibrated with each, and 10-μL volumes of model serum were injected repeatedly. For the water eluent, a peak was observed at the column's exclusion volume but the area was substantially less than that obtained when SDS-containing eluents were used (see Figure 1). On the basis of Bradford assay responses for peaks collected with and without the use of the μBondapak C_{18} column, only about 6% of the injected BSA was eluted by the water eluent.

All of the SDS-containing eluents produced a large BSA peak at the column's exclusion volume, as indicated in Figure 1 for the 1 and 10 mM SDS eluents (corresponding to SDS concentrations above and below the CMC value of 8 mM). However, the peak areas observed were not identical for all eluents. Figure 2A summarizes the trends observed during

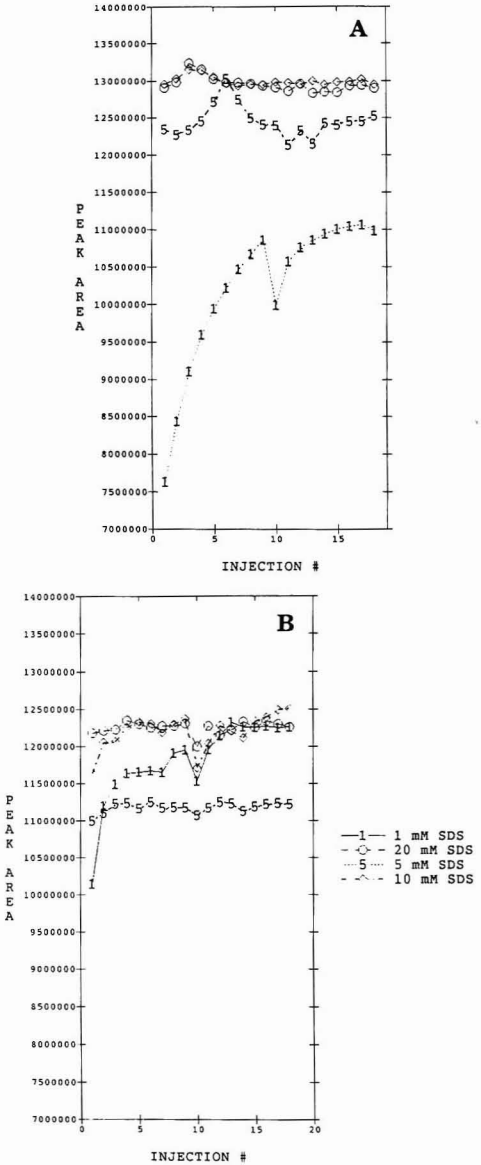

Figure 2. Effect of SDS concentration on peak area for BSA in (A) aqueous and (B) 15% (w/w) methanol/water eluents. The SDS concentration for each eluent is shown in the key.

the first 18 model serum injections for each column/eluent combination. Note that three blank injections were made between injections 9 and 10 of each set.

In Figure 2A, peak areas are stable for 5, 10, and 20 mM SDS, although the average peak area for the 5 mM eluent is about 4% lower than that observed for 10 or 20 mM. The 1 mM eluent behaves quite differently, the BSA peak area rising with each injection and gradually reaching a plateau corresponding to 85% of the peak area observed for the 10 and 20 mM eluents. Note that the 15-min delay between injections 9 and 10 is sufficient to cause a drop in peak area for the 1 mM eluent, followed by a gradual rise to a plateau level.

The trends observed for 1 mM SDS indicate that this eluent can be used, provided that care is taken to ensure that the plateau level of Figure 2 has been reached. In general, we have found that this requires only one or two injections for columns previously exposed to a series of model serum injections. In Figure 2, the differences in average peak area between the 1 mM eluent (at the plateau level observed for injections 15–18) and the peak areas in the other eluents are believed not to be significant. One possible explanation of the differences is that changes in the UV spectrum of serum albumin, which are known to occur upon denaturation (*22*), are present to different extents in the four eluent/column combinations. Tanford has shown that, in the subcritical micellar region, small changes in the concentration of the surfactant lead to significant changes in the number of molecules of SDS surfactant bound to a BSA molecule (*23*). This change may alter the spectroscopic properties of the protein and, hence, affect the observed UV response (peak area or peak height).

To study the 1 mM eluent more closely, a fresh μBondapak C_{18} cartridge/column was equilibrated with aqueous 1 mM SDS. Repeated 10-μL injections of model serum were made as before, and 2-mL fractions containing the entire BSA peak were collected. When seven peaks corresponding to the plateau level of peak area in Figure 2A were collected, the effort was ended. For comparison, the column was removed and three additional 2-mL fractions containing the BSA peak were collected. As blanks, 2-mL fractions of eluent were collected, both with and without the column in place.

UV absorbance at 280 nm was measured for all of the collected fractions, relative to the blanks. The seven with-column fractions had an average absorbance value of 0.134 (±3.3% RSD), compared to 0.129 (±0.4% RSD) for the without-column fractions. Thus, there is no evidence for loss of BSA on-column when the 1 mM SDS eluent is used, confirming the conclusion based on Bradford assay data. Apparently, the peak area differences of Figure 2A do not reflect mass recovery differences but, as discussed earlier, may reflect a change in UV absorbance (*22*, *23*).

The study was expanded to include a set of 15% (w/w) methanol-containing eluents, again at SDS concentrations of 1, 5, 10, and 20 mM and with four fresh μBondapak C_{18} cartridges from the same manufacturing batch. The peak area data are summarized in Figure 2B. Results for the 5, 10, and 20 mM eluents are similar to that of the 100% aqueous eluents. However, the 1 mM eluent rises more quickly to a plateau level, and the resulting maximum peak area is equal to that of the 10 and 20 mM SDS eluents. Overall, no unexpected change in BSA elution is observed above or below the CMC for the methanol-containing eluents.

Octanesulfonic acid (OSA) is commonly used at the 5–10 mM level in eluents for paired-ion chromatographic separations. This surfactant has a CMC of 136 mM (*24*) and is not generally used in micellar LC applications. By use of 5 mM OSA in water as the eluent, 10-μL injections of model serum were eluted quantitatively from a μBondapak C_{18} column. Quantitative elution was verified by the Bradford dye-binding assay. Unlike SDS, however, we were unable to use OSA in methanolic eluents (see below).

An eluent containing 1 mM SDS and 15% methanol was used in a preliminary test of capacity for protein loading. For this experiment, model serum was spiked with theophylline at two levels such that 20- and 200-μL injections of the resulting samples contained the same amount of theopylline (50

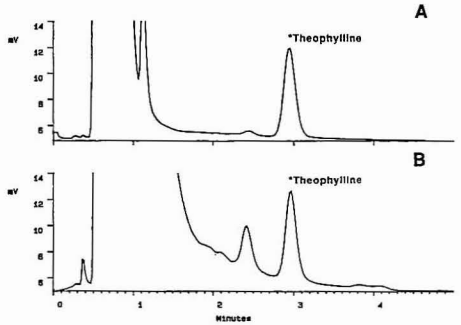

Figure 3. Elution of 50 ng of theophylline in the presence of BSA: (A) 20-μL injection of 50 mg/mL BSA solution spiked with theophylline; (B) 200-μL injection of the same solution spiked with 10× less theophylline per milliliter. Detection was at 254 nm.

Table I. Effect of Adsorbed Surfactant Amount of Elution of Bovine Serum Albumin[a] from μBondapak C_{18} Columns

% MeOH	1 mM SDS	5 mM OSA	5 mM OSA 10 mM phosphate
0	+ 64.6 mg[b]	+ 12.2 mg[c]	+ 21.6 mg[c]
10	+ 35.7 mg[b]	− 8.0 mg[c]	− 13.2 mg[c]
20	+ 19.3 mg[b]	−	NT
30	+	−	NT
40	+	−	NT
50	−	−	NT

[a] + = successful elution of BSA. − = nonelution or unstable elution of BSA. NT = not tested. [b] New steel column (0.39 × 15 cm). [c] New Radial PAK cartridge (0.8 × 10 cm).

ng) in the presence of 10-fold different levels of BSA. The resulting chromatograms (Figure 3) show that theophylline can be quantitated readily in either case, despite the substantial increase in the tailing of the BSA peak. The 200-μL injection of model serum, representing 10 mg of BSA, indicates the ability of eluents containing relatively low concentrations of SDS to successfully elute substantial quantities of protein at the column void volume.

Surfactant/Packing Interaction. Once initial experiments indicated that surfactant concentrations above *and* below the CMC are able to elute serum albumin, the influence of organic solvent on the surfactant/packing interaction was investigated. The influence of organic solvent on surfactant-containing systems such as those used in paired-ion chromatography (25) is well-known. One reason to limit the amount of organic solvent in eluents designed for direct serum injection might be the need to maintain an adequate coating of surfactant on the reverse-phase packing and thereby prevent protein adsorption. To determine whether a critical level of surfactant coating must be present in order to allow the quantitative elution of proteins, fresh columns were equilibrated with eluents containing SDS or OSA in the presence of various amounts of methanol. The eluents used are summarized in Table I. For each experiment, a fresh column was equilibrated with eluent until the signal from a differential refractometer indicated that surfactant was no longer being adsorbed onto the column packing. The calculated amount of adsorbed surfactant is indicated in Table I for each eluent and column.

As a critical test of the surfactant/packing contribution to the successful elution of BSA, 1 mM SDS was chosen as the

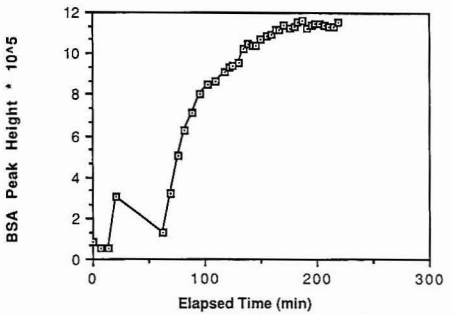

Figure 4. BSA peak height for sequential injections using an unsatisfactory eluent of 36/64 methanol/water (v/v) with 1 mM sodium pentadecyl sulfate.

concentration for the SDS-containing eluents of Table I. All peak heights and areas used for decision-making correspond to the stable plateau level illustrated in Figure 2. At higher SDS concentrations, the influence of methanol may be less significant than indicated in this study.

The eluents tested were deemed successful (i.e. potentially suitable for direct serum injection) if 10-μL injections of model serum gave quantitative and repeatable elution of serum albumin at the column void volume, regardless of the delay between injections. Eluents containing SDS were successful up to 40% (w/w) methanol, while those containing OSA were only effective in 100% aqueous eluents. The unsuccessful eluents listed in Table I were of two types. Some eluents (e.g. 5 mM OSA in 90% water/10% methanol, w/w) simply led to nonquantitative elution of BSA. Other eluents eluted BSA quantitatively only after exposure to continuous injections of model serum. Figure 4 provides an example of this unsuccessful elution behavior. This behavior is much more dramatic than the behavior observed in Figure 2A for the 1 mM SDS eluent. In Figure 4, BSA peak height is plotted as a function of time. Injections of model serum were made every 7 min, except during the gap between the fourth and fifth injection. During the first four injections, BSA peak height increased, and an additional equilibration time was allowed on the assumption that the column had not reached equilibration. After the delay, the BSA peak height was much lower than before. As additional injections were made, BSA peak height finally leveled. However, stopping the injection sequence at any point caused a drop in the peak height for BSA. The reason for this phenomenon is unclear at this time. However, the observed behavior may reflect the formation of a relatively tenuous protein coating on the stationary phase which can be removed from the column by washing with the eluent. For purposes of the present study, it was sufficient to avoid these unstable systems.

For the SDS-containing eluents of Table I, Figure 5 compares the adsorbed amount of SDS and the BSA peak height obtained for eluents of various methanol contents and 1 mM SDS. In this figure, the peak heights indicate quantitative elution of BSA for eluents containing as much as 40% (w/w) methanol. At this same methanol composition, the SDS coating level has dropped very nearly to zero. This is consistent with the hypothesis that a certain level of adsorbed surfactant is required for direct serum injection. However, the OSA results complicate the picture.

For the OSA-containing eluents in Table I, there were no successes in the presence of 10% methanol. It was assumed initially that this might be due to the 34% reduction of the OSA coating level caused by the use of 10% methanol. To test this, 10 mM K_2HPO_4 was included in a 5 mM OSA eluent.

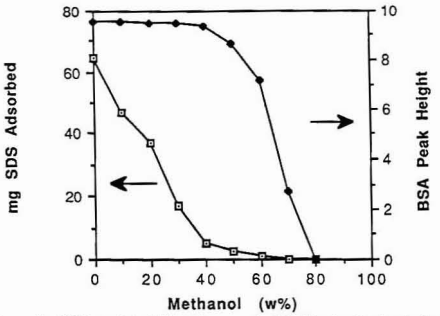

Figure 5. BSA peak height and amount of SDS adsorbed onto fresh μBondapak C_{18} columns (steel, 0.39 × 15 cm) as a function of methanol composition. All eluents contained 1 mM SDS. See text for discussion.

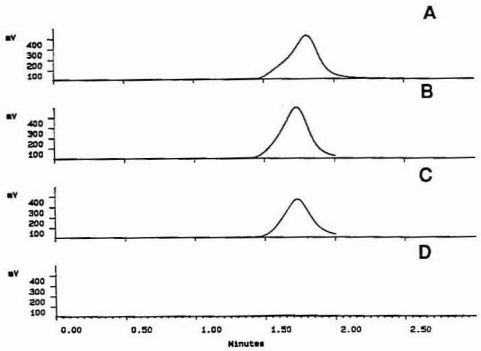

Figure 6. Elution of BSA from Protein-Pak SP-5PW column. All eluents contained 1 mM SDS and (A) 0% methanol, (B) 20% methanol, (C) 40% methanol, and (D) 50% methanol. Detection was at 280 nm.

The presence of salt increases the adsorption of OSA to the C_{18} packing, as reflected in Table I. With 10 mM potassium phosphate present, a coating level of 13.2 mg of OSA/column was obtained in the 10% methanol eluent. This is a higher adsorbed amount than was obtained for OSA in the 100% aqueous eluent which successfully eluted BSA. Nonetheless, BSA was not quantitatively eluted from the 10 mM phosphate/10% methanol system. This suggests that the adsorbed amount of surfactant is only partly responsible for the successful elution of serum albumin.

For 1 mM SDS eluents, a methanol content of 40% (w/w) or less appears to be the maximum level compatible with direct serum injection. Some additional organic modifiers were briefly explored. 2-Propanol up to 40% (w/w) was found to quantitatively elute BSA from model serum at an SDS concentration of 1 mM. Acetonitrile was used successfully at the 10% level, but this modifier has not yet been evaluated at higher concentrations.

Surfactant/Protein Interaction. The reason for the 40% upper limit on methanol or 2-propanol content was explored further by changing the column packing to one that does not absorb SDS when the eluents of Table I are used. In this way, the importance of the surfactant/protein interaction can be evaluated independently of the surfactant/packing interaction. In place of the μBondapak C_{18} column, a Protein-Pak SP-5PW column was used. This weak cation exchanger has a bonded sulfopropyl phase that was expected to have little affinity for SDS. This was verified by breakthough experiments, which indicated no adsorption of SDS from the eluents of Table I.

For eluents containing 1 mM SDS and 0–50% (w/w) methanol, chromatograms resulting from the injection of model serum are presented in Figure 6. At 0% and 20% methanol (top two chromatograms), the influence of methanol is only on the peak shape. BSA is quantitatively eluted at the void volume in both cases. For the 40% eluent (third chromatogram), the peak area is reduced to 72% of that seen at lower methanol concentrations. When the percentage of methanol is increased to 50, BSA is not eluted from the column. However, a later switch to an aqueous SDS-containing eluent successfully eluted the adsorbed protein. The nonelution is not believed to be the result of solubility considerations, as solution experiments showed that BSA could be dissolved at a concentration of 50 mg/mL in the presence of up to 80% methanol.

The combination of Figures 5 and 6 and Table I suggests that surfactant/protein interactions are critical for the successful elution of serum proteins in direct serum injection applications. The chromatographic packing must also be coated with surfactant, but manipulation of the coating level (e.g. by addition of salt) cannot guarantee elution of protein if eluent conditions are unfavorable for protein/surfactant interactions. It is interesting to note that the loss of binding of SDS, both to protein and to the C_{18} stationary phase occur at approximately 40% (w/w) methanol. This may be coincidental or may be related to similar effects of hydrophobicity in each situation.

Surfactant concentration can be above or below the CMC, but some limitations on the use of organic solvents as eluent additives for direct serum injection are required. These limitations are not based on considerations of micelle stability but rather upon the need to favor surfactant/protein as well as surfactant/packing interactions. For the example discussed here, SDS interactions with both the protein and the C_{18} bonded phase appears to be too limited in salt-free eluents containing more than 40% methanol to allow direct serum injection.

Effect of pH, Salts, and Packing Type. For most protein separations by LC, the eluent pH is adjusted to safely avoid the isoelectric point (p*I*), due to the limited solubility of proteins at this pH value. For SDS-containing eluents which successfully elute BSA, it is expected that this requirement can be eliminated because of the charge (and solubility) imparted to the protein through its interaction with SDS. This was verified experimentally for the 15% methanol/1 mM SDS eluent, which was modified to contain a 0.1 M phosphate buffer. Peak height, peak area, and retention time for BSA were constant at pH values from 4.5 to 9.5, a range which includes the p*I* of 5.6 for BSA.

The presence of salts can influence the interaction of surfactant with both packing and protein. However, the only salt-related limitation we have thus far observed relates to surfactant solubility. Certain combinations of salt, SDS, and methanol lead to immediate precipitation. Notably problematic are potassium phosphate salts, which we could not use at any concentration. Sodium phosphate salts were soluble up to at least 100 mM in eluents containing 1 mM SDS and up to 50% methanol.

The selectivity differences offered by changing the packing type are in line with expectations based on other reverse-phase LC modes such as paired-ion chromatography (*25*). For example, a change from a C_{18} to a phenyl bonded phase or even from one type of C_{18} phase to another can produce substantial changes in peak spacing of several xanthines. We have not encountered any limitations in the reverse-phase packings that can be used with the eluents described in this report. Even unbonded silica (*26*) can be used successfully with surfactant-containing reverse-phase eluents.

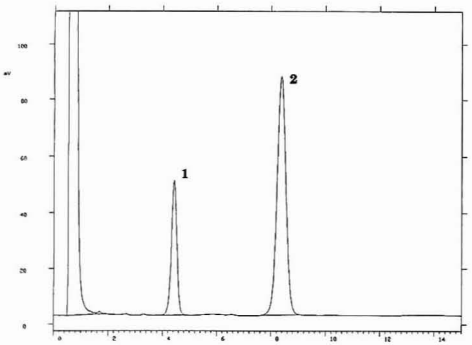

Figure 7. Analyses of (1) carbamazepine 10,11-epoxide and (2) carbamazepine from model serum. Conditions: column, Nova-Pak Phenyl (steel 0.39 × 7.5 cm); eluent, methanol/water 35/25 (w/w) with 1 mM SDS; detection, at 254 nm.

Use of Other Surfactants. The physiological function of serum albumin includes the transport of fatty acids and lipids, so it is not surprising that anionic surfactants such as SDS and OSA are able to solubilize serum albumin in aqueous eluents. In the presence of methanol, however, OSA cannot be used for direct serum injection. We have also evaluated decyl sulfate and pentadecyl sulfate, but found neither of these to quantitatively elute BSA when methanol was present in the eluents. In fact, sodium pentadecyl sulfate had limited solubility in eluents containing less than 30% methanol and was, therefore, not of general utility. We tested one nondenaturing anionic surfactant, sodium desoxycholate, and found that a 1 mM aqueous solution was able to successfully elute BSA from model serum injections. The CMC for sodium desoxycholate is approximately 5 mM.

We have also had some success in working with nonionic and zwitterionic surfactants. These "zero net charge" surfactants are generally classified as nondenaturing and are thought to have a much gentler interaction with BSA than SDS (*19*). The zwitterionic surfactant CHAPS (3-[(3-cholamidopropyl)dimethylammonio]propanesulfonate) was successfully used in a 1 mM aqueous eluent, well below its CMC of 8 mM. In agreement with previous reports (*13*), we found that aqueous eluents containing Brij-35 at concentrations above the CMC were able to elute BSA. Two nonionic surfactants, Nonidet P40 and Brij-35, were not suitable for the elution of BSA from model serum when used at or below the CMC. Additionally, many workers have reported that cationic surfactants are unable to solubilize serum albumin, and our work with cetyltrimethylammonium bromide (CTAB) confirmed this finding.

Analysis of Drugs from Model Serum. Since the role of several eluent variables had already been explored, the next step was to determine whether a standard reverse-phase column would withstand hundreds of injections of model serum. Carbamazepine analysis was selected as a typical application, since HPLC is the current method of choice for the quantitation of this drug and its epoxide metabolite from serum in clinical laboratories. Because its therapeutically useful range is very narrow, the proper administration of carbamazepine requires routine monitoring of serum levels. Presently used sample preparation based on semiautomated solid-phase extraction is labor intensive, and the time savings which could be provided by direct serum injection is therefore of great interest (*27*).

The separation of carbamazepine and its epoxide from model serum is shown in Figure 7. The analysis time of less than 9 min is acceptable for clinical usage, and the retention

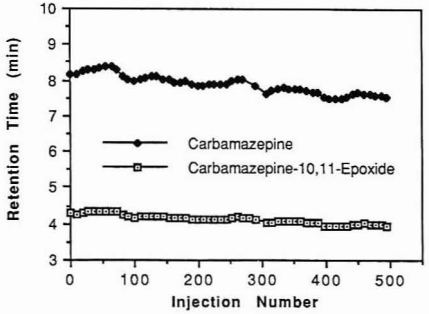

Figure 8. Retention time stability for carbamazepine and its 10,11-epoxide over the course of 500 injections of spiked model serum. See text for details.

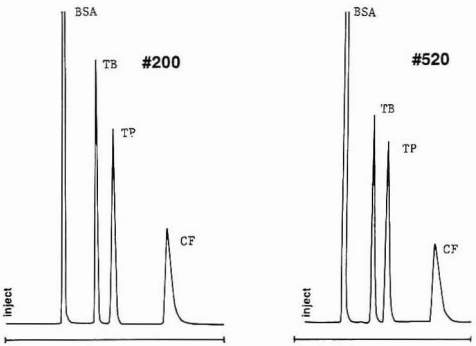

Figure 9. Example chromatograms for the xanthine mixture selected from 520 injections of spiked model serum. Conditions: column, μBondapak C_{18} (3.9 × 150 mm); mobile phase, 15/85 ((w/w) methanol/water + 1 mM SDS; flow rate, 1.0 mL/min; detection, 280 nm. Compounds were theophylline (TP), theobromine (TB), and caffeine (CF) each at 0.1 mg/mL in a solution of bovine serum albumin (BSA) at 50 mg/mL. Injection volume was 20 μL. See text for additional details.

of the earlier eluting component has been adjusted to allow adequate separation from the protein peak. To test the suitability of this separation for routine use a column lifetime study was conducted with model serum spiked with carbamazepine (5 μg/mL) and its epoxide (25 μg/mL). Over the course of 500 sequential 10-μL injections on a single column, retention time stability was excellent (Figure 8). As a precaution an in-line filter containing a 2-μm frit was installed and changed periodically, but no unusual pressure problems were encountered.

As a second application, several xanthines were separated and quantitated from spiked model serum. The 200th and 520th separation of this mixture are shown in Figure 9. It was necessary to change the in-line filter frit only twice during the 520 injections on this column. As Figure 9 indicates, peaks broadened somewhat during the study so peak areas were preferred for quantitation.

The results presented here demonstrate that a broader than expected range of surfactant and organic solvent compositions can be used in eluents designed for direct serum injections. Since all of the results presented are for model serum, verification with animals and human serum is still required. This work is ongoing in our laboratory and in a collaborating clinical laboratory, and results to date support the findings for model serum (*28*). Specifically, the analysis of carbamazepine and its epoxide is possible at clinical levels with direct sample injection using surfactant-containing eluents both in a sin-

gle-column approach (29) and in a column-switching approach (30).

ACKNOWLEDGMENT

We thank L. Bowers and P. Froehlich for helpful discussions and perspective, as well as C. Galgano and J. Newman for their assistance with the preparation of the manuscript.

LITERATURE CITED

(1) McDowall, R. D.; Pearce, J. D. In *Developments in Analytical Methods in Pharmaceutical, Biomedical, and Forensic Sciences*; Piemente, G., Ed.; Plenum: New York, 1987; pp 217–225.
(2) Roth, W.; Besche, K.; Jauch, R.; Zinner, A.; Ross, F. W. *J. Chromatogr.* **1981**, *222*, 13.
(3) Westerlund, D. *Chromatographia* **1987**, *24*, 155.
(4) Hagestam, I. H.; Pinkerton, T. C. *Anal. Chem.* **1985**, *57*, 1759.
(5) Wong, S. H. Y.; Butts L. A.; Larson, A. C. *J. Liq. Chromatogr.* **1988**, *11*, 2039.
(6) Pinkerton, P. C.; Miller, T. D.; Cook, S. E.; Perry, J. A.; Ratcike, J. D.; Szczerba, T. J. *Biochromatography* **1986**, *1*, 96.
(7) Gisch, D. J.; Hunter, B. T.; Feibush, B. J. *J. Chromatogr.* **1988**, *433*, 264.
(8) Meriluoto, J.; Bjorklund, H. *LC-GC* **1989**, *7*, 738.
(9) Yoshida, H.; Morita, I.; Tamai, G.; Masujima, T.; Tsuru, T.; Takai, N.; Imai, H. *Chromatographia* **1984**, *19*, 466.
(10) Adamovics, J. A. *J. Pharm. Biomed. Anal.* **1987**, *5*, 267.
(11) Weinberger, M.; Chidsey, C. *Clin. Chem.* **1975**, *21*, 834.
(12) Bui, R. H.; French, S. B. *J. Liq. Chromatogr.* **1989**, *12*, 861.
(13) Cline Love, L. J.; Zibas, S.; Noroski, J.; Arunyanart, M. *J. Pharm. Biomed. Anal.* **1985**, *3*, 511.
(14) Cline Love, L. J.; Arunyanart, M. *J. Chromatogr.* **1985**, *342*, 293.
(15) Sentell, K. B.; Clos, J. F.; Dorsey, J. G. *BioChromatography* **1989**, *4*, 35.
(16) Dorsey, J. G. *Adv. Chromatogr.* **1987**, *27*, 167.
(17) Bidlingmeyer, B. A.; Warren, F. V. *Anal. Chem.* **1982**, *54*, 2351.
(18) Montelaro, R. C.; West, M.; Issel, C. J. *Anal. Biochem.* **1981**, *114*, 398.
(19) Buckley, J. J.; Wetlaufer, D. B. *J. Chromatogr.* **1989**, *464*, 61.
(20) Scopes, R. *Protein Purification: Principles and Practice*; Springer-Verlag: New York, 1982.
(21) Bidlingmeyer, B. A.; Warren, F. V.; Grohs, R. A., U.S. Patent Appl. 364,057, June 1989.
(22) Lehninger, A. L. *Biochemistry*; Worth: New York, 1977; p 831.
(23) Tanford, C. *The Hydrophobic Effect: Formation of Micelles and Biological Membranes*; Wiley-Interscience: New York, 1980; pp 150–152.
(24) Hinze, W. L. In *Ordered Media in Chemical Separations*; Hinze, W. L., Armstrong, D. W., Eds.; ACS Symposium Series No. 342; American Chemical Society: Washington, DC, 1987; Chapter 1.
(25) Bidlingmeyer, B. A. *J. Chromatogr. Sci.* **1980**, *18*, 525.
(26) Bidlingmeyer, B. A.; Del Rios, J. K.; Korpi, J. *Anal. Chem.* **1982**, *54*, 442.
(27) Bowers, L. Personal communication.
(28) Bentrop, D.; Warren, F. V.; Schmitz, S.; Bidlingmeyer, B. A. A Generalized Liquid Chromatographic Approach to the Analysis of Drugs from Serum Using Direct Injection Techniques with Surfactant Containing Eluents. Presented at HPLC 1990 Conference, Boston, MA, May 21–25, 1990.
(29) Bentrop, D.; Warren, F. V.; Schmitz, S.; Bidlingmeyer, B. A. *J. Chromatogr.* **1990**, *535*, 293.
(30) Schmitz, S.; Warren, F. V.; Bidlingmeyer, B. A. Unpublished results.

RECEIVED for review December 27, 1989. Revised manuscript received June 25, 1990. Accepted October 9, 1990.

High-Repetition-Rate Laser Ablation for Elemental Analysis in an Inductively Coupled Plasma with Acoustic Wave Normalization

Ho-ming Pang, Daniel R. Wiederin, R. S. Houk, and Edward S. Yeung*

Ames Laboratory—U.S. Department of Energy and Department of Chemistry, Iowa State University, Ames, Iowa 50011

A laser ablation system with 100-Hz repetition rate for direct elemental analysis of solids by inductively coupled plasma atomic emission spectrometry (ICP-AES) and inductively coupled plasma mass spectrometry (ICP-MS) is described. Detection limits of 12 μg/g and 4 ng/g for ICP-AES and ICP-MS, respectively, are observed. These improvements are attributed to the use of low vaporization laser powers (50 mJ), which may produce a more uniform and finer spray. Precision is improved by a factor of 2 or more by averaging over a larger number of laser pulses within the same measurement and by normalizing the emission signal to the amplitude of the acoustic wave generated during the ablation process.

INTRODUCTION

Inductively coupled plasma atomic emission spectrometry (ICP-AES) and inductively coupled plasma mass spectrometry (ICP-MS) have been widely used as rapid and sensitive techniques for trace elemental analysis. The use of laser ablation to introduce solid samples into the carrier gas flow of the ICP is very attractive because of minimal sample preparation and efficient atomization of the solid sample surface regardless of the sample conductivity. In these experiments, either a high-energy (1-J) single-pulse ruby laser (*1–3*) or a medium-energy (~100-mJ) low-repetition-rate (10–20-Hz) Nd:YAG laser (*4*, *5*) was used to ablate the samples. Due to sample inhomogeneity and pulse-to-pulse laser power fluctuations, poor measurement precision has been observed for single-pulse laser experiments. In addition, the formation of large particles reduces sample transfer and atomization efficiency. Also, large particles likely cause fluctuations and optical heterogeneity in emission signal as has been observed during nebulization of solutions (*6–8*). Even with lasers with high enough repetition rate to generate a "steady-state" signal, an internal standard is usually required in order to obtain reasonable precision. A continuous wave (cw) Nd:YAG laser has been used to ablate powdered solid samples with good precision and reasonable sensitivity for ICP-AES analysis (*9*). However, due to the low laser power density (10^4 W/cm^2), metallic targets cannot be vaporized. A higher repetition rate (40-Hz) excimer laser was used to ablate sample into ICP (*10*); no precision measurement was reported.

In an attempt to improve the measurement precision and sensitivity, a high-repetition-rate (100-Hz) laser ablation system with moderate laser energy (50 mJ) is employed here. Lower laser energy at similar pulse duration may generate smaller particles (*11*), thus improving atomization efficiency, sample transfer efficiency (*5*), and precision. Another approach for improving precision is to measure the amount of material ablated by an independent means. For example, if

0003-2700/91/0363-0390$02.50/0

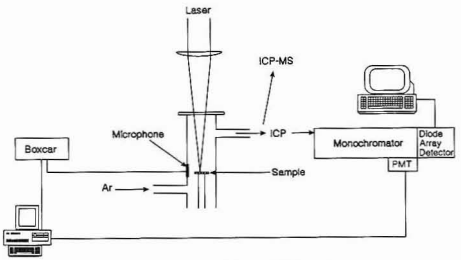

Figure 1. Schematic diagram of laser ICP systems.

the sample is truly homogeneous, the emission line of an internal standard can be used to correct for variations in the analytical signal (*12*).

The ablation process also creates acoustic (pressure) waves in the sample cell. We have previously demonstrated that the amplitude of this acoustic signal is proportional to the total amount of material vaporized for each laser pulse. This acoustic measurement has been used as an internal standard to normalize the atomic emission signal (*13*) or laser-enhanced ionization signal (*14*) from the laser-generated plume. In this report, the acoustic signal is used to normalize the ICP emission signal to minimize contributions from laser power fluctuations and effects due to the changing surface properties.

EXPERIMENTAL SECTION

An XeCl pulsed excimer laser (Lumonics, Ottawa, Canada, Model HyperEX 460) operated at 308 nm was used for solid sample ablation. This laser provided up to 70 mJ per pulse at 100-Hz repetition rate with a pulse width of 25 ns. The ultraviolet (UV) laser light was reflected 90° downward onto the sample and focused into a ~1-mm-diameter spot on the sample surface with an 8-cm focal length lens. The estimated laser peak power density was on the order of 1×10^8 W/cm^2 at repetition rates of 10–100 Hz, with a specified amplitude stability of ±5% (peak-to-peak).

NIST standard samples (C1150a cast steel, 1222 low-allow steel, and 1258 aluminum alloy) were cut into 5-mm × 5-mm × 1-mm square plates and cleaned with methanol prior to use. The sample was rotated at 1 rpm in order to minimize degradation of the surface after prolonged laser ablation. The center of the laser struck the sample at a position 2 mm from the axis of rotation. The Pyrex ablation cell (volume ~ 20 cm^3) is shown in Figure 1. This cell was mounted onto an aluminum base with an O-ring seal. The top of the cell was closed by a quartz plate (1.6 mm thick) for UV light transmission. Tygon tubing (4-mm i.d., 130 cm long) was used to connect the sample cell to the ICP torch for emission measurements. For ICP-MS experiments, a 7.6-m length of Tygon tubing was used due to restrictions on equipment location.

Typical operating conditions for ICP-AES and ICP-MS are listed in Table I. Most of the operating conditions for the ICP were essentially the same as those used during conventional nebulization of solutions and were not optimized during actual laser ablation. For experiments with the photodiode array detector, a normal aerosol gas flow rate (1.0 L/min) was used. For time-resolved experiments with the photomultiplier and acoustic measurement, the aerosol gas flow rate was increased to 3.0 L/min, for reasons described in the next section.

The detection limit was evaluated as the analyte concentration necessary to yield a net signal equivalent to 3 times the standard deviation of the background. The background and background noise were evaluated at the wavelength or m/z of interest with the plasma on but the laser off.

A microphone (Knowles Electronics, Model BA-1501) was attached at the middle of the sample cell wall to observe the acoustic wave generated from the laser ablation process. The height of the first acoustic peak was monitored as a function of time with a boxcar averager and gated integrator (EG&G, Model 162 boxcar averager and Model 164 gated integrator). An effective time constant of 0.5 s was used to achieve a reasonable signal-to-noise ratio (S/N) and response time. The signal from the photomultiplier tube (PMT) was amplified by a Keithley 485 autoranging picoammeter with a time constant of 0.06 s. An IBM PC/AT computer was used to record and process the PMT signal from the ICP emission and the averaged acoustic signal from the boxcar simultaneously.

Table I. Apparatus and Operating Conditions

	ICP-AES
monochromator (*15*)	McPherson M2051, 1-m focal length, holographic grating, 3600 grooves/mm, entrance slit width = 20 μm
ICP generator	Plasma-Therm HFS 5000D, 27.12 MHz, 1100 W forward power
torch	Fassel type (*16*)
AR flow rate	
outer	16 L/min
auxiliary	0.4 L/min
aerosol carrier	(A) 1.0 L/min for photodiode array detection (B) 3.0 L/min for PMT detection with acoustic normalization
observation height	20 and 15 mm above load coil for emission spectroscopy and mass spectrometry, respectively
detector	(A) Princeton Applied Research, Model 1453 photodiode array, 1024 elements, unintensified, cooled to −15 °C; Model 1461 detector interface linked to DEC 11/34 computer; this covers approximately a 5.3-nm wavelength region; total signal accumulation time for each measurement, 3 s (B) ENI-Gencom PMT RFI/B-289F; Keithley 485 autoranging picoammeter
	ICP-MS
spectrometer	Perkin-Elmer Sciex Elan-500, 1250-W forward power
Ar flow rate	
outer	12 L/min
auxiliary	0.2 L/min
aerosol carrier	1.5 L/min
sampling position	20 mm above load coil
measurement	scanning mode; 0.1-s measurement time, 10 measurement/mass unit over m/z 4–240 range peak hopping mode; 0.2-s measurement time, 20-ms dwell time for m/z 58, 60, 61, 62

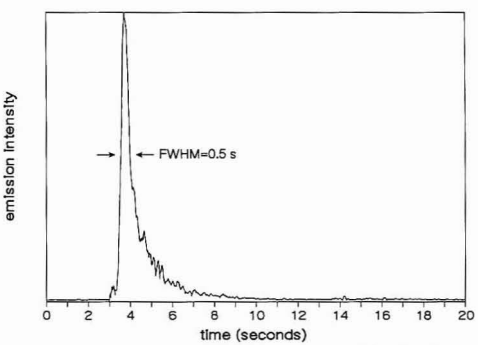

Figure 2. Transient signal response of Cu I emission (324.75 nm) after ablation of a NIST cast steel sample (C1150a) by a single laser pulse. The laser was fired at time zero.

RESULTS AND DISCUSSION

Response to Single Laser Shot. The transient signal obtained with a single laser pulse of 70 mJ when the Cu emission line at 324.75 nm was monitored by a PMT detector

Table II. Dependence of Emission Line Intensity on the Laser Repetition Rates[a]

rep rate, Hz	Fe I 322.58 nm	Ti II 323.45 nm	Cu I 324.75 nm	V II 326.77 nm
10	3600	790	1300	60
50	20000	4500	7700	460
100	38000	9200	14000	860

[a] 3-s integration time.

is shown in Figure 2. The sample was cast steel that contained 0.2% Cu. The emission signal rose to a maximum after the laser pulse and decayed with a full width at half-maximum (FWHM) of 0.5 s. The delayed response and the tailing shown in Figure 2 are due to the dead volume of the cell and transfer tubing, which totals roughly 90 cm^3. This transient response is sufficiently long to produce a steady-state signal if a high-repetition-rate laser is used.

Emission Spectra. Figure 3 shows a typical emission spectrum of a C1550a steel sample obtained with a 3-s exposure time from a single 1024 diode array detector centered around 325 nm. The laser was operated at 100 Hz, and the steel sample contained 0.2% Cu, 0.04% Ti, and 0.04% V. The Ti, Cu, and V elemental emission lines have been marked in Figure 3. The remaining lines were mainly from Fe. The sensitivity of the emission measurement increased as the repetition rate increased (as listed in Table II). As expected, more sample was ablated and transported to the ICP per unit time at the higher repetition rates. A S/N of ~5 was observed for Ti II 323.452 nm from a different low alloy steel (NIST 1222), which contained 20 ppm Ti (100-Hz repetition rate). The ablation rate was estimated by measuring the mass change of the sample over a 4-min period; each laser pulse removed ~30 ng of sample. Therefore, the absolute detection limit and concentration detection limit for Ti in this steel sample were ~100 pg and ~12 $\mu g/g$, respectively, at S/N of 3 and a measurement time of 3 s. This estimate indicates that detection limits of high-repetition-rate and moderated laser powers are comparable to or better than those from low-repetition-rate and high laser powers (*2, 3, 6, 12*).

More importantly, the measurement precision was improved with the use of high repetition rates, as listed in Table III. These statistic data are based on eight replicate 3-s integration measurements with background correction. The same NBS steel sample (C1150a) was used throughout. A 10-Hz repetition rate was used first, followed by 50-Hz and 100-Hz repetition rates; then the same sequence was repeated again. As the sample rotation under the laser, an annular depression was formed on the surface with ~0.7-mm width and ~300-μm depth. Therefore, the surface degraded more and more as the experiment progressed. In addition, each laser pulse created a crater with deposition around the rim. Subsequent laser shots irradiated this area as the sample was rotated further. This crater rim may cause signal fluctuations as a result of the change in the laser focusing conditions and surface physical

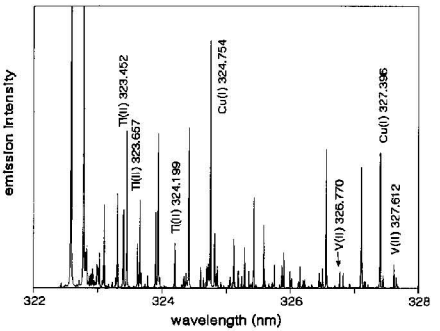

Figure 3. Net emission spectrum of NIST cast steel sample (C1150a) obtained with the use of a 100-Hz repetition rate excimer laser and with the sample rotated at 1 rpm. The total accumulation time was 3 s. The sample contains 0.04% Ti, 0.2% Cu, and 0.04% V. The horizontal axis corresponds to an intensity of zero.

properties. Nevertheless, from Table III, it is clear that the precision for the major and trace elements is improved with the use of high repetition rates even when the surface was severely damaged toward the end of the experiments. With giant laser pulses (>10^{10} W/cm^2) and low repetition rates, a large relative standard deviation (RSD 10–20%) (*1, 17, 18*) for the measurements was observed. However, the use of high repetition rate laser here improves the precision without sacrificing the sensitivity.

There exist several reasons for the improvement in precision. The moderate laser power and shorter wavelength may generate finer particles than the higher power (100–500 mJ/pulse) Nd:YAG lasers commonly use. Further, the redeposition on the crater rim was minimized because of better atomization. The formation of small size particles certainly will increase the sample transfer efficiency and minimize spiking due to the introduction of discrete large particles into the ICP. The use of high repetition rates compensates for the low powers used so that the total amount of material sent to the ICP per second did not change significantly compared with the high-power, low-repetition-rate laser experiments. Also, signals from more vaporization events were averaged to improve the statistics. The fact that the precision was still at an acceptable level for rough surfaces (i.e., the second set of results in Table III) is important for applications in which the surface properties cannot be easily controlled. When Fe I 322.58 nm was used as the internal standard line, a RSD <2% can be obtained for the determination of Cu and V. An internal standard can account for the noise attributed to the ICP, the vaporization events, and the sample transfer process. Naturally, an elemental internal standard can only be used for homogeneous samples.

Mass Spectra. Figure 4 shows the ICP-MS spectrum of Al alloy after background correction. All certified trace elements have been observed and identified (note the logarithmic

Table III. Dependence of Precision (RSD) on Laser Repetition Rates for Six Consecutive Runs

	Fe I 322.58 nm	Ti II 323.45 nm	Cu I 324.75 nm	Cu I 327.4 nm	V II 326.77 nm
1, 10 Hz	7.2	18.1 (12.9)[a]	7.6 (2.1)	7.0 (4.5)	7.4 (4.9)
2, 50 Hz	4.0	14.9 (14.8)	2.5 (2.8)	3.0 (1.8)	4.2 (1.9)
3, 100 Hz	3.3	8.1 (6.2)	3.6 (2.0)	3.7 (1.6)	3.4 (1.2)
4, 10 Hz	11.0	23.0 (17.7)	13.9 (4.9)	12.4 (4.2)	13.4 (9.3)
5, 50 Hz	10.0	14.9 (11.0)	12.4 (3.4)	10.9 (2.1)	11.2 (1.9)
6, 100 Hz	10.6	11.5 (16.4)	10.1 (1.8)	9.7 (1.5)	10.4 (2.0)

[a] The numbers in parentheses refer to the RSDs in percent of the normalized intensities using Fe I 322.58 nm as the internal standard. Statistics are based on eight replicate 3-s measurements.

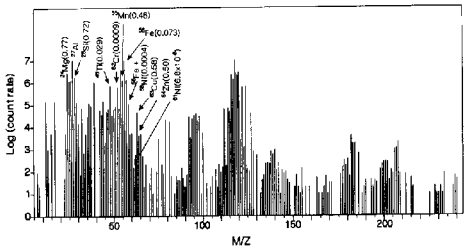

Figure 4. Mass spectrum (background subtracted) of NIST aluminum alloy (1258) obtained with the use of a 100-Hz repetition rate excimer laser and with the sample rotated at 1 rpm. The total scan time was approximately 4 min. The numbers in parentheses refer to elemental composition in weight percent.

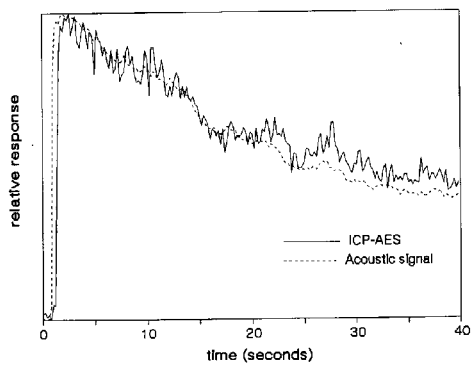

Figure 5. Temporal profile of Cu I emission (324.75 nm) and acoustic signal obtained with the use of a 100-Hz repetition rate laser irradiating a fixed spot on the sample surface at a power density of 1×10^8 W/cm^2. Sample is NIST C1150a cast steel that contains 0.2% Cu. The aerosol gas flow rate was 3 L/min for this and subsequent figures.

intensity scale). The detection limit was determined from the count rate for minor isotopes such as ^{61}Ni. The background Ni signal generated from the skimmer was negligible. Since this sample contained 6 ppm total Ni, the concentration of ^{61}Ni was ~0.07 ppm. In Figure 4, the signal-to-noise ratio for ^{61}Ni was about 40. The detection limit was ~4 ppb at $S/N = 3$. A similar detection limit (~3 ppb) was estimated for ^{53}Cr, since the signal from 1 ppm ^{53}Cr has S/N of ~1300. The absolute detection limit for both elements (3 μg of total material vaporized/s) was ~10 fg. These detection limits are comparable to or slightly better than those obtained from other laser ablation ICP-MS experiments with the use of high laser powers (*1*, *4*, *17*).

Acoustic Wave Normalization. Figure 5 shows the ICP emission signal and acoustic wave measurement when the laser irradiated the same surface area for 40 s at 100 Hz. A PMT was used to monitor the Cu emission (324.75 nm) throughout the entire experiment. The acoustic wave was produced by the expansion of the microplasma formed from ablated material above the sample surface. The amplitude of the acoustic wave depends primarily on two factors: (a) the distance between the ablation position and the microphone, and (b) the gas pressure in the cell. The acoustic wave is not very sensitive to sample size, shape, or the method for mounting the sample. Both signals decreased due to crater formation and the change in focusing conditions after a prolonged exposure. However, the acoustic wave intensity and emission signal showed a similar trend. Thus, the acoustic wave reflects the total amount of material ablated by each laser pulse and accounts for fluctuations in emission signal caused by crater formation

Table IV. Measurement Precision (RSD) of Cu Emission (324.75 nm) Obtained at 100-Hz Repetition Rate at a Fixed Spot[a]

	RSD, %	
trial	before acoustic normalization	after acoustic normalization
1	23.5	6.3
2	24.1	15.2
3	19.9	9.8

[a] Statistics based on 33 replicate measurements with 1-s integration time for each trial. After each trial, a new sample surface was used. The steel sample C1150a contains 0.2% Cu.

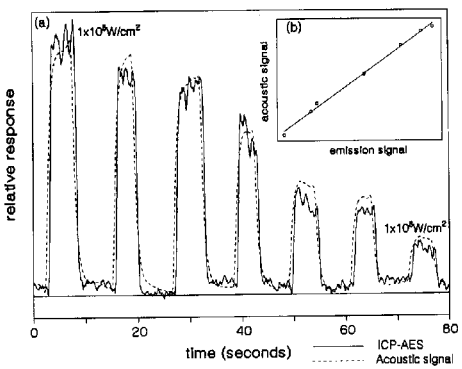

Figure 6. (a) Power dependence of Cu emission (324.75 nm) and acoustic signal obtained with the use of a 100-Hz repetition rate laser at power densities from 1×10^8 to 1×10^6 W/cm^2 with increments of 1.6×10^7 W/cm^2 per run. (b) Acoustic signal versus emission intensity plot with 3-s signal averaging at different laser power densities. The sample is the same as in Figure 5 except with a rotation speed of 1 rpm.

and changes of focusing conditions.

It should be noted that there is a 3-s delay between the emission signal and the acoustic signal in Figure 2. This delay corresponded to the time required for the ablated material to reach the ICP. This delay time can broaden the individual sample pulses (*2*, *19*). As a result, the emission intensity and acoustic wave were not correlated perfectly. In order to minimize this delay for a better correlation, the Ar carrier flow rate was increased to 3 L/min so that the delay time was reduced to less than 1 s. However, the emission intensity became lower and noisier since the operating conditions for the ICP were not optimized. Even with the signal fluctuations in Figure 5, the acoustic wave can still be used to normalize this emission signal to substantially improve the measurement precision, as indicated by the results shown in Table IV. Figure 5 also shows that the acoustic signal follows the slow drift (5–10 s) in the emission signal but not the sharp spikes (duration < 1 s). This is a direct result of the different time constants used in obtaining the two signals.

Figure 6a shows the ICP emission signal and acoustic wave measurement at different laser powers when the sample was rotated. The laser beam was blocked between power settings. The laser power density was varied from $\sim 1 \times 10^8$ to 1×10^6 W/cm^2. The signals from emission and acoustic wave have been normalized to the same scale for comparison. The acoustic signal decayed more slowly than the emission signal because of the use of different time constants. A linear relationship between the acoustic signal and the emission signal was observed ($R^2 = 0.9958$), as shown in Figure 6b. Thus, the acoustic wave measurement can be used to correct for fluc-

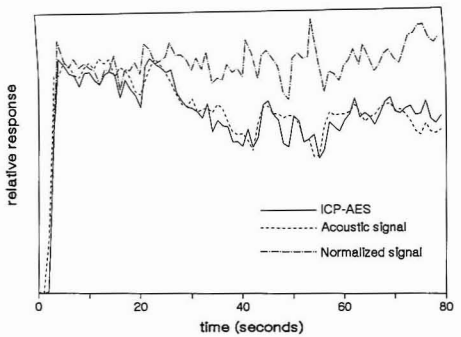

Figure 7. Temporal profile of Cu emission (324.75 nm), acoustic signal, and normalized emission signal obtained with the use of a 100-Hz, 1 × 10^8 W/cm^2 laser. The sample is the same as described in Figure 5 except with a rotation speed of 1 rpm. A time constant of 2 s was used for acoustic wave measurements.

Table V. Measurement Precision (RSD) of Cu Emission (324.75 nm) Obtained at 100-Hz Repetition Rate on a Rotating Sample (1 rpm)[a]

	RSD, %	
trial	before acoustic normalization	after acoustic normalization
1	13.6	10.6
2	12.5	9.6
3	10.5	7.1
4	11.7	7.5
5	13.6	6.6
6	11.3	9.3
av	12.2	8.5

[a] Statistics based on 75 replicate measurements of 1-s integration for each trial. The steel sample C1150a contains 0.2% Cu.

tuations in the amounts of material ablated due to changes in laser power. Acoustic normalization should also correct for changes in laser power delivered to the sample caused by deposition of previously ablated material on the cell window.

Figure 7 shows the ICP emission signal, acoustic signal, and the normalized ICP emission signal at 100-Hz repetition rate with the sample rotated at 1 rpm. Table V lists the measurement precision before and after acoustic wave normalization for six consecutive analyses of the same sample. These results indicate that acoustic wave normalization can improve emission measurement precision. The relatively poor precision found in Tables IV and V compared to the best results obtained from photodiode array detection (Table III) was probably due to the different integration periods and nonoptimized ICP operating conditions.

CONCLUSION

The use of high-repetition-rate lasers for ablating solid samples can improve the measurement precision and sensitivity in elemental analysis. The deleterious effects of laser power fluctuations, surface properties, and defocusing effects caused by crater formation can be minimized by normalizing the ICP emission signal with respect to the acoustic wave. This paper also illustrates the feasibility of acoustic wave normalization in a flowing, atmospheric pressure ablation cell, as opposed to the static, low-pressure cells used previously (*13*, *14*). In future experiments, a cell with a very low dead volume, like those described by Carr and Horlick (*20*) and Tremblay et al. (*10*), may be useful to maximize the transport efficiency and the time correlation between emission signal and acoustic signal. It will also be interesting to apply these normalization techniques to the more sensitive ICP-MS measurement and to determine whether acoustic normalization can be used for many different sample types to compensate for the usual lack of matrix-matched standards.

ACKNOWLEDGMENT

We are grateful to Royce K. Winge of Ames Laboratory for helping with ICP-AES operation and emission spectral assignment.

LITERATURE CITED

(1) Gray, A. L. *Analyst* **1985**, *110*, 551–556.
(2) Ishizuka, T.; Uwamino, Y. *Spectrochim. Acta, Part B* **1983**, *38B*, 519–527.
(3) Thompson, M.; Goulter, J. E.; Sieper, F. *Analyst* **1981**, *106*, 32–39.
(4) Arrowsmith, P. *Anal. Chem.* **1987**, *59*, 1437–1444.
(5) Arrowsmith, P.; Hughes, S. K. *Appl. Spectrosc.* **1988**, *42*, 1231–1239.
(6) Olesik, J. W.; Smith, L. J.; Williamsen, E. J. *Anal. Chem.* **1989**, *61*, 2002–2008.
(7) Cicerone, M. T.; Farnsworth, P. B. *Spectrochim. Acta, Part B* **1989**, *44B*, 897–908.
(8) Winge, R. K.; Crain, J. S.; Houk, R. S. Unpublished results.
(9) Su, G.; Lin, S. *J. Anal. At. Spectrom.* **1988**, *3*, 841–847.
(10) Tremblay, M. E.; Smith, B. W.; Leong, M. B.; Winefordner, L. D. *Spectrosc. Lett.* **1987**, *20*, 311–318.
(11) Huie, C. W.; Yeung, E. S. *Anal. Chem.* **1986**, *58*, 1989–1993.
(12) Dittrich, K.; Niebergall, K.; Wennrich, R. *Fres. Z. Anal. Chem.* **1987**, *328*, 330–339.
(13) Chen, G.; Yeung, E. S. *Anal. Chem.* **1988**, *60*, 2258–2263.
(14) Pang, H.; Yeung, E. S. *Anal. Chem.* **1989**, *61*, 2546–2551.
(15) Winge, R. K.; Fassel, V. A.; Edelson, M. C. *Spectrochim. Acta, Part B* **1988**, *43B*, 85–91.
(16) Scott, R. H.; Fassel, V. A.; Kniseley, R. N.; Nixon, D. E. *Anal. Chem.* **1974**, *46*, 75–80.
(17) Mochizuki, T.; Sakashita, A.; Iwata, H.; Kagaya, T.; Shimanura, T.; Blair, P. *Anal. Sci.* **1988**, *4*, 403–409.
(18) Mitchell, P. G.; Sneddon, J.; Radziemski, L. J. *Appl. Spectrosc.* **1987**, *41*, 141–148.
(19) Iida, Y. *Spectrochim. Acta* **1990**, *45B*, 427–438.
(20) Carr, J. W.; Horlick, G. *Spectrochim. Acta, Part B* **1982**, *37B*, 1–15.

RECEIVED for review August 27, 1990. Accepted November 27, 1990. The Ames Laboratory is operated by Iowa State University for the U.S. Department of Energy under Contract W-7405-Eng-82. This work was supported by the Director of Energy Research, Office of Basic Energy Sciences, Division of Chemical Sciences.

TECHNICAL NOTES

Carbon-Fiber Ultramicroelectrodes Modified with Conductive Polymeric Tetrakis(3-methoxy-4-hydroxyphenyl)porphyrin for Determination of Nickel in Single Biological Cells

Frederick Bailey and Tadeusz Malinski*

Department of Chemistry, Oakland University, Rochester, Michigan 48039-4401

Frederick Kiechle

Department of Clinical Pathology, William Beaumont Hospital, Royal Oak, Michigan 48072

INTRODUCTION

Chemically modified microelectrodes add the dimension of selectivity to the inherent sensitivity of ultramicroelectrodes (*1*, *2*). The modification of conventional scale electrodes (1-mm diameter) with conductive nickel poly(tetrakis(3-methoxy-4-hydroxyphenyl)porphyrin) has been described previously (*3*). In this work, this modification is applied to ultramicroelectrodes for the detection of nickel in a single biological cell.

Although no specific function for nickel has been established, evidence exists that supports the hypothesis that Ni(II) is an essential metal that occurs at trace concentrations in physiological and environmental systems. At higher concentrations, it has been found to cause contact dermatitis, fibrosis, emphysema, and pulmonary lesions, and of most concern, it was found to be carcinogenic (*4*, *5*). Subsequently, it is desirable to monitor the levels of nickel in organisms and the environment. Inhalation is the predominant route of exposure in man. Studies have shown that following inhalation, nickel is distributed in the following way, listed from high to low concentrations: lung, heart, kidney = brain, liver (*6*). Total nickel concentrations in cells have been determined by using radiochemical or liquid scintillation counting techniques with ^{63}Ni. However, autoradiographic techniques cannot differentiate between nickel bound by proteins or adsorbed onto cellular membranes and unbound nickel in intracellular fluids. Ultramicroelectrodes can be used as an invasive technique to determine unbound nickel directly in intracellular fluids.

Ultramicroelectrodes have been designed for the detection of small biological molecules and drugs in physiological fluids (*7*). They can be fabricated with appropriate dimensions to be inserted in a single cell or tissue. Microelectrodes have increased mass transport, decreased double-layer capacitance, and decreased ohmic loss with the general effect of an increased signal to noise ratio, a time independent response, and higher sensitivity (*1*, *8*). Selectivity of ultramicroelectrodes can be achieved by modification of the electrode surface (*9*).

This paper presents a method for determination of the unbound nickel in single biological cells, through the use of ultramicroelectrodes modified with a conductive polymeric porphyrin film. Nickel tetrakis(3-methoxy-4-hydroxyphenyl)porphyrin (TMHPPNi) is used as an agent to modify the carbon-fiber microelectrodes. Initial oxidation of the monomeric TMHPPNi leads to polymerization and formation of highly conductive polymer film on the electrode surface.

The polymer undergoes facile demetalation in acid solution leaving an intact, adherent, conductive film on the electrode surface that then selectively chemically incorporates Ni(II) cations from analyte solutions. The electrode can then be transfered to a blank electrolysis solution where current, due to either the Ni(II)/Ni(III) oxidation or the catalytic oxidation of water, can be used as an analytical signal observed by differential-pulse voltammetry (DPV) (*3*).

* To whom correspondence should be addressed.

EXPERIMENTAL SECTION

Reagents and Materials. Nickel tetrakis(3-methoxy-4-hydroxyphenyl)porphyrin was synthesized according to a procedure described previously (*10*). Celion G50-300 carbon fibers with a diameter of 6 μm were obtained from BASF. All acids and bases used were Suprapure (Ultrex, J. T. Baker). Standard solutions of cations were prepared from 1000 μg mL^{-1} ICP reference stock standards (Spex Industries) for Ni(II), Fe(III), Cd(II), Pb(II), Cu(II), and Co(II). NBS 1643b Trace Elements in Water, used as an analytical standard, was obtained from the U.S. National Bureau of Standards. A culture of H4-II-C3 rat hepatoma cells were grown on glass plates with Dalbecco's modified Eagle medium (Gibco Laboratories), which contained L-glutamine at a concentration of 4 mM and 15% controlled-process serum replacement (Sigma). Nickel accumulations and analytical measurements were performed with the cells in Trizma buffer. This solution was held at 37 °C.

Apparatus. A classical, three-electrode system in a quartz cell fitted with a Teflon cap was used for modification of carbon fibers with poly-TMHPP and for Ni(II) determinations. The working electrode was a poly-TMHPP ultramicroelectrode prepared as described below. Platinum wire was used as the auxiliary electrode, and a saturated calomel electrode (SCE), as the reference electrode. The SCE was separated from the analytical solution by a bridge, fitted with a Vycor disk (IBM), containing saturated KCl. All potentials are reported vs SCE.

A PAR Model 174A polarographic analyzer with a PAR Model 181 current-sensitive preamplifier were used for DPV, and the resulting current–voltage curves were recorded with a PAR Model 9002A X-Y recorder.

Ultramicroelectrode Fabrication. Ultramicroelectrodes were produced by threading an individual carbon fiber (Celion G50-300) through the pulled end of a capillary tube with approximately 1 cm left protruding. Nonconductive 5-min epoxy (Devcon) was put at the glass/fiber interface. When the epoxy that is drawn into the tip of the capillary dried, the carbon fiber was sealed in place.

A key factor in these studies is that the length and area of the electroactive surface must be appropriate for the dimensions of the cells under investigation. Submerging the end of the electrode in melted wax coats the carbon fiber. Carefully burning the coated fiber in a controlled temperature gradient obtained with a microburner sharpens the tip (*11*). The length and shape of the electroactive area obtained is controlled by the thickness of the wax coating, which is controlled by the temperature of the melted wax. In this work, the sharpened tip (0.5–1 μm) of the fiber was covered electrochemically with 10–90 monolayers of polymeric porphyrin, demetalated, implanted, and used for Ni(II) accu-

0003-2700/91/0363-0395$02.50/0

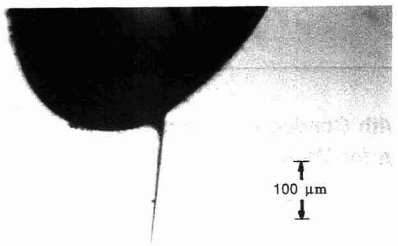

Figure 1. Microscopic photograph of a carbon-fiber ultramicroelectrode.

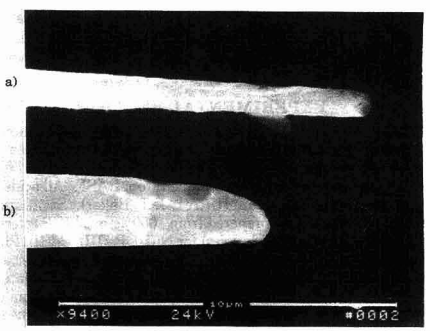

Figure 2. Scanning electron micrograph of an unplated electrode (a), and an electrode which has been plated with the polymeric TMHPPNi (b).

mulations and current determinations.

Figure 1 is a photograph of a sharpened electrode observed under a microscope. Waxing prior to the thermal sharpening step produces a short "spearhead" that is the only electrically conductive area that can be plated with polymeric TMHPPNi film. Electron micrographs of the carbon fiber with and without the film are shown in Figure 2. In the final step of electrode fabrication, the other end of the carbon fiber was attached to a copper wire lead with the use of silver epoxy (A. I. Technology).

Poly-TMHPP Electrode Modification. The electrode modification process begins with deposition of conductive, poly-TMHPPNi film on the electrode surface and verification of film deposition. Deposition is followed by demetalation and verification of demetalation.

Polymeric film is deposited from a solution of 0.1 M NaOH containing 5×10^{-4} M TMHPPNi by constant-potential electrolysis at 0.7 V. A peak attributable to the Ni(II)/Ni(III) couple appears at $E_{1/2} = 0.50$ V in a DPV scan. The number of monolayers deposited is dependent upon the initial concentration of TMHPPNi and the time of electrolysis. After film formation, the electrode is removed from the deposition solution, rinsed, and immersed in 0.1 M NaOH. The presence of poly-TMHPPNi film is confirmed by the Ni(II)/Ni(III) couple, which appears at $E_{1/2} = 0.50$ V.

The poly-TMHPPNi film is then demetalated by placing the electrode in a stirred 0.1 M HCl solution for 120 s. The electrode then is removed from the solution, rinsed, and immersed in 0.1 M NaOH. The absence of peaks associated with the Ni(II)/Ni(III) couple when scanning between 0.0 and 0.70 V confirms the absence of Ni in the demetalated poly-TMHPP film..

Electrodes have been stored with intermittent use for periods as long as 1 month without deterioration in response. Chemical

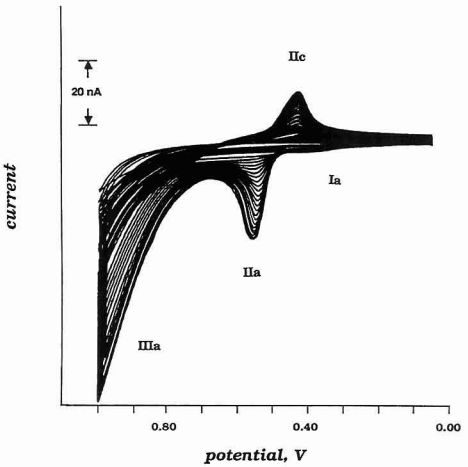

Figure 3. Continuous-scan cyclic voltammogram of TMHPPNi on a carbon-fiber ultramicroelectrode (area of 20 μm^2) in 0.1 M NaOH (scan rate 100 mV s^{-1}).

preconcentration of nickel was performed in 5-mL solutions contained in a quartz cell or from a single biological cell. Implantation of the ultramicroelectrodes into individual cells was effected by using a Nikon TMS inverted microscope and a Stoelting HS 6 micromanipulator. Preconcentration times studied varied from 1.5–30 min. Solutions were not stirred.

The poly-TMHPP film electrode with its incorporated nickel was removed from the analyte solution, rinsed with H_2O, and then transferred to 0.1 or 1.0 M NaOH, and nickel was determined by DPV.

Liquid Scintillation Counting of ^{63}Ni. A tissue culture of H4-II-C3 rat hepatoma cells was solubilized in organic quaternary amines (PCS, New England Nuclear). Typically, 0.2–0.3 g of the wet cell sample was vortexed with 1–2 mL of the amines, incubated overnight at 50 °C, and then mixed with liquid scintillator (Aquasol-Beckman). A 1-mL aliquot of solubilized sample was added to 15–20 mL of liquid scintillator. The counting efficiency, using the tritium channel ($E\beta$-max, 60 keV), was about 50%. Samples were standardized internally with no more than 25 μL of ^{63}Ni/20 mL of counting mixture.

RESULTS AND DISCUSSION

A detailed characterization of the TMHPPNi film formation on conventional electrodes has been the subject of previous works (*10*). Figure 3 shows the growth patterns for TMHPPNi in continuous-scan cyclic voltammetry from 0.00 to 1.00 V at a carbon-fiber electrode (20-μm^2 surface area). Peak Ia corresponds to the oxidation of the porphyrin ring on an ultramicroelectrode and peaks IIa and IIc, observed at $E_{1/2} = 0.50$ V, correspond to the Ni(II)/Ni(III) redox couple. Peak IIIa corresponds to the catalytic oxidation of water to molecular oxygen. Deposition of polymeric TMHPPNi on ultramicroelectrodes during continuous-scan cyclic voltammetry is relatively slow and requires about 90–100 scans from 0.00 to 0.70 V (scan rate 0.10 V s^{-1}) to obtain 30 equivalent monolayers on a 78-μm^2 electrode. This is less efficient than at larger electrodes (area of 0.07 cm^2) on which polymerization and film formation is observed after a few scans using cyclic voltammetry.

In order to obtain an electrode capable of preconcentrating Ni(II) from the analyte solution, the original Ni in the polymeric TMHPPNi film has to be removed. The extent of the demetalation process was observed by placing the poly-TMHPPNi/carbon-fiber ultramicroelectrode electrode that

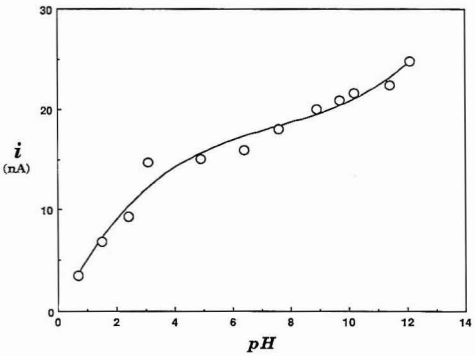

Figure 4. pH dependance of demetalation for polymeric TMHPPNi. The film thickness was 83 monolayer equivalents, and the electrode area was 720 μm^2.

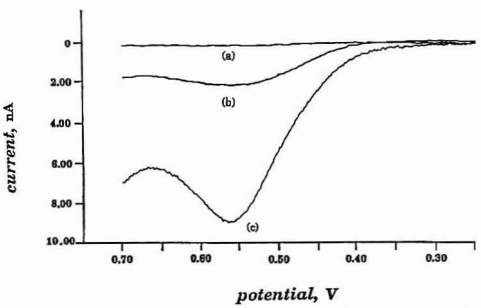

Figure 5. Differential-pulse voltammograms of nickel obtained with polymeric TMHPPNi film in 0.1 M NaOH (a) background and of preconcentrated nickel from 1×10^{-4} M (b) and 5×10^{-4} M (c) solutions at pH 7.4 for 15 min.

had been previously immersed in acid, which leaches the Ni(II) from the porphyrin, in a 0.1 M NaOH solution and monitoring the current due to oxidation of Ni(II) to Ni(III) (peak IIa) or the catalytic oxidation of water (peak IIIa). A demetalation time of 2 min in a 0.1 M HCl solution was found to be sufficient to remove the Ni(II) to a concentration level below that detectable by differential-pulse voltammetry. Demetalation of the polymeric porphyrin film strongly depends on the pH of the solution. Figure 4 shows the relationship between pH of the solution and demetalation of the film on an ultramicroelectrode. This figure gives an indication of the useable pH range. Once demetalated, the poly-TMHPP film can be expected to readily reincorporate nickel from the analytical system (*3*).

Figure 5 shows the anodic Ni(II) oxidation wave obtained with the poly-TMHPP ultramicroelectrode for three concentrations of standard nickel solutions. The reincorporation of nickel occurs with high efficiency from solutions having pH values of 7.0–9.0. In solutions with pH values lower than 6, a significant decrease in the rate of reincorporation of Ni(II) is observed. On the other hand, if the pH is greater than 10.0, the Ni(II) forms insoluble $Ni(OH)_2$ ($k_{sp} = 1.6 \times 10^{-14}$), decreasing the concentration of Ni and inhibiting the metalation process (*3*).

Both preconcentration time and initial nickel concentration should affect chemical preconcentration (*12*). Preconcentration yield was studied for each of these parameters. Solution concentrations of 5–10 000 μM Ni(II) were investigated. For 1.5–3.0-min preconcentration times, a linear relationship

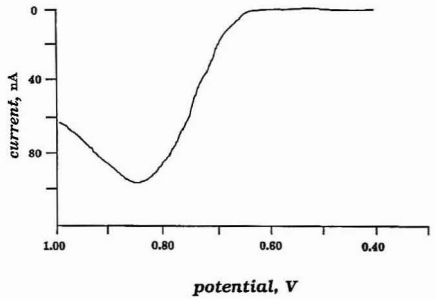

Figure 6. Differential-pulse voltammogram of catalytic oxidation of water obtained with polymeric TMHPPNi film in 0.1 M NaOH. Nickel was preconcentrated from 1×10^{-5} M solutions at pH 7.4 for 15 min; the electrode area was 20 μm^2.

between preconcentration time and peak current was observed. In general, with longer preconcentration time (greater than 3 min for 1×10^{-4} M), a steady decrease of $\Delta i/\Delta t$ will be observed due to the decrease of the nickel concentration gradient, between the solution and film.

A linear relationship between the current of the Ni(II)/Ni(III) reaction in the film and nickel concentration in the bulk solution was observed for the concentration range between 1×10^{-4} and 1×10^{-2} M. A detection limit of 5×10^{-5} M was obtained by using this redox couple as the analytical signal. However, the high current observed for catalytic oxidation of water on poly-TMHPPNi (wave III) using ultramicroelectrodes creates a means of lowering detection limits. A good linear relationship between concentration of nickel in solution and catalytic current was observed with ultramicroelectrodes. Thus, in addition to voltammetric determination of nickel based on wave IIa, a convenient method based on monitoring a catalytic current due to oxidation of water to oxygen (wave III) can be used. The catalytic current is several orders of magnitude higher than current due to Ni(II)/Ni(III) process. Therefore, a decrease of the detection limit by this same order magnitude would be expected. The relationship between Ni concentration and catalytic current in 0.1 M NaOH is linear between 5×10^{-3} and 5×10^{-6} M Ni(II) with a detection limit approaching 10^{-6} M.

The analytical signal due to the catalytic process can be enhanced by 1 order of magnitude if 1.0 M NaOH is used for the Ni determination step instead of 0.1 M NaOH. This is consistent with the mechanism of the oxidation of water on polymeric TMHPPNi surfaces (*10*).

Figure 6 shows the differential-pulse voltammogram of catalytic oxidation of water by nickel accumulated in the porphyrinic film from a 2×10^{-5} M solution of Ni(II) at a pH of 7.4 for 15 min. No interferences were observed for solutions of 1×10^{-5} M Ni(II) that contained 50-fold excesses of Cu(II), Pb(II), Cd(II), or Fe(III). The interference of the Co(II), when the catalytic peak was observed, was less significant (about 40% reduction of current) compared to that seen in earlier studies (80% for 50-fold excess) when the Ni(II)/Ni(III) peak was followed under similar conditions.

In order to determine whether the presence of protein molecules in biological fluid would block the electrode surface, thereby interfering with the uptake of Ni(II), solutions mimetic of intercellular fluids, were prepared containing 50 mg of albumin in 5 mL of H_2O. This concentration should be representative of total protein concentrations in cells. Determination of Ni(II) was then successfully performed in this solution. This experiment showed that Ni(II) uptake did occur. Therefore, the electrode surface is not significantly blocked by the high cellular protein content.

The use of ultramicroelectrodes, now proven for the measurement of Ni(II) concentrations in solution, was applied to the measurement of Ni(II) in an individual cell of a cell culture of H4-II-C3 rat hepatoma cells. Cells in this particular cell line have an approximately spherical shape with a diameter nearing 10-15 μm. Thus the length of the sharpened/electroactive tip, which is plated with TMHPP, should be somewhat less than this dimension.

The cell culture was grown directly on glass plates in Dalbecco's modified Eagle medium at 37 °C in a 10% CO_2 atmosphere. The media was drawn off, and Tris buffer (containing 3% BSA, 2 mM glucose, and 1×10^{-4} M Ni) was added. The cells were soaked in this Tris buffer solution for 45 min in order to allow Ni uptake. Following the uptake time, this Tris buffer was withdrawn and a fresh Tris buffer solution that did not contain Ni(II) was added. Cells grown on glass slides in a Petri dish were placed on the inverted microscope, and the electrode was implanted by using the micromanipulator. When the electrode pierced the cell wall, the timing was initiated. The electrode was left in place for the desired preconcentration time. At the end of this time period the electrode was extracted, rinsed with deionized water, and placed in a 0.1 M NaOH solution for the determination of Ni(II). The current from this analysis relates to the concentration of unbound Ni(II) in the cell. For a 2-min preconcentration time, if the measurement was taken after the cell culture was subjected to a buffer with 1.0×10^{-4} M Ni(II) for 45 min, the resulting current represented a $(1.0 \pm 0.1) \times 10^{-5}$ M Ni(II) concentration in the cell. Total nickel accumulation, for conditions which were identical with those employed with the microelectrode studies, was determined by using liquid scintillation counting of ^{63}Ni. The calculated nickel accumulation was 10 μg/million cells. Assuming the cells have a spherical shape with a radius of 7 μm, the total concentration of accumulated nickel, bound and unbound, in each cell would be 1×10^{-4} M. Therefore, in a single rat hepatoma cell after 45 min, the total nickel accumulation was 0.01 pg and only 6% (0.6 fg) of this amount was unbound, as determined by using the ultramicroelectrode and differential-pulse voltammetry. After 5 h of allowed accumulation, the total amount of nickel doubled to 0.02 pg/cell. However, no significant change in the amount of unbound nickel was observed. A similar total accumulation of nickel (0.015 pg/cell) for a 4 h incubation period from 3×10^{-4} M nickel solution was observed for FM3H cells from C3H mammary tissue (*13*).

These data indicate that relatively high amounts of nickel accumulate in the cells studied. This effect has been noted previously and attributed to the fact that the cell membrane is negatively charged, enabling it to compete for nickel binding with other ligands. Nickel internalization by the cell is possible by either active transport, most likely through calcium and/or magnesium channels, or passive diffusion of neutral, lipophilic complexes (*14*). While the exact nature of the nickel-binding sites in the cell is unknown, studies have pointed to the involvement of phosphate groups of both RNA and to a lesser extent DNA along with proteins, phospholipids, amino acids, mononucleotides, and other ligands. These extensive binding capabilities within the cell for nickel account for the relatively small proportion of total nickel concentration left unbound.

ACKNOWLEDGMENT

We thank Drs. J. R. Fish and K. Kasprzak for helpful comments and suggestions.

Registry No. Ni, 7440-02-0; nickel poly(tetrakis(3-methoxy-4-hydroxyphenyl)porphyrin), 126752-50-9.

LITERATURE CITED

(1) Fleischmann, M.; Pons, S.; Rolison, D. R.; Schmidt, P. P. *Ultramicroelectrodes*; Datatech Systems Inc.: Morganton, NC, 1987.
(2) Guadalupe, A. R.; Abruna, H. D. *Anal. Chem.* **1985**, *57*, 142-149.
(3) Malinski, T.; Ciszewski, A.; Fish, J. R.; Czuchajowski, L. *Anal. Chem.* **1990**, *62*, 909-914.
(4) Fishbein, L.; Mehlman, M. A. *Advances in Modern Environmental Toxicology*; CRC Press: Boca Raton, FL, 1987; pp 145-183.
(5) Costa, M. *Env. Health. Perspect.* **1989**, *81*, 73-76.
(6) Coogan, T. P.; Latta, D. M.; Snow, E. T.; Costa, M. *Crit. Rev. Toxicol.* **1989**, *19*, 341-384.
(7) Ponchon, J. L.; Cespuglio, R.; Gonon, F.; Jouvet, M.; Pujol, J. F. *Anal. Chem.* **1979**, *51*, 1483-86.
(8) Tanaka, K.; Kashiwagi, N. *J. Electroanal. Chem. Interfacial Electrochem.* **1989**, *275*, 95-98.
(9) Turner, A. P. F.; Karube, I.; Wilson, G. S. *Biosensors Fundamentals and Applications*; Oxford University Press: Oxford, New York, Tokyo, 1987.
(10) Malinski, T.; Ciszewski, A.; Bennett, J. E.; Czuchajowski, L. *Proceedings of the Symposium on Nickel Hydroxide Electrodes*; The Electrochemical Society Meeting, Hollywood, FL, October 1989; Corrigan, D. A., Zimmerman, A. H. Eds.; The Electrochemical Society: Pennington, NJ, 1990; pp 177-193.
(11) Josowicz, M.; Potje, K.; Liess, H.-D.; Besenhard, J. O.; Kurtze, A. *Electrochemistry, Sensors and Analysis*; Elsevier: Amsterdam, 1987; pp 87-104.
(12) Whiteley, L. D.; Martin, C. R. *Anal. Chem.* **1987**, *59*, 1746-1751.
(13) Nishimura, M.; Umeda, M. *Mutat. Res.* **1979**, *68*, 337-349.
(14) Nieboer, E.; Stafford, A. E.; Evans, S. L.; Dolovich, J. *Nickel in the Human Environment*; Sunderman, F. W., Ed.; IARC Science Publication No. 53; International Agency for Research on Cancer: Lyon, 1984; pp 321-331.

RECEIVED for review June 20, 1990. Accepted October 26, 1990. This work was supported by a grant from William Beaumont Hospital Research Institute.

Tissue Bioelectrode for Eliminating Protein Interferences

Joseph Wang,* Li Huey Wu, Sandra Martinez, and Juanita Sanchez

Department of Chemistry, New Mexico State University, Las Cruces, New Mexico 88003

One of the major difficulties in clinical applications of voltammetry stems from the adsorption of proteins onto the electrode surface. A degraded and irreproducible response characterizes these deactivation processes. Such loss of electrode activity is commonly referred to as "fouling" or "poisoning". Various approaches have been used to alleviate the protein fouling problem. Permselective coatings represent one useful avenue. Size-selective cellulose acetate films have been particularly attractive for this task (*1*, *2*). Reactivation schemes, based on electrochemical or laser pulses, have also proved useful for the prevention of surface passivation effects (*3*, *4*).

This paper describes a novel and highly useful approach, based on tissue-modified electrodes, for the prevention of biofouling. The rich biocatalytic activity of tissue-containing surfaces is exploited for in situ enzymatic digestion of interfering proteins. The use of plant or animal tissues in place of isolated enzymes can offer attractive properties for biosensing probes, including extended lifetimes, high enzymatic activity, and low cost (*5*, *6*). These advantages have been

* To whom correspondence should be addressed.

0003-2700/91/0363-0398$02.50/0

illustrated for effective detection of numerous substrates of enzymes present in these cellular materials (7). We have also illustrated recently the utility of tissue electrodes for eliminating interferences from coexisting electroactive constituents (8). For example, zucchini electrodes, rich with the enzyme ascorbic acid oxidase, were employed for effective depletion of ascorbic acid from the surface. Similar enzymatic digestion is employed in the present work for eliminating major interferences from coexisting surface-active proteins. This concept is illustrated by using a papaya-containing carbon-paste electrode. The presence of the protease enzyme papain in the papaya tissue (9) effectively eliminates protein interferences. The broad action of papain toward the cleavage of numerous peptide bonds (10) makes it an ideal choice for this antifouling action. The mixed tissue–carbon-paste configuration (11), with its immediate proximity of biocatalytic and sensing sites, is particularly attractive for this task, as it rapidly "destroys" the approaching protein. The smaller peptides resulting from the cleavage of the protein do not passivate the surface. The needs for protective layers or reactivation schemes are thus greatly alleviated. These advantages are illustrated below for measurements of numerous compounds of biological and pharamceutical significance, in the presence of representative proteins.

EXPERIMENTAL SECTION

Apparatus. Experiments were performed with a Bioanalytical System (BAS) Model VC-2 voltammetric cell that had a working volume of 10 mL. The cell was joined to the working electrode, reference electrode, (Ag/AgCl (3 M NaCl), Model RE-1, BAS) and the platinum-wire auxiliary electrode through holes in its Teflon over. Voltammograms were recorded with an EG&G PAR Model 264A voltammetric analyzer and a Houston Instruments X-Y recorder.

The papaya-modified electrode was prepared in the following manner. A 0.2-g section of the papaya (from ca. 2 mm below the skin of the fruit) was ground with a mortar and pestle and hand-mixed (with spatula) with 1.8 g of carbon paste (made of 60% (w/w) graphite powder and 40% (w/w) mineral oil). Mixing proceeded for 20 min to ensure uniform distribution of the tissue. A portion of this modified carbon paste was packed into a 2 mm diameter cavity of a cylindrical Teflon shaft. The surface was smoothed on a weigh paper, and was preconditioned, by immersion for 12 h (at 5 °C) in a 5 mM cysteine solution.

Reagents. All solutions were prepared with doubly distilled water. The supporting electrolyte was 0.05 M phosphate buffer (pH 7.4). Acetaminophen, dopamine, uric acid, cysteine, papain (E.C.3.4.22.2, crude type), theophylline, albumin, globulin, gelatin, and casein (Sigma) were used without further purification. The papayas used in this study were purchased from a local grocery store.

RESULTS AND DISCUSSION

Papain is the main protein constituent of the latex of the fruit, leaves, and trunk of the papaya tree (*Carica papaya*). Such thiol protease breaks down proteins by hydrolyzing specific peptide bonds. This protein-digesting property has found a wide range of industrial uses (e.g. meat tenderization), but has not been exploited for analytical purposes. Figure 1 illustrates the prevention of protein biofouling achieved by incorporating the papaya tissue within the carbon-paste matrix. It shows typical differential pulse voltammograms for 2×10^{-4} M acetaminophen, in the presence of increasing levels of albumin (200–1000 ppm), as obtained at the unmodified (A) and papaya-modified (B) carbon-paste electrodes. The plain electrode exhibits rapid depressions (up to 63%) and shifts of the acetaminophen peak on successive additions of the proteins. In contrast, essentially the same acetaminophen response is observed at the tissue electrode in the absence and presence of albumin. Apparently, the tissue-based papain rapidly destroys the protein molecules upon their approach to the surface, thus minimizing passivation effects.

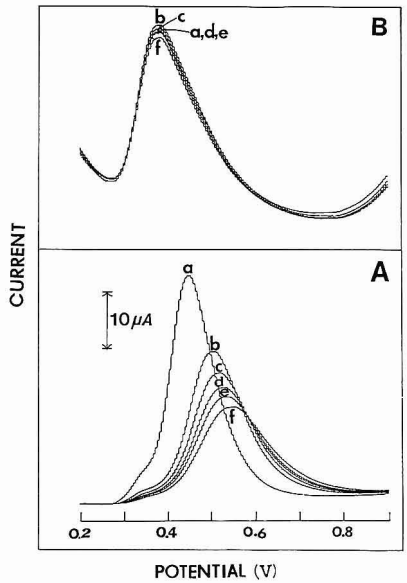

Figure 1. Differential pulse voltammograms at the plain (A) and tissue (10% w/w papaya) (B) electrodes, for 2×10^{-4} M acetaminophen: (a) analyte alone; (b–f) same as a but after successive additions of 200 ppm albumin. Conditions: scan rate, 10 mV/s; amplitude, 25 mV; electrolyte, 0.05 M phosphate buffer (pH 7.4).

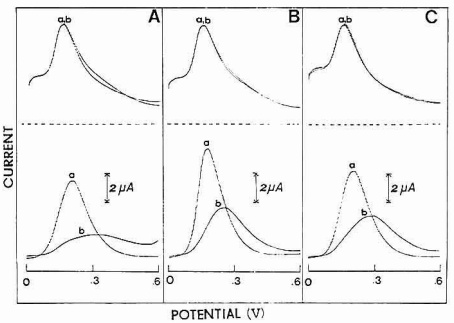

Figure 2. Differential pulse voltammograms, at the unmodified (bottom) and tissue-modified (top) electrodes, for 5×10^{-5} M dopamine in the absence (a) and presence (b) of 100 ppm casein (A), albumin (B), and gelatin (C). Other conditions are given in Figure 1.

The slightly smaller peak at the tissue electrode is attributed to the reduced graphite content. Significantly larger sensitivity losses characterize the use of permselective protective layers (e.g., ref 2).

The interference of different proteins upon the measurement of various oxidizable analytes can be effectively addressed at the papaya-modified electrode. Figure 2 compares differential pulse voltammograms for dopamine, as obtained before (a) and after (b) addition of 100 ppm casein (A), albumin (B), and gelatin (C). All three proteins result in appreciable (45–90%) loss of the activity of the plain electrode (bottom). The tissue electrode, in contrast, exhibits a highly stable dopamine response, with no apparent change in the peak currents (top, a vs b). Similar advantages were observed in measurements of 2×10^{-4} M uric acid in the presence of 400 ppm globulin and of 2.5×10^{-4} M theophylline in the

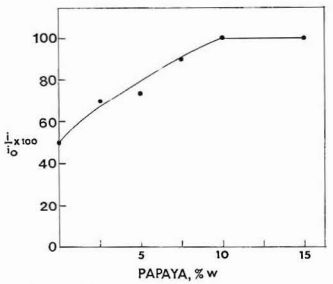

Figure 3. Effect of the paste composition (tissue "loading") on the diminution of the 1×10^{-4} M acetaminophen peak in the presence of 200 ppm albumin. Other conditions are given in Figure 1.

presence of 200 ppm casein (not shown).

The paste composition has a profound effect on the prevention of protein interference. Figure 3 shows the dependence of the acetaminophen-peak diminution (in the presence of 200 ppm albumin) upon the tissue loading. As expected from the increased protease activity of the electrode, the protein interference decreases upon increasing the amount of tissue in the paste (from 50 to 10% depression at 0–7.5% (w/w) papaya, respectively). A 10% (w/w) tissue loading offers complete elimination of the protein interference. It should be noted, however, that the paste composition needed for effective prevention of protein fouling must be adjusted to suit the conditions of each particular case (mass transport, protein and its level, etc.). No apparent difference in the resistance to biofouling was observed when papaya sections from different locations in the fruit were employed.

Tissue electrodes are particularly attractive for the task of prevention of interferences, because cellular materials represent a rich source of biocatalytic activity. Unlike substrate measurements (for which control of the enzymatic activity is often desired), the destruction of interferences requires a large excess of the enzyme, as provided by the surface-containing tissue. Additional activation of the crude papain was obtained by a simple preconditioning step—immersion the tissue electrode in a cysteine solution—aimed at incorporating essential sulfhydryl groups. Other sensing advantages of the tissue-containing papain are its broad optimum pH (6–7.5), heat stability (up to 80 °C), and extremely low cost. No apparent interference from other enzymatic pathways, that may be present in the tissue, or from the variety of smaller peptides resulting from the papain action (*10*) was observed throughout this study.

Control experiments, utilizing the enzyme (papain)-modified carbon pastes (10% w/w) yielded similar elimination of protein interferences (not shown). This fact, coupled with the cysteine dependence, supports that it is the papain in the papaya which is responsible for the antifouling effect (although other proteases present in smaller levels in the papaya latex, chymopapain and papaya peptidase, may assist in the protection process).

The high enzymatic activity, characteristic of tissue bioelectrodes, results in excellent resistance to biofouling over a wide concentration range of different proteins. For example, Figure 4 shows the effects of albumin (A), globulin (B), casein (C), and gelatin (D) on the voltammetric response of acetaminophen. Successive additions of these proteins, over the 200–1000 ppm range, caused significant peak current depressions at the unmodified electrode (b). With the papaya-modified electrode, in contrast, the quantitation of the drug is not affected by the presence of the proteins over their entire concentration range (a). In order to be practical for routine biosensing applications, the resistance to fouling should be

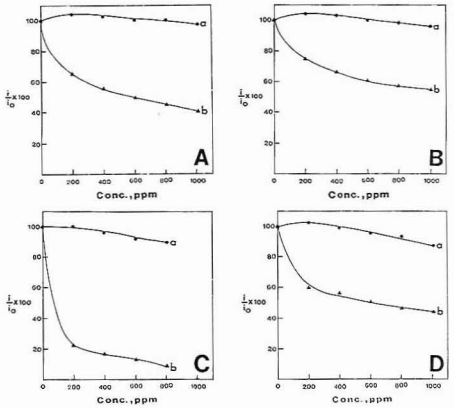

Figure 4. Effect of albumin (A), globulin (B), casein (C), and gelatin (D) on the voltammetric peak of 2×10^{-4} M acetaminophen, at the tissue (a) and plain (b) carbon-paste electrodes. Other conditions are given in Figure 1.

maintained over a long period of time. The stability of the response of the tissue electrode was tested by checking its behavior, in the presence of 200 ppm globulin, during a long run of 24 successive determinations of dopamine, carried out over a 2-h period. No apparent change in the sensitivity was observed throughout this operation. Indeed, tissue-containing surfaces have been employed over an entire week, performing hundreds of measurements with excellent prevention of protein passivation effects.

In conclusion, the present study illustrates that tissue bioelectrodes can be employed to circumvent protein passivation effects, hence imparting high stability during electrochemical measurements. Such in situ destruction of potential interferences should simplify sample cleanup procedures and eliminates the need for protective membranes or reactivation schemes. Hence, this concept should be highly suitable for routine sensing applications based on finite-current measurements. Other tissues, e.g. pineapple or fig, rich with the proteases bromelain and ficin, respectively, should yield similar advantages. The mixed carbon-paste configuration permits simultaneous incorporation of other biological and chemical modifiers, as well as convenient miniaturization. For example, simultaneous elimination of major electroactive constituents may be accomplished via coimmobilization of enzymes, such as uricase, ascorbic acid oxidase, or tyrosinase, while lipid interferences may be addressed in the presence of lipase.

Registry No. Papain, 9001-73-4; carbon, 7440-44-0.

LITERATURE CITED

(1) Sittampalam, G.; Wilson, G. S. *Anal. Chem.* **1983**, *55*, 1608.
(2) Wang, J.; Hutchins, L. D. *Anal. Chem.* **1985**, *57*, 1536.
(3) Room, M.; McCreery, R. L. *Anal. Chem.* **1986**, *58*, 2745.
(4) Wang, J.; Lin, M. S. *Anal. Chem.* **1988**, *60*, 499.
(5) Rechnitz, G. A. *Science (Washington, D.C.)* **1981**, *214*, 287.
(6) Arnold, M. A. *Am. Lab. (Fairfield, CT)* **1983**, *15*(6), 34.
(7) Wang, J. *Electroanalysis*, in press.
(8) Wang, J.; Naser, N.; Ozsoz, M. *Anal. Chim. Acta* **1990**, *234*, 315.
(9) Liener, I. E. The Sulfhydryl Porteases in *Food Related Enzymes*; Whitaker, J., Ed.; American Chemical Society: Washington, DC, 1974.
(10) Hill, R. In *Hydrolysis of Proteins*; Anfinsen, C. B., Anson, M. L., Edsall, J. T., Richards, F. M., Eds.; Advances in Protein Chemistry; Academic Press: New York, 1965; Vol. 20.
(11) Wang, J.; Lin, M. S. *Anal. Chem.* **1988**, *60*, 1545.

RECEIVED for review August 6, 1990. Accepted November 7, 1990. This work was supported by grants from the National Institutes of Health (GM 30913-06, GM 07667-14, and RR 08136-16).

The Best Software for Chemists at the Best Prices

from The American Chemical Society

ACS Software brings you two of the most popular software programs for analytical chemists . . .

Analytical Chemistry by Open Learning (ACOL)

Gets up to speed on major analytical methods

With this interactive software/text teaching tool, you can quickly learn how to operate analytical instruments with skill and proficiency. *ACOL* provides ideal training for technicians and scientists, covering both the philosophy and basics of the best-known instrumentation techniques.

Realistically simulates the analytical environment

ACOL modules provide training, continuing education, and updating in seven of the most widely used analytical methods. Each package consists of a software-based training disk and a text that complements it. The software offers interactive experience in making decisions during an analysis, and provides immediate feedback on the computer screen, simulating instrument output.

***ACOL* programs cover seven top analytical techniques**

- Atomic Absorption Spectroscopy
- Gas Chromatography
- High Performance Liquid Chromatography
- Polarography
- Radiochemistry
- Fluorescence Spectroscopy
- Quantitative IR and UV

Software and book (all programs); books also sold separately, call for full details.

For each program:

List price $395
Member price $335
Academic price $295

Hardware requirements: *IBM PC or compatibles; EGA or VGA graphics board; color monitor.*
Produced by: *ACOL, Thames Polytechnic*

UN-PLOT-IT Plus

Automated digitizing for PCs and MACs

Now you can automatically digitize strip chart output, (x,y) recorder output, instrumental output, published graphs, old graphs, shapes, figures, and just about anything else.

The data is saved in ASCII format and an be imported into almost any commercial graphics package. You can also use our software to re-scale and re-plot graphs, integrate peak areas, smooth data, perform regression analysis, take derivatives, etc.

Simple, logical menus make the use of *UN-PLOT-IT-Plus* a breeze. Choose from "line follow" mode, raster scan mode, and manual mode to match your data and your requirements. In addition, *UN-PLOT-IT Plus* delivers accuracy of 0.05 mm; speed of up to 200 points per minute; the ability to store up to 5,000 data points; and much more.

List price $385
Member price $325
Academic price $345

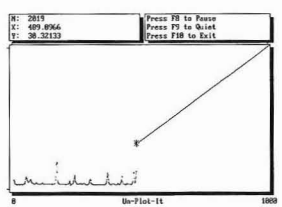

Hardware requirements:

IBM: IBM PC and compatibles, HPGL compatible; pen plotter

Mac: Any Macintosh; 256K RAM; pen plotter.

Produced by: *Silk Scientific, Inc.*

To order these and other ACS Software products, call TOLL FREE 1-800-227-5558. In Washington, DC, call (202) 872-4363. Or fax your order to (202) 872-6067.

See it at PittCON '91! Booth #3062.

The best benchtop GC/MS just got better... and costs less!

HP 5890 Series II GC sets new industry standards with high temperature operation, cool on-column injection and pressure programming.

Universal, specific and picogram-sensitive, the HP 5971A MSD produces true EI spectra.

Microsoft® Windows 3.0 with improved memory management allows faster execution of numerous programs simultaneously.

Custom Reports software links GC/MS results with Excel spreadsheet and graphics.

HP ChemStation (MS-DOS® series), coupled with new MS software, speeds integration and quantitation of complex mixtures.

HP DeskJet 500 Printer.

84 Mbyte disk drive boosts capacity and speeds processing.

If you thought our benchtop GC/MS broke price-performance barriers before, check these enhancements. Microsoft® Windows 3.0 for greater speed and ease of use. New ChemStation for faster multitasking. High speed integrator for rapid quantitation. Powerful, easy-to-use Custom Report function. And DeskJet Printer. All this—along with true EI spectra—for $48,940.

For even higher throughput, options include a 486-based ChemStation, LaserJet Series III Printer, LaserMaster® card, autosampler and bar-code reader. CI spectra is also an option.

Put the system to work in any lab performing qualitative, quantitative or target compound analysis. Then enjoy the highest uptime in the industry because HP is consistently ranked number 1 for service and support. For more information, call **1 800 334-3110, Ext. 10245.**

HEWLETT PACKARD

CIRCLE 60 ON READER SERVICE CARD